UNIVERSITÄT PADERBORN
Die Universität der Informationsgesellschaft

FAKULTÄT FÜR
ELEKTROTECHNIK,
INFORMATIK UND
MATHEMATIK

Semi-guided waves in integrated optical waveguide structures

Von der Fakultät für Elektrotechnik, Informatik und Mathematik
der Universität Paderborn

zur Erlangung des akademischen Grades

Doktor der Ingenieurwissenschaften (Dr.-Ing.)

genehmigte Dissertation

von

M. Sc. Lena Ebers

Erster Gutachter:	Prof. Dr. Jens Förstner
Zweiter Gutachter:	Prof. Dr. Carsten Rockstuhl

Tag der mündlichen Prüfung: 09.02.2022

Paderborn 2022

Diss. EIM-E/365

Danksagung

Mein Dank gilt allen, die mich während der Anfertigung dieser Arbeit unterstützt haben. Eine wissenschaftliche Arbeit ist nie das Werk einer einzelnen Person, daher bedanke ich mich besonders bei

... Prof. Dr. Jens Förstner für die Aufnahme in seine Gruppe, die Betreuung und die regelmäßigen konstruktiven Diskussionen.

... Prof. Dr. Carsten Rockstuhl für die Übernahme des Zweitgutachtens dieser Arbeit.

... Dr. Manfred Hammer für die unglaubliche Hilfe und Unterstützung, für jegliche Diskussionen und Anregungen, die maßgeblich zu dieser Arbeit beigetragen haben, und für die penible Durchsicht der Arbeit.

... J.-Prof. Dr. Tim Bartley, J.-Prof. Dr. Polina Sharapova und allen beteiligten Kollegen der Fachbereiche für die tolle Zusammenarbeit.

... meinen Arbeitskollegen für hilfreiche Diskussionen, während der manchmal zu langen Kaffeepausen, und ganz besonders Henna für ihre Unterstützung.

... meiner Familie, meinen Freunden und Kevin für ihren Rückhalt.

Contents

Abstract

In this work, the electromagnetic wave propagation in integrated optical waveguides is studied by using semi-analytical and numerical simulation methods.

In the first part, 2-D high-index contrast Si/SiO_2 dielectric slab waveguide configurations are investigated. The structures are excited with semi-guided waves at oblique angles of propagation. Due to this, power transfer to specific outgoing modes can be suppressed, resulting in completely lossless configurations. In particular, the wave propagation in bent slab waveguides, compositions of bent and straight slab waveguides, representing corner- and step-like structures, and optical microresonators, consisting of one or two rectangular cavities, is studied. The structures are investigated for their modal properties, transmission/reflection and resonance behavior. The excitation is further examined for incoming, laterally confined wave bundles of semi-guided waves to realize practically more relevant 3-D configurations. Additionally, a stepwise angular spectrum method in combination with full vectorial 2-D finite element solutions for subproblems of lower complexity to numerically simulate the wave propagation in full 3-D planar lens-like waveguides is presented. The method offers a fast design optimization of these 3-D lens structures.

In the second part, the wave propagation in lithium niobate waveguide structures is examined, which are used for quantum optical effects. On the one hand, superconducting nanowires on titanium in-diffused lithium niobate waveguides with an additional tapered silicon layer are used for single photon detection. The wave propagation in these 3-D multiscale tapers is studied by introducing a unidirectional finite element modal matching method based on a staircase approximation, where eigenmodes are propagated along the waveguide segments with constant 2-D cross sections. The method enables an efficient and fast optimization for 3-D taper shapes. On the other hand, lithium niobate rib waveguides on silicon dioxide platforms are analyzed, focusing on the nonlinear parametric down-conversion process used for the generation of entangled photons. Examples for structures that exhibit an appropriate nonlinear coupling of the involved fields are presented. Concepts, as discussed in the context of semi-guided waves, can be applied here.

Zusammenfassung

In dieser Arbeit wird die elektromagnetische Wellenausbreitung in integrierten optischen Wellenleitern mit Hilfe von halb analytischen und numerischen Simulationsmethoden untersucht.

Im ersten Teil werden 2-D Si/SiO_2-Wellenleiterkonfigurationen mit hohem Brechungsindexkontrast betrachtet. Die Strukturen werden mit halb geführten Wellen unter schrägen Ausbreitungswinkeln angeregt. Dadurch kann die Leistungsübertragung zu bestimmten ausgehenden Moden unterdrückt werden, wodurch vollständig verlustfreie Systeme entstehen. Betrachtet wird insbesondere die Wellenausbreitung in gebogenen Schichtwellenleitern, in Zusammensetzungen aus gebogenen und geraden Schichtwellenleitern, die ecken- und stufenförmige Strukturen darstellen, sowie in optischen Mikroresonatoren, die eine oder zwei rechteckige Kavitäten besitzen. Die Strukturen werden bezüglich ihrer modalen Eigenschaften, ihres Transmissions- und Reflexionsverhaltens sowie ihres Resonanzverhaltens analysiert. Zusätzlich dient die Anregung mit einem seitlich begrenzten, einfallenden Wellenbündel aus halb geführten Wellen dazu, praktisch relevantere 3-D Konfigurationen zu realisieren. Darüber hinaus wird eine schrittweise Winkelspektrum-Methode (engl.: angular spectrum method) vorgestellt, die es ermöglicht, in Kombination mit voll vektoriellen 2-D Finite-Elemente-Lösungen für Teilprobleme mit geringerer Komplexität, die Wellenausbreitung in planaren, linsenförmigen Wellenleitern numerisch in drei Raumrichtungen zu berechnen. Die Methode ermöglicht eine schnelle Designoptimierung dieser 3-D Linsenstrukturen.

Im zweiten Teil dieser Arbeit wird die Ausbreitung in Wellenleiterstrukturen aus Lithiumniobat untersucht, welche für quantenoptische Effekte genutzt werden. Zur Detektion einzelner Photonen werden supraleitende Nanodrähte auf eindiffundierten Lithiumniobat Wellenleitern mit zusätzlicher Taperschicht aus Silizium betrachtet. Um die Wellenausbreitung in diesen 3-D Wellenleitern zu beschreiben, wird eine einseitig gerichtete Finite-Elemente "Modal Matching" Methode eingeführt. Diese basiert auf einer Stufenapproximation, bei der sich Eigenmoden entlang der Wellenleitersegmente mit konstanten 2-D Querschnitten ausbreiten. Auch hier eignet sich die Methode für eine effiziente und schnelle Optimierung der 3-D Taperformen. Abschließend werden Rippenwellenleiter aus Lithiumniobat analysiert, die auf Siliziumdioxid Plattformen aufgebracht sind. Der Schwerpunkt liegt hier auf dem nichtlinearen "Parametric Down-Conversion" Prozess, der für die Erzeugung verschränkter Photonen verwendet wird. Verschiedene Beispiele für Strukturen werden vorgestellt, die eine entsprechende nichtlineare Kopplung der beteiligten Felder aufweisen. Hier können Konzepte, wie sie im Zusammenhang mit halb geführten Wellen diskutiert wurden, angewandt werden.

Chapter 1

Introduction

Silicon photonics has become a promising platform in integrated optics as it offers many advantages [1–3]. One major benefit is the compatibility with standard complementary metal-oxide semiconductor (CMOS) fabrication technologies [4]. Thus, the integration of silicon-photonic devices combining optical and electric components on the same chip is feasible. Moreover, the strong light confinement in high-index contrast silicon structures enables a high-density integration of photonic components within a small area and makes it robust, e.g., for bends or crossings [2, 5, 6]. Furthermore, it is a cost efficient and reliable solution with an extensive supply for the future [2,3,6]. Its applications cover a broad spectrum in the fields of computing, communication, sensing and imaging [6].

The basic building block of an integrated optical device are optical waveguides which are used to interconnect various components on the chip with relatively low losses [7]. Dielectric waveguides consist of a core with higher medium than the surrounding cladding region, so that an electromagnetic wave is guided in a specific direction and confined in the core region due to total internal reflection. Dielectric slab waveguides are the simplest form of an optical waveguide because the Maxwell equations can be solved almost analytically. The guided waves in these 2-D structures are semi-guided because their field profile is localized in only one transverse direction. The study of these simple waveguide structures is fundamental to get an understanding of more complex structures in photonic technologies [8, 9].

In the first part of this work, we will especially focus on 2-D dielectric slab waveguides that connect to a "discontinuity" region of rather arbitrary shape, such as bends or gaps. Discontinuities in dielectric slab waveguides are commonplace in many optoelectronic systems and usually cause losses and reflections [9]. But they are necessary to manipulate the field behavior for prescribed applications and functionalities. We are particularly interested in the excitation of these 2-D structures at oblique angles of propagation normal to the waveguide axis because radiation losses as well as power transfer to certain outgoing modes can be suppressed beyond specific incidence angles [10–21].

We start in Chapter 2 with the introduction of some basic 2-D optical waveguide concepts, including Maxwell's equations, dielectric slab waveguides and optical fibers. The theoretical part is concluded with the derivation of the modal properties of the fields in slab waveguide

discontinuities at oblique propagation angles, and with an analysis of the excitation of these 2-D structures with laterally confined beams of semi-guided waves to realize more realistic 3-D structures.

The propagation of light in these dielectric waveguides is described by the Maxwell equations. In most cases, they are solved by numerical methods. Throughout this work, we use the simulation software COMSOL Multiphysics [22], which is based on the finite element method [23,24]. Therefore, we introduce the theory of the finite element method in Chapter 3 and outline the required settings for the simulations in COMSOL.

Specific 2-D slab waveguide discontinuities are then analyzed in Chapters 4–6. We start in Chapter 4 with a semi-analytical derivation of the modal properties of spiral modes guided at oblique angles in bent slab waveguides [18]. This includes the calculation of their wavenumbers and the corresponding mode profiles. A combination of different bent and straight slab waveguides – step and corner structures – serving as couplers for full power transmission on different levels [13, 25–27], is then studied in Chapter 5 regarding their transmission and reflection behavior depending on the incidence angle. The bent steps are further analyzed in a 3-D setting for incoming laterally confined wave packets of semi-guided waves. Another field of 2-D concepts are optical microresonators which are considered in Chapter 6 consisting of two parallel slab waveguides connected via a rectangular cavity, serving as a power divider or add-drop filter [28, 29], and are analyzed for their resonance behavior.

Dielectric waveguide lenses are basic building blocks in integrated optics for focusing, imaging, spatial filtering, Fourier transforming and convolving operations [30]. In Chapter 7, we consider these in full 3-D. One basic tool to calculate the propagation of light in optical systems is the angular spectrum method [31–46], as a part of diffraction theory [47–49]. The method was already extended to calculate the diffraction of light from or to curved surfaces [46]. We present a modified version of the stepwise angular spectrum method to calculate the wave propagation in curved waveguide structures. This concerns, on the one hand, 2-D curved interfaces of different materials, for which the method is derived mainly for illustration, and, on the other hand, full 3-D waveguide lenses consisting of slab waveguides with different cross sections which are separated via one or two curved surfaces. The method requires less computational time and memory space compared to rigorous 3-D simulation techniques. Furthermore, we show that different optimization algorithms can be easily applied to our method with reasonable effort.

Besides silicon, lithium niobate has become a promising material in integrated photonics due to its large electro-optic coefficient and large second-order nonlinear susceptibility [50, 51]. It provides an ideal platform for integrated quantum photonics [52], e.g., for photon absorption [53–55] or nonlinear interaction of waves to generate entangled photons [56–58]. We do not intent to go into details in quantum optics, but study the wave propagation in optical waveguide structures that are used for quantum optical effects.

For photon detection, superconducting nanowires are deposited on top of titanium in-diffused lithium niobate (Ti:LN) waveguides [53–55]. Ti:LN waveguides offer a promising platform because they have the advantage of low loss and high efficient coupling to standard optical fibers [59]. But the detection rate is limited as the guided modes of the Ti:LN waveguide are distributed some micrometers below the waveguide surface, thus the overlap with the detecting

nanowires is small. A possible way to increase the detection rate is by applying an additional high refractive index silicon taper on top of the Ti:LN waveguide to pull up the mode closer to the wires [55].

Tapers are a fundamental component for photonic integrated circuits to achieve efficient coupling with minimal loss between optical waveguides of different cross sections by changing the size and the shape of the optical waveguide mode [60–67]. However, an efficient design requires an appropriate software that correctly simulates the wave propagation in these 3-D structures. A simple and effective simulation technique offers the modal matching method [60–63, 68], which describes the modal behavior at a waveguide junction of different cross sections. In Chapter 8, we introduce a unidirectional finite element modal matching method to calculate the wave propagation in 3-D multiscale tapers. The approach is based on a staircase approximation of the taper, where eigenmodes are propagated along the waveguide segments with constant 2-D cross sections. We are searching for taper geometries that exhibit a high transmission and compact size. Additionally, optimization algorithms are applied that provide swift results. An optimized shape of the taper is presented that leads to a high absorption for small taper lengths.

Finally, lithium niobate on insulator (LNOI) rib waveguides are studied for their nonlinear interaction of waves to generate entangled photons in Chapter 9 [69]. LNOI waveguides combine the advantages of lithium niobate and silicon used in integrated quantum photonics [70–72]. One of the most common nonlinear processes to generate entangled photons is the parametric down-conversion process [50], where the signal, idler and pump photons are interacting. Usually, the signal and idler photons exhibit different group velocities, but this is compensated by considering LNOI rib waveguides of specific size [73, 74]. By choosing the geometry accordingly, the signal and idler fields are (quasi) degenerate modes of the waveguide, propagate together, but still have different mode profiles. In Chapter 9, we present specific rib waveguide structures that enable nonlinear interaction. Finally, circling back to the beginning of this thesis, we show that an excitation of the structure with a pump mode, guided by the adjoining slab of the rib at oblique angles of propagation, can also lead to nonlinear interaction of the involved fields.

The work on this thesis was supervised by and carried out in cooperation with colleagues from the *Theoretical Electrical Engineering* group at Paderborn University. Chapters 4 and 5 are already part of a bachelor and master thesis, but for the sake of completeness, we include the results as they fit thematically very well to the topic of this thesis. The work on Chapters 8 and 9 was accompanied by colleagues from the departments of *Mesoscopic Quantum Optics* and *Theoretical Quantum Optics* at Paderborn University, respectively.

Publications

The work on this thesis was accompanied by the following publications and conference proceedings:

- L. Ebers, A. Ferreri, M. Hammer, M. Albert, C. Meier, J. Förstner, and P. R. Sharapova. Flexible source of correlated photons based on LNOI rib waveguides. *arXiv:2110.10562 [quant-ph]*, 2021.
- L. Ebers, M. Hammer, and J. Förstner. Light diffraction in slab waveguide lenses simulated with the stepwise angular spectrum method. *Opt. Express*, 28(24):36361–36379, 2020 [75].
- L. Ebers, M. Hammer, M. B. Berkemeier, A. Menzel, and J. Förstner. Coupled microstrip-cavities under oblique incidence of semi-guided waves: a lossless integrated optical add-drop filter. *OSA Continuum*, 2(11):3288–3298, 2019 [28].
- L. Ebers, M. Hammer, and J. Förstner. Oblique incidence of semi-guided planar waves on slab waveguide steps: effects of rounded edges. *Opt. Express*, 26(14):18621–18632, 2018 [13].
- L. Ebers, M. Hammer, and J. Förstner. Spiral modes supported by circular dielectric tubes and tube segments. *Optical and Quantum Electronics*, 49(4):176, 2017 [18].
- M. Hammer, L. Ebers, and J. Förstner. Configurable lossless broadband beam splitters for semi-guided waves in integrated silicon photonics. (2021, submitted) [20].
- J. P. Höpker, V. B. Verma, M. Protte, R. Ricken, V. Quiring, C. Eigner, L. Ebers, M. Hammer, J. Förstner, C. Silberhorn, R. P. Mirin, S. Woo Nam, and T. J Bartley. Integrated superconducting nanowire single-photon detectors on titanium in-diffused lithium niobate waveguides. *Journal of Physics: Photonics*, 3(3):034022, 2021 [53].
- M. Hammer, L. Ebers, and J. Förstner. Resonant evanescent excitation of guided waves with high-order optical angular momentum. *J. Opt. Soc. Am. B*, 38(5):1717–1728, 2021 [19].
- M. Hammer, L. Ebers, and J. Förstner. Hybrid coupled mode modelling of the evanescent excitation of a dielectric tube by semi-guided waves at oblique angles. *Optical and Quantum Electronics*, 52(472), 2020 [21].

- M. Protte, L. Ebers, M. Hammer, J. P. Höpker, M. Albert, V. Quiring, C. Meier, J. Förstner, C. Silberhorn, and T. J. Bartley. Towards semiconductor-superconductor-crystal hybrid integration for quantum photonics. In *OSA Quantum 2.0 Conference*, page QTh7A.8. Optical Society of America, 2020 [55].

- L. Ebers, M. Hammer, M. B. Berkemeier, A. Menzel, J. Förstner Lossless optical microstrip filters for semi-guided waves at oblique incidence *Theoretical and Numerical Tools for Nanophotonics, TNTN2020 / XXVIII International Workshop on Optical Wave & Waveguide Theory and Numerical Modelling, OWTNM2020*, Berlin, Germany, Proceedings 43 (2020)

- M. Hammer, L. Ebers, and J. Förstner. Oblique quasi-lossless excitation of a thin silicon slab waveguide: a guided-wave variant of an anti-reflection coating. *J. Opt. Soc. Am. B*, 36(9):2395–2401, 2019 [12].

- M. Hammer, L. Ebers, and J. Förstner. Oblique evanescent excitation of a dielectric strip: A model resonator with an open optical cavity of unlimited Q. *Opt. Express*, 27(7):9313–9320, 2019 [10].

- L. Ebers, M. B. Berkemeier, A. Menzel, M. Hammer, J. Förstner Integrated optical add-drop filter based on oblique excitation of rectangular microstrip-cavities *8th doctoral conference on optics, DoKDoK 2019*, Eisenach, Germany, Proceedings, 2019 [76]

- L. Ebers, M. Hammer, J. P. Höpker, T. Bartley, J. Förstner Unidirectional vectorial eigenmode propagation for multiscale tapered waveguides in 3D *XXVII International Workshop on Optical Wave & Waveguide Theory and Numerical Modelling, OWTNM2019*, Málaga, Spain, Proceedings 19, 2019 [77]

- M. Hammer, L. Ebers, A. Hildebrandt, A. Alhaddad, and J. Förstner. Oblique semi-guided waves: 2-D integrated photonics with negative effective permittivity. *2018 IEEE 17th International Conference on Mathematical Methods in Electromagnetic Theory (MMET)*, pages 5–9, 2018 [11].

Chapter 2

Optical waveguide theory

In the following chapter, the theoretical basics for our numerical simulations are presented. Fundamentals are the Maxwell equations introduced in Section 2.1. Most of the content in this work deals with dielectric optical waveguides, in particular, dielectric slab waveguides and optical step-index fibers. The mathematical foundations are presented in Section 2.2. Note that the theory is subject of standard textbooks on optical waveguide theory, e.g., [8, 9, 78].

We are specifically interested in compositions of dielectric slab waveguides separated by almost arbitrary shaped 2-D linear discontinuities and the excitation of these structures with a semi-guided mode propagating at oblique angles. Beyond certain incidence angles, excitation of specific outgoing modes is forbidden and losses are fully suppressed, i.e., completely lossless 2-D waveguides can be realized. The modal properties of the involved fields are derived analytically and presented in Section 2.3.

For practically more relevant full 3-D solutions, we consider excitation by laterally limited 3-D wave bundles of semi-guided waves into the 2-D waveguide structures. These wave packets can be excited by placing a wide rib waveguide in front of the structure to excite a mode that is confined in the transverse plane. The theory of excitation with a rib waveguide mode is derived in Section 2.4.

The discussion of lithium niobate on insulator (LNOI) waveguides in Chapter 9 requires a review of certain aspects of the theory of nonlinear optics. For convenience, these are introduced directly at the beginning of that respective part of the thesis.

2.1 Maxwell's equations

The Maxwell equations are the fundamental laws of classical electrodynamics and describe the behavior of electromagnetic fields in the presence of charges and currents. These are coupled partial differential equations for the electric field $\hat{\mathbf{E}}$, magnetic field $\hat{\mathbf{H}}$, dielectric displacement $\hat{\mathbf{D}}$ and magnetic flux density $\hat{\mathbf{B}}$. The four macroscopic Maxwell equations, consisting of Gauss's

law, no-monopole law, Faraday's law and Ampère's law, are written as [79]

$$\begin{aligned} \nabla \cdot \hat{\mathbf{D}} &= \rho, \\ \nabla \cdot \hat{\mathbf{B}} &= 0, \\ \nabla \times \hat{\mathbf{E}} &= -\frac{\partial}{\partial t}\hat{\mathbf{B}}, \\ \nabla \times \hat{\mathbf{H}} &= \frac{\partial}{\partial t}\hat{\mathbf{D}} + \hat{\mathbf{J}}, \end{aligned} \tag{2.1}$$

with the current density $\hat{\mathbf{J}}$ and charge density ρ. All electric and magnetic field components are assumed to be time t and space (x, y, z) dependent. The constitutive equations

$$\begin{aligned} \hat{\mathbf{D}} &= \varepsilon_0 \hat{\mathbf{E}} + \hat{\mathbf{P}}, \\ \hat{\mathbf{B}} &= \mu_0(\hat{\mathbf{H}} + \hat{\mathbf{M}}) \end{aligned} \tag{2.2}$$

complete the set of equations [79]. Here, $\hat{\mathbf{P}}$ and $\hat{\mathbf{M}}$ are the polarization and magnetization, and ε_0 and μ_0 are the free space permittivity and free space permeability, respectively.

We are interested in stationary optical electric $\hat{\mathbf{E}}$ and magnetic $\hat{\mathbf{H}}$ fields with a harmonic time dependence $\sim \mathrm{e}^{\mathrm{i}\omega t}$, thus

$$\begin{pmatrix} \hat{\mathbf{E}} \\ \hat{\mathbf{H}} \end{pmatrix}(x, y, z, t) = \mathrm{Re}\left\{ \begin{pmatrix} \tilde{\mathbf{E}} \\ \tilde{\mathbf{H}} \end{pmatrix}(x, y, z)\mathrm{e}^{\mathrm{i}\omega t} \right\}, \tag{2.3}$$

where $\tilde{\mathbf{E}}$ and $\tilde{\mathbf{H}}$ are the optical fields in the frequency domain. The fields are characterized by their angular frequency $\omega = k_0 c_0 = 2\pi \dfrac{c_0}{\lambda_0}$ with vacuum wavelength λ_0, vacuum speed of light $c_0 = \dfrac{1}{\sqrt{\varepsilon_0 \mu_0}}$ and vacuum wavenumber k_0.

Thus, the Maxwell equations can be written in the frequency domain as

$$\begin{aligned} \nabla \cdot \tilde{\mathbf{D}} &= \rho, \\ \nabla \cdot \tilde{\mathbf{B}} &= 0, \\ \nabla \times \tilde{\mathbf{E}} &= -\mathrm{i}\omega \tilde{\mathbf{B}}, \\ \nabla \times \tilde{\mathbf{H}} &= \mathrm{i}\omega \tilde{\mathbf{D}} + \tilde{\mathbf{J}} \end{aligned} \tag{2.4}$$

with the material equations

$$\begin{aligned} \tilde{\mathbf{D}} &= \varepsilon_0 \varepsilon_r \tilde{\mathbf{E}}, \\ \tilde{\mathbf{B}} &= \mu_0 \mu_r \tilde{\mathbf{H}} \end{aligned} \tag{2.5}$$

for a linear, dielectric material with polarization $\tilde{\mathbf{P}} = \varepsilon_0 \chi_e \tilde{\mathbf{E}}$ and magnetization $\tilde{\mathbf{M}} = \chi_m \tilde{\mathbf{H}}$, electric susceptibility χ_e, magnetic susceptibility χ_m, relative permittivity $\varepsilon_r = 1 + \chi_e$ and relative permeability $\mu_r = 1 + \chi_m$.

The considered medium is assumed to be lossless, dielectric, isotropic, non magnetic and space dependent, thus $\mu_r = 1$ and $\varepsilon_r(x, y, z) = n^2(x, y, z)$. Here, n is the refractive index of the

material. Furthermore, currents and free charges are not included, thus $\tilde{\mathbf{J}} = 0$ and $\rho = 0$. Then, the Maxwell equations in the frequency domain for a dielectric, linear, non-magnetic and isotropic material are given by

$$\begin{aligned} \nabla \times \tilde{\mathbf{E}} &= -\mathrm{i}\omega\mu_0\tilde{\mathbf{H}}, \\ \nabla \times \tilde{\mathbf{H}} &= \mathrm{i}\omega\varepsilon_0\varepsilon_r\tilde{\mathbf{E}}. \end{aligned} \tag{2.6}$$

These can be combined to the wave-equations for either the electric $\tilde{\mathbf{E}}$ or magnetic $\tilde{\mathbf{H}}$ field with non constant permittivity $\partial\varepsilon_r \neq 0$

$$\begin{aligned} \nabla \times (\nabla \times \tilde{\mathbf{E}}) - k_0^2\varepsilon_r\tilde{\mathbf{E}} &= 0, \\ \varepsilon_r\nabla \times (\frac{1}{\varepsilon_r}\nabla \times \tilde{\mathbf{H}}) - k_0^2\varepsilon_r\tilde{\mathbf{H}} &= 0. \end{aligned} \tag{2.7}$$

2.2 Dielectric waveguides

Light can be confined in optical dielectric waveguide structures. A typical dielectric waveguide consists of a core that is coated with a cladding medium of lower refractive index than the core medium. Due to total internal reflection, the light is confined in the core region and the wave is able to propagate in the direction of the core. There are several types of optical waveguide structures, e.g., slabs or fibers are among the many types of optical waveguide structures [8, 78].

We assume a waveguide with arbitrary but finite cross section in the x-y-plane, that is constant along the z-axis with $\partial_z\varepsilon_r = 0$. Potential waves are propagating in the z-direction, thus they exhibit a field dependence

$$\begin{pmatrix} \tilde{\mathbf{E}} \\ \tilde{\mathbf{H}} \end{pmatrix}(x, y, z) = \begin{pmatrix} \mathbf{E} \\ \mathbf{H} \end{pmatrix}(x, y)\mathrm{e}^{-\mathrm{i}k_z z}, \tag{2.8}$$

where k_z is the propagation constant or wavenumber, and $(\mathbf{E}, \mathbf{H})^{\mathrm{T}}$ is the mode profile depending on the transverse coordinates only.

When considering regions with constant refractive index ε_r, the wave equations (2.7) can be rewritten by using the ansatz in Eq. (2.8)

$$\begin{aligned} \Delta_{\mathrm{T}}\mathbf{E} + (k_0^2\varepsilon_r - k_z^2)\mathbf{E} &= 0, \\ \Delta_{\mathrm{T}}\mathbf{H} + (k_0^2\varepsilon_r - k_z^2)\mathbf{H} &= 0, \end{aligned} \tag{2.9}$$

where $\Delta_{\mathrm{T}} = \partial_x^2 + \partial_y^2$ is the Laplacian operator in the transverse plane only. This represents a system of partial differential equations which is to be completed by suitable boundary and interface conditions. Applying these conditions results in an eigenvalue problem of the abstract form

$$\mathsf{M}(k_z)\mathbf{A} = 0. \tag{2.10}$$

Here, $\mathbf{A}$ represents a vectorial profile or field and M is the system matrix depending on k_z. Both depend on the specific system under study. We will see examples on this in the following sections.

Modes are solutions of the eigenvalue problem (2.10). Generally, we are looking for guided modes that have a real propagation constant $k_z \in \mathbb{R}$ and are confined in the core region, thus the integral over the cross section of the Poynting vector

$$\mathbf{S} = \frac{1}{2}\mathrm{Re}\{\mathbf{E}^* \times \mathbf{H}\} \tag{2.11}$$

in propagation direction z should be finite, i.e.,

$$\int S_z \mathrm{d}x\mathrm{d}y < \infty. \tag{2.12}$$

The integral (2.12) represents the power flow of the electromagnetic wave in propagation direction.

By using the ansatz (2.8), it is possible to express the transverse components E_x, E_y, H_x and H_y through the electric and magnetic components in propagation direction, E_z and H_z. Thus, it is only necessary to solve a coupled system of 2-D partial differential equations for the two longitudinal electric and magnetic components E_z and H_z

$$\begin{aligned} \Delta_\mathrm{T} E_z + (k_0^2 \varepsilon_r - k_z^2) E_z = 0, \\ \Delta_\mathrm{T} H_z + (k_0^2 \varepsilon_r - k_z^2) H_z = 0. \end{aligned} \tag{2.13}$$

The remaining components are obtained directly by transforming Maxwell's equations to

$$\begin{aligned} E_x &= \frac{-\mathrm{i}}{k_0^2 \varepsilon_r - k_z^2}(k_z \partial_x E_z + \omega \mu_0 \partial_y H_z), \\ E_y &= \frac{-\mathrm{i}}{k_0^2 \varepsilon_r - k_z^2}(k_z \partial_y E_z - \omega \mu_0 \partial_x H_z), \\ H_x &= \frac{-\mathrm{i}}{k_0^2 \varepsilon_r - k_z^2}(k_z \partial_x H_z - \omega \varepsilon_0 \varepsilon_r \partial_y E_z), \\ H_y &= \frac{-\mathrm{i}}{k_0^2 \varepsilon_r - k_z^2}(k_z \partial_y H_z + \omega \varepsilon_0 \varepsilon_r \partial_x E_z). \end{aligned} \tag{2.14}$$

Alternative formulations are possible as well, relying on the transverse electric components E_x and E_y or on the transverse magnetic components H_x and H_y as principal components (instead of E_z and H_z).

Finally, we can further distinguish between different classes of modes, where the longitudinal field components are either vanishing or not [8]:

- $E_z = H_z = 0$: Transverse electromagnetic modes (TEM modes) that have electric and magnetic field components orthogonal to the propagation direction z. They only exist if $k_0^2 \varepsilon_r - k_z^2 = 0$
- $E_z = 0$, $H_z \neq 0$: Transverse electric modes (TE modes) with electric field components orthogonal to the propagation direction z.
- $H_z = 0$, $E_z \neq 0$: Transverse magnetic modes (TM modes) with magnetic field components orthogonal to the propagation direction z.
- $H_z \neq 0$, $E_z \neq 0$: Hybrid modes with all six components non-zero. They can further be distinguished in TE-like (EH) and TM-like (HE) modes, where either the electric or magnetic principal field component is dominant.

2.2.1 Slab waveguide

In the following, we discuss the optical dielectric slab waveguide in more detail, which is one of the simplest forms and can even be considered almost analytically [8, 9, 78].

Figure 2.1 shows a configuration of such a slab waveguide that consists of three layers with different dielectric materials n_c, n_s and n_f. The whole structure is infinitely expanded in the y-z-direction and the wave is propagating in the z-direction. The core has a thickness of d, while the cladding regions are half-infinite in $\pm x$-direction. If the refractive index in the core n_f is larger than the ones in the cladding n_c and substrate n_s, waves can be guided in this structure.

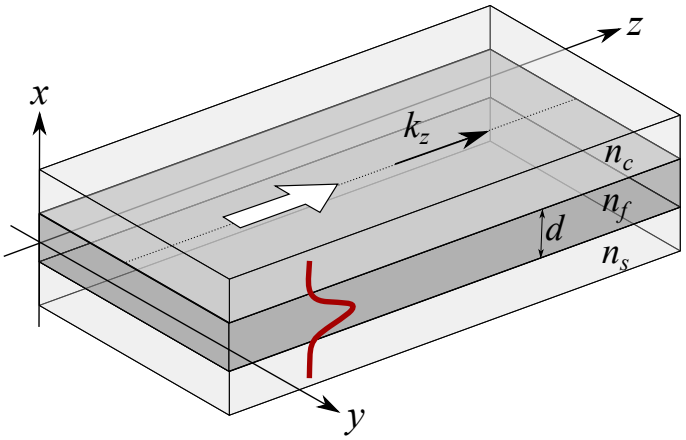

Figure 2.1: Dielectric slab waveguide with refractive indices n_c, n_f, n_s, thickness d and wave propagation in the z-direction with wavenumber $k_z = k_0 N_{\text{eff}}$.

The fields are assumed to propagate in the positive z-direction with wavenumber k_z. As the structure is constant along the y-direction, we are also looking for fields that are constant along that direction with $\partial_y = 0$. Thus, we can predict a field dependence

$$\begin{pmatrix} \tilde{\mathbf{E}} \\ \tilde{\mathbf{H}} \end{pmatrix} (x, y, z) = \begin{pmatrix} \mathbf{E} \\ \mathbf{H} \end{pmatrix} (x) \mathrm{e}^{-\mathrm{i}k_z z}. \tag{2.15}$$

In this case, the Maxwell equations (2.6) reduce to two separate sets of equations, representing either the transverse electric (TE) modes or the transverse magnetic (TM) modes as introduced in the previous section.

For the TE modes, the solution of the Maxwell equations is given by

$$\mathbf{E}(x) = \begin{pmatrix} 0 \\ \Psi(x) \\ 0 \end{pmatrix} \quad \text{and} \quad \mathbf{H}(x) = \frac{1}{\omega\mu_0} \begin{pmatrix} -k_z \Psi(x) \\ 0 \\ \mathrm{i}\partial_x \Psi(x) \end{pmatrix}, \tag{2.16}$$

where the principal electric field component $E_y(x) = \Psi(x)$ has to fulfill the TE-Helmholtz equation (2.7) (with $\partial_y \varepsilon_r = \partial_z \varepsilon_r = 0$)

$$\partial_x^2 \Psi + (k_0^2 \varepsilon_r - k_z^2)\Psi = 0. \tag{2.17}$$

On the other hand, the solution for the transverse magnetic modes is

$$\mathbf{E}(x) = \frac{1}{\omega\varepsilon_0\varepsilon_r}\begin{pmatrix} k_z\Psi(x) \\ 0 \\ -\mathrm{i}\partial_x\Psi(x) \end{pmatrix} \quad \text{and} \quad \mathbf{H}(x) = \begin{pmatrix} 0 \\ \Psi(x) \\ 0 \end{pmatrix}, \tag{2.18}$$

where the principal magnetic field component $H_y(x) = \Psi(x)$ has to satisfy the TM-Helmholtz equation (2.7) (with $\partial_y\varepsilon_r = \partial_z\varepsilon_r = 0$)

$$\varepsilon_r\partial_x(\frac{1}{\varepsilon_r}\partial_x\Psi) + (k_0^2\varepsilon_r - k_z^2)\Psi = 0. \tag{2.19}$$

Looking for guided modes that are localized around the core region, $\Psi(x)$ is a trigonometric function in the core and an exponential decaying function in the claddings. Considering the continuity conditions at both interfaces (E_y, H_x and H_z are continuous for TE modes; H_y, E_y and $\varepsilon_r E_x$ are continuous for TM modes), one obtains an eigenvalue equation for either TE or TM modes in the form of Eq. (2.10). This transcendental equation has to be solved numerically to find eigenvalue solutions k_z.

The calculated TE and TM modes are determined by their mode profile $\Psi(x)$ and their propagation constant $k_z = k_0 N_{\text{eff}}$, where $N_{\text{eff}} = k_z/k_0$ is the unitless effective refractive index or mode index of the mode. For symmetric waveguides with $n_c = n_s$, the solutions can be further classified in even and odd TE and TM modes. The number of guided modes in the waveguide depends on the considered wavelength, the geometry and the material parameters of the structure [8, 9].

For a mode to be guided in the waveguide, the value of k_z needs to satisfy the guidance condition [9]

$$\max(n_s, n_c) \leq N_{\text{eff}} \leq n_f. \tag{2.20}$$

If $N_{\text{eff}} < \max(n_s, n_c)$ applies, the field is radiating in at least one of the cladding regions and is no longer localized around the core. Thus, $N_{\text{eff}} = \max(n_s, n_c)$ is the cut-off condition of the waveguide. Contrarily, for $N_{\text{eff}} > n_f$, no modal solutions exist at all. With "fundamental TE" (TE_0) or "fundamental TM" (TM_0) mode, we refer to guided modes with the largest effective refractive index for either the TE or TM case.

n_c	n_f	n_s	$d/\,\mu$m	$\lambda_0/\,\mu$m	N_{TE_0}	N_{TM_0}	Ref.
1.6	1.7	1.6	1	1.3	1.6603	1.6575	Chapter 4
1.5	2	1.5	0.4	1.3	1.7979	1.7241	Chapter 4
1.45	3.4	1.45	0.25	1.55	2.8612	2.2280	Chapter 5
1.45	3.45	1.45	0.22	1.55	2.8227	2.0397	Chapters 6–7
1.45	3.45	1.45	0.05	1.55	1.7245	1.4612	Chapter 7
1.0	1.5	1.0	0.4	1.55	1.2303	1.1091	Section 6.4
1.0	2.1565	1.4589	0.25	0.775	1.9281	1.7804	Section 9.4
1.0	2.2242	1.4589	0.25	0.775	1.9943	1.8401	Section 9.4

Table 2.1: Effective mode indices N_{TE_0} and N_{TM_0} of specific slab waveguide configurations with refractive indices n_f (core), n_c (cladding), n_s (substrate) and core thickness d for vacuum wavelength λ_0.

The fundamental TE and TM modes guided by the slab waveguide structures considered in this work, defined by their material n_s, n_f and n_c, their thickness d and the wavelength λ_0, are displayed in the following Table 2.1. All configurations only support the fundamental TE and TM modes with effective mode indices N_{TE_0} and N_{TM_0}, respectively [80].

2.2.2 Step-index fiber

Optical waveguide fibers are mainly used in long distance telecommunication because of their huge advantage of low losses combined with low dispersion effects. Among others, the step-index fiber or the gradient-index fiber belong to this category of waveguides. In this section, we will consider the step-index fiber in more detail, as it can also be analyzed almost rigorously [8].

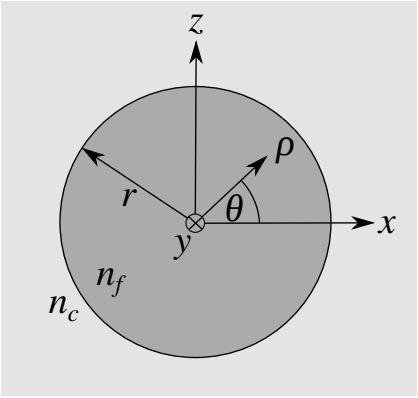

Figure 2.2: Cross section view of an optical step-index fiber with core radius r, core refractive index n_f and cladding refractive index n_c. The cladding region is assumed to be sufficiently large. The modes are propagating along the fiber axis in the y-direction.

The step-index fiber consists of a core with refractive index n_f and radius r, which is surrounded by a cladding material with refractive index $n_c < n_f$, as illustrated in Figure 2.2. Note that we now introduce the y-axis as the propagation direction while the x-z-coordinates represent the transverse cross section plane, so that it fits to the notation in Chapter 4.

The structure is described in cylindrical coordinates (ρ, θ, y). We consider time harmonic electric and magnetic fields that propagate in positive y-direction

$$\begin{pmatrix} \tilde{\mathbf{E}} \\ \tilde{\mathbf{H}} \end{pmatrix} (\rho, \theta, y) = \begin{pmatrix} \mathbf{E} \\ \mathbf{H} \end{pmatrix} (\rho, \theta) \mathrm{e}^{-\mathrm{i}k_y y}. \tag{2.21}$$

The modes that are guided by the fiber satisfy the Maxwell equations (2.6), which are given in

cylindrical coordinates as

$$\begin{aligned}
\frac{1}{\rho}\partial_\theta E_y + \mathrm{i}k_y E_\theta &= -\mathrm{i}\omega\mu_0 H_\rho,\\
-\mathrm{i}k_y E_\rho - \partial_\rho E_y &= -\mathrm{i}\omega\mu_0 H_\theta,\\
\frac{1}{r}\partial_\rho(\rho E_\theta) - \frac{1}{\rho}\partial_\theta E_\rho &= -\mathrm{i}\omega\mu_0 H_y,\\
\frac{1}{\rho}\partial_\theta H_y + \mathrm{i}k_y H_\theta &= \mathrm{i}\omega\varepsilon_0\varepsilon_r E_\rho,\\
-\mathrm{i}k_y H_\rho - \partial_\rho H_y &= \mathrm{i}\omega\varepsilon_0\varepsilon_r E_\theta,\\
\frac{1}{\rho}\partial_\rho(\rho H_\theta) - \frac{1}{\rho}\partial_\theta H_\rho &= \mathrm{i}\omega\varepsilon_0\varepsilon_r E_y
\end{aligned} \tag{2.22}$$

and the wave equations (2.7) are given by

$$\partial_\rho^2\Psi + \frac{1}{\rho}\partial_\rho\Psi + \frac{1}{\rho^2}\partial_\theta^2\Psi + (k_0^2\varepsilon_r - k_y^2)\Psi = 0, \tag{2.23}$$

for either $\Psi = E_y(\rho,\theta)$ or $\Psi = H_y(\rho,\theta)$ in regions with constant refractive index ε_r. The remaining other components are then calculated as

$$\begin{aligned}
E_\rho &= \frac{-\mathrm{i}}{k_0^2\varepsilon_r - k_y^2}(k_y\partial_\rho E_y + \frac{\omega\mu_0}{\rho}\partial_\theta H_y),\\
E_\theta &= \frac{-\mathrm{i}}{k_0^2\varepsilon_r - k_y^2}(\frac{k_y}{\rho}\partial_\theta E_y - \omega\mu_0\partial_\rho H_y),\\
H_\rho &= \frac{-\mathrm{i}}{k_0^2\varepsilon_r - k_y^2}(k_y\partial_\rho H_y - \frac{\omega\varepsilon_0\varepsilon_r}{\rho}\partial_\theta E_y),\\
H_\theta &= \frac{-\mathrm{i}}{k_0^2\varepsilon_r - k_y^2}(\frac{k_y}{\rho}\partial_\theta H_y + \omega\varepsilon_0\varepsilon_r\partial_\rho E_y).
\end{aligned} \tag{2.24}$$

We assume $\Psi(\rho,\theta) = f(\rho)g(\theta)$ with radial and angular functions f and g, respectively. The azimuthal dependency, $g(\theta)$, of the electromagnetic fields in axially symmetric fibers is expressed by the dependence

$$g(\theta) \propto \mathrm{e}^{\pm\mathrm{i}\nu\theta}, \tag{2.25}$$

where ν is an integer, representing the angular order of the mode. The optical fiber modes are degenerate in the sense that any eigenvalue k_y corresponds to two solutions $\pm\nu$.

Alternatively, the angular ansatz $\sin(\nu\theta)$ or $\cos(\nu\theta)$ can be chosen instead of the one introduced in Eq. (2.25). Both approaches are valid solutions of the differential equation. The former represents traveling-wave modes that have a vorticity in $\pm\theta$-direction. These modes exhibit a specific orbital angular momentum (OAM), thus they are called OAM modes [81–83]. In contrast to this, the latter is of standing-wave type [84]. However, complex superposition of two modes of opposite angular order $\pm\nu$ and suitable amplitudes easily transforms the approaches into each other. Both solutions are valid, they only differ in the choice of basis functions.

Applying Eq. (2.25), transforms Eq. (2.23) to

$$\partial_\rho^2 f + \frac{1}{\rho}\partial_\rho f + (k_0^2\varepsilon_r - k_z^2 - \frac{\nu^2}{\rho^2})f = 0, \tag{2.26}$$

where f only depends on the radial component ρ. The solution for a finite field in the core and a decaying field in the cladding is given by the Bessel function J_ν in the core and by the modified Bessel functions K_ν in the cladding [85].

Apart from TE ($E_y = 0$) and TM ($H_y = 0$) modes, hybrid modes ($E_y, H_y \neq 0$) are also present in optical fibers. All of them have to satisfy Eq. (2.26), but only the hybrid modes have all six components non-zero. Additionally, the hybrid modes can be split into HE and EH modes depending on the polarization character of the mode. TE-like hybrid modes exhibit a comparably small electrical field component E_y in propagation direction, thus these are called EH modes, and TM-like modes have a small H_y component and are called HE modes [86].

The tangential components of the electric and magnetic fields have to be continuous at the core-cladding interface $\rho = r$, from which follows (after some considerations, see [9]) that the integer order ν of the Bessel functions has to be equal to zero when considering TE or TM modes. Then, Eqs. (2.24)–(2.26) can be further simplified. For TE modes, H_y has to fulfill

$$\partial_\rho^2 H_y + \frac{1}{\rho}\partial_\rho H_y + (k_0^2\varepsilon_r - k_y^2)H_y = 0 \tag{2.27}$$

with the remaining non-zero components given by

$$\begin{aligned} E_\theta &= \frac{\mathrm{i}\omega\mu_0}{k_0^2\varepsilon_r - k_y^2}\partial_\rho H_y, \\ H_\rho &= \frac{-\mathrm{i}k_y}{k_0^2\varepsilon_r - k_y^2}\partial_\rho H_y. \end{aligned} \tag{2.28}$$

And for TM modes, E_y has to satisfy

$$\partial_\rho^2 E_y + \frac{1}{\rho}\partial_\rho E_y + (k_0^2\varepsilon_r - k_y^2)E_y = 0 \tag{2.29}$$

with the non-zero components

$$\begin{aligned} E_\rho &= \frac{-\mathrm{i}k_y}{k_0^2\varepsilon_r - k_y^2}\partial_\rho E_y, \\ H_\theta &= \frac{-\mathrm{i}\omega\varepsilon_0\varepsilon_r}{k_0^2\varepsilon_r - k_y^2}\partial_\rho E_y. \end{aligned} \tag{2.30}$$

The eigenvalues k_y are again determined by an eigenvalue equation in the form of Eq. (2.10) (exchanging k_z by k_y) that has to be solved for the eigenvalues k_y. For a guided mode the wavenumber has to fulfill the condition

$$n_c \leq \frac{k_y}{k_0} = N_{\mathrm{eff}} \leq n_f. \tag{2.31}$$

In accordance to the step-index slab waveguide, it is also possible to define a fiber with three layers [78]. The mathematical approach is almost identical to the two-layer structure, however, the additional interfaces have to be considered as well. The mode is now guided in the middle layer, which exhibits the highest refractive index. The distinction between TE, TM and hybrid modes is still possible.

2.2.3 Power orthogonality

Modal orthogonality properties, e.g., reciprocity or power orthogonality [78, 87], play an important role in the theory of guided wave systems. These are briefly derived in the following.

2.2.3.1 Lorentz reciprocity

We assume two particular fields $(\tilde{\mathbf{E}}_1, \tilde{\mathbf{H}}_1)^T$ and $(\tilde{\mathbf{E}}_2, \tilde{\mathbf{H}}_2)^T$ (depending on (x, y, z)) that exist is the same medium (same ε_r) and fulfill the time harmonic Maxwell equations (2.6)

$$\nabla \times \tilde{\mathbf{E}}_j = -\mathrm{i}\omega\mu_0\tilde{\mathbf{H}}_j, \tag{2.32}$$

$$\nabla \times \tilde{\mathbf{H}}_j = \mathrm{i}\omega\varepsilon_0\varepsilon_r\tilde{\mathbf{E}}_j, \tag{2.33}$$

with $j \in \{1, 2\}$. By performing the dot products of $\tilde{\mathbf{H}}_2$ with the complex conjugate of Eq. (2.32) for $j = 1$ and the dot product of $\tilde{\mathbf{E}}_1^*$ with Eq. (2.33) for $j = 2$ and subtracting the equations, results in

$$\nabla \cdot (\tilde{\mathbf{E}}_1^* \times \tilde{\mathbf{H}}_2) = \mathrm{i}\omega\mu_0\tilde{\mathbf{H}}_2 \cdot \tilde{\mathbf{H}}_1^* - \mathrm{i}\omega\varepsilon_0\varepsilon_r\tilde{\mathbf{E}}_1^* \cdot \tilde{\mathbf{E}}_2. \tag{2.34}$$

In an analogous manner, this can be done for Eq. (2.32) with $j = 2$ and Eq. (2.33) with $j = 1$, resulting in

$$\nabla \cdot (\tilde{\mathbf{E}}_2 \times \tilde{\mathbf{H}}_1^*) = -\mathrm{i}\omega\mu_0\tilde{\mathbf{H}}_1^* \cdot \tilde{\mathbf{H}}_2 + \mathrm{i}\omega\varepsilon_0\varepsilon_r\tilde{\mathbf{E}}_2 \cdot \tilde{\mathbf{E}}_1^*. \tag{2.35}$$

Combining Eq. (2.34) and Eq. (2.35) leads to

$$\nabla \cdot (\tilde{\mathbf{E}}_1^* \times \tilde{\mathbf{H}}_2 + \tilde{\mathbf{E}}_2 \times \tilde{\mathbf{H}}_1^*) = 0. \tag{2.36}$$

Eq. (2.36) is the Lorentz reciprocity relation. It is applicable to all lossless media.

2.2.3.2 Orthogonality of guided modes

Now, we further consider that the waveguide has a uniform cross section and is infinitely long in the z-direction. Looking at two guided modes that are propagating in positive z-direction along the waveguide, their field dependence is given by

$$\begin{pmatrix}\tilde{\mathbf{E}}_j \\ \tilde{\mathbf{H}}_j\end{pmatrix}(x, y, z) = \begin{pmatrix}\mathbf{E}_j \\ \mathbf{H}_j\end{pmatrix}(x, y)\mathrm{e}^{-\mathrm{i}k_{z,j}z}, \quad j \in \{1, 2\}, \tag{2.37}$$

where $k_{z,j}$ are positive wavenumbers of each propagating mode with $k_{z,1} \neq k_{z,2}$.

Substituting the field dependence in Eq. (2.36) yields to

$$\nabla \cdot [(\mathbf{E}_1^* \times \mathbf{H}_2 + \mathbf{E}_2 \times \mathbf{H}_1^*)\mathrm{e}^{\mathrm{i}(k_{z,1}-k_{z,2})z}] = 0 \tag{2.38}$$

or

$$\nabla \cdot (\mathbf{E}_1^* \times \mathbf{H}_2 + \mathbf{E}_2 \times \mathbf{H}_1^*) = \mathrm{i}(k_{z,2} - k_{z,1})(\mathbf{E}_1^* \times \mathbf{H}_2 + \mathbf{E}_2 \times \mathbf{H}_1^*). \tag{2.39}$$

Integrating the equations over the cross section A of the waveguide and applying the divergence theorem results in

$$\underbrace{\int_A \nabla \cdot (\mathbf{E}_1^* \times \mathbf{H}_2 + \mathbf{E}_2 \times \mathbf{H}_1^*)\mathrm{d}A}_{=\int_C (\mathbf{E}_1^* \times \mathbf{H}_2 + \mathbf{E}_2 \times \mathbf{H}_1^*) \cdot \mathrm{d}\vec{s}} = \int_A \mathrm{i}(k_{z,2} - k_{z,1})(\mathbf{E}_1^* \times \mathbf{H}_2 + \mathbf{E}_2 \times \mathbf{H}_1^*) \cdot \mathbf{e}_z \mathrm{d}A, \tag{2.40}$$

where C is a closed contour of the cross section of the waveguide. For optical waveguides, the fields $|\mathbf{E}_j|$ and $|\mathbf{H}_j|$ for $j \in \{1, 2\}$ of the guided modes decay exponentially outside the core region, thus the contour integral vanishes completely when the contour tends to infinity, and so does the right hand side of Eq. (2.40). Since the two modes are not degenerate, $k_{z,1} \neq k_{z,2}$, this gives

$$\int_A (\mathbf{E}_1^* \times \mathbf{H}_2 + \mathbf{E}_2 \times \mathbf{H}_1^*) \cdot \mathbf{e}_z \mathrm{d}A = 0. \tag{2.41}$$

Eq. (2.41) is the orthogonality relation of guided modes, depends only on the transverse field components and holds for guided modes that are not degenerate or identical.

Considering a single mode j of the waveguide, the total time-averaged power carried by this mode is given by [78]

$$\begin{aligned} P_j &= \frac{1}{2} \int_A \mathrm{Re}\{\tilde{\mathbf{E}}_j^* \times \tilde{\mathbf{H}}_j\} \cdot \mathbf{e}_z \mathrm{d}A \\ &= \frac{1}{4} \int_A (\mathbf{E}_j^* \times \mathbf{H}_j + \mathbf{E}_j \times \mathbf{H}_j^*) \cdot \mathbf{e}_z \mathrm{d}A. \end{aligned} \tag{2.42}$$

Combining Eq. (2.41) and Eq. (2.42), we get the power orthogonality relation

$$\begin{aligned} (\mathbf{\Phi}, \mathbf{\Psi})_{x,y} &:= \frac{1}{4} \int_{-\infty}^{\infty} \int_{-\infty}^{\infty} (E_{1x}^* H_{2y} - E_{1y}^* H_{2x} + H_{1y}^* E_{2x} - H_{1x}^* E_{2y}) \mathrm{d}x \mathrm{d}y \\ &= \begin{cases} 0, & k_{z,1} \neq k_{z,2} \\ P_1, & k_{z,1} = k_{z,2} \end{cases} \end{aligned} \tag{2.43}$$

with $\mathbf{\Phi} = (\mathbf{E_1}, \mathbf{H_1})$ and $\mathbf{\Psi} = (\mathbf{E_2}, \mathbf{H_2})$.

For 2-D structures with waveguides that exhibit a 1-D cross section, e.g., slab waveguides, a respective analysis needs to take into account the vanishing y-derivatives of all fields. This leads to the product of fields

$$(\mathbf{\Phi}, \mathbf{\Psi})_x := \frac{1}{4} \int_{-\infty}^{\infty} (E_{1x}^* H_{2y} - E_{1y}^* H_{2x} + H_{1y}^* E_{2x} - H_{1x}^* E_{2y}) \mathrm{d}x \tag{2.44}$$

that allows to express power orthogonality in 2-D.

2.3 Slab waveguide discontinuities

The structures considered in this work consist of compositions and connections of different waveguides to achieve a desired functionality. In particular, we study slab waveguides that are connected via a linear and (almost) arbitrary discontinuity, and excited at oblique angles of propagation. Certain general properties of these 2-D composited configurations can be derived analytically [10–20]. A variant of Snell's law applies to these structures, which implies that beyond particular incidence angles, power transfer to specific outgoing modes can be suppressed, thus power transfer to non-guided modes can be excluded, resulting in a completely lossless structure (within the theoretical model that disregards material attenuation and surface roughness). Hence, in this section, we consider a 2-D scattering problem, where slab waveguides encounter a discontinuity at oblique angles of propagation φ, as illustrated in Figure 2.3.

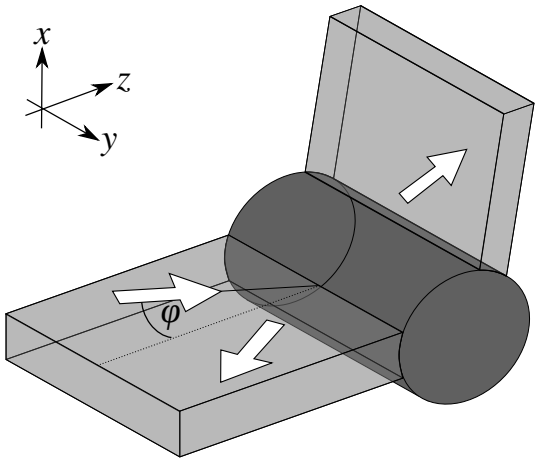

Figure 2.3: Slab waveguide discontinuity with incoming wave guided at oblique angles of propagation φ.

Before deriving the critical angles for power suppression to specific outgoing modes, we briefly introduce oblique propagation with respect to the coordinate axes in dielectric slab waveguide structures. This is equivalent to a rotation of the coordinate system for the slab waveguides considered in Section 2.2.1.

2.3.1 Oblique propagation in dielectric slab waveguides

Rotating the coordinate system leads to a rotated version of the TE and TM modes, which still solve the Maxwell equations. However, the rotation can also be interpreted as oblique propagation of the wave with respect to the coordinate axes as shown in Figure 2.4. The wave reaches the waveguide at an oblique angle of propagation φ normal to the z-axis. Hence, the fields are no longer constant in the y-direction ($\partial_y \neq 0$). But the whole waveguide structure is invariant in y-direction, such that, at all positions, the overall field solution can be restricted to a single Fourier component given by the in-plane wavenumber k_y in the form

$$\begin{pmatrix} \tilde{\mathbf{E}} \\ \tilde{\mathbf{H}} \end{pmatrix} (x, y, z) = \begin{pmatrix} \mathbf{E} \\ \mathbf{H} \end{pmatrix} (x) \mathrm{e}^{-\mathrm{i}(k_y y + k_z z)}. \tag{2.45}$$

The wave is now propagating in the y-z-direction, thus the wavenumbers k_y and k_z are non-zero and have to fulfill the dispersion equation $k^2 = k_0^2 N_{\text{eff}}^2 = k_y^2 + k_z^2$, to be a valid solution of the Maxwell equations. Fixing $k_y = k_0 N_{\text{eff}} \sin\varphi$ results in $k_z = k_0 N_{\text{eff}} \cos\varphi$ (resulting from geometrical considerations, see Figure 2.4). Here, N_{eff} is still the mode index from the waveguide solution with normal incidence.

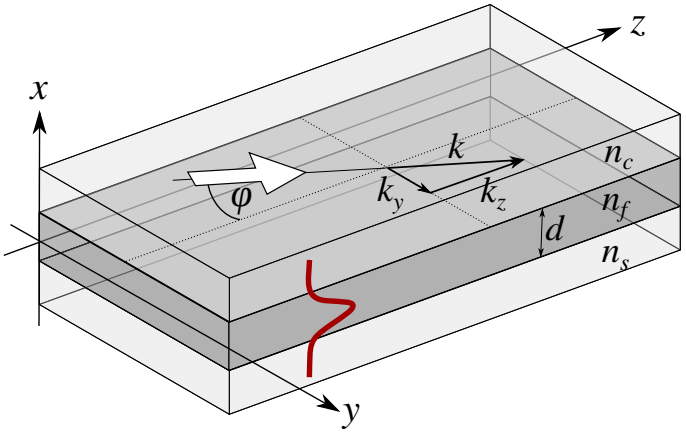

Figure 2.4: Dielectric slab waveguide with refractive indices n_c, n_f, n_s and thickness d with oblique propagation in the y-z-direction at an angle φ.

With the help of ansatz (2.45), the Maxwell equations (2.6) lead to fields for TE modes

$$\mathbf{E}(x) = \begin{pmatrix} 0 \\ k_z \Psi / k^2 \\ -k_y \Psi / k^2 \end{pmatrix} \quad \text{and} \quad \mathbf{H}(x) = \frac{1}{\omega \mu_0} \begin{pmatrix} -\Psi \\ \mathrm{i} k_y \partial_x \Psi / k^2 \\ \mathrm{i} k_z \partial_x \Psi / k^2 \end{pmatrix}, \tag{2.46}$$

where $\Psi(x)$ has to fulfill the equation

$$\partial_x^2 \Psi + (k_0^2 \varepsilon_r - k^2)\Psi = 0. \tag{2.47}$$

And for TM modes the components are given by

$$\mathbf{E}(x) = \frac{1}{\omega \varepsilon_0 \varepsilon_r} \begin{pmatrix} \Psi \\ -\mathrm{i} k_y \partial_x \Psi / k^2 \\ -\mathrm{i} k_z \partial_x \Psi / k^2 \end{pmatrix} \quad \text{and} \quad \mathbf{H}(x) = \begin{pmatrix} 0 \\ k_z \Psi / k^2 \\ -k_y \Psi / k^2 \end{pmatrix}, \tag{2.48}$$

and $\Psi(x)$ has to satisfy the differential equation

$$\varepsilon_r \partial_x \frac{1}{\varepsilon_r} \partial_x \Psi + (k_0^2 \varepsilon_r - k^2)\Psi = 0. \tag{2.49}$$

2.3.2 Critical angles

A 2-D cross section of the slab waveguide discontinuity is shown in Figure 2.5. The structure as well as the electromagnetic field solution is supposed to be constant along one axis, here the y-axis. Two half-infinite slab waveguides, both not necessarily of the same thickness, are connected via the discontinuity, illustrated by the elliptic darker region, which can be of arbitrary shape. The incoming semi-guided wave, guided by the waveguide parallel to the z-axis, is

propagating in z-direction and reaches the discontinuity at an oblique incidence angle φ. Possible back reflections are guided waves in negative z-direction and transmitted waves, that have passed the discontinuity and are guided by the remaining slab waveguide, are propagating in ξ_1-direction in the x-z-plane. Radiating fields are propagating in arbitrary ξ_2-direction.

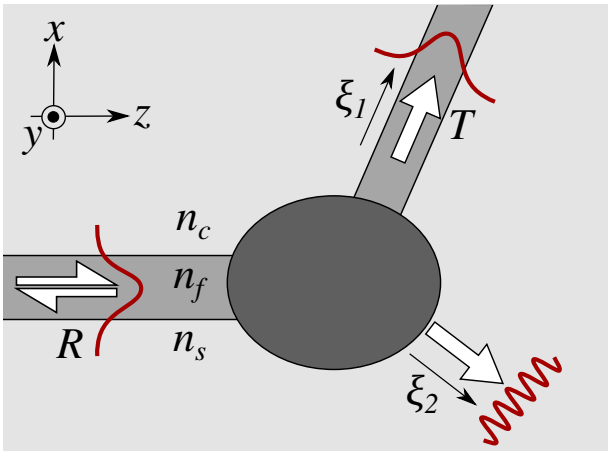

Figure 2.5: Slab waveguide discontinuity of two slab waveguides (potentially different thicknesses) with refractive indices n_c, n_f, n_s. The connected discontinuity is of arbitrary shape.

The incoming semi-guided wave is propagating in the y-z-plane at an oblique incidence φ, which results in a field dependence

$$\sim \mathbf{\Psi}_{\mathrm{in}}(k_y; x)\mathrm{e}^{-\mathrm{i}(k_y y + k_z z)}. \tag{2.50}$$

Here, $\mathbf{\Psi}_{\mathrm{in}} = (\mathbf{E}_{\mathrm{in}}, \mathbf{H}_{\mathrm{in}})^{\mathrm{T}}$ is the vectorial profile of the incoming oblique wave with effective refractive index N_{in} and wavenumbers $k_y = k_0 N_{\mathrm{in}} \sin\varphi$ and $k_z = k_0 N_{\mathrm{in}} \cos\varphi$, which fulfill the relation $k_0^2 N_{\mathrm{in}}^2 = k_y^2 + k_z^2$ as already introduced for the slab waveguide in Section 2.2.1.

In an analogues manner, the outgoing waves are defined by a mode profile $\mathbf{\Psi}_{\mathrm{out}} = (\mathbf{E}_{\mathrm{out}}, \mathbf{H}_{\mathrm{out}})^{\mathrm{T}}$ and an effective refractive index N_{out} with a field dependence

$$\sim \mathbf{\Psi}_{\mathrm{out}}(k_y; .)\mathrm{e}^{-\mathrm{i}(k_y y + k_\xi \xi)}. \tag{2.51}$$

The wave is propagating in the ξ-y-plane, i.e., $\xi = -z$ for the reflected waves, $\xi = \xi_1$ for the transmitted waves, and $\xi = \xi_2$ for scattered waves in arbitrary direction ξ_2.

Since the whole structure is assumed to be constant along the y-direction, all fields share the field dependence $\sim \mathrm{e}^{-\mathrm{i}k_y y}$ with wavenumber $k_y = k_0 N_{\mathrm{in}} \sin\varphi$. Furthermore, the dispersion equation $k_0^2 N_{\mathrm{out}} = k_y^2 + k_\xi^2$ has to be fulfilled for all types of outgoing waves, resulting in an equation for k_ξ. Looking at one particular outgoing wave with effective mode index N_{out}, two cases have to be distinguished:

- $k_0^2 N_{\mathrm{out}}^2 > k_y^2$: The wavenumber $k_\xi = k_0 N_{\mathrm{out}} \cos\varphi_{\mathrm{out}}$ is a real value, describing a propagating wave, where φ_{out} is the outgoing propagation angle calculated via a variant of Snell's law

$$\sin\varphi_{\mathrm{out}} = N_{\mathrm{in}}/N_{\mathrm{out}} \sin\varphi. \tag{2.52}$$

- $k_0^2 N_{\mathrm{out}}^2 < k_y^2$: The wavenumber $k_\xi = -\mathrm{i}\sqrt{k_y^2 - k_0^2 N_{\mathrm{out}}^2}$ becomes imaginary and the outgoing fields are evanescent.

Altogether, it is possible to define a critical angle with $k_0^2 N_{\mathrm{out}}^2 = k_y^2$ given by

$$\sin\varphi_{\mathrm{crit}} = N_{\mathrm{out}}/N_{\mathrm{in}}. \tag{2.53}$$

Power transfer to the outgoing mode with mode index N_{out} is suppressed, if the structure is excited at angles larger than φ_{crit}.

Now, one can identify certain critical angles in relation to the structure of interest in Figure 2.5. In this work, we assume the fundamental TE_0 mode as the incoming field (otherwise the following has to be adapted), hence $N_{\mathrm{in}} = N_{\mathrm{TE}_0}$. Then critical angles can be defined by:

- Considering the cover region, there is no optical power radiating in that layer for angles $\varphi \geq \varphi_c$ with $\sin\varphi_c = n_c/N_{\mathrm{TE}_0}$ because all modes that relate to scattered waves with oscillatory behavior in the cladding ("cladding modes") have effective indices below n_c, i.e., $N_{\mathrm{eff}} \leq n_c$.
- Considering the substrate region, there is no optical power radiating in that region for angles $\varphi \geq \varphi_s$ with $\sin\varphi_s = n_s/N_{\mathrm{TE}_0}$ because fields that can propagate in that region are given by an effective mode index of $N_{\mathrm{eff}} \leq n_s$.
  For the case $n_c \leq n_s < n_f$, there is no power lost in the cladding regions. Hence, all radiation losses vanish.
- For an incidence angle $\varphi \geq \varphi_m$ with $\sin\varphi_m = N_{\mathrm{TM}_0}/N_{\mathrm{TE}_0}$, where N_{TM_0} is the effective refractive index of the fundamental TM_0 mode with $N_{\mathrm{TE}_0} > N_{\mathrm{TM}_0}$, all power is carried away by TE modes, since all TM polarized modes supported by these waveguides have effective mode indices below N_{TM_0}.

For a standard 2-D setting, meaning normal incidence with $\varphi = 0°$, the configuration results in separate problems for either TE or TM polarized waves. For the more general case of oblique incidence $\varphi \neq 0°$, the polarization states become coupled. Then, this is no longer a scalar 2-D problem. Apart from the transverse coordinates x and z, also the given strictly harmonic dependence on y becomes relevant. Hence, we call this a 2.5-D or quasi-2-D problem.

2.4 Excitation of wave bundles

The previously introduced 2.5-D slab waveguide discontinuities involve oblique incoming semi-guided waves that are infinitely extended along the y-direction. To consider more practically relevant 3-D solutions as well, we investigate x-guided, laterally y-limited wave bundles of semi-guided waves as the incoming field in our structures [13, 14, 19, 75, 88].

The general form of a 2-D wave packet in the y-z-plane, propagating in the z-direction, is calculated as a weighted superposition of oblique plane waves via a Fourier transform [48]

$$\frac{1}{2\pi}\int_{-\infty}^{\infty} w(k_y)\mathrm{e}^{-\mathrm{i}(k_y y + k_z z)}\mathrm{d}k_y, \tag{2.54}$$

where $w(k_y)$ is the weighting function that defines the spectral shape of the wave in the lateral direction, e.g., a Gaussian function, and the exponential term covers the plane wave propagation in directions (k_y, k_z) [9].

In our case, these plane waves are replaced by the 2.5-D slab waveguide solutions, hence the solution is further restricted in the x-direction. Then, a 3-D wave bundle for incoming primary incidence angle φ_0 is given by a superposition of weighted 2.5-D slab waveguide solutions for a range of wavenumbers k_y (or incidence angles φ) around the primary wavenumber $k_{y_0} = k_0 N_{\text{eff}} \sin\varphi_0$ (or primary incidence angle φ_0) and is evaluated by

$$\begin{pmatrix} \mathbf{E} \\ \mathbf{H} \end{pmatrix}(x,y,z) = \frac{1}{2\pi}\int_{-\infty}^{\infty} w(k_y)\{\mathbf{\Psi}_0(k_y;x)\mathrm{e}^{-ik_z(k_y)(z-z_0)}\}\mathrm{e}^{-ik_y(y-y_0)}\mathrm{d}k_y. \tag{2.55}$$

The term in curly brackets depicts the former 2.5-D slab waveguide solutions in the x-z-plane with the vectorial mode profile $\mathbf{\Psi}_0$, where the index indicates TE_0 incidence. The last phase factor represents the individual harmonic y-dependence of the elementary quasi-2-D solutions. Offsets y_0 and z_0 serve to adjust the global phase of the bundle. The weighting function is again given by $w(k_y)$, which can be of Gaussian shape [13, 14, 19, 88] or determined by the excitation of an incoming rib waveguide with shallow etching in front of the structure [75]. The second approach is used in this work and therefore derived in the following.

2.4.1 Excitation by a waveguide mode

Such wave bundles can be excited by placing a rib waveguide in front of a slab waveguide, as illustrated in Figure 2.6. Here, we consider rib waveguides of width W, thickness d and shallow etch depth d'. A wave that is guided in the rib waveguide and confined in the core center, remains to be reasonably confined in the adjoining slab. To avoid spreading of the wave and to guarantee beams that almost resemble the fundamental guided slab modes, the width of the rib is assumed to be much larger than the etch depth $W \gg d'$. Furthermore, we can assume that back reflections at the transition between rib and slab waveguide are negligible. To realize oblique incidence, the rib waveguide is presented in local coordinates (x, y', z'), where the z'-direction is parallel to the waveguide axis, i.e., parallel to the propagation direction of the incoming beam at incidence angle φ_0 (cf. Figure 2.6 (b)). The global coordinate system is given by (x, y, z).

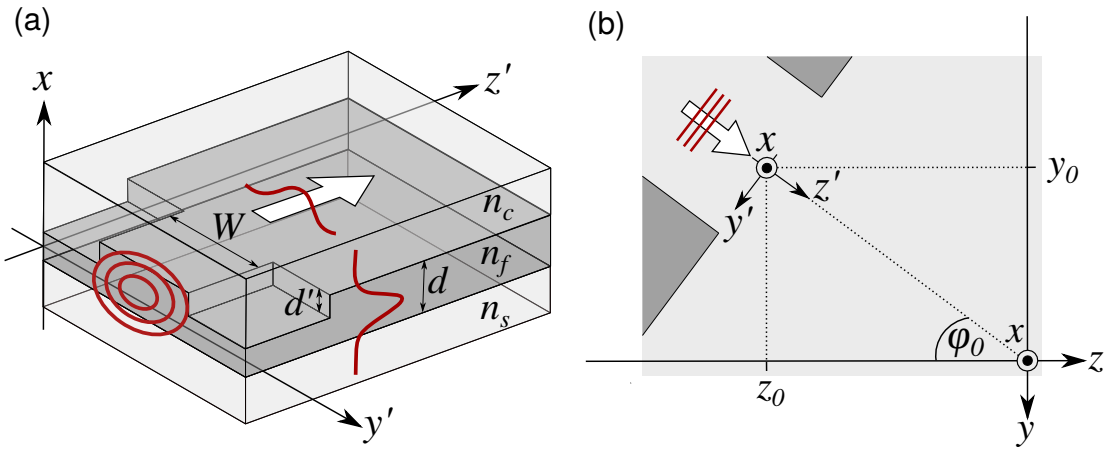

Figure 2.6: (a) Connection of a rib and slab waveguide of thickness d, width W and etch depth d' with refractive indices n_f, n_c and n_s in rotated coordinates $(x,' y, z')$. (b) The view from above with primary incidence angle φ_0.

Assuming TE incidence, the unknown weight $w(k_y)$ from Eq. (2.55) is now determined by the TE-like mode $\mathbf{\Phi}_0(x, y')$ of the adjoining rib waveguide. For simplicity, the following derivations are only shown for normal incidence $\varphi_0 = 0°$. Otherwise, for $\varphi_0 \neq 0$, the fields and coordinates have to be rotated by the appropriate angle and calculations are carried out respectively.

At the junction, where rib and slab waveguide adjoin each other ($z = z_0$), the incoming rib mode profile $\mathbf{\Phi}_0(x, y)$ can be written as a superposition of wave packets (2.54) of individually weighted slab modes $\mathbf{\Psi}_p(x)$ with mode order p and weight $w_p(k_y)$[1]

$$\mathbf{\Phi}_0(x, y) = \frac{1}{2\pi} \sum_p \int_{-\infty}^{\infty} w_p(k_y) \mathbf{\Psi}_p(k_y; x) \mathrm{e}^{-\mathrm{i}k_y(y-y_0)} \mathrm{d}k_y. \tag{2.56}$$

Using the product for mode orthogonality (2.44), i.e., multiplying the equation with $(\mathbf{\Psi}_0, \cdot)_x$, and assuming mode orthogonality and normality of all slab waveguide modes results in

$$(\mathbf{\Psi}_0, \mathbf{\Phi}_0)_x = \frac{1}{2\pi} \int_{-\infty}^{\infty} w_0(k_y) \mathrm{e}^{-\mathrm{i}k_y(y-y_0)} \mathrm{d}k_y. \tag{2.57}$$

Then, the weight w_0 for the excited TE_0 slab mode is given by a Fourier transformation

$$w_0(k_y) = \int_{-\infty}^{\infty} (\mathbf{\Psi}_0, \mathbf{\Phi}_0)_x \mathrm{e}^{\mathrm{i}k_y(y-y_0)} \mathrm{d}y. \tag{2.58}$$

Here, it is only necessary to consider the weight $w_0(k_y)$ of the TE_0 slab mode. Because of the wide rib and low etching, the fundamental TE-like rib mode becomes more the TE slab mode. Thus, contributions from higher order or TM modes in Eq. (2.56) can be neglected.

2.4.2 Power transmittance

For some configurations it may further be of interest to calculate the power of the outgoing beam after passing the discontinuity, as sketched in Figure 2.7. Therefore, a second rib waveguide is placed at the outset of the structure (here, the outgoing waveguide is parallel to the incoming waveguide). Again, we only derive the equations for normal incidence $\varphi_0 = 0°$.

For the configurations in this work, we assume the outgoing slab waveguide to be identical with the incoming slab (same thickness), hence the incoming and outgoing angles are identical $\varphi_{\mathrm{out}} = \varphi_0$ and the same local coordinate systems can be used $(x, y'', z'') = (x, y', z')$. The position of the outgoing rib waveguide, i.e., the outgoing beam, strongly depends on the geometry of the discontinuity and the incoming and outgoing incidence angles. Here, the spatial variation of the outgoing beam is represented by the displacement δ. Furthermore, the incoming and outgoing field profiles of the fundamental TE_0 mode of the rib waveguide match and only differ in their amplitude with a pre-factor $u_0 \in \mathbb{C}$ that represents the transmission coefficient. To determine this coefficient, the outgoing field profile $\mathbf{\Psi}_{\mathrm{out}}(x, y)$ (given by Eq. (2.55) with

[1] Strictly speaking, Eq. (2.56) holds only for the transverse components of the involved fields. However, since we apply a orthogonality product (cf. Eq. (2.43)) in Eq. (2.57), which only includes transverse components, the notation is acceptable for the derivation of w_p.

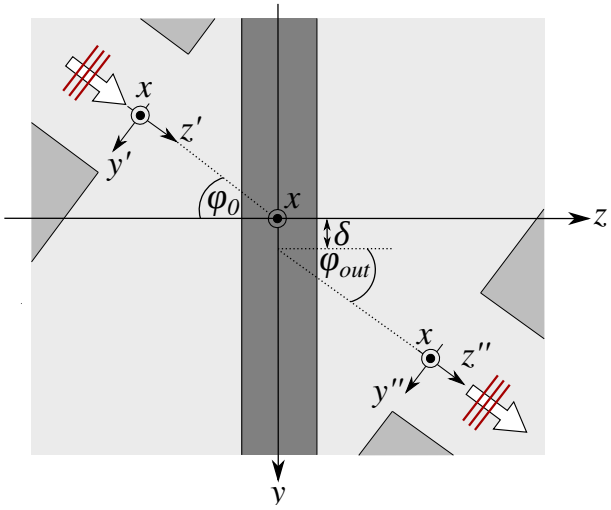

Figure 2.7: Top view of the slab waveguide discontinuity with additional incoming and outgoing rib waveguides, rotated by the primary incidence angle φ_0. The discontinuity is illustrated by the darker region and the spatial displacement of the outgoing beam is given by δ [13].

rib weight $w(k_y)$) can be written as a superposition of all modes guided by the rib waveguide $\mathbf{\Phi}_q(x, y)$, which leads to [2]

$$\mathbf{\Psi}_{\text{out}}(x, y) = \sum_q u_q \mathbf{\Phi}_q(x, y). \tag{2.59}$$

Using the 2-D mode orthogonality product (2.43) and assuming mode orthogonality and normality of all guided modes of the rib waveguide, the transmission coefficient of the quasi-TE_0 rib mode is determined as

$$u_0 = (\mathbf{\Phi}_0, \mathbf{\Psi}_{\text{out}})_{x,y}, \tag{2.60}$$

and the transmittance T is directly given by $|u_0|^2$.

[2] Again, this holds strictly only for the transverse components; see footnote 1 on page 24 for a detailed explanation.

Chapter 3

Finite element method

The behavior of electric and magnetic fields in optical systems is described by Maxwell's equations with appropriate boundary conditions. Together they describe a system of partial differential equations (PDE). Solving a partial differential equation analytically is usually impossible, except for certain very simple structures. Instead numerical methods are required to approximate a reasonably accurate solution. Rather famous methods are the finite difference time domain method (FDTD), finite integration method (FIT), boundary element method (BEM) and the finite element method (FEM). The latter is implemented in the simulation program COMSOL Multiphysics [22], which is used throughout this work and therefore the theory is briefly introduced in this section. More details can be found in references [23, 24, 89].

For the configurations considered in this work, the electric or magnetic wave equation (2.7) are the PDEs of interest. Together with suitable boundary conditions (BC) on the boundary of the domain, they describe the complete boundary value problem. Here, we consider two types of problems. On the one hand, scattering or mode propagation problems are studied by exciting a structure with an input field that is propagating through the structure, e.g., a slab waveguide discontinuity as discussed in Section 2.3. On the other hand, eigenvalue or mode analysis problems are considered when calculating the guided modes of a 2-D waveguide cross section.

We introduce the finite element theory in Section 3.1. Corresponding boundary conditions used in this work and implemented in COMSOL are explained in Section 3.1.3. Finally, some remarks on the settings in the COMSOL software, also concerning the appropriate boundary conditions, as required for the structures in this thesis, are collected in Section 3.2.

3.1 Theory

The finite element method calculates an approximated solution of the original PDE by discretizing the problem in small, finite elements. The basic steps include the following [23, 24]:

1. Deriving the weak form of the original PDE.
2. Division of the computational domain into small, finite, non-overlapping elements (meshing).

3. Approximation of the solution by basis functions to yield local matrices for each element.
4. Assemble local matrices to a global matrix, and solve the corresponding system of linear algebraic equations.

To illustrate the principles of the finite element method, we consider an abstract problem of the form

$$\mathsf{D}\mathbf{u} = \mathbf{f} \quad \text{in } \Omega \tag{3.1}$$

with partial differential operator D, source $\mathbf{f}$, unknown $\mathbf{u}$ and a domain Ω. Mathematically, this is an inhomogeneous, linear partial differential equation that needs to be solved for the unknown variable $\mathbf{u}$.

In principle, scattering problems exhibit an incident field that leads to a non-zero right hand side $\mathbf{f} \neq 0$ in Eq. (3.1). Contrarily, eigenvalue problems are described by a homogeneous PDE with $\mathbf{f} = 0$, as we are interested in the eigenvalues of the system. We will give some more details on the specific BCs in Section 3.1.3.

3.1.1 Weak formulation

The first step to calculate a valid approximated solution of the original PDE is to transform Eq. (3.1) into an integral formulation, called the weak formulation, which is an equivalent re-formulation of the original PDE. Therefore, the equation is multiplied with an arbitrary, vectorial test function $\mathbf{\Phi} \in V$, where V is an infinite dimensional function space, and integrated over the domain Ω

$$\int_\Omega (\mathsf{D}\mathbf{u})\mathbf{\Phi} \mathrm{d}\Omega = \int_\Omega \mathbf{f}\mathbf{\Phi} \mathrm{d}\Omega, \qquad \forall \mathbf{\Phi} \in V. \tag{3.2}$$

The formulation is called weak, since it weakens the requirement of Eq. (3.1) to hold for every point $\mathbf{u}$ in the domain Ω to every test function $\mathbf{\Phi}$ in the space of test functions V. The weak formulation only requires equality in an integral sense and is reduced in differentiation order, which is mostly easier to solve than the original PDE. It can be shown that a solution of the weak formulation is also a solution of the original PDE [23].

3.1.2 Galerkin-method

To discretize the PDE, finite-dimensional subspaces $V_h \subset V$ with $\dim(V_h) = \mathcal{N} < \infty$ are created. The Galerkin-method, also called method of weighted residuals, requires an approximation $\tilde{\mathbf{u}}_h$ of the solution $\tilde{\mathbf{u}}$ to a subspace $V_h \subset V$. The better V_h approximates the space V, the better is the approximation $\tilde{\mathbf{u}}_h$ of $\tilde{\mathbf{u}}$. Now, one has to find a discrete solution $\mathbf{u}_h \in V_h$ of Eq. (3.2) that solves the equation

$$\int_\Omega (\mathsf{D}\mathbf{u}_h)\mathbf{\Phi} \mathrm{d}\Omega = \int_\Omega \mathbf{f}\mathbf{\Phi} \mathrm{d}\Omega, \qquad \forall \mathbf{\Phi} \in V_h. \tag{3.3}$$

$\mathbf{u}_h$ represents the discrete solution of Eq. (3.1) in V_h. One can show that a solution $\mathbf{u}_h$ exists, is unique and the discrete problem is well posed.

3. Finite element method

We assume a finite-dimensional subspace V_h with basis $(\mathbf{\Phi}_1, ..., \mathbf{\Phi}_\mathcal{N})$ of piecewise polynomial ansatz functions that are just non-zero over a small interval. Then, the solution $\tilde{\mathbf{u}}_h$ of the discrete problem can be approximated by

$$\mathbf{u} \approx \tilde{\mathbf{u}}_h = \sum_{i=1}^{\mathcal{N}} c_i \mathbf{\Phi}_i \in V_h, \tag{3.4}$$

where c_i are coefficients and Eq. (3.3) can be written as

$$\sum_{i=1}^{\mathcal{N}} c_i \int_\Omega (\mathsf{D}\mathbf{\Phi}_i)\mathbf{\Phi}_j \mathrm{d}\Omega = \int_\Omega \mathbf{f}\mathbf{\Phi}_j \mathrm{d}\Omega, \qquad j = 1, ..., \mathcal{N}. \tag{3.5}$$

This can further be identified as

$$\sum_{i=1}^{\mathcal{N}} c_i a_{ji} = b_j, \qquad j = 1, ..., \mathcal{N}, \tag{3.6}$$

with matrix elements

$$a_{ji} = \int_\Omega (\mathsf{D}\mathbf{\Phi}_i)\mathbf{\Phi}_j \mathrm{d}\Omega, \tag{3.7}$$

and right hand side

$$b_j = \int_\Omega \mathbf{f}\mathbf{\Phi}_j \mathrm{d}\Omega. \tag{3.8}$$

This is a linear system of equations of the form

$$\mathsf{A}\mathbf{c} = \mathbf{b}, \tag{3.9}$$

where $\mathsf{A} = (a_{ji})_{1 \leq i,j \leq \mathcal{N}}$ is the system or stiffness matrix of size $\mathcal{N} \times \mathcal{N}$, $\mathbf{b} = (b_j)_{1 \leq j \leq \mathcal{N}}$ is the source and $\mathbf{c} = (c_i)_{1 \leq i \leq \mathcal{N}}$ is the unknown vector.

The advantage of the choice of basis functions is that they are just non-zero over a small interval and therefore the integrals from Eq. (3.5) are zero everywhere, except for a few limited regions where the test functions $\mathbf{\Phi}_j$ and basic functions $\mathbf{\Phi}_i$ match. Hence, most of the entries of the matrix A are zero because each triangular element consists only of a few neighboring elements. The matrix A is therefore sparsely populated, which simplifies the numerical solution of the system (3.9).

The division in subspaces V_h is equivalent to discretizing the domain Ω in arbitrary elements Ω_h. Mostly the domain Ω is discretized in triangular elements, since they approximate complex structures sufficiently good. This is called triangulation $\mathcal{T}$ of the domain Ω. On each of these elements one defines piecewise linear functions, which are chosen as the basis functions $\mathbf{\Phi}_i$ of V_h.

The error of the Galerkin approximation is at most a constant factor worse than the distance of the solution to its best approximation of V_h. The error can therefore essentially be controlled by the choice of suitable approximation spaces V_h. The denser the discretization (the meshing), the better the approximation of the solution to the real solution. More details about the meshing for the structures considered in this work are explained in Section 3.2.

3.1.3 Boundary conditions

So far we did not specify the boundary conditions that determine the right hand side of Eq. (3.1) in more detail. As mentioned before, we consider scattering and eigenvalue problems, where both require different boundary conditions. This section briefly records and explains the boundary conditions used in this work which are implemented in COMSOL [90]. A closer look on the implementation in the software COMSOL Multiphysics [22] is given in the next section.

3.1.3.1 Electric boundary conditions

The electric boundary condition is the simplest BC, since the tangential components of the electric field are zero along that boundary. Consequently, the normal component of the magnetic flux density is zero as well. By setting the matrix entries in A at the specific points to zero, the BC is easily implemented. The electrical boundary condition behaves like a perfect electrical conductor (PEC), thus it is also often called PEC boundary condition [90, 91]. Here, we use these for our mode analysis studies. As we mainly consider waveguide structures with a finite core region, the fields are zero at the outer cladding boundaries. Thus, PEC is a suitable boundary condition.

3.1.3.2 Perfectly matched layer

Perfectly matched layers (PML) are used to model open boundaries in a finite computational domain. By placing PMLs around the structure of interest, a wave that is entering the PML region is damped in that layer without undesired boundary effects like back reflections. Hence, PMLs create open boundaries that are transparent to any radiation to simulate an infinite structure [91, 92]. We apply PMLs around the structures, when considering scattering problems like the waveguide discontinuity introduced in Section 2.3 to absorb all types of radiation and simulate an open domain.

3.1.3.3 Port boundary conditions

Sometimes it is advantageous to excite or absorb waves of specific shape and direction at the boundaries of a structure. Therefore, port boundary conditions can be added to a boundary. They are helpful to excite and absorb waves of specific shape [90]. We use ports for guided wave excitation and absorption in combination with PMLs, when considering scattering problems. The incident field from the port contributes to the right hand side of Eq. (3.1).

3.2 Settings in COMSOL

COMSOL Multiphysics [22] provides an implementation of the FEM for a variety of physical problems. In our case, the differential equations are given by the Maxwell equations for our 2.5-D structures. Additionally, the “radio frequency” [90] module is used to specifically solve electromagnetic wave problems, e.g., wave propagation in optical waveguides or mode analysis of waveguide cross sections. The module offers ports to excite the structure and calculate S-parameter, and perfectly matched layers to simulate an infinite space.

A variety of different port types are available, but in this work we use “numeric” ports that excite and absorb a specific mode that is calculated via a “boundary mode analysis” on the

corresponding boundary. With the help of this property, COMSOL is able to directly calculate the incoming modes of the considered slab waveguide – by giving a value close to N_{in} as an input value – and excites the structure with this mode. Ports have the advantage that they directly calculate the transmittance and reflectance scattering parameter $|S_{ij}|^2$, where S_{ij} is the time averaged power transmission or reflection coefficient from port j to port i. Additionally, one can directly define an "out-of-plane wave number" k_y that realizes oblique excitation in a 2-D environment. Here, COMSOL automatically includes the field dependence $\sim \mathrm{e}^{-ik_y y}$ for given wavenumber $k_y = k_0 N_{\mathrm{in}} \sin\varphi$. Thus, to simulate our oblique 2.5-D problems that are homogeneous along one spatial direction, only a 2-D model setting is necessary.

Furthermore, PMLs are placed around the 2-D simulation domain. They absorb all kinds of radiation by damping the waves in thickness-direction. Optimal behavior is achieved by using unstructured meshing for the PML region, e.g., mesh of rectangular shape in 2-D models. For our 2.5-D models, the typical wavelength that reaches the PMLs is given by $2\pi/(k_0 N_{\mathrm{eff}} \cos\varphi)$ due to the oblique incidence, where N_{eff} is the effective refractive index of the mode that reaches the outgoing PML region. In most of the cases considered in this work, the 2.5-D simulations concern incidence angles larger than the critical angle for loss suppression (cf. Section 2.3). As a result, PMLs are not required because the power is completely transmitted through the guided modes of the waveguide system and outgoing guided modes are directly absorbed by respective ports. Omitting the PMLs reduces the size of the computational domain and thus the computational time. However, to implement a model that is applicable for arbitrary incidence angles, we added PMLs around our structures.

In addition to wave propagation problems, i.e., exciting the structure with a port, COMSOL is further used for mode analysis, thus calculating the mode profiles of a waveguide with finite and constant 2-D cross section along the propagation direction. Here, mode analysis is carried out only on the 2-D cross section. For guided modes, which exhibit localized fields in the core region, and sufficiently large cladding regions, PMLs are mostly not needed as the fields are already decayed at the outer simulation domain, thus PEC boundary conditions are used instead.

The right choice of the mesh size is important as it strongly influences the required computational time. In COMSOL, structured (rectangles) and unstructured (triangles) elements are offered for 2-D simulations [91]. As mentioned before, PMLs require structured mesh, while the remaining domain is filled with unstructured mesh to accurately discretize all objects of the configuration, e.g., curves. For the following 2.5-D simulations, we always choose mapped mesh in the PML region with a PML thickness of λ_0. Otherwise, triangular mesh with a maximum element size of $\lambda_0/10$ is selected. For all configurations, convergence could be observed for this choice of element size [93]. The corresponding computational 2-D runtimes require $5 - 60\,\mathrm{s}$ for our 2.5-D settings depending on the geometry under study and the size of the simulation domain, e.g., the bent steps from Figure 5.6 require approximately 25 s.

Chapter 4

Bent slab waveguides[1]

Bends in dielectric waveguides usually cause losses that are more or less pronounced depending on the considered properties of the system under study [9]. But they are basic building blocks in integrated optics, thus there is keen interest in studying the losses in bent waveguides, focusing on their appearance, their strength and the possibility to suppression. The last point was already addressed in Section 2.3 for dielectric slab waveguide discontinuities at oblique angles of propagation.

In this chapter, a simple 2-D slab waveguide that is regularly bent around one axis is considered. Such structures have already been studied theoretically [95–97] and experimentally [98], with focus on resonant properties [95], far-field properties [97] and excitation by external free-space plane waves or focused Gaussian beams. But we are interested in the modal properties, i.e., propagation constants and mode profiles, of the guided (attenuated) modes depending on the geometry and material parameters. The modal analysis related to the curvature of the waveguide can be studied by looking at analytical 2-D models [9, 99] of bent slab waveguides with 1-D cross sections. In line with the arguments of Section 2.3, we have a particular look at waves that propagate at oblique angles of incidence. The modes are guided in the waveguide and spiral around the center of curvature, thus we call these modes "spiral modes" [18, 94].

The mathematical formulation (Section 4.1) leads to an eigenvalue problem, which is solved by numerical methods using the computer algebra system Maple [100]. The results, concerning the propagation constants and mode profiles, are displayed in Section 4.2. Our approach describes the transition from bend modes [14] at normal incidence to general spiral modes at arbitrary angle of incidence to a discrete number of lossless OAM modes (Section 2.2.2) at specific incidence angles beyond the critical angle (see Section 2.3).

4.1 Spiral modes theory

The structure under study (see Figure 4.1 (a)) consists of a three-layer bent slab waveguide with core thickness d. The refractive indices are given by n_s in the interior region, n_f in the core

[1] The chapter is based on [18, 94]. Parts of the results were already part of the candidate's bachelor thesis [94]. However, we extended our investigations on bent slab waveguides even further [18]. For the sake of completeness, we show the results here, as they fit perfectly to the topic of this thesis.

region and n_c in the outer cladding region with $n_s \leq n_f > n_c$. The waveguide is regularly bent around the y-axis with an outer core radius r. Such a structure can be considered as a kind of discontinuity (Section 2.3) when connecting the bent slab waveguide to a normal straight slab waveguide (Figure 4.1 (b)). The incoming wave is guided in the y-z-plane at oblique angles of propagation φ.

As a first step, we are interested in the semi-guided modes that propagate in the curved segment. Thus, we neglect the transition between straight and bent slab waveguide initially and analyze the modal properties of the bent part only. This work was motivated by a similar study [99] of bend mode configurations for normal incidence $\varphi = 0°$. For that case, scalar 2-D bend modes of particular TE- or TM-polarization are present.

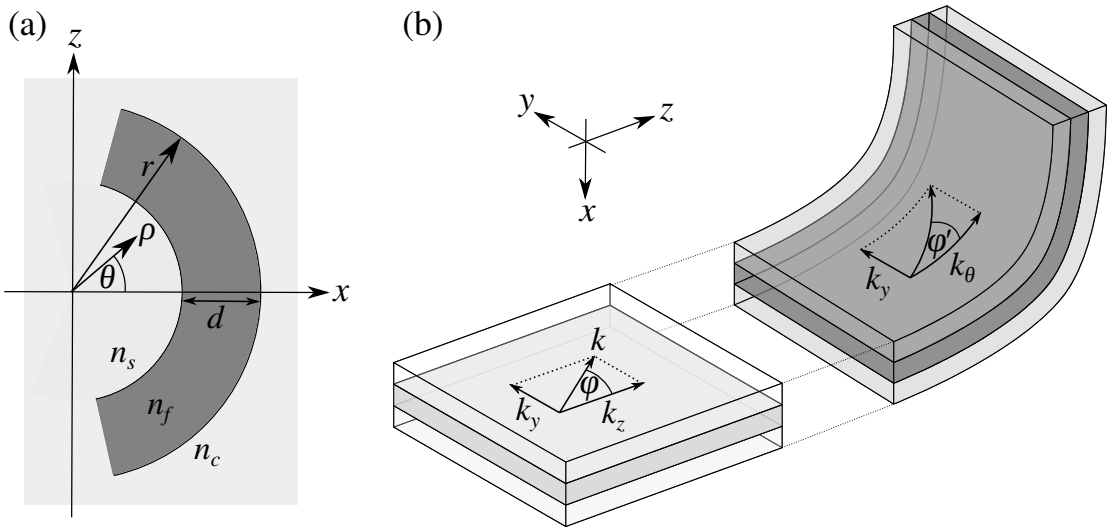

Figure 4.1: (a) Bent slab waveguide structure with refractive indices n_f, n_s and n_c and core thickness d. The structure is regularly bent around the y-axis with outer curvature radius r, and constant along the y- and θ-direction. (b) Illustration of an imagined excitation of the bent waveguide by a straight slab waveguide with the same parameters. The incoming semi-guided wave reaches the structure at oblique angles of incidence φ in the y-z-plane. This leads to wavenumbers k_y and k_θ in the bent structure. The propagating mode in the bent part "spirals" at an angle φ' [18].

Here, we consider a 2-D cross section, as shown in Figure 4.1 (a). Because of the symmetry of the structure under study, further investigations are carried out in cylindrical coordinates (ρ, θ, y). The whole system is constant along the y- and θ-direction. We are interested in quasi-guided attenuated waves that propagate along the curved slab with non-zero wavenumbers k_y and k_θ, thus waves that propagate in y-θ-direction at an angle φ', with a confined mode profile along the radial r-direction. Note that the outgoing propagation angle φ' is not necessarily identical to φ due to different guidance properties. The wavenumber k_y is determined by the incoming oblique semi-guided wave of the (imagined) adjoining straight slab waveguide because the structure is constant in the y-direction, and therefore we can adopt the field dependence also for the bent part. These kind of waves describe spirals along the waveguide segment, thus we call these modes "spiral modes". Depending on the considered incidence angle of the spiral

mode, three different scenarios are distinguished:

- For normal incidence $\varphi = 0°$ or $k_y = 0$, scalar 2-D bend modes are present [99].
- For angles $\varphi \gg \varphi_c, \varphi_s$ (cf. Section 2.3) and close to $90°$, the waves become lossless (cf. Section 2.3) and for real and integer angular orders, the segment can be continued to a full tube with guided OAM modes, as introduced in Section 2.2.2.
- In between exists a continuum of hybrid, vectorial waves – spiral modes – that propagate along the core segment and spiral around the tube axis with different levels of radiation losses (depending on the incidence angles φ or wavenumber k_y, respectively). In line with the argumentation in Section 2.3 the losses fully vanish beyond an incidence angle $\varphi > \max(\varphi_s, \varphi_c)$.

Hence, a smooth transition from 2-D lossy bend modes, to lesser-damped 2.5-D hybrid spiral modes, to guided OAM modes emerges, as we shall see below.

4.1.1 Mathematical formulation

The field solution for the electric and magnetic field in cylindrical coordinates is given by

$$\begin{pmatrix}\tilde{\mathbf{E}}\\ \tilde{\mathbf{H}}\end{pmatrix}(\rho,\theta,y) = \begin{pmatrix}\mathbf{E}\\ \mathbf{H}\end{pmatrix}(\rho,\theta)\mathrm{e}^{-\mathrm{i}k_y y}, \tag{4.1}$$

with fixed wavenumber $k_y = k_0 N_{\text{eff}} \sin\varphi$, which is determined and adopted from the field dependence of the adjoining straight slab waveguide. Here, N_{eff} is the effective refractive index of the straight slab waveguide and φ is the oblique incidence angle of the incoming wave that is propagating in the y-z-plane.

Substituting the ansatz in the Maxwell equations (2.6) in analogy to Section 2.2.2, the H_y and E_y components have to fulfill the electric and magnetic wave equation (2.23) in regions with constant refractive index

$$\partial_\rho^2\Psi + \frac{1}{\rho}\partial_\rho\Psi + \frac{1}{\rho^2}\partial_\theta^2\Psi + (k_0^2\varepsilon_r - k_y^2)\Psi = 0, \tag{4.2}$$

with $\Psi = H_y$ or $\Psi = E_y$. The remaining components are again given by Eq. (2.24). In contrast to the fiber modes, we do not make the assumption of an integer order in angular direction. Here, we consider a more general approach and use separation of variables by defining

$$\Psi(\rho,\theta) = f(\rho)\, g(\theta) \tag{4.3}$$

to solve Eq. (4.2), where f is a radial- and g an angular-dependent function. Replacing the assumption in Eq. (4.2) leads to two separate differential equations for f and g

$$g'' + \alpha g = 0 \qquad \wedge \qquad \rho^2 f'' + \rho f' + (\rho^2(k_0^2 n^2 - k_y^2) - \alpha) f = 0, \tag{4.4}$$

where the dashes denote derivatives, $\alpha \in \mathbb{C}$ is a constant and $n^2 = \varepsilon_r$ is the refractive index of the considered layer.

Now, we can define an angular order ν and a propagation constant k_θ by $\alpha = \nu^2$ and $\nu = k_\theta r$, such that the general solution of Eq. (4.4) can be written as

$$g(\theta) \propto \mathrm{e}^{-\mathrm{i}\sqrt{\alpha}\theta} = \mathrm{e}^{-\mathrm{i}k_\theta r\theta}. \tag{4.5}$$

Note that the definition of k_θ depends on the definition of the bend radius r [99] and has to be adjusted for other definitions. We are interested in propagating waves that decay in positive θ-direction, therefore we restrict the discussion to values $k_\theta \in \mathbb{C}$ with positive real and negative imaginary part. The outgoing propagation angle φ' is then determined by the propagation constant (real part of k_θ) via

$$\varphi' = \tan^{-1}\left(\frac{k_y}{\mathrm{Re}\{k_\theta\}}\right). \tag{4.6}$$

To find a solution for the radial function f, two cases have to be distinguished:

(I) For $k_0^2 n^2 > k_y^2$, Eq. (4.4) is a standard Bessel differential equation, and its elementary solutions are Bessel functions of the first kind J_ν and of the second kind Y_ν with complex order $\nu = k_\theta r$ [85].

(II) For $k_0^2 n^2 < k_y^2$, Eq. (4.4) can be transformed into the modified Bessel equation

$$\rho^2 f'' + \rho f' - (\rho^2(k_y^2 - k_0^2 n^2) - \alpha) f = 0, \tag{4.7}$$

with positive value $k_y^2 - k_0^2 n^2$. The solutions are the modified Bessel functions of the first kind I_ν and the second kind K_ν [85], which can be expressed through the Bessel functions J_ν and the Hankel function $\mathrm{H}_\nu^{(2)}$ of complex order $\nu = k_\theta r$.

The exact choice of solution functions depends on the considered region and is determined by the physical conditions that have to be fulfilled: in the center of the structure ($\rho = 0$) the fields should be zero, which is only fulfilled by the Bessel function of the first kind J_ν for case (I) and by the modified Bessel function I_ν for case (II). The functions fulfill the relation $\mathrm{I}_\nu(x) \sim \mathrm{J}_\nu(\mathrm{i}x)$, thus we can use the Bessel function J_ν for both cases with either real (I) or complex (II) argument.

For the cover region, where outgoing (partly decaying) propagating fields are physically correct solutions, the Hankel function $\mathrm{H}^{(2)}$ fulfills this condition when looking at the asymptotic expansion for large arguments [85, 99]. For the second case (II), the solution is given by the modified Bessel function K_ν, which can again be rewritten as the Hankel function $\mathrm{H}^{(2)}$ with negative and complex argument.

In the core region, the refractive index always fulfills $n_f \geq n_c, n_s$, which implies that $k_0 n_f \geq k_y$ and case (I) is always valid. The solution is therefore given by a linear combination of the Bessel function J_ν and the modified Bessel function Y_ν.

Then the full ansatz for $\Psi = E_y$ or $\Psi = H_y$ is

$$\Psi(\rho,\theta) = \begin{cases} A\,\mathrm{J}_\nu(\rho\chi_s)\,\mathrm{e}^{-\mathrm{i}\nu\theta}, & 0 \leq \rho \leq r-d, \\ \left(B\,\mathrm{J}_\nu(\rho\chi_f) + C\,\mathrm{Y}_\nu(\rho\chi_f)\right)\,\mathrm{e}^{-\mathrm{i}\nu\theta}, & r-d \leq \rho \leq r, \\ D\,\mathrm{H}_\nu^{(2)}(\pm\rho\chi_c)\,\mathrm{e}^{-\mathrm{i}\nu\theta}, & \rho \geq r, \end{cases} \tag{4.8}$$

where for simplicity we define $\chi_j = \sqrt{k_0^2 n_j^2 - k_y^2}$, $j \in \{s, f, c\}$, where the square root symbol is meant to indicate the positive real root, for a positive radicand, or the imaginary root with positive imaginary part, in case of a negative radicand. In the third case, the $\pm$-sign distinguishes

the cases for $k_y \leqslant k_0 n_\mathrm{c}$. Note that different expressions (4.8) need to be written for E_y and H_y, with separate coefficients A_E, B_E, C_E and D_E for the electric field component E_y and A_H, B_H, C_H and D_H for the magnetic field component H_y. As mentioned before, the other components are given by Eq. (2.24).

Now, the remaining unknown parameters are the eight amplitudes and the complex angular propagation number k_θ. In order to identify these values, the boundary conditions of the structure are considered (till now Eq. (4.8) is only valid in the layers, not yet on the boundaries): the tangential electric field components E_y, E_θ, all magnetic field components H_y, H_θ, and H_ρ, and the normal component $n^2 E_\rho$ of the dielectric displacement are continuous at the boundaries $\rho = r^- = r - d$ and $\rho = r$. Setting up the equations for E_y, H_y, E_θ and H_θ (the other variables do not provide any further insights) leads to a system of eight equations,

$$A_E \mathrm{J}_\nu(r^-\chi_\mathrm{s}) = B_E \mathrm{J}_\nu(r^-\chi_\mathrm{f}) + C_E \mathrm{Y}_\nu(r^-\chi_\mathrm{f}), \tag{4.9}$$

$$A_H \mathrm{J}_\nu(r^-\chi_\mathrm{s}) = B_H \mathrm{J}_\nu(r^-\chi_\mathrm{f}) + C_H \mathrm{Y}_\nu(r^-\chi_\mathrm{f}), \tag{4.10}$$

$$\begin{aligned} &\frac{1}{\chi_\mathrm{s}^2}\Big(-\mathrm{i}\frac{k_y \nu}{r^-} A_E \mathrm{J}_\nu(r^-\chi_\mathrm{s}) - \omega\mu_0\chi_\mathrm{s} A_H \mathrm{J}'_\nu(r^-\chi_\mathrm{s})\Big) \\ = \;& \frac{1}{\chi_\mathrm{f}^2}\Big(-\mathrm{i}\frac{k_y \nu}{r^-} \left(B_E \mathrm{J}_\nu(r^-\chi_\mathrm{f}) + C_E \mathrm{Y}_\nu(r^-\chi_\mathrm{f})\right) \\ &-\omega\mu_0\chi_\mathrm{f} \left(B_H \mathrm{J}'_\nu(r^-\chi_\mathrm{f}) + C_H \mathrm{Y}'_\nu(r^-\chi_\mathrm{f})\right)\Big), \end{aligned} \tag{4.11}$$

$$\begin{aligned} &\frac{1}{\chi_\mathrm{s}^2}\Big(-\mathrm{i}\frac{k_y \nu}{r^-} A_H \mathrm{J}_\nu(r^-\chi_\mathrm{s}) + \omega\varepsilon_0 n_\mathrm{s}^2\chi_\mathrm{s} A_E \mathrm{J}'_\nu(r^-\chi_\mathrm{s})\Big) \\ = \;& \frac{1}{\chi_\mathrm{f}^2}\Big(-\mathrm{i}\frac{k_y \nu}{r^-} \left(B_H \mathrm{J}_\nu(r^-\chi_\mathrm{f}) + C_H \mathrm{Y}_\nu(r^-\chi_\mathrm{f})\right) \\ + \;& \omega\varepsilon_0 n_\mathrm{f}^2\chi_f \left(B_E \mathrm{J}'_\nu(r^-\chi_\mathrm{f}) + C_E \mathrm{Y}'_\nu(r^-\chi_\mathrm{f})\right)\Big), \end{aligned} \tag{4.12}$$

$$B_E \mathrm{J}_\nu(r\chi_\mathrm{f}) + C_E \mathrm{Y}_\nu(r\chi_\mathrm{f}) = D_E \mathrm{H}_\nu^{(2)}(\pm r\chi_\mathrm{c}), \tag{4.13}$$

$$B_H \mathrm{J}_\nu(r\chi_\mathrm{f}) + C_H \mathrm{Y}_\nu(r\chi_\mathrm{f}) = D_H \mathrm{H}_\nu^{(2)}(\pm r\chi_\mathrm{c}), \tag{4.14}$$

$$\begin{aligned} &\frac{1}{\chi_\mathrm{f}^2}\Big(-\mathrm{i}\frac{k_y \nu}{r} \left(B_E \mathrm{J}_\nu(r\chi_\mathrm{f}) + C_E \mathrm{Y}_\nu(r\chi_\mathrm{f})\right) \\ &-\omega\mu_0\chi_\mathrm{f} \left(B_H \mathrm{J}'_\nu(r\chi_\mathrm{f}) + C_H \mathrm{Y}'_\nu(r\chi_\mathrm{f})\right)\Big) \\ = \;& \frac{1}{\chi_\mathrm{c}^2}\Big(-\mathrm{i}\frac{k_y \nu}{r} D_E \mathrm{H}_\nu^{(2)}(\pm r\chi_\mathrm{c}) \mp \omega\mu_0\chi_\mathrm{c} D_H \mathrm{H}_\nu^{(2)'}(\pm r\chi_\mathrm{c})\Big), \end{aligned} \tag{4.15}$$

$$\begin{aligned} &\frac{1}{\chi_\mathrm{f}^2}\Big(-\mathrm{i}\frac{k_y \nu}{r} \left(B_H \mathrm{J}_\nu(r\chi_\mathrm{f}) + C_H \mathrm{Y}_\nu(r\chi_\mathrm{f})\right) \\ &+\omega\varepsilon_0 n_\mathrm{f}^2\chi_\mathrm{f} \left(B_E \mathrm{J}'_\nu(r\chi_\mathrm{f}) + C_E \mathrm{Y}'_\nu(r\chi_\mathrm{f})\right)\Big) \\ = \;& \frac{1}{\chi_\mathrm{c}^2}\Big(-\mathrm{i}\frac{k_y \nu}{r} D_H \mathrm{H}_\nu^{(2)}(\pm r\chi_\mathrm{c}) \pm \omega\varepsilon_0 n_\mathrm{c}^2\chi_\mathrm{c} D_E \mathrm{H}_\nu^{(2)'}(\pm r\chi_\mathrm{c})\Big), \end{aligned} \tag{4.16}$$

which can be written as an eigenvalue problem

$$\mathsf{M}_{k_y}(k_\theta)\mathbf{A} = 0, \tag{4.17}$$

where the matrix $\mathsf{M}_{k_y} \in \mathbb{C}^{8\times 8}$ for fixed k_y depends on the unknown wavenumber k_θ, and the vector $\mathbf{A} = (A_E, B_E, C_E, D_E, A_H, B_H, C_H, D_H)^T$ lists all unknown amplitudes from Eq. (4.8). For a propagating and/or decaying hybrid spiral mode, we are searching for complex, non-zero values of k_θ. This is the case, if the matrix M becomes singular, i.e., the determinant of the matrix is zero. The equations can not be solved analytically, therefore numerical methods have to be used (see Section 4.2).

4.1.2 Bend modes

As mentioned before, the now introduced vectorial quasi-guided spiral modes are a general formulation for the complete range of incidence angles $\varphi \in [0°, 90°)$. For vanishing axial wavenumber $k_y = 0$, meaning an incidence angle $\varphi = 0°$ when considered in the context of an adjoining straight slab waveguide, standard 2-D bend modes [9, 99] are found. Eqs. (2.22) then split into two separate sets of TE and TM modes. The TE modes have non-zero components H_ρ, H_θ and E_y given by

$$H_\rho = \frac{\mathrm{i}}{\omega\mu_0\rho}\partial_\theta E_y, \tag{4.18}$$

$$H_\theta = \frac{-\mathrm{i}}{\omega\mu_0}\partial_\rho E_y \tag{4.19}$$

and E_y has to fulfill the scalar TE wave equation (cf. Eq. (4.2))

$$\partial_\rho^2 E_y + \frac{1}{\rho}\partial_\rho E_y + (k_0^2\varepsilon_r - \frac{k_\theta^2 r^2}{\rho^2})E_y = 0. \tag{4.20}$$

For the TM case, the non-zero components E_ρ, E_θ and H_y are given by

$$E_\rho = \frac{-\mathrm{i}}{\omega\varepsilon_0\varepsilon_r\rho}\partial_\theta H_y, \tag{4.21}$$

$$E_\theta = \frac{\mathrm{i}}{\omega\varepsilon_0\varepsilon_r}\partial_\rho H_y \tag{4.22}$$

and H_y has to fulfill the magnetic wave equation (cf. Eq. (4.2))

$$\partial_\rho^2 H_y + \frac{1}{\rho}\partial_\rho H_y + (k_0^2\varepsilon_r - \frac{k_\theta^2 r^2}{\rho^2})H_y = 0. \tag{4.23}$$

Hence, the problem reduces to a scalar problem for either E_y or H_y.

4.1.3 OAM modes

When considering large oblique incidence angles with $\varphi > \varphi_c$ or $k_y > k_0 n_c$, the spiral modes are guided in the curved structure without any losses. Looking at Eq. (4.8), the argument $\chi_c = \sqrt{k_0^2 n_c^2 - k_y^2}$ for the Hankel function is then always imaginary, representing a decaying function. Hence, the fields become evanescent in the cladding region. Consequently, we expect real eigenvalues k_θ of the eigenvalue equation (4.17). One can find a continuum of lossless spiral modes.

In case the angular order $\nu = k_\theta r$ (with real k_θ) is of integer order $\nu \in \mathbb{Z}$, the solutions match those of the OAM modes presented in Section 2.2.2. The bent waveguide structure can then be

continued to an entire tube, where the spiral modes are valid solutions and match those of the OAM modes with distinct angular order ν. Since only a discrete number of OAM modes exists, the set of spiral modes with integer angular order should be countable as well.

To identify these OAM modes in our approach, one can change the roles of k_y and k_θ. We assume and predict an integer angular order $\nu = k_\theta r$ and k_y represents the unknown parameter, accordingly. Hence, Eq. (4.17) can be written as

$$\mathsf{M}_\nu(k_y)\mathbf{A} = 0, \tag{4.24}$$

which is a standard eigenvalue problem as described in Section 2.2.2. The matrix M_ν is now defined for given angular order ν. We are searching for real values of k_y. To fulfill the guidance condition (2.31), $k_0 n_\mathrm{c} < k_y < k_0 n_\mathrm{f}$ has to be satisfied.

4.2 Results

This section provides some example results for spiral modes. Parameters, as already introduced in Table 2.1, with high (hc) and low (lc) refractive index contrast, for fixed wavelength $\lambda_0 = 1.3\,\mu$m and varying outer radius r are considered:

(lc) $n_c = n_s = 1.6$, $n_f = 1.7$, $d = 1\,\mu$m (values adopted from [99] for benchmark)

(hc) $n_c = n_s = 1.5$, $n_f = 2$, $d = 0.4\,\mu$m (standard high index contrast Si/Si0_2 waveguide)

As discussed in Section 2.3, the critical angles for radiation suppression are given by $\varphi_c = \varphi_s = 74.5°$ for the low index contrast and by $\varphi_c = \varphi_s = 56.54°$ for the high index contrast, since we assume $n_c = n_s$.

4.2.1 Implementation

When determining the spiral modes, we are searching for complex values for k_θ, with $\mathrm{Re}\{k_\theta\} > 0$ and $\mathrm{Im}\{k_\theta\} < 0$, that solve the eigenvalue problem $\mathsf{M}_{k_y}(k_\theta)\mathbf{A} = 0$ by looking for values where the determinant of M_{k_y} vanishes, i.e., $\det(\mathsf{M}_{k_y}(k_\theta)) = 0$.

Therefore, we use the complex secant method [101] to find zero points of the determinant, which we implemented in the computer algebra system Maple [100]. As a starting point, for fixed incidence angle and large curvature radius, we choose the value of k_z as we know that the solution for large radii converges to the wavenumber of the corresponding straight slab waveguide $k_\theta \approx k_z = k_0 N_\mathrm{eff}\cos\varphi$ with an additional small imaginary part. The curvature radius is then decreased and the new start point is adopted from the determined solution before. Hence, we trace the solution step by step, using the solution of the preceding step as the next initial value.

4.2.2 Spiral mode eigenvalues

The calculated real and imaginary part of the effective mode index k_θ/k_0 for TE- and TM-like spiral modes for low and high index contrast are shown in Figures 4.2–4.5. The complex mode indices are illustrated twice, either depending on the curvature radius r (left panel) or on the incidence angle φ (right panel). Note that the imaginary part is plotted on a logarithmic scale for the dependence on the radius (left panel).

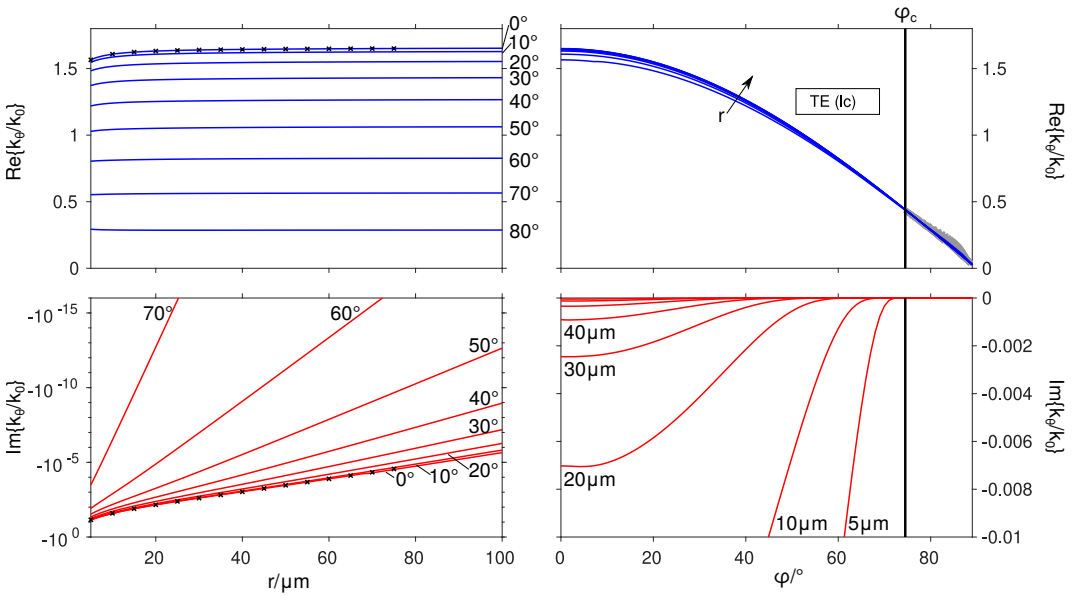

Figure 4.2: TE-like spiral mode wavenumbers for low refractive index contrast (lc) waveguide parameters. The real and imaginary part are shown depending on the curvature radius r or incidence angle φ (critical angle $\varphi_c = 74.5°$) [18]. The gray region for $\varphi > \varphi_c$ marks the corresponding TE-like OAM modes and the black crosses are reference values from [99].

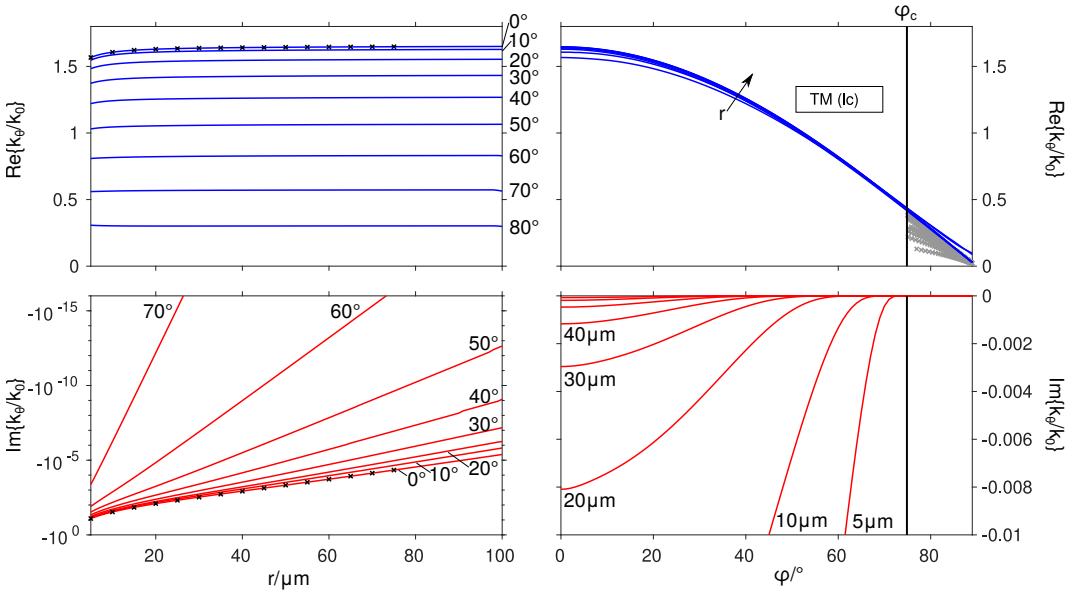

Figure 4.3: TM-like spiral mode wavenumbers for low refractive index contrast (lc) waveguide parameters. The real and imaginary part are shown depending on the curvature radius r or incidence angle φ (critical angle $\varphi_c = 74.86°$) [18]. The gray region for $\varphi > \varphi_c$ marks the corresponding TM-like OAM modes and the black crosses are reference values from [99].

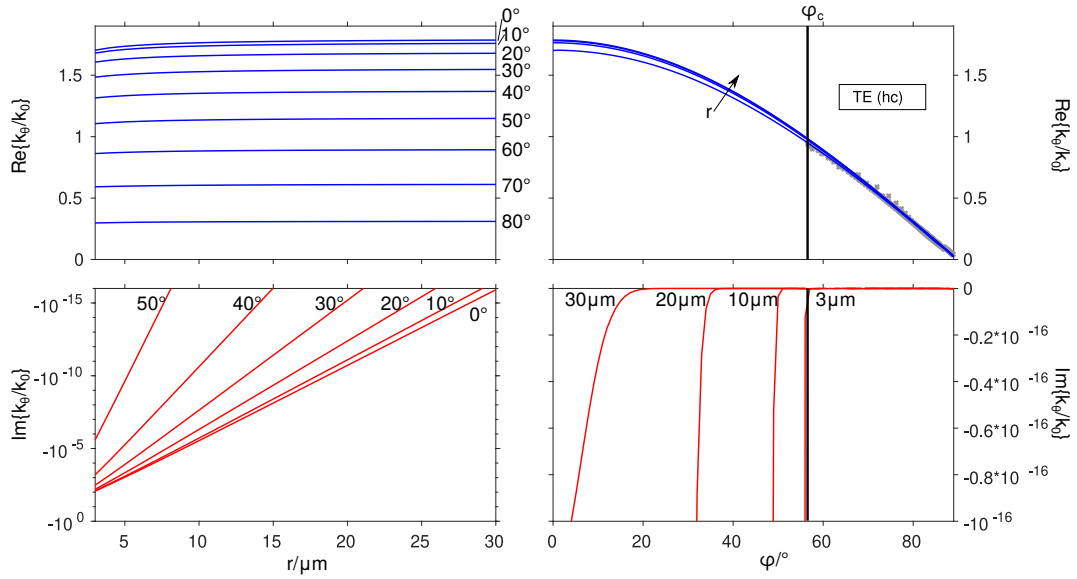

Figure 4.4: TE-like spiral mode wavenumbers for high refractive index contrast (hc) waveguide parameters. The real and imaginary part are shown depending on the curvature radius r or incidence angle φ (critical angle $\varphi_c = 56.54°$). The gray region for $\varphi > \varphi_c$ marks the corresponding TE-like OAM modes [18].

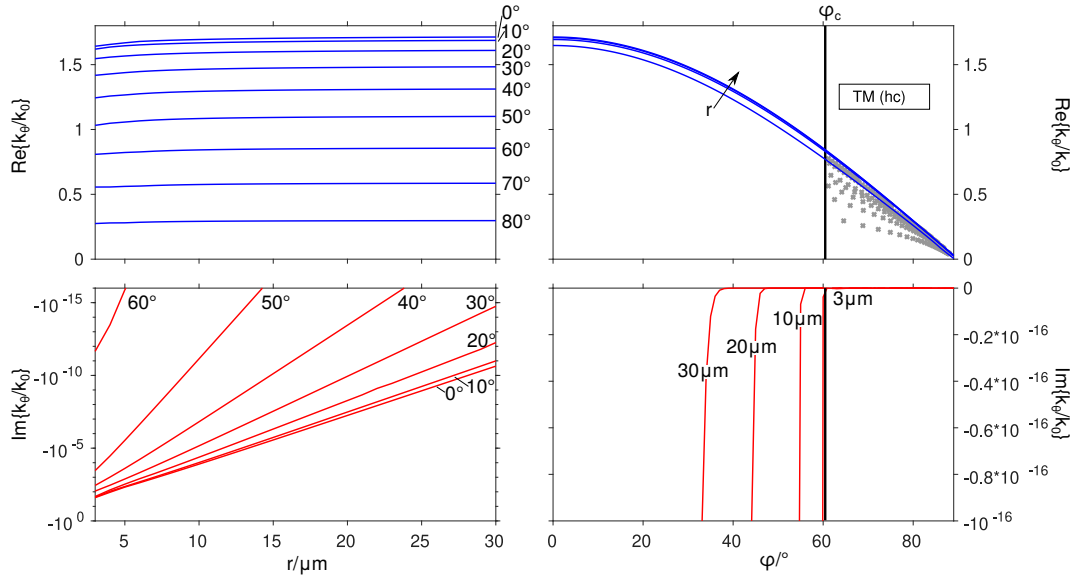

Figure 4.5: TM-like spiral mode wavenumbers for high refractive index contrast (hc) waveguide parameters. The real and imaginary part are shown depending on the curvature radius r or incidence angle φ (critical angle $\varphi_c = 60.46°$). The gray region for $\varphi > \varphi_c$ marks the corresponding TM-like OAM modes [18].

The following characteristics can be identified. For large radii and arbitrary angle of incidence, one expects the real part of the mode indices to correspond to those of the straight waveguide with oblique propagation. Hence, $k_y = k_0 N_{\text{eff}} \sin\varphi$ and $k_\theta \approx k_z = k_0 N_{\text{eff}} \cos\varphi$. This explains the convergence behavior (in the limit of large bend radii) of the real parts in the left panels and the cosine function shape of the real parts in the right panel of the figures. The values agree well, just small differences for strongly curved structures are observed due to the bending. The imaginary part represents the attenuation of the spiral modes that relate to mode profiles with pronounced oscillatory behavior in the cladding region. We observe a logarithmic dependence, as seen in the lower left linear plots. For small curvature radii, the attenuation is strong, while it decreases as the angle of incidence increases, since the bending has less effect.

For incidence angles $\varphi = 0°$ or wavenumber $k_y = 0$, the bend modes [99] are present. The Maxwell equations are separated and can either be solved for TE or TM modes. The calculated values from [99] (just for the low refractive index contrast) are marked in Figures 4.2–4.3 by the black crosses for $\varphi = 0°$ and varying curvature radius. They coincide perfectly with the calculated values of the spiral modes. The attenuation of the bend modes is strong, but decreases with increasing curvature radius and converges against the values of the corresponding slab waveguide with $k_y = 0$ and $k_\theta \approx k_z = k_0 N_{\text{eff}}$.

As discussed, for the lossless region $\varphi > \varphi_c$, i.e., large propagation angles, the spiral modes are fully lossless and for specific integer angular orders $\nu = k_\theta r \in \mathbb{Z}$, the wavenumbers match those

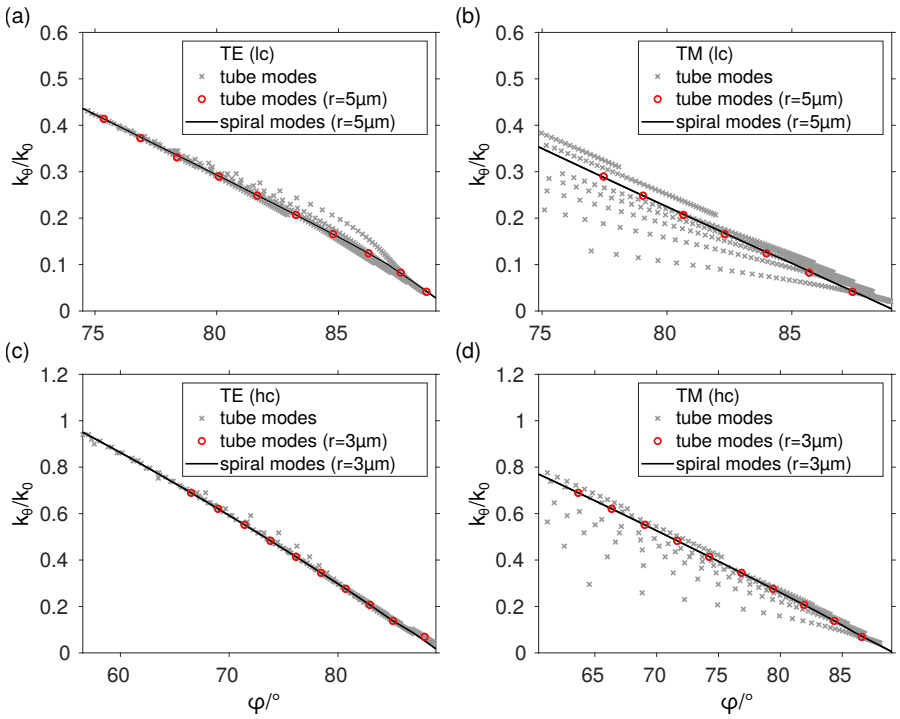

Figure 4.6: Enlargements of Figures 4.2–4.5; effective mode indices versus the incidence angle $\varphi > \varphi_c$; the gray crosses mark the wavenumbers of all OAM modes, the red dots represent the OAM modes for fixed curvature radius r and the solid black line marks the wavenumbers of the spiral modes for fixed curvature radius r [18].

of a circular dielectric fiber with a single layer refractive index contrast (Section 2.2.2). Our approach can be modified to calculate these OAM modes by additionally assuming $\nu = k_\theta r \in \mathbb{Z}$. Hence, the OAM modes are a special case of the spiral modes that have the additional condition of an integer order (instead of complex real values). The solution $(k_y, \nu = k_\theta/r)$ can then be transferred to a corresponding incidence angle for the spiral modes via $\sin\varphi = k_y/(k_0 N_{\text{eff}})$. The calculated wavenumbers for the OAM modes are illustrated by the gray markers in the figures and match with some of the spiral modes. An enlargement of this region is shown in Figure 4.6 for fixed curvature radius r in the region $\varphi > \varphi_c$. As can be seen, the wavenumbers for the spiral modes match those associated with the discrete OAM modes for equal radius and polarization. Finally, for high index configurations (Figures 4.4–4.5), one observes a qualitatively similar behavior for both TE and TM modes with substantially higher losses.

4.2.3 Mode profiles

For some specific configurations (fixed incidence angle and curvature radius), the radial mode profiles are illustrated in Figure 4.7. The gray bar marks the core of the bent waveguide structure. Shown is the transverse electric field component

$$E_\perp = \cos\varphi E_y - \sin\varphi E_\theta \tag{4.25}$$

that is perpendicular to the in-plane wavevector (k_θ, k_y), hence perpendicular to the propagation direction. The fields are power normalized to unit power, in a sense that the angular optical power flow per axial unit length

$$P_\theta = \frac{1}{2}\int_0^\infty \mathrm{Re}\{\mathbf{E}^* \times \mathbf{H}\} \cdot \mathbf{e}_\theta \mathrm{d}\rho \tag{4.26}$$

is unity, where $\mathbf{e}_\theta$ is the unit vector in angular direction θ. As previously stated, the losses reduce drastically for increasing curvature radius or incidence angle, which is observed by a less pronounced oscillatory behaviour in the cladding region. Furthermore, for small curvature radius and incidence angle, the maximum of the mode profile is shifted to the outer region of the core and the mode profile becomes more symmetric for increasing radius/incidence angle (more similar to the shape of a TE slab mode). Additionally, the mode profiles of the bend modes ($\varphi = 0°$) are shown in the first row, which have the strongest attenuation for small curvature radii.

Figure 4.8 and Figure 4.9 show the propagation of the spiral modes along the waveguide core for small fixed curvature radii and varying incidence angle. Next to the transverse field component $E_\perp$, the energy density w

$$w = \frac{1}{4}(\varepsilon_0\varepsilon|\mathbf{E}|^2 + \mu_0|\mathbf{H}|^2) \tag{4.27}$$

is also shown. For small incidence angles, the wave is propagating along the core section with decaying amplitude and radiating in the radial direction, i.e., the external cladding region with $\rho > r$. Increasing the angle of incidence leads to less pronounced radiation up to complete lossless guidance of the fields.

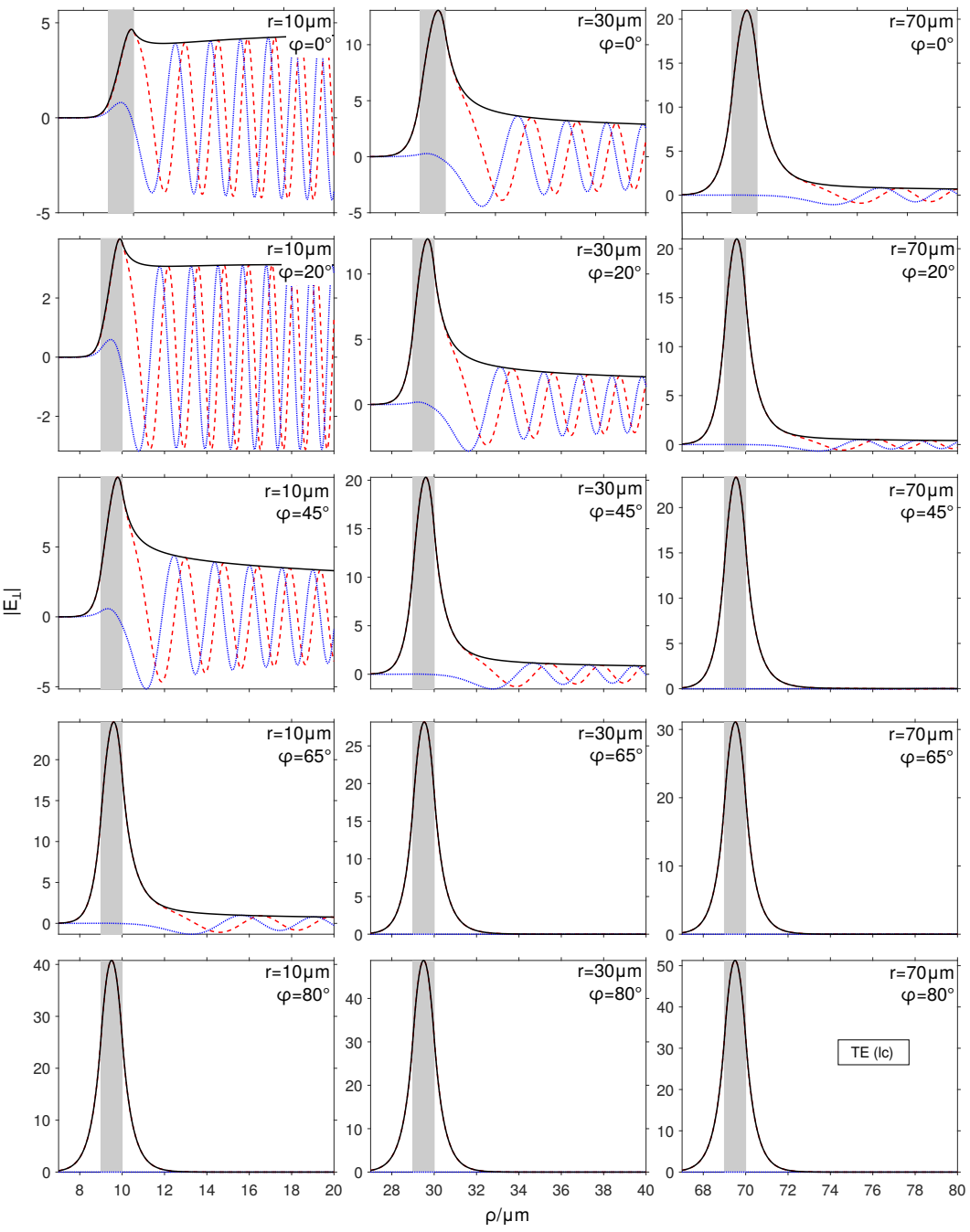

Figure 4.7: Normalized radial mode profiles of TE-like spiral modes supported by low refractive index contrast bends for different radii r and angles φ. Shown is the absolute value (continuous line), the real part (dashed), and the imaginary part (dotted) of the transverse component $E_\perp$ [18].

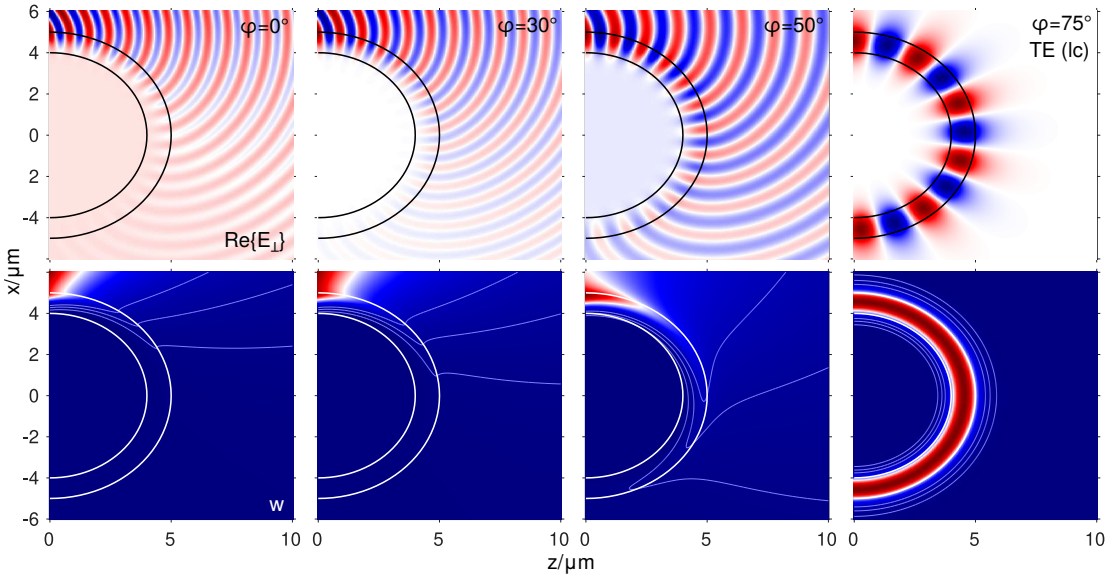

Figure 4.8: Transverse electric fields $\mathrm{Re}\{E_\perp\}$ (top row) and energy density w (bottom row) for TE-like spiral modes supported by a low index contrast bent waveguide with curvature radius $r = 5\,\mu$m for different angles of propagation φ. The contour lines (bottom row) mark the levels of the absolute value at 2%, 5% and 10% [18].

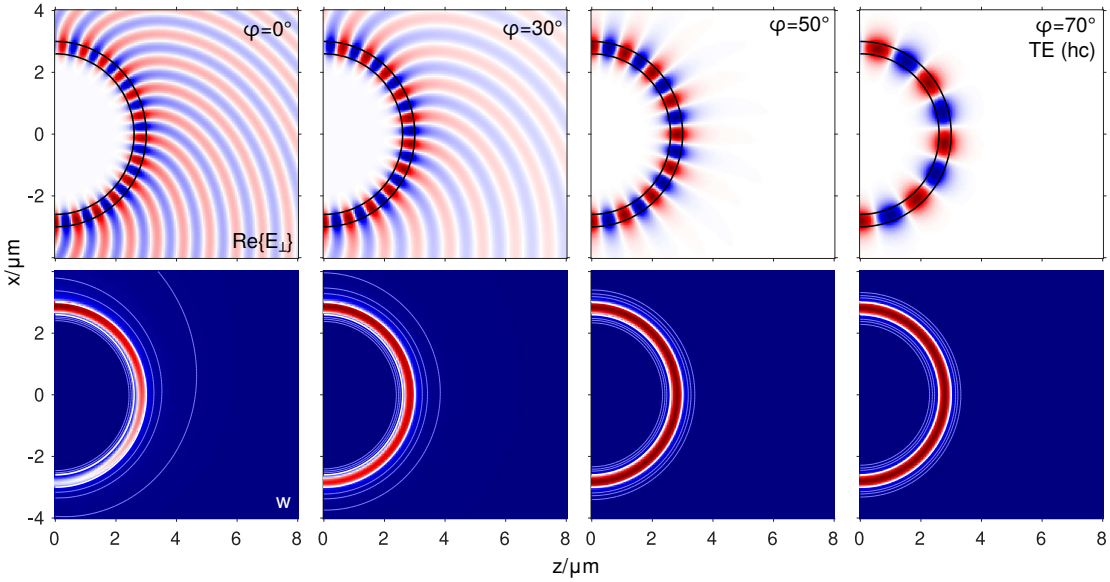

Figure 4.9: Transverse electric fields $\mathrm{Re}\{E_\perp\}$ (top row) and energy density w (bottom row) for TE-like spiral modes supported by a high index contrast bent waveguide with curvature radius $r = 3\,\mu$m for different angles of propagation φ. The contour lines (bottom row) mark the levels of the absolute value at 2%, 5% and 10% [18].

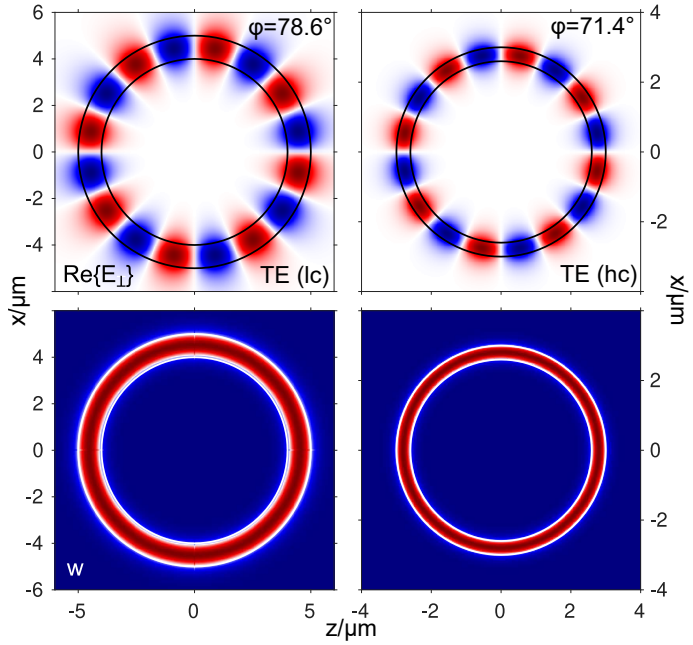

Figure 4.10: Transverse electric fields $\mathrm{Re}\{E_\perp\}$ and the electromagnetic energy density w of TE-like OAM modes with angular order $\nu = 8$ or spiral modes with incidence angle φ, for high and low refractive index contrast and fixed curvature radii $r = 5\,\mu$m (left column) and $r = 3\,\mu$m (right column) [18].

Furthermore, Figure 4.10 shows two examples of OAM modes or spiral modes with integer order. Here, the bent segment can be extended to a full circular cylinder, since the continuity condition at $\theta = 0$ and $\theta = 2\pi$ is additionally fulfilled. Shown are the field patterns of OAM modes of angular order $\nu = 8$, for the small radii as considered in Figure 4.8 and Figure 4.9. The fields coincide with the spiral modes of identical geometry with incidence angles $\varphi = 78.6°$ (lc, left column) and $\varphi = 71.4°$ (hc, right column).

4.2.4 Polarization

The introduced spiral modes are full vectorial hybrid modes, thus an interesting property is the polarization character of these modes. Therefore, we consider the relative strength

$$\Gamma_\mathrm{E} = \int_0^\infty |E_\perp|^2 \mathrm{d}\rho \Big/ \int_0^\infty |\mathbf{E}|^2 \mathrm{d}\rho \tag{4.28}$$

of the in-plane electric field component $E_\perp$ perpendicular to the local wavevector. For large curvature radii, i.e., nearly a straight slab waveguide, the value is given by 1 for 2-D TE slab modes, and by 0 for the TM slab modes. Additionally, for incidence angle $\varphi = 0°$ and arbitrary curvature radii, the values are also given by 1 or 0, respectively, as the problem also splits into the scalar TE or TM bend modes. Figure 4.11 shows the polarization ratios for the hybrid spiral modes for both index contrasts.

As expected, for large radii or normal incidence angles, the values are given by 1 or 0 for the TE or TM case, respectively. For increasing but intermediate angles the modes become

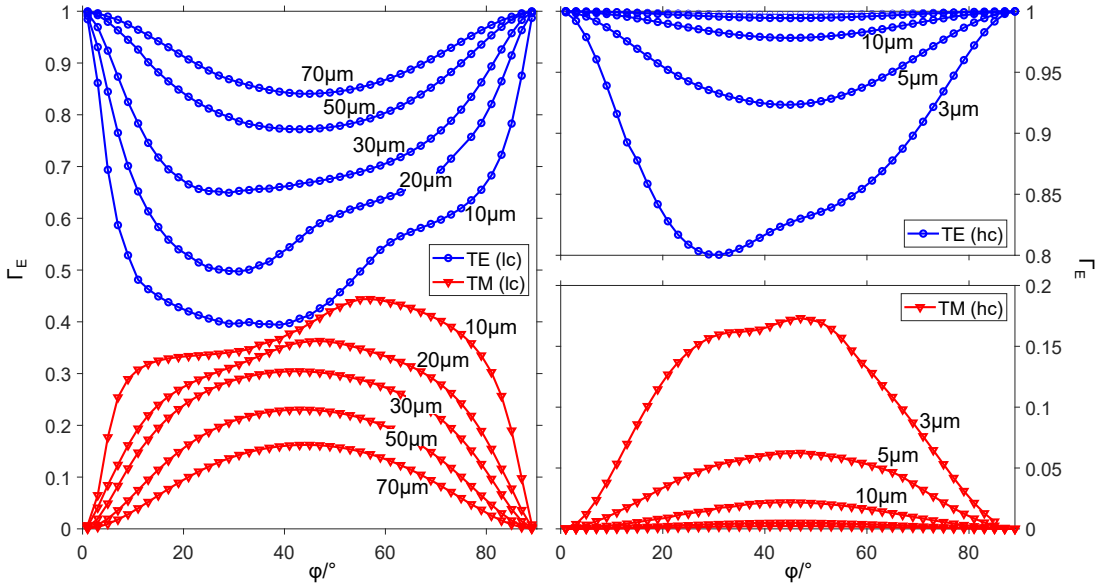

Figure 4.11: Polarization ratios Γ_{E} for the hybrid spiral modes for low (a) and high (b) refractive index contrast and different radii r depending on the propagation angle φ [18].

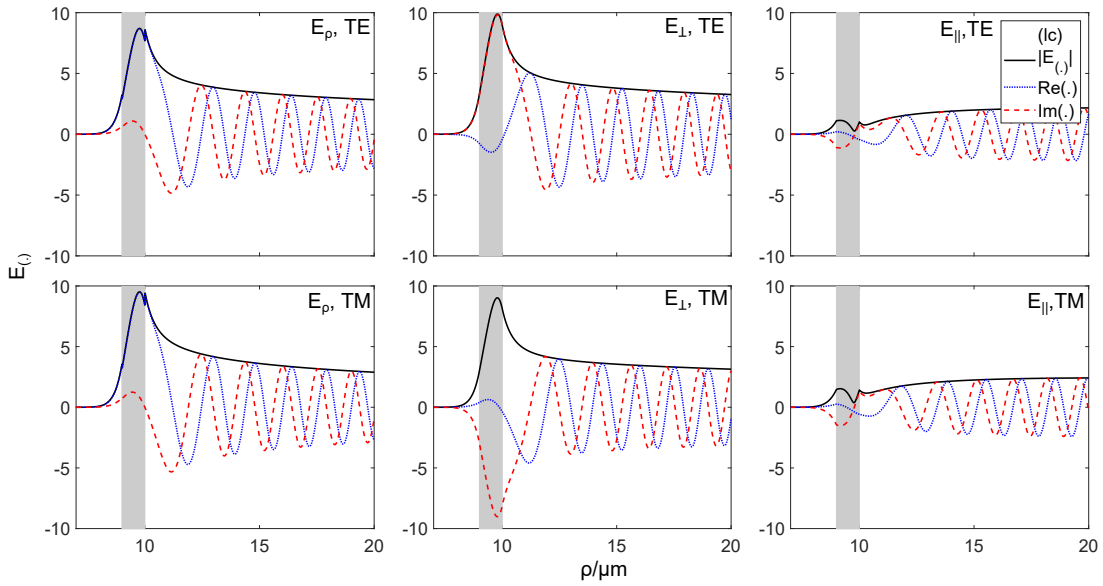

Figure 4.12: Electric profiles of TE- and TM-like hybrid spiral modes supported by a low-contrast bend of radius $r = 10\,\mu$m. These are modes with equal k_y, given by angles $\varphi = 45.0°$ (TE) and $\varphi = 45.1°$ (TM). The curves show the absolute value (continuous), the real part (dotted), and the imaginary part (dashed) of the electric components in radial direction E_ρ, and in-plane in directions perpendicular $E_\perp$ and parallel $E_\parallel$ to the direction of propagation [18].

more hybrid, especially for small curvature radii. We observe that for a higher refractive index contrast (hc), which exhibits a stronger field confinement, the mixture in polarization is lesser

than for the low index contrast (lc). To have a closer look at the polarization character of these hybrid modes, Figure 4.12 compares the normalized vectorial electric field profiles of TE and TM spiral modes at intermediate angle $\varphi \approx 45^\circ$ and curvature radius $r = 10\,\mu$m for the low index contrast.

In addition to the radial component E_ρ and the transverse component $E_\perp$, also the longitudinal electric component

$$E_\parallel = \cos\varphi E_\theta + \sin\varphi E_y, \tag{4.29}$$

parallel to the local in-plane wavevector (k_θ, k_y) is shown.

The fields still resemble the major electric components of straight slab TE and TM modes, except that they also exhibit strong transverse fields E_ρ and $E_\perp$. The modes differ in the relative signs of these large transverse electric profile components.

Chapter 5

Bent corner and step configurations[1]

New proposals for 3-D integrated platforms with compact, high-index-contrast dielectric optical waveguides at different height levels on photonic platforms have been presented [25–27]. However, the challenging task is the transfer of optical power between levels without too much losses and/or crosstalk. Moreover, configurations that fulfill this property should ideally work for arbitrary vertical distances.

A variety of concepts that are able to transfer power between different levels were already introduced, e.g., vertically stacked integrated couplers [102], vertically overlapping tapered cores [103, 104], radiative transfer through grating couplers [105] or resonant interaction between vertically stacked microrings [106]. But, as far as we know, all these structures have certain disadvantages, e.g., large size, difficulties in design or fabrication, incomplete power transfer or tight tolerances. Alternatively, in [14, 107] two slab waveguides of different heights are connected by a third vertical segment, representing a step waveguide configuration with sharp kinks. When the structure is excited at oblique angles of incidence, full transmission is achieved for certain heights. This is due to a resonance effect that depends strongly on the height and angle.

In this chapter, we study an almost similar step configuration by replacing the sharp edges with bends (see Figure 5.1). These investigations are especially important in terms of manufacturing. The sensitive conditions on sharp edges are difficult to realize and mostly result in slight curvatures. We adopt the waveguide parameters from [14], i.e., slab thicknesses and Si/SiO_2 index contrast, to have a direct comparison of both configurations. We will see that the rounded edges are advantageous in terms of manufacturing tolerances and the strong condition on the angle of incidence and vertical distance, which lead to the resonance effect of full transmission, is mitigated.

More specifically, we study 2-D slab waveguides connected by a curved discontinuity, representing corner (Section 5.1.1) or step configurations (Section 5.1.2) with small bends as shown in Figure 5.1. Due to the oblique propagation of the incoming semi-guided wave and the high refractive index contrast, it is possible to guide waves without losses even in bent slab waveg-

[1] This topic was already part of the candidate's master thesis [93]. We show the results of the corresponding published paper [13] for the sake of completeness.

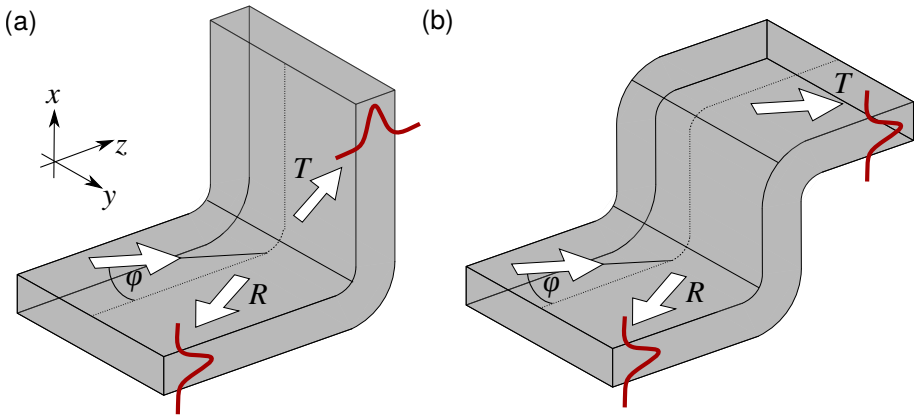

Figure 5.1: Bent corner (a) and bent step (b) configuration. The incoming wave is propagating at an incidence angle φ. Images show incoming, reflected (R) and transmitted (T) waves [13].

uide configurations with very small curvature radii (cf. Chapter 4). We are interested in high transmittance values to transfer power to another level of height on a photonic chip.

The FEM software COMSOL Multiphysics [22] is used to simulate the wave propagation in these structures by applying port boundary conditions, for exciting the structure, and perfectly matched layers, for simulating infinite space. Furthermore, we consider full 3-D solutions by exciting the structure with a laterally confined wave packet in Section 5.2.

The shapes of the structures are motivated by earlier studies investigating discontinuities of sharp corner-, step-, bridge- or U-turn-like structures [14–16, 107], straight interfaces of different heights [17] and bent waveguides at normal [99] or oblique incidence [18,93] (cf. Chapter 4).

5.1 2-D bent structures

Sketches of the 2-D cross section of the bent corner and bent step structure are shown in Figure 5.2. The corner configuration (a) consists of an incoming and outgoing dielectric slab waveguide that are connected by a curved slab waveguide. The step configuration in Figure 5.2 (b) comprises two bends that are connected by a third vertical segment of height h. Thus, the step can be considered as a combination of two corner structures. For both configurations, the refractive indices are given by $n_f = 3.45$ in the core and $n_c = 1.45$ in the claddings for vacuum wavelength $\lambda_0 = 1.55\,\mu$m, representing a standard high-index Si/SiO_2 waveguide. The thickness of the core is given by $d = 0.25\,\mu$m. The bends possess an outer curvature radius r with a constant slab thickness $d = 0.25\,\mu$m. The structures are assumed to be constant along the y-direction and the incoming wave is semi-guided in the y-z-plane at oblique angles of propagation φ (Figure 5.2 (a)). Hence, we can consider the whole problem in a 2.5-D setting. We are interested in transmittance T and reflectance R values for both configurations depending on the curvature radius r, the incidence angle φ and the vertical height h.

The considered slab waveguides only guide the fundamental TE and TM modes, as introduced in Table 2.1. In line with the arguments from Section 2.3, critical angles are defined as $\varphi_c = 30.45°$ and $\varphi_m = 51.14°$ for either radiation or TM suppression, when assuming TE_0 incidence.

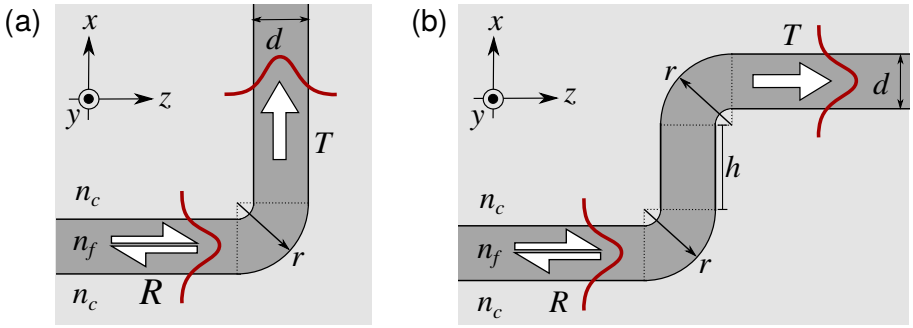

Figure 5.2: Side view of the cross section of the bent corner (a) and bent step (b) structure from Figure 5.1; waveguide parameters are given by the refractive indices n_f in the core, n_c in the cladding regions and the core thickness d. The bends have an outer curvature radius r. Additionally, the step structure (b) has a vertical segment of height h [13].

Note that other definitions of the curvature radius give different results. In [93], equal curvature radii for inner and outer interfaces of the bends are considered, which leads, in certain circumstances, to strong resonance effects with full reflection. Since we are interested in full transmission, we stay with the introduced definition which also fits to the studies in Chapter 4.

5.1.1 Bent corner

We start by analyzing the bent corner configuration from Figure 5.2 (a). The calculated transmittance T and reflectance R values, further separated in TE or TM, are illustrated in Figure 5.3 for fixed curvature radii $r \in \{0.26, 0.35, 0.5\}\,\mu$m and varying incidence angle $\varphi \in [0, 90)^\circ$. The critical angles φ_c and φ_m are additionally marked in the plots.

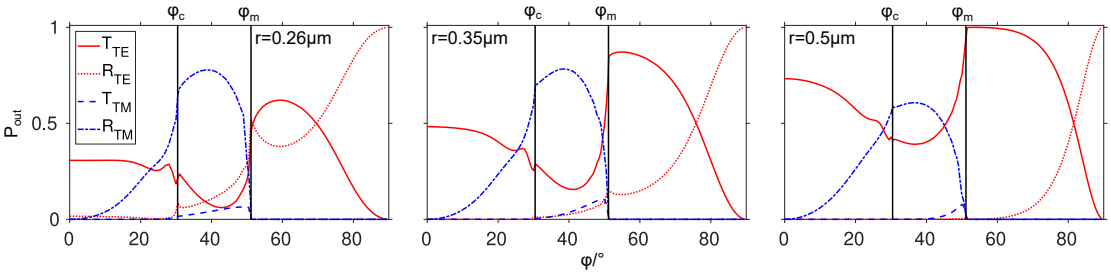

Figure 5.3: Calculated transmittance T and reflectance R values for TE and TM modes of the bent corner structure for varying incidence angle φ and different curvature radii r. Critical angles φ_c and φ_m are marked [13].

Considering the angular dependence, it can be observed that radiation losses appear for incidence angles smaller than φ_c, as already predicted in Section 2.3. For angles larger than φ_c, losses are fully vanishing and the power is completely guided by the fundamental TE or TM modes. Additionally, for angles larger than φ_m, no power is transferred to TM modes and only TE modes are present and excited. Hence, our results agree with the derived theory in Section 2.3.

Apart from this, with regard to the radial dependence, it can be generally stated that with increasing radius of curvature, the reflectance R decreases, while the transmittance T tends to increase. Furthermore, the TE reflectance increases rapidly at angles close to $90°$. Maximal TE transmission is achieved in the area $\varphi \in [\varphi_m, 90°]$ and maximal TM transmission in the range $\varphi \in [\varphi_c, \varphi_m]$.

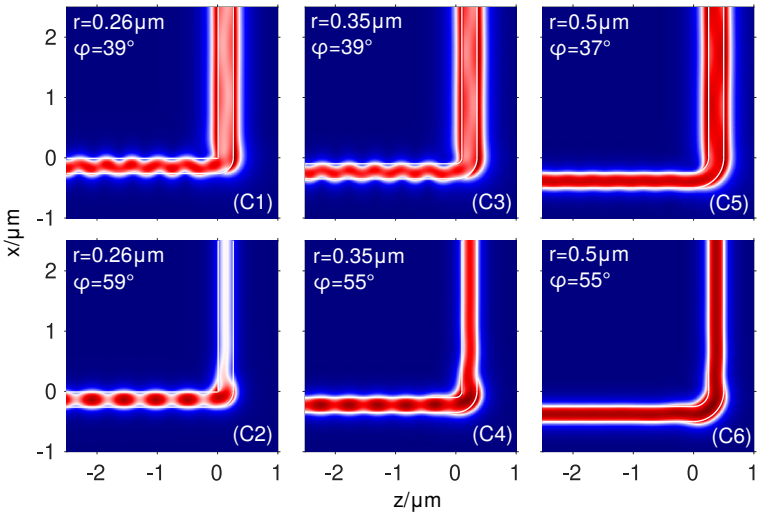

Figure 5.4: Field plots of the absolute electric field $|\mathbf{E}|$ for the configurations of Figure 5.3 at maximal TE (top row) or TM transmittance (bottom row) [13].

To illustrate the field behavior, Figure 5.4 shows the corresponding field pattern of the absolute electric field $|\mathbf{E}|$ for fixed radius r and incidence angles φ that belong to either maximal TM (C_1,C_3,C_5) or TE (C_2,C_4,C_6) transmittance, taken from Figure 5.3. All selected angles belong to the lossless case $\varphi > \varphi_c$. One observes less reflection in the incoming slab and higher transmittance in the outgoing slab for increasing curvature radius.

5.1.2 Bent step

The combination of two curved corner structures results in a step-like configuration as shown in Figure 5.2 (b). Now, the waves propagate upward and downward between the two bends, resulting in a Fabry-Pérot-like effect. Such a structure is of great relevance for the power transfer from one level to another of different height. For our studies, the height h between the bends is a new variable parameter in addition to the radius of curvature r and the angle of incidence φ.

We assume the same waveguide parameters as for the corner structure (Section 5.1.1). To simplify our calculations further, we additionally fix the curvature radius r and the angle of incidence φ, which correspond to maximal TE or TM transmittance (cf. Figure 5.4) and vary only the step height h.

The transmission T and reflection R values of the fundamental guided TE and TM modes for varying step height h are shown in Figure 5.5, when exciting the structure again with the TE_0 mode. The adopted radii r and angles φ from Figure 5.4 are displayed in the plots.

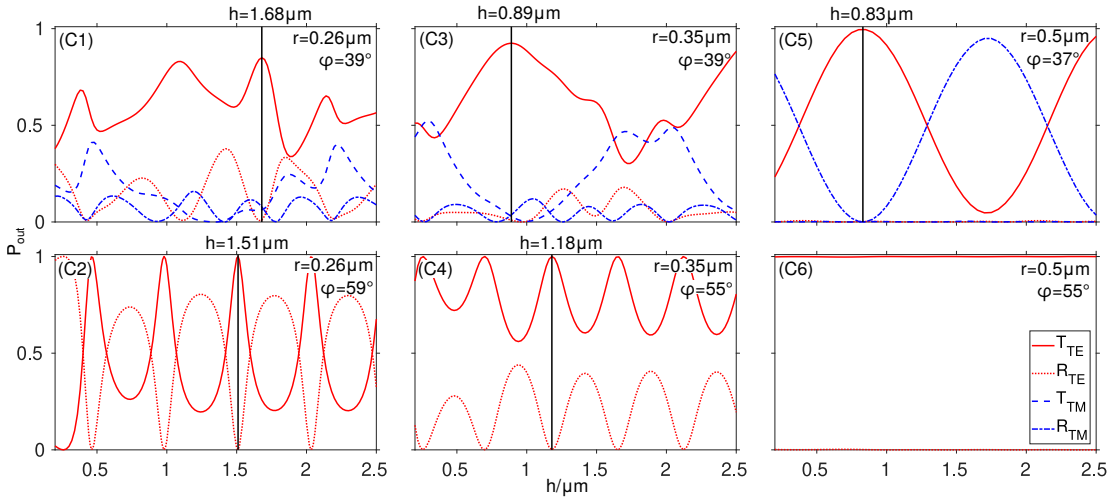

Figure 5.5: Transmittance and reflectance values of the fundamental TE and TM modes for the bent step structure depending on the vertical step height h for fixed curvature radii r and incidence angles φ. The vertical lines mark the heights with maximal TE transmittance [13].

For the configurations with large incidence angles (C_2) and (C_4), we observe a strong periodic behavior which is comparable to a Fabry-Pérot interferometer, where the waves propagate up and down between the vertical slab and the corners play the role of the reflectors. At smaller angles, this oscillating behavior becomes more irregular, as upward and downward propagating TM modes are now also involved in the interference process. With increasing radius of curvature (cf. (C_4),(C_6)), this periodic behavior becomes less pronounced. Full transmission to the TE mode is achieved, independent of the vertical step height h for (C_6). For the remaining configurations (C_1)-(C_5), respective heights h that belong to maximal TE transmittance are marked by vertical lines.

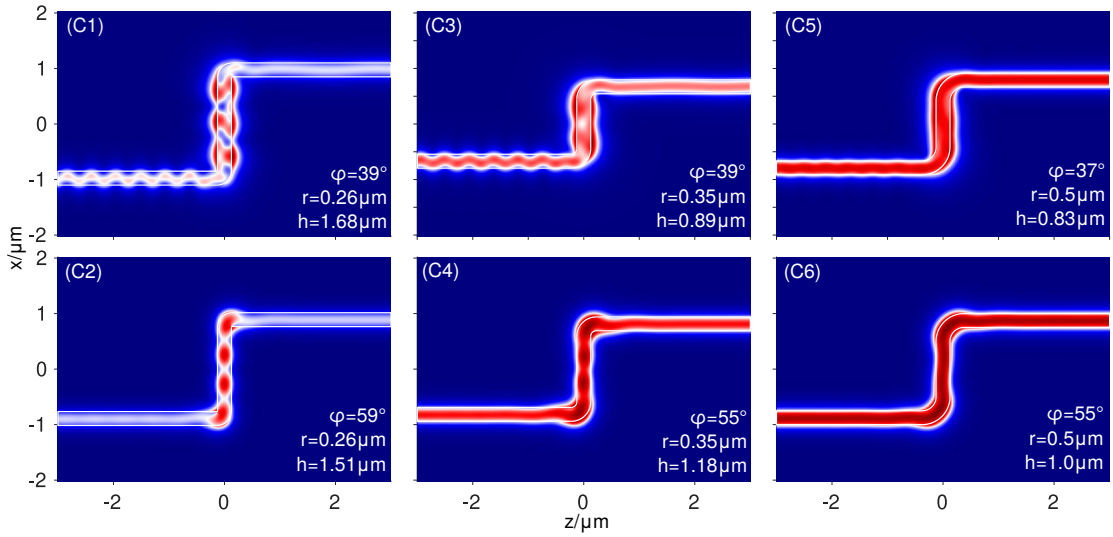

Figure 5.6: Field plots of the absolute electric field value $|\mathbf{E}|$ of the bent step structure for different waveguide parameters (φ, r, h) for maximal TE transmittance from Figure 5.5 [13].

Corresponding 2-D field plots of the absolute electric field value $|\mathbf{E}|$ for step heights h that lead to maximal TE transmittance are shown in Figure 5.6. The incidence angles φ and curvature radii r are similar to Figure 5.5. The interference in the vertical part can be best observed in configurations (C_1)-(C_3) and (nearly) full transmission with only little to no interference pattern in (C_4)-(C_6).

Additionally, Figure 5.7 shows the transmittance and reflectance values depending on the incidence angle φ for a range of angles around the angle for maximal TE or TM transmission that was chosen from Figure 5.4. This plot becomes relevant in Section 5.2 when considering full 3-D solutions and is therefore analyzed later.

5.2 3-D wave bundles in bent steps

Finally, we take a closer look at full 3-D bent step configurations that are practically more relevant. Now, the incoming wave is laterally confined also in the y-direction by exciting the structure with a rib waveguide mode, as already introduced in Section 2.4. After propagating between the steps, the outgoing mode is trapped by a second rib waveguide, identical to the incoming one, at the end of the structure. A sketch of the top view of the rib waveguides in combination with a discontinuity was already shown in Figure 2.7. Both rib waveguides are rotated around the primary incidence angle φ_0 of the incoming and outgoing wave bundles. The displacement δ between the axes of the incoming and outgoing ribs is related to the vertical propagation through the step (marked by the gray bar in the middle of Figure 2.7) and is selected depending on the vertical height. Also, the distance between step and rib, which depends on the width of the rib and the angle, is adjusted so that any back reflections do not touch the incoming rib.

We assume a wide rib of width W and low etch depth $d' = 0.01\,\mu$m to guarantee lateral guidance of the mode and to avoid too much spreading at the transition between rib and slab waveguide. The form and dispersion of the wave packet depends strongly on the lateral beam width, which is related to the rib width W.

We adopt the waveguide configurations from Figure 5.6 and choose the 2-D incidence angles as the primary incidence angles φ_0 of the incoming beams for the 3-D simulations. The smaller the beam width, the wider the range of incidence angles/wavenumbers of the 2-D solution that have influence on the field properties. Thus, Figure 5.7 provides information about the angular dependence of the 3-D bent step fields. The figure shows the transmission and reflection values for the 2-D configurations depending on the incidence angle φ, around the primary incidence angle φ_0, for fixed height h and curvature radius r. As can be observed, (C_6) shows only small deviations for varying incidence angle, so a small rib width is possible to yield comparable transmittance values to the 2-D case also in 3-D. However, if the transmission values change more rapidly, e.g., as for (C_2), a substantially wider beam is required in 3-D to guarantee a similar transmission to the 2-D solution. Altogether, we observe that for small curvature radii, the angular dependence changes more rapidly by slightly varying the incidence angle, which leads to a change in transmission and reflection values. Hence, these structures require larger rib widths W to guarantee transmittances comparable to the corresponding 2-D solutions. However, the rib width can be reduced when considering a larger curvature radius because the angular dependence is lower.

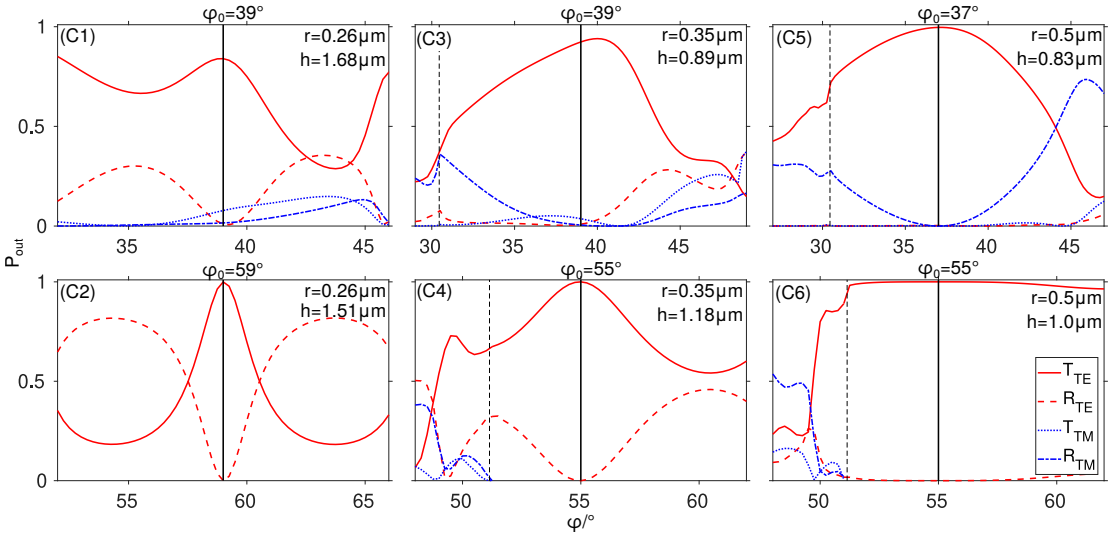

Figure 5.7: Transmittance and reflectance values of the fundamental TE and TM modes for the bent step structure depending on the incidence angle φ for fixed curvature radii r and vertical step heights h. The vertical lines mark the primary incidence angles φ_0 with maximal TE transmittance from Figure 5.5 [13].

This behavior can also be observed in Figure 5.8. Shown is the outgoing/transmitted TE power for the six configurations (C_1)-(C_6) for different incoming beam widths W. According to Section 5.2, the TE transmittance (see Eq. (2.60)) is directly given by the coefficient $|u_0|^2$. For increasing width W, the values converge towards the transmittances that are achieved for the 2-D solution with infinite beams. For smaller widths, the transmittances decrease. In particular, for configurations with small radii of curvature, which have a strong angular dependence, the outgoing transmittance changes significantly. However, the reduction of the width has less influence for configurations with a larger radius of curvature.

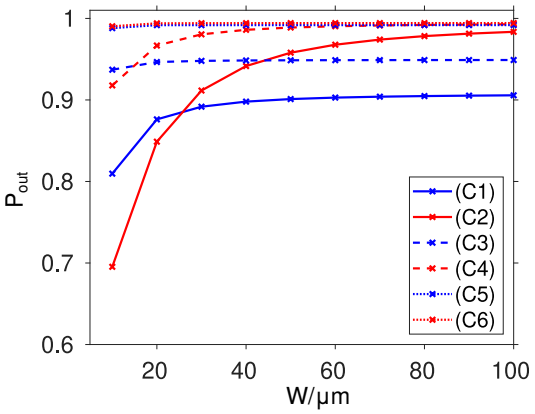

Figure 5.8: Outgoing transmitted TE_0 power versus the rib waveguide width W for the 3-D bent steps.

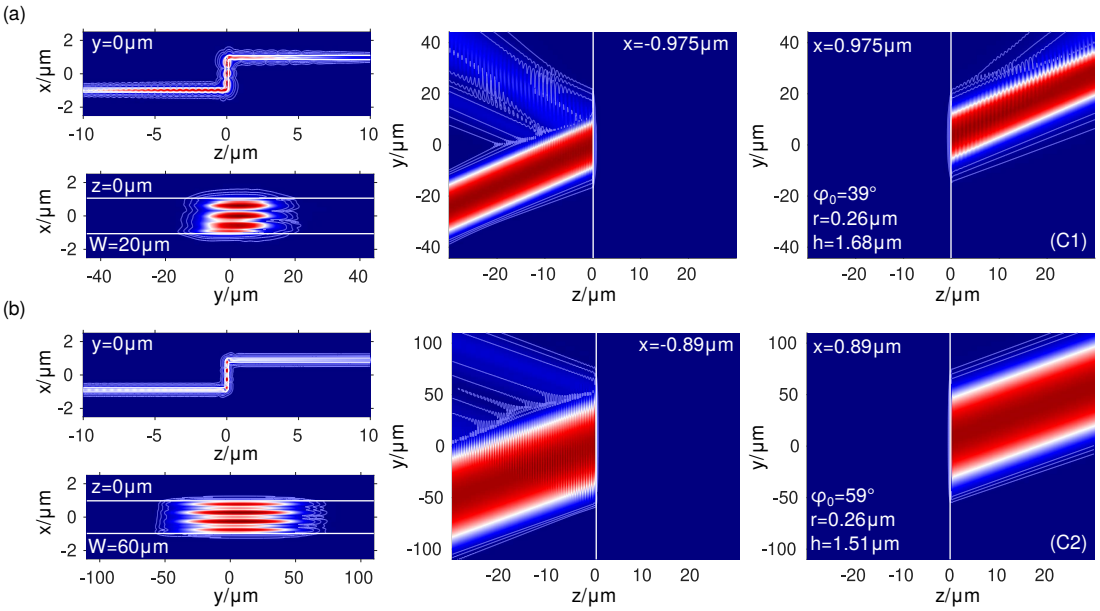

Figure 5.9: Field plots of the absolute electric field $|\mathbf{E}|$ for the bent step structure with fixed curvature radius $r = 0.26\,\mu$m, primary incidence angle φ_0 and vertical step height h, adopted from Figure 5.6 for rib widths $W = 20\,\mu$m (a) or $W = 60\,\mu$m (b) [13].

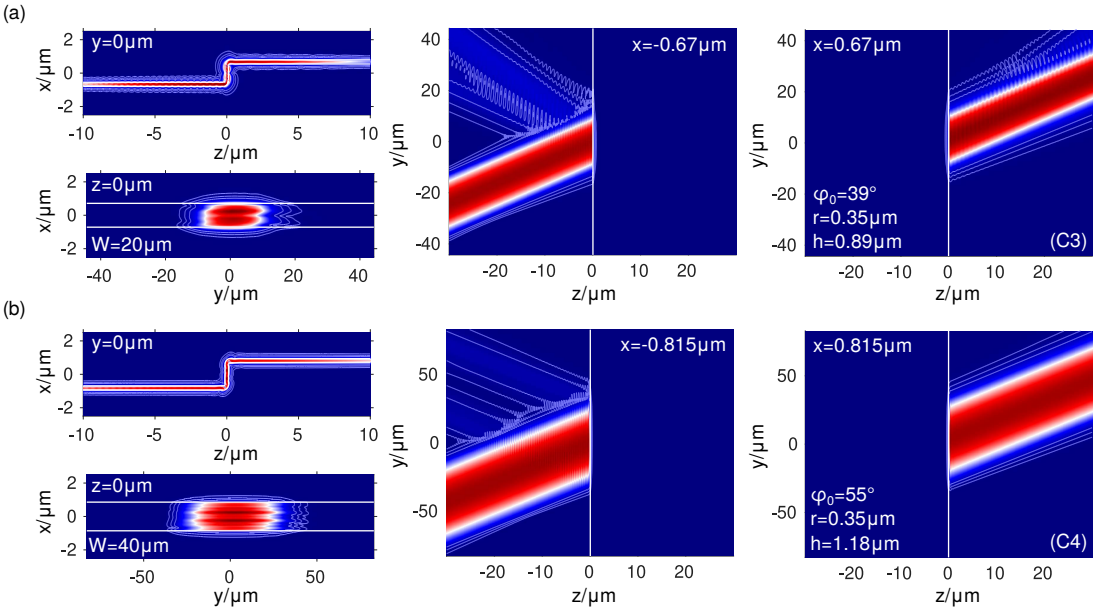

Figure 5.10: Field plots of the absolute electric field $|\mathbf{E}|$ for the bent step structure with fixed curvature radius $r = 0.35\,\mu$m, primary incidence angle φ_0 and vertical step height h, adopted from Figure 5.6 for rib widths $W = 20\,\mu$m (a) or $W = 40\,\mu$m (b) [13].

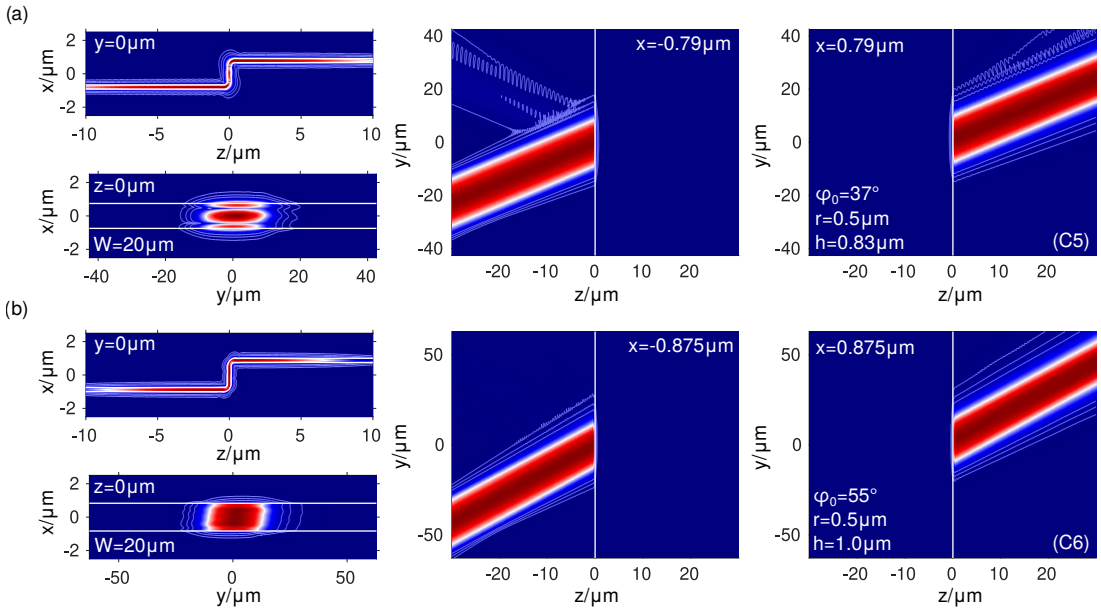

Figure 5.11: Field plots of the absolute electric field $|\mathbf{E}|$ for the bent step structure with fixed curvature radius $r = 0.5\,\mu$m, primary incidence angle φ_0 and vertical step height h, adopted from Figure 5.6 for rib widths $W = 20\,\mu$m [13].

Some 3-D configurations for incoming beams with specific rib widths W are shown in Figures 5.9–5.11. The width W is chosen such that comparable transmission values to the 2-D solutions are achieved and that neither pronounced reflections nor significant scattering of the wave bundles are present. For each configuration the figure shows a cross-sectional view of the x-z-plane in the upper left image, the field in the vertical segment that is propagating in the x-y-plane in the lower left image, and top views of the horizontal slabs for the incoming wave and transmitted wave in the y-z-plane in the middle and right image. All figures show the absolute electric field value $|\mathbf{E}|$. Note that only the fields propagating in the step structure are shown, not the fields in the adjacent rib.

As expected, small to no reflections can be observed for large radii, while for small radii they are still present. We hardly see any divergence of the wave bundles excited by the incoming rib mode. For the present parameters, widths between $20\,\mu$m to $60\,\mu$m are sufficient to guarantee good transmission values. For the structures with sharp edges in [14], much larger beam widths up to $180\,\mu$m are necessary to avoid unintentional reflections and to yield comparable transmission values. Thus, the step structure with smooth/bent corners provides better performance when considering the practically relevant 3-D solutions.

Chapter 6

Optical dielectric microresonators[1]

Another important group of applications, where oblique propagation of semi-guided waves offers new advantages, are optical microresonators. They are typically used for numerous functionalities in integrated optics such as wavelength modulation, switching or filtering. Due to their small size, strong light confinement and broad spectral tunability, they have attracted remarkable interest. Thus, they are an important building block in silicon photonics integrated circuits, especially in the area of optical telecommunication [29].

One of the basic configurations is a four-port system consisting of a microcavity that is surrounded by an upper and lower slab waveguide. The lower slab serves as the input bus and the upper slab as the output bus or receiver [84]. When the structure is excited at resonance conditions, power transfer from the input to the output bus via evanescent excitation of the cavity mode is possible. Many varieties of cavity shapes are feasible, but earlier concepts mostly deal with circular cavities [108–113]. In recent works, rectangular cavities have also gained interest [10, 84, 88, 114–116]. So far, the disadvantage of these usually 2-D concepts is that they are inherently lossy [29] and require certain cavity dimensions to observe resonant behavior of sufficient quality [84, 114, 115].

Four-port microresonators have been studies theoretically, using a time domain coupled mode theory [84] or by general analysis of tunneling processes through localized resonant states [117, 118]. At resonance, it is predicted that a configuration with one localized state (here, one guided mode in the cavity) is able to drop half of the input power to the receiver (upper waveguide), while the remaining part is transferred to the input bus (lower waveguide) or is lost to radiation. Thus, for a lossless configuration, a quarter of the input power is transmitted to each output port. Furthermore, a lossless configuration that consists of two localized states is able to achieve full power drop to the forward port. Here, this is caused by even and odd modes guided by the cavities that are "accidentally" degenerate due to the presence of the slabs.

In this chapter, we analyze the 4-port systems in a 2.5-D setting with incoming waves at oblique angles of propagation, as shown in Figure 6.1 (a). For sufficiently large angles, losses are suppressed regardless of the selected cavity dimension (Section 2.3). As mentioned before, a single cavity is able to drop a quarter of the input power to each of the four output ports [84].

[1] Sections 6.1–6.3 are based on the publication [28] of the candidate, Section 6.4 is based on our publication [21].

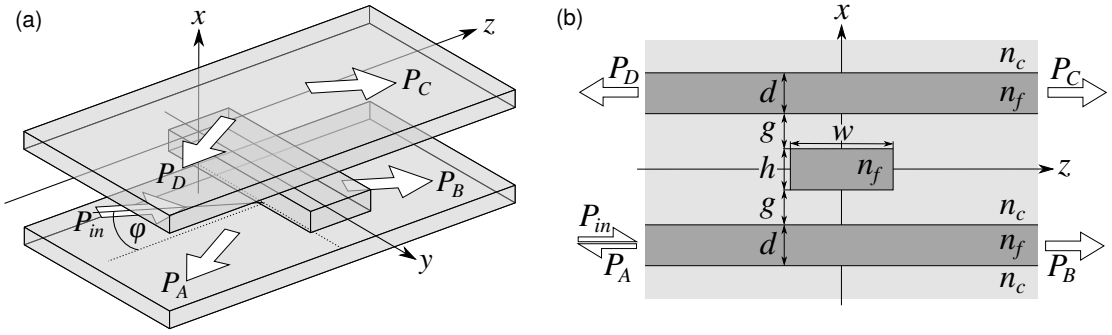

Figure 6.1: 3-D (a) and 2-D cross section (b) sketch of a dielectric resonator with rectangular micro-strip cavity of width w and height h. The cavity is evanescently excited by adjoining upper and lower slab waveguides of thickness d at a distance g. Material parameters are given by the refractive indices n_f and n_c. The incoming semi-guided wave propagates at oblique angles φ. $P_\mathrm{A}, P_\mathrm{B}, P_\mathrm{C}$ and P_D indicate the outgoing power at the respective ports [28].

When a second cavity is added, the input power is, under certain circumstances, fully transferred to one single output port, realizing an add-drop filter [119]. Therefore, after analyzing a single cavity in Section 6.2, we also consider a microresonator with two cavities due to its resonance behavior in Section 6.3.

An almost identical structure, comprising a slab waveguide with a single cavity on top (two-port system) was already considered in one of our previous works [10]. Oblique excitation leads to a system with non-radiating bound state (the guided modes of the cavity) and a wave continuum (the semi-guided modes of the slab) that realizes, what we call, a "bound state coupled to a continuum" [10]. For consistency and comparison, we adopt the slab and cavity parameters for this work.

Furthermore, we studied 2-port microresonators consisting of a circular cavity in some of our works [19, 21]. The structures are also excited at oblique angles of propagation and generate traveling-wave resonances related to OAM modes of specific high angular order. Therefore, we will conclude this chapter by briefly showing some of the results in Section 6.4.

6.1 4-port rectangular microresonator

The considered microresonators consist of a rectangular, standing wave micro-strip cavity of width $w = 0.5\,\mu$m and height $h = 0.22\,\mu$m. Two dielectric slab waveguides of thickness $d = 0.22\,\mu$m are placed above and below the cavity at a varying distance g, as shown in Figure 6.1 (b). In contrast to standard notions of open dielectric cavities with a more or less confined resonance mode, in the present 2.5-D setting, the strip is infinitely extended along its axis and supports a mode that is propagating in y-direction. The resonances observed in our structures are based on these lossless guided modes. We consider a standard Si/SiO_2 waveguide structure with refractive index $n_f = 3.45$ in the core and $n_c = 1.45$ in the surrounding cladding region for vacuum wavelength $\lambda_0 = 1.55\,\mu$m. The structure is constant along the y-direction and excited by the lower left port A with a semi-guided TE_0 mode that is propagating in the y-z-plane at oblique angles φ. Again, the slabs only support the fundamental TE and TM modes (cf. Table 2.1), which results in the two critical angles (Section 2.3) $\varphi_c = 30.9°$, beyond which

radiation losses are completely suppressed, and $\varphi_m = 46.3°$, beyond which the input power is fully reflected and/or transmitted into one of the four outgoing TE modes, as all TM modes become evanescent.

We are interested in the resonance behavior of the two configurations for varying incidence angle φ and gap g. The FEM Software COMSOL Multiphysics [22] is used to solve the frequency domain Maxwell equations using port boundary conditions and perfectly matched layers in a 2-D setting (Section 3.1.3).

All the results discussed in this work refer to structures that are infinitely extended in the y-direction; especially the infinite extent of the incident wave is important for the calculated results. To use this structure in real 3-D integrated photonic circuits, it is necessary to assume incoming waves that are also confined in the lateral direction. This is possible by exciting the structure with an additional wide and weakly etched rib waveguide, as introduced in Section 2.4 and applied to the bent steps in Section 5.2. Assuming wide and extremely narrowband incoming beams, that cover only a small range of wavenumbers k_y, the structures behave comparably to the present infinite 2.5-D models.

6.2 Single cavity resonator

Our considerations start with the mode analysis of the cavity. For the given waveguide parameters, COMSOL predicts a fundamental TE mode with effective refractive index $N_k = 2.4192$ (further modes are supported as well). To excite the cavity mode with the evanescent fields of the incoming oblique slab waveguide mode, reasonable matching

$$k_0 N_k = k_y = k_0 N_{\mathrm{TE}_0} \sin\varphi_k \tag{6.1}$$

of y-wavenumbers can be expected to be necessary. Here, N_{TE_0} is the effective refractive index of the TE_0 slab mode. Rearranging the equation leads to a cavity angle

$$\varphi_k = \sin^{-1}\left(\frac{N_k}{N_{\mathrm{TE}_0}}\right) = 58.99°. \tag{6.2}$$

When the incoming wave is oriented at a specific incidence angle – called the resonance angle φ_r – close to φ_k, the cavity mode is evanescently excited and resonance behavior can be observed. Note that the resonance angle φ_r does not necessarily have to be equal to φ_k because of a coupling induced resonance shift [120] caused by the presence of the slab waveguides. The larger the distance between slabs and cavity, the smaller the influence of the slabs and the more φ_r equals φ_k.

To identify the resonance angle φ_r, Figure 6.2 (a) presents respective sweeps over the incidence angle φ for different gap distances $g \in \{200, 300, 400\}$ nm. Shown are the reflection at port A and transmissions to ports B–D. For all cases, the presented range of incidence angles is above the critical angles $\varphi_c = 30.9°$ and $\varphi_m = 46.3°$. Thus, the structure is lossless and TM modes are not excited. For each gap, we can identify a specific resonance angle φ_r at which the incident power is evenly distributed to all output ports, i.e., $P_\mathrm{A} = P_\mathrm{B} = P_\mathrm{C} = P_\mathrm{D} = 25\%$. At resonance, the incoming slab mode evanescently excites the mode in the cavity, which in turn radiates equally into both slab waveguides along the positive and negative z-directions, which leads to the same output power at each port [117, 121]. As predicted, the resonance angle φ_r is

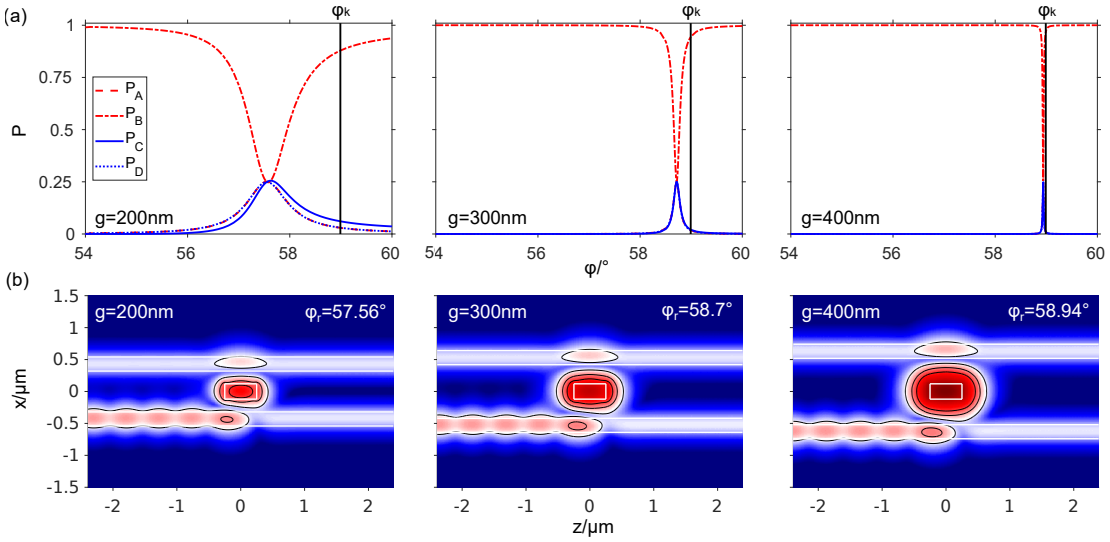

Figure 6.2: (a) Outgoing power to port A (reflection), and B, C and D (transmissions) for a single cavity resonator depending on the incidence angle φ (around the predicted cavity angle φ_k) for different gaps g. (b) Corresponding logarithmic field plots of the absolute electric field $\log_{10}|\mathbf{E}|$ at resonance angle φ_r for different gaps g from (a). The contour lines indicate the levels of 2%, 5% and 10% of the overall field maximum [28].

close but not equal to the cavity angle φ_k. For increasing gap the difference becomes smaller, while the resonance peak sharpens and the curves for P_A, P_C and P_D become more similar (they overlap in the plots).

To make a comparison, at normal incidence $\varphi = 0°$ and small cavity gap $g = 200\,\mathrm{nm}$ (not shown in the plots), the wave just passes by and hardly notices the presence of the cavity. COMSOL predicts a transmitted power of $P_\mathrm{B} = 98.93\%$ to port B and little to no power transfer (in the range of 10^{-4}) to port A, C and D. Radiation losses occur, but remain negligible.

To illustrate the field behavior, some corresponding field plots of the absolute electric field $\log_{10}|\mathbf{E}|$ at resonance angle φ_r for the considered gaps g are shown in Figure 6.2 (b). One observes that the field in the cavity resembles the fundamental TE cavity mode, as the gap increases. We chose a logarithmic scaling of the plots so that the field strength in the slabs is visible as it is much smaller compared to the strength in the cavity. In particular for large gaps, the field amplitude in the cavity is much larger.

This behavior is also visible in Figure 6.3. The resonance angles φ_r are displayed for varying gap g (see (a)). To calculate the resonance angles, we use a bisection method, starting with a relatively large range of incidence angles and reducing this to the resonance angle φ_r that satisfies $P_\mathrm{A} = P_\mathrm{B} = P_\mathrm{C} = P_\mathrm{D} = 25\%$ best. As noted before, the resonance angle converges against the cavity angle φ_k for increasing gap g because the coupling induced resonance shift shrinks.

Furthermore, the field intensity in the cavity $|\mathbf{E}_c|^2$ related to the intensity $|\mathbf{E}_o|^2$ in the incoming

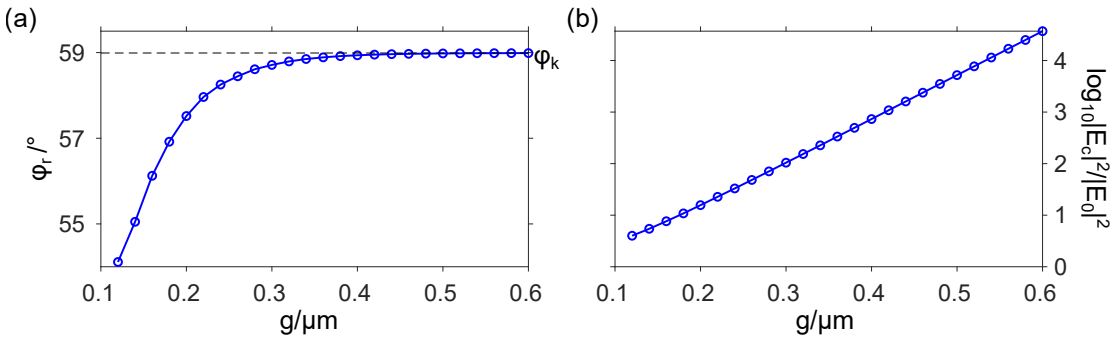

Figure 6.3: Resonance angles φ_r (a) and absolute square of the electric field maximum $\mathbf{E}_\mathrm{c}$ in the center of the cavity relative to the absolute square of the field maximum $\mathbf{E}_0$ of the isolated slab at $\varphi = 58.99°$ (b) depending on the gap g for a single cavity resonator [28].

slab is illustrated (see Figure 6.3 (b)). More precisely, the normalized ratio

$$\log_{10}(|\mathbf{E}_c|^2/|\mathbf{E}_o|^2) \tag{6.3}$$

of the electric field magnitude in the center of the cavity at resonance, to the field in the center of the incoming slab without cavity and upper slab is shown in logarithmic scaling. The curve shows exponential growth for increasing gap, which is equivalent to a high quality factor (Q-factor) [29]. For this reason, we chose the logarithmic scaling of the field pattern in Figure 6.2 (b). Generally, we can state that the resonance behavior is controlled by the interaction between the cavity and the slabs, which strongly depends on the gap g.

6.3 Add-drop filter

To realize an add-drop filter [84], two identical rectangular cavities, separated by a horizontal distance s, are placed between the slabs as shown in Figure 6.4. Such a configuration is able to transfer the complete input power to one output port [84, 117, 118, 121]. In this work, we consider a symmetric structure with identical gap distance g to the slabs for both cavities and the waveguide parameters stay the same as for the single cavity resonator, i.e., $n_f = 3.45$, $n_c = 1.45$, $d = h = 0.22\,\mu$m and $w = 0.5\,\mu$m. The incoming wave, guided by the lower slab waveguide, reaches the structure at oblique angles of propagation φ. Thus, variable parameters are again the incidence angle φ, the gap g and now also the separation s.

Again, we start with analyzing the cavity modes first. Since we consider a system of two cavities, the mode analysis depends strongly on the separation s. For a small horizontal distance, the coupled system needs to be considered, as the cavities directly interact with each other. Then, two "supermodes" of even and odd symmetry with respect to the plane $x = 0$ are guided in this structure. The effective refractive indices are indicated as $N_{k,e}$ (even) and $N_{k,o}$ (odd) in the following. Generally, these values are not identical for small separations, e.g., for a small cavity distance of $s = 530\,$nm, COMSOL predicts values of $N_{k,e} = 2.4199$ and $N_{k,o} = 2.4186$, which can again be translated with Eq. (6.1) to cavity angles $\varphi_{k,e} = 59.01°$ and $\varphi_{k,o} = 58.95°$, respectively.

When the separation s is sufficiently large, the cavities do not directly affect each other anymore and can be considered separately. Each cavity then guides the same modes as in Section 6.2,

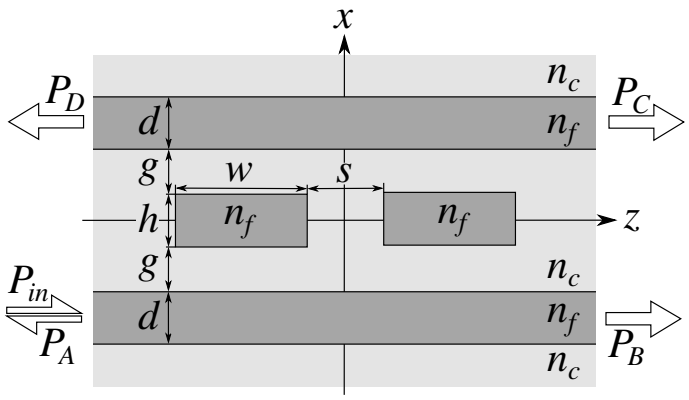

Figure 6.4: Cross section view of a microresonator consisting of two identical rectangular cavities of width w, height h and separation s. The input and output slabs, of thickness d and refractive indices n_f and n_c, exhibit a gap g to the cavities. The incoming semi-guided wave propagates at oblique angles φ (cf. Figure 6.1 (a)). $P_\mathrm{A}, P_\mathrm{B}, P_\mathrm{C}$ and P_D indicate the outgoing power at the respective ports [28].

i.e., the fundamental TE mode with $N_k = 2.4192$ and $\varphi_k = 58.99°$. For increasing separation distance s, the values of $N_{k,e}$ and $N_{k,o}$ converge to N_k, representing the transition from a coupled to an uncoupled system. The variation of the effective refractive indices $N_{k,e}$ and $N_{k,o}$ with the separation s is displayed in Figure 6.5. The convergence towards the single cavity mode N_k is clearly visible.

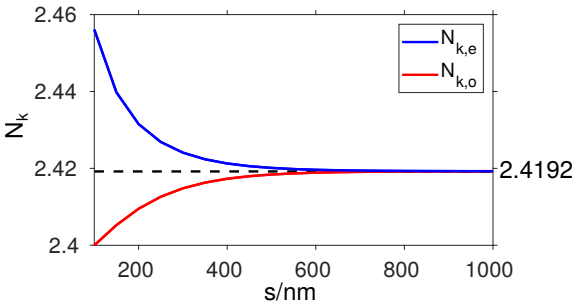

Figure 6.5: Effective refractive indices of even $N_{k,e}$ and odd $N_{k,o}$ cavity modes depending on the separation s.

We know from [84] that full power transfer to the forward drop (outgoing port C) is possible, when modes of even and odd symmetry (here, with respect to the symmetry plane $x = 0$) are present. Thus, we will mainly focus on the transmission P_C to port C in the following.

6.3.1 Directly coupled cavities

At first, we consider a configuration with sufficiently small separation $s = 100\,\mathrm{nm}$, for which a coupled cavity system must be assumed. The transmission values P_C for varying incidence angle and different gap distances $g \in \{200, 300, 400\}$ nm are displayed in Figure 6.6 (a) by the dotted red line. For this narrow distance, we can find an even and odd supermode that belong to cavity angles $\varphi_{k,e}$ and $\varphi_{k,o}$, respectively, which are indicated in the plots. By exciting the structure at a resonance angle φ_r close to these values, either the even or odd supermode is

evanescently excited in the cavity. This results in an identical behavior as for the single cavity resonator in Section 6.2. The input power is equally split to the four ports, each with 25%. Again, the resonance peaks become sharper for increasing gap g. For a small gap $g = 200\,\text{nm}$, the curves even overlap as they are quite wide. So it is not possible to excite only one supermode and the outgoing power is slightly larger than 25%.

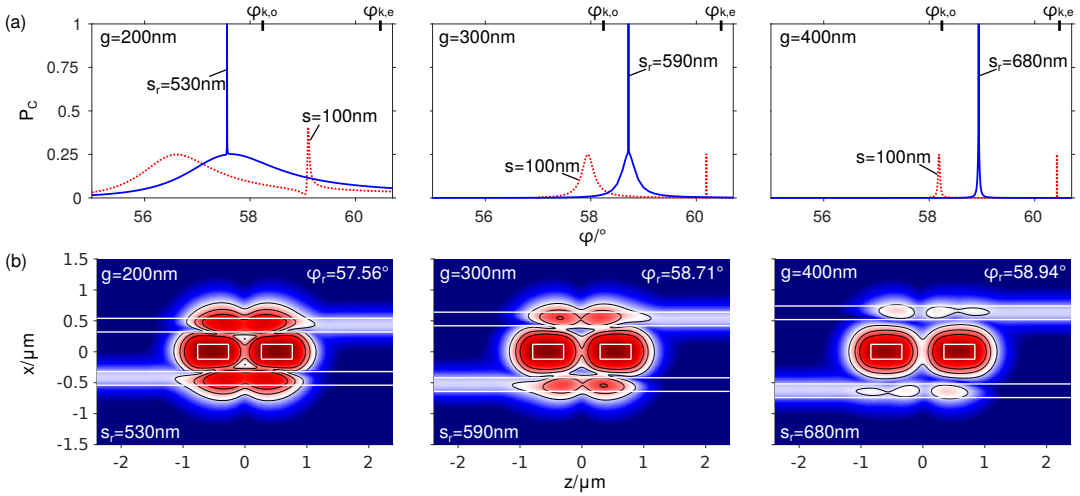

Figure 6.6: (a) Outgoing power P_C to port C (forward drop) depending on the incidence angle φ (in the range around φ_r) for different separations s and gaps $g \in \{200, 300, 400\}$ nm. The even and odd cavity angles $\varphi_{k,e}$ and $\varphi_{k,o}$ for a separation $s = 100\,\text{nm}$ are indicated. (b) Logarithmic field plots of the absolute electric field $\log_{10}|\mathbf{E}|$ at resonance (φ_r, s_r) for different gaps g. Contour lines indicate the levels at 2%, 5% and 10% of the overall field maximum [28].

In the following, we will indicate resonance states that lead to full transmission to port C with (φ_r, s_r). To find these, we again use the bisection method, but now for a range of incidence angles φ and separations s, and fixed gap g. The results are also shown in Figure 6.6. The absolute electric field value (logarithmic scale) at resonance (φ_r, s_r) for different gaps $g \in \{200, 300, 400\}$ nm is displayed in (b). Additionally, the transmission P_C depending on the incidence angle in the range around φ_r for fixed gap g and resonance separation s_r is illustrated in (a) by the solid blue line. At resonance angle φ_r, the even and odd modes are excited simultaneously, which leads to full power drop to the forward port, i.e., $P_\text{C} = 1$. In the graph, this becomes obvious by the coincidence of the positions of the overlapping peaks.

Analogously to a single cavity at resonance, here, the incoming slab mode excites the even and odd modes in the cavity, which in turn leak into the slab waveguides in both directions. However, now two supermodes are relevant. At resonance, the even mode excites the slab modes in forward and backward directions with the same phase, while exciting the odd mode results in a π-phase-shift between the forward and backward propagating slab modes. At resonance, the two modes are excited simultaneously because of accidental degeneracy. Thus, both processes occur and the waves in backward direction get fully canceled due to the phase-shift. Furthermore, the incoming wave interferes destructively with the forward slab mode excited by the cavities, which results in a full power drop into the upper waveguide [117, 121].

6.3.2 Interpretation in terms of leaky modes

For a separation of $s = 100\,\text{nm}$ in Figure 6.6 (a), the resonance peaks for the even and odd modes show different shapes. On the one hand, one observes a wide hill for the odd mode, and on the other hand, a narrow sharp peak that corresponds to the even mode at a larger incidence angle. To explain the difference, we have a look at the guided modes of the complete system, meaning the structure including the cavities and the slabs. In such a structure, the modes are leaky due to the presence of the slabs. The calculated complex effective refractive index values N_s of the leaky modes for varying separation s are shown in Figure 6.7. The positive real part (see (a)) and the negative imaginary parts (see (b)) are illustrated for the even (solid line) and the odd (dashed line) modes and different gaps $g \in \{200, 300, 400\}\,\text{nm}$.

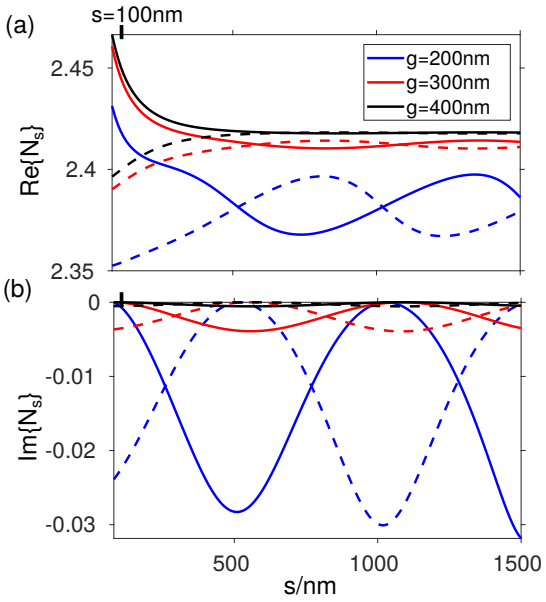

Figure 6.7: Real (a) and imaginary (b) parts of the effective refractive index N_s for the even (solid line) and odd (dashed line) leaky modes of the overall structure (including cavities and slabs) depending on the separation s for different gaps $g \in \{200, 300, 400\}\,\text{nm}$ [28].

Comparing the even and odd modes at a separation of $s = 100\,\text{nm}$ shows that the imaginary part of the even mode is almost zero (nearly a guided mode), while that of the odd mode is comparably large. Generally, the imaginary part corresponds to the strength of the leakage of the mode. Thus, the large imaginary part of the odd mode indicates a strong leaky mode and explains the broad resonance in the plots. As the even mode is hardly a leaky mode, the resonance peak is very narrow.

Furthermore, one observes a periodic behavior of the imaginary parts in Figure 6.7 (b) for increasing separation s. This can be explained by analytical arguments, as both cavities radiate into the slab waveguide where the fields overlap. Depending on the separation s, this interference is either destructive or constructive, which results in a periodic behavior. The curves for the even and odd modes are shifted by half a period due to a phase-shift of the contributions of the individual cavities.

Another advantage of considering the leaky modes of the overall structure is a more accurate prediction of the resonance angle φ_r. Before, we just considered the cavity modes and their corresponding cavity angles $\varphi_{k,e}$ and $\varphi_{k,o}$ as approximated values for the resonance angles.

But the calculated mode indices for the leaky modes can also be transferred to a corresponding angle via Eq. (6.1). At resonance, the modes are degenerate, thus they exhibit the same real part of the effective refractive index. Looking at Figure 6.7 (a), the real parts match at separations $s = 520\,\text{nm}, s = 585\,\text{nm}$ and $s = 680\,\text{nm}$ (for increasing gap $g \in \{200, 300, 400\}\,\text{nm}$). This results in corresponding angles of $57.53°, 58.72°$ and $58.94°$, respectively. These values agree very well with the resonance angles φ_r from Figure 6.6 (a), which have been determined by solving the scattering problem of the full system.

In the same way, this analysis is also applicable for the single cavity resonator in Section 6.2. Again, mode analysis is done with COMSOL for the complete system comprising the slabs and the cavity. For increasing gap, the structure possesses leaky modes with complex effective refractive indices that correspond to incidence angles $57.54°, 58.71°$ and $58.94°$. These values also provide better approximations for the resonance angle φ_r in Figure 6.2 (b). Even if the values fit very well for both configurations, it must be noted that completely different problems are considered (leaky eigenvalue problem versus mode propagation problem).

6.3.3 Wavelength filter

The microresonators with two cavities also represent an add-drop filter for one specific wavelength $\lambda_r = 1.55\,\mu\text{m}$ when considered in terms of wavelength dependence. Respective sweeps over the wavelength λ_0, around the resonance wavelength λ_r, are shown in Figure 6.8 for different gaps $g \in \{200, 300, 400\}\,\text{nm}$, fixed resonance separation s_r and fixed incidence angle φ_r from Figure 6.6 (a). One observes full power transfer $P_\text{C} = 1$ at resonance wavelength $\lambda_r = 1.55\,\mu\text{m}$.

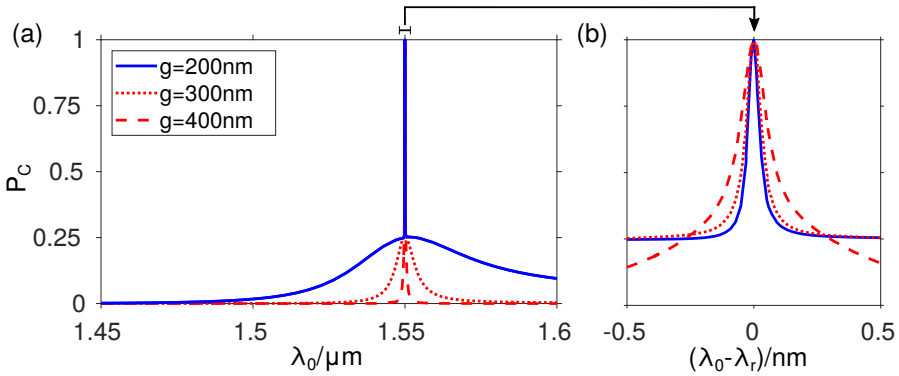

Figure 6.8: (a) Outgoing power scans P_C over the wavelength λ_0 for different gap distances g at resonance with the corresponding values (φ_r, s_r) adopted from Figure 6.6 (a). (b) Enlargement of the resonance peak for a smaller range of wavelengths around the resonance wavelength $\lambda_r = 1.55\,\mu\text{m}$ [28].

Again, the shape of the peak consists of a wider lower hill at a level of 25% with an additional superimposed narrower peak at a level of 100%. For increasing gap, the lower hill becomes narrower, just as for the single cavity resonator in Figure 6.2, and the upper peak widens. This can especially be seen in the enlargements of the wavelength scans in Figure 6.8 (b). The width of the hill is attributed primarily to the width of the elementary cavity resonances, while the width of the peaks is determined by the positions of the resonances of the individual cavity

supermodes [28]. Apparently, these positions depend more on the angle/wavelength parameter for smaller distances g, resulting in the narrower peaks.

6.3.4 Indirectly coupled cavities

Finally, we investigate the two-cavity system for large separations s. The cavities do not directly affect each other, i.e., they are uncoupled and must be considered individually. We restrict our analysis to a single small gap of $g = 200\,\text{nm}$. Furthermore, the resonance angle $\varphi = 57.56°$ for a single cavity resonator (cf. Section 6.2) can also be adopted for the uncoupled system, as the resonance angles should be the same for both systems. The solid blue line in Figure 6.9 (a) shows the outgoing power to port C depending on the separation s. For certain equal distances, the power is fully dropped, i.e., $P_\text{C} = 1$. Otherwise, for distances above $s \approx 500\,\text{nm}$, the power is equally dropped to 25% at each of the four output ports (the remaining outputs are not displayed). At these positions, the composite system behaves similar to a single cavity resonator from Section 6.2. Respective logarithmic field plots of the absolute electric field $\log_{10}|\mathbf{E}|$ are shown in Figure 6.9 (b) for separations that belong to the second and third full transmission peak in Figure 6.9 (a). The first peak belongs to the coupled system with separation $s = 530\,\text{nm}$, as shown in Figure 6.6 (b) (first image).

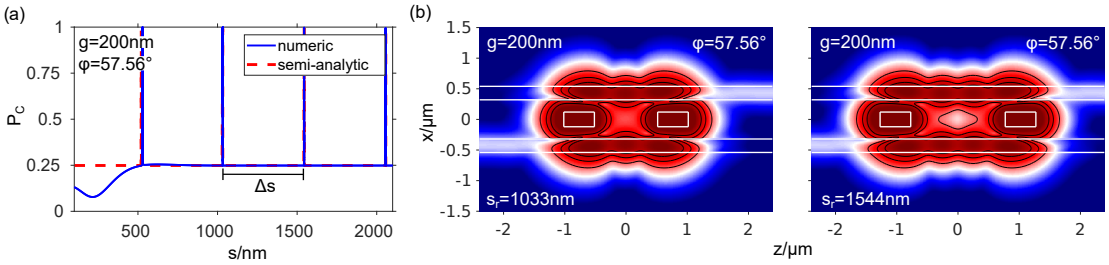

Figure 6.9: Outgoing power P_C in the forward drop port depending on the cavity distance s for fixed gap $g = 200\,\text{nm}$ and incidence angle $\varphi = 57.56°$ (a) and corresponding logarithmic field plots of the absolute electric field $\log_{10}|\mathbf{E}|$ at resonance separations s_r (b) [28].

The periodicity of $P_\text{C}(s)$ in Figure 6.9 (a) can also be predicted by semi-analytical arguments. For sufficiently large separation distances s, the system can be split in three subsystems, as illustrated in the sketch of Figure 6.10. The first and third subsystem are single cavity resonators (Section 6.2), consisting of two parallel slab waveguides with a rectangular cavity in between, representing the left and right cavity of the overall configuration. The remaining middle part comprises two identical parallel slab waveguides separated by the distance $2g + h$ that connect the two single cavity systems. We can assume that the slabs themselves do not interact with each other.

The scattering behavior of the subsystems is described by its transfer or scattering matrices. For the single cavity resonator, the transfer matrix $\mathsf{T}_\text{I} \in \mathbb{C}^{4\times4}$ at resonance is determined by the numerically calculated scattering parameters from COMSOL (Figure 6.2 (a)). In the parallel slabs, we can assume harmonic forward and backward z-propagating waves with a field dependence $\sim \mathrm{e}^{\pm\mathrm{i}k_z z}$. Thus, the transfer matrix is given by

$$\mathsf{T}_\text{II} = \operatorname{diag}\left(\mathrm{e}^{\mathrm{i}k_z L}, \mathrm{e}^{-\mathrm{i}k_z L}, \mathrm{e}^{\mathrm{i}k_z L}, \mathrm{e}^{-\mathrm{i}k_z L}\right), \tag{6.4}$$

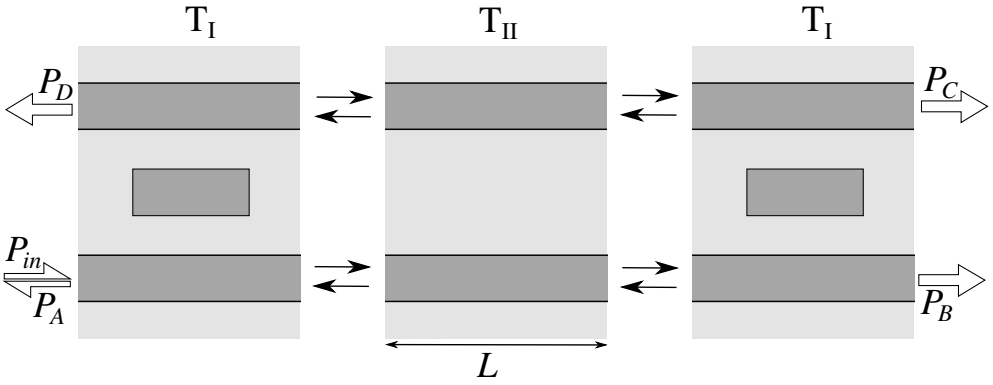

Figure 6.10: Division of a microresonator with two cavities in three subsystems. Each subsystem is described by its transfer matrix T_{I} or T_{II}.

where L is the distance of the second subsystem. Note that L differs from s depending on the size of the single cavity systems. Combining the three elements via

$$\mathsf{T} = \mathsf{T}_{\mathrm{I}}\mathsf{T}_{\mathrm{II}}\mathsf{T}_{\mathrm{I}} \tag{6.5}$$

determines the behavior of the overall system depending on the separation s.

The semi-analytical results are shown in Figure 6.9 (a) by the dashed red line and agree very well with the simulations, except for the area $s < 500\,\mathrm{nm}$. Here, we can not make the assumption of an uncoupled system and thus the division in three subsystems gives wrong results. In this area, the cavities are directly interacting with each other and not only via the slab waveguides. The calculated semi-analytical results depend sensitively on the scattering parameters calculated numerically with COMSOL. Already small changes lead to different values.

With this model, we are now also able to predict the distance

$$\Delta s = \lambda_0/(2N_{\mathrm{TE}}\cos\varphi) \tag{6.6}$$

between the resonance separations s_r that lead to full transmission. The value $\Delta s = 512\,\mathrm{nm}$ for our waveguide parameters agrees well with the numerical COMSOL calculations. When one resonance state s_r is found, the following resonances occur at distances $s_r + n\Delta s$, where n is an integer. Increasing the distance by Δs adds another hotspot, representing a standing wave pattern in the slabs between the cavities. This can be seen easily by comparing the two pictures in Figure 6.9 (b), which differ exactly by one field maxima.

6.4 Circular cavities

Two-port resonator systems can just as well be of interest in the present context of semi-guided waves [10]. As an example, we investigated configurations with circular cavities [19, 21], as illustrated in Figure 6.11. The cavity consists of a step-index fiber with outer radius r and inner radius $r - d$. With an outer layer with refractive index $n_f > n_c$, the structure supports possible OAM modes (cf. Section 2.2.2) of specific angular order ν.

On the contrary to the rectangular shape, which supports resonances of standing-wave type [84], traveling-wave resonances can be excited in the structure with the circular cavity [122].

Resonant fields with large orbital angular momentum and strong fields in the core are observed, similar to the OAM modes in Section 2.2.2.

We are interested in the generation and excitation of OAM modes of high angular order. A variety of approaches exist, including spiral phase plates [123], tailored lens arrangements [124], spatial light modulators [125], and helical gratings [126, 127], fiber couplers [128] or nonlinear parametric processes [129]. In this work, we show some of the results derived in [21], where the fiber is evanescently excited by the semi-guided mode of the adjoining slab waveguide at oblique angles of propagation. For more details, we refer the reader to [19, 21].

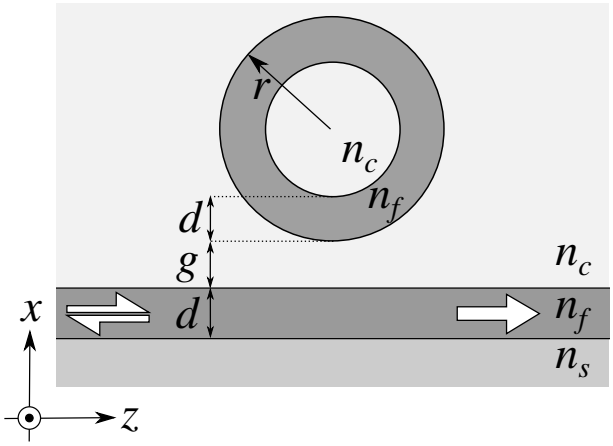

Figure 6.11: Two-port resonator system consisting of a circular step-index cavity of radius r and thickness d that is evanescently excited by a slab waveguide of thickness d separated by the distance g with refractive indices n_f in the core and n_s and n_c in the cladding region [21].

The slab waveguide parameters are given by refractive indices $n_s = n_c = 1.0$ and $n_f = 1.5$ with slab thickness $d = 0.4\,\mu$m for vacuum wavelength $\lambda_0 = 1.55\,\mu$m. The corresponding effective refractive index values of the fundamental slab modes are $N_{\mathrm{TE}_0} = 1.23026$ and $N_{\mathrm{TM}_0} = 1.10914$ (cf. Table 2.1), which result in critical angles $\varphi_c = 54.37°$ and $\varphi_m = 64.36°$, respectively, when assuming TE_0 incidence. For our studies, we restrict the incidence angle to the region $\varphi > \varphi_c$ to suppress radiation losses.

The tube exhibits the same core thickness and material parameters as the slab waveguide. The $\mathrm{OAM}_{\pm\nu,l}$ modes are strictly degenerate. Here, ν refers to the angular order and $l \in [1, 2]$ to the number of modes that exhibit an angular order $\pm\nu$, which are TE- ($l = 1$) or TM-like ($l = 2$). For the given waveguide parameters, the structure guides 48 modes: TE_0, TM_0, $\mathrm{OAM}_{\pm\nu,1}$, $\nu \in [1, 14]$ (TE-like), $\mathrm{OAM}_{\pm\nu,2}$, $\nu \in [1, 9]$ (TM-like).

Simulations are carried out with the 2-D FEM simulation software COMSOL Multiphysics [22] and validated with the hybrid analytical/numerical coupled mode theory (HCMT) model introduced in [130]. Advantageous is that the latter offers a clear distinction between the degenerate OAM modes of opposite angular order $\pm\nu$, so that much more details are discussed and analyzed in [21].

Respective sweeps over the incidence angle are illustrated in Figure 6.12 for different gap distances $g \in \{1.0, 1.4, 1.8\}\,\mu$m showing the transmission T and reflection R to the fundamental TE and TM modes. Resonances are observed for incidence angles that fulfill the phase matching in the y-direction (cf. Eq. (6.1), where N_k represents the corresponding effective refractive index of the OAM mode). Each pronounced reflection peak, observed at angles close to φ_k,

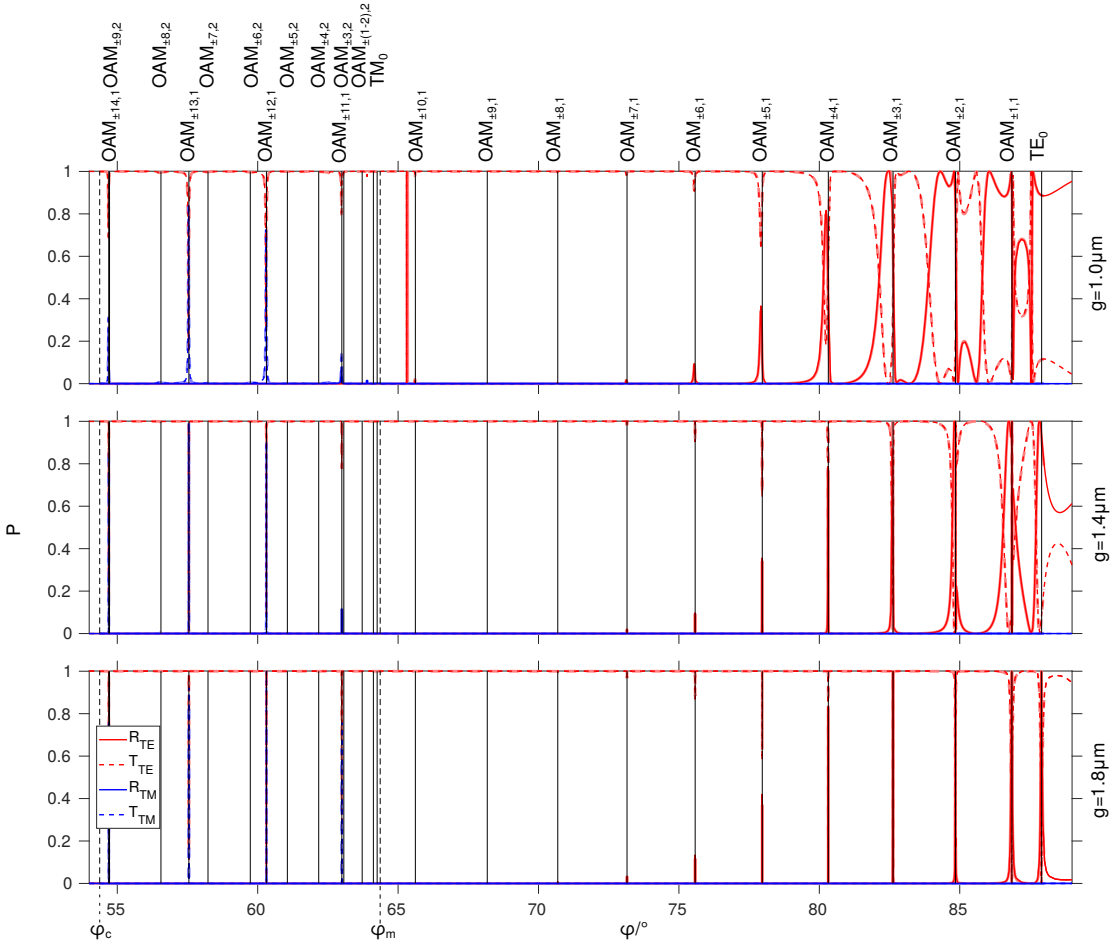

Figure 6.12: Transmission T and reflection R values of the fundamental TE and TM modes for incoming TE_0 mode depending on the incidence angle φ for different gap distances $g \in \{1.0, 1.4, 1.8\}\,\mu$m calculated with COMSOL. The lighter curves belong to the HCMT result from [21]. The vertical solid lines indicate the angle φ_k for the guided OAM modes in the structure and the dashed lines refer to the critical angles φ_c, φ_m.

corresponds to a pair of degenerate OAM modes. The resonances are mostly well separated, except in the area of grazing incidence $\varphi \approx 90°$, where the peaks overlap. Again, the gap distance g has strong influence on the resonance characteristics as the peaks become narrower, more defined and move close to the predicted cavity angles φ_k for increasing gap.

Figure 6.13 shows field profiles $|\mathbf{E}|$ for different selected resonance angles φ and a fixed gap $g = 1.4\,\mu$m. The fields in (a)-(e) consist mostly of degenerate $\mathrm{OAM}_{\pm l,1}$ modes for $l \in \{13, 12, 5, 2, 1\}$. However, the field in (f), even if the angle φ is close to the TE_0 mode angle φ_k, consists of a superposition of the TE_0 and $\mathrm{OAM}_{\pm1,1}$ mode as the peaks are not strictly separated for the chosen gap $g = 1.4\,\mu$m. This is further visible due to the difference in amplitude along the angular direction in the tube core where both fields overlap. However, for increasing gap, the influence of the $\mathrm{OAM}_{\pm1,1}$ mode reduces.

As we know from [21], the degenerate OAM modes are excited with highly differing ampli-

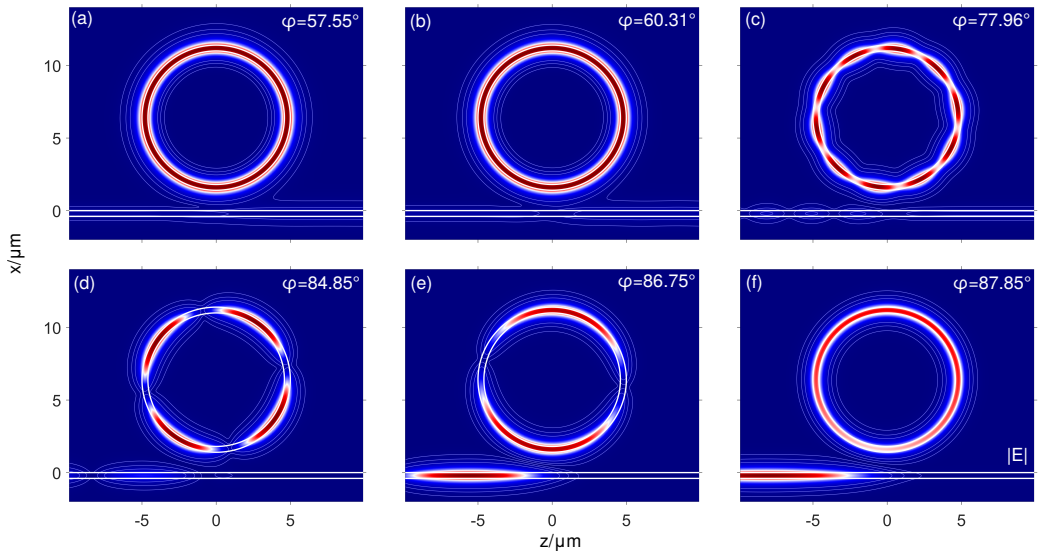

Figure 6.13: Field plots of the absolute electric field $|\mathbf{E}|$ for different incidence angles φ at resonance and fixed gap $g = 1.4\,\mu$m that excite OAM modes of different angular order in the tube. The contour lines mark the levels of the absolute field at 2%, 5% and 10%.

tudes, as directly noticed by the HCMT solver. For high angular order (corresponding to smaller incidence angles), mostly exclusively the anticlockwise propagating OAM mode with angular order $-\nu$ contributes to the fields. Thus, the fields in (a) and (b) exhibit a constant amplitude along the fiber core, since only the $\mathrm{OAM}_{-13,1}$ (a) and $\mathrm{OAM}_{-12,1}$ (b) modes are excited. The interference pattern becomes more pronounced for lower angular order (or increasing resonance angle) in the subplots (c)-(e), where OAM modes of opposite order are almost equally excited.

The whole setting, with more realistic material parameters (silicon and silicon dioxide), was further analyzed in 3-D for incoming Gaussian beams of limited lateral width [19]. For the considered high-index contrast configurations, a substantial amount of the input power – around 80% for the examples in [19] – can be transferred to the guided OAM modes, with a distinction between degenerate modes of opposite angular order $\pm\nu$ by several orders of magnitude.

Chapter 7

Integrated optical waveguide lens[1]

So far, we only investigated structures that are constant along one outstanding spatial direction (here, the y-direction). Thus, our studies were always carried out in a 2.5-D setting with oblique excitation. However, in this chapter, we want to focus on configurations that are no longer constant in the previous outstanding region. Especially, dielectric slab waveguide lenses are investigated, i.e., the considered systems consist of curved interfaces.

Sketches of potential slab waveguide lenses are illustrated in Figure 7.1 for a convex (a) or concave (b) shape. The structures consist of a dielectric slab waveguide with an additional lens shaped part of higher or lower, but constant, thickness. Such a configuration is able to focus the input light at the output to a specific focal point depending on the properties of the waveguide and the shape of the lens. We are interested in numerical simulation methods that rapidly calculate the diffraction behavior in these slab waveguide lenses.

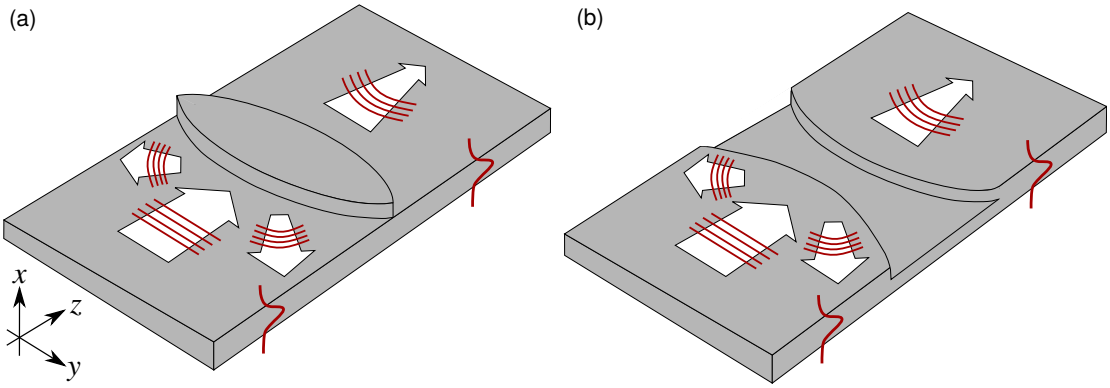

Figure 7.1: Sketches of a convex (a) and concave (b) integrated-optical slab waveguide lens [75].

Optical waveguide lenses are basic components for many integrated devices used for information processing or optical communication [131, 132]. They were already discussed in earlier

[1] Sections 7.1–7.4 are based on the publication [75] of the candidate.

concepts [132–137], e.g., mode-index, geodesic or grating types, which were mostly investigated experimentally. When comparing the considered wavelength ($\lambda_0 = 1.55\,\mu$m) to the size of the structure (several tens of micrometers), these configurations are potentially huge. Thus, rigorous full 3-D simulations require a lot of memory space and computation time. More recent techniques to simulate wave propagation in optical waveguides are the effective index method, where the 3-D system is reduced to two spatial dimensions, or variants of the beam propagation method, that rely on the slowly varying envelope assumption. They are mostly used for systems with low radiation losses and small refractive index contrasts. However, the high index contrast Si/SiO_2 configurations considered in this work exhibit comparably large, pronounced radiation losses and non-negligible back reflections. Hence, both methods are not applicable and give inconsistent results.

A more promising approach offers the angular spectrum method (ASM), which is a powerful tool to calculate the diffraction of an imaging system consisting of curved interfaces [42–46,75]. Thus, in this chapter, we are presenting a numerical method, which is based on an extended approach of the ASM that needs less time and space to simulate the wave propagation in slab waveguide lenses. A modified version of the ASM was already introduced in [46] to simulate the scattering of fields from or to 2-D curved surfaces. The interface is divided into a finite number of small, flat elements to calculate the propagation of the fields. Here, we extend the stepwise angular spectrum method (SASM) to make it also applicable to full 3-D slab waveguide lenses.

We start our studies by introducing the basic concept of the ASM in Section 7.1. The extended stepwise ASM is then adapted to a simple 2-D interface, mainly for illustration of our approach consisting of two different materials separated by a curved interface. The theory and examples are presented in Section 7.2. A system consisting of two curved interfaces, where the waves propagate between the surfaces, is considered in Section 7.3. This already represents a simple 2-D lens. Again, the theory of the approach is derived and corresponding examples are shown. Finally in Section 7.4, we extend our ansatz to full 3-D slab waveguide lenses by combining the stepwise ASM with full vectorial 2-D COMSOL [22] solutions of lower complexity. All presented examples are validated by rigorous 2-D and 3-D FEM COMSOL simulations.

Finally, we show the versatility and applicability of the SASM by applying standard optimization algorithms to the 3-D slab waveguide lens. The mathematical formulation of optimization theory, which can be found in standard textbooks [138], is briefly recalled in Section 7.5.1. The basic concepts of the global optimizers used in this chapter are explained in Sections 7.5.2–7.5.3, and finally we show some optimized lens configurations in Section 7.5.4.

7.1 Angular spectrum representation of optical fields

The angular spectrum method is a rigorous and essential technique in diffraction theory [31–46] to model the propagation of a light wave in homogeneous media by expanding the field into a series of plane and evanescent waves. The mathematical background lies in the field of Fourier Optics [47], but has been further investigated in the area of integrated optics.

Some of the oldest and most general formulations describe the propagation of light from an input to an output plane. Almost all of these concepts are based on the scalar diffraction theory, which was invented by Huygens, Fresnel, Kirchhoff and others [47–49]. All these concepts

are built up from the behavior of spherical waves from point sources (Huygens principle) and diffraction is developed by the superposition of these spherical waves. A big advantage is that these methods can easily be extended to more complex structures like tilted, shifted [36–41] or curved [42–46] surfaces. The angular spectrum method offers another useful tool to describe the propagation of an optical field from an input plane to an output plane by identifying the optical fields as a superposition of plane and evanescent waves.

In this chapter, we review the theory behind the angular spectrum representation [139]. For simplicity, we introduce the schematic in a 2-D setting in the y-z-plane (the fields are assumed to be constant in the x-direction).

Given is a scalar input field $E_0(y) = E(y, z = 0)$, defined along the y-axis at position $z = 0$. Its inverse Fourier transform

$$\begin{aligned} A(k_y) &= \int E_0(y) \mathrm{e}^{\mathrm{i}k_y y} \mathrm{d}y \\ &= \mathcal{F}^{-1}\{E_0(y)\} \end{aligned} \tag{7.1}$$

describes the amplitude of various plane-wave components that comprise the input source according to the basic principle of Fourier transformation. Naturally, the input field is then the Fourier transform of the angular spectrum

$$\begin{aligned} E(y, z = 0) &= \frac{1}{2\pi} \int A(k_y) \mathrm{e}^{-\mathrm{i}k_y y} \mathrm{d}k_y \\ &= \mathcal{F}\{A(k_y)\}. \end{aligned} \tag{7.2}$$

The complex exponential $\mathrm{e}^{-\mathrm{i}k_y y}$ is the projection on the y-plane of a plane wave propagating with the wavevector (k_y, k_z) with $k_z = \sqrt{k^2 - k_y^2}$. Thus, the input field can be identified as a projection of many plane wave components propagating in various directions (k_y, k_z) with complex amplitudes $A(k_y)$.

After propagation over a distance z_0, each plane wave component acquires a phase factor $\mathrm{e}^{-\mathrm{i}k_z z_0}$ so that the outgoing field at position $z = z_0$ is

$$\begin{aligned} E(y, z = z_0) &= \frac{1}{2\pi} \int A(k_y) \mathrm{e}^{-\mathrm{i}(k_y y + k_z z_0)} \mathrm{d}k_y \\ &= \mathcal{F}\{A(k_y) \mathrm{e}^{-\mathrm{i}k_z z_0}\}, \end{aligned} \tag{7.3}$$

which is the Fourier transform of $A(k_y)\mathrm{e}^{-\mathrm{i}k_z z_0}$. An extended version of the ASM method is now applied to our lens configurations.

7.2 2-D curved interfaces

At first, we start our investigations with a simple 2-D curved interface, as illustrated in Figure 7.2. The structure consists of two media n_1 and n_2 separated by a curved surface that is determined by the function $g(y)$. The interface can have an almost arbitrary shape, but multiple reflections at the same interface are not included in our method, so the shape is restricted to

this limitation. The whole structure is assumed to be constant along the x-direction. Thus, we consider electromagnetic fields

$$\begin{pmatrix} \mathbf{E} \\ \mathbf{H} \end{pmatrix} (y, z) \tag{7.4}$$

that are also constant along x. A laterally y-restricted wave packet serves as the incoming field and reaches the boundary at oblique angles of incidence φ_0 with respect to the z-axis. Thus, the wave is propagating in the y-z-plane with a range of wavenumbers k_y and k_z around a primary wavenumber $k_{y_0} = k_0 n_1 \sin\varphi_0$.

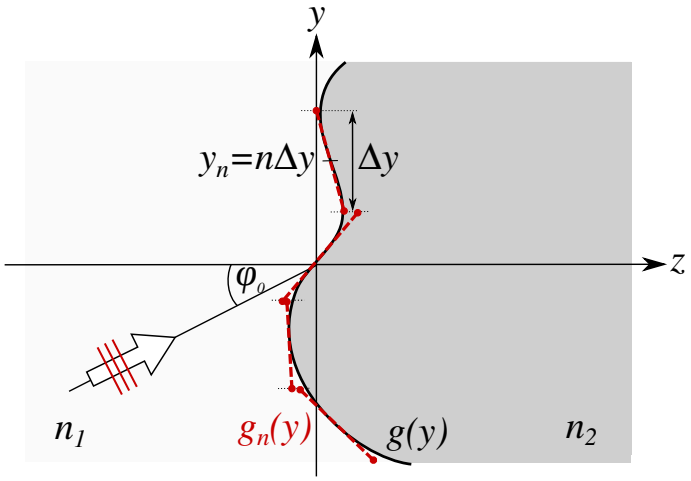

Figure 7.2: 2-D sketch of an interface with materials n_1 and n_2 separated by a curved surface $g(y)$. The incoming wave propagates in the y-z-plane at oblique angles φ_0. The SASM approximation is illustrated by the red dashed lines [75].

We are interested in the transmitted and reflected fields at the interface for a given incoming wave bundle. To calculate the fields, we make use of an extended variant of the angular spectrum method and apply it to an approximation of the curved surface. Therefore, the interface is discretized in $\mathcal{N}$ equidistant elements along the transverse y-direction of width Δy with center $y_n, n \in [1, \mathcal{N}]$ [46]. Each element is approximated by a piecewise flat surface $g_n(y)$, tangential to the interface at y_n. This stepwise approximation is illustrated in Figure 7.2 by the red dashed lines.

Then, the stepwise angular spectrum method (SASM) is applied to the approximated structure and requires four important steps:

1. Calculating the incoming field on each of the $\mathcal{N}$ elements.
2. Inverse Fourier transformation of the fields to receive their angular spectra.
3. Determining the scattered fields via a Fourier transform.
4. Superposition of the individual results to get the overall field solution.

This ansatz is further an extension of the approach from [46], where straight elements perpendicular to the longitudinal direction (z-axis) were used to approximate the curved surface. We compare the two approximation techniques with straight and oblique elements in Section 7.2.3.

Generally, the piecewise composite function (dashed red line in Figure 7.2) that approximates the curved interface is most likely discontinuous. But this does not have a strong negative influence on the results because the smooth scattered fields from the $\mathcal{N}$ individual elements are superimposed for the overall solution. Additionally, we choose the number of elements $\mathcal{N}$ large enough to observe convergence. Furthermore, the curved elements are less discontinuous than the staircase approximation used in the original method [46], where already good results are achieved.

7.2.1 Rotation of the coordinate system

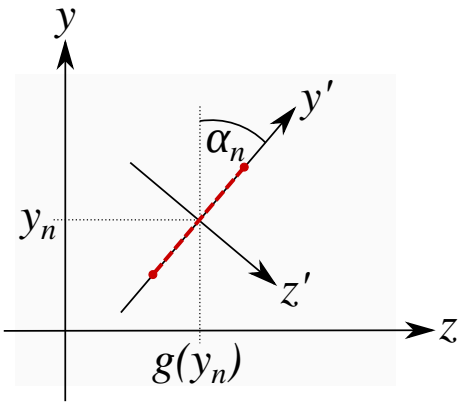

Figure 7.3: Rotation of the coordinate system (y, z) by the inclination angle α_n to obtain the shifted local coordinate system (y', z') for the approximated n-th element of the curved surface. The red dashed element indicates an approximated element from Figure 7.2.

When using oblique approximation elements, the solution for each element is, for simplicity, calculated in a new rotated, local coordinate system (y', z') such that the flat surface of the approximated element is parallel to the y'-direction (see Figure 7.3). The rotation is useful as now in local coordinates (y', z'), the setting for each element is similar to a simple 2-D plane wave interface [79]. Therefore, the global coordinate system (y, z) has to be rotated by the inclination angle α_n defined by

$$\tan\alpha_n = \frac{\mathrm{d}g(y)}{\mathrm{d}y}\Big|_{y=y_n} \tag{7.5}$$

and the local, rotated and shifted coordinate system for the n-th element is

$$\begin{aligned} y' &= \cos\alpha_n(y - y_n) + \sin\alpha_n(z - g(y_n)) =: \xi_n(y, z), \\ z' &= \cos\alpha_n(z - g(y_n)) - \sin\alpha_n(y - y_n) =: \eta_n(y, z). \end{aligned} \tag{7.6}$$

A rotation of the coordinate system implicitly leads to a rotation of the wavenumbers (k_y, k_z) with

$$\begin{aligned} k_y' &= \cos\alpha_n k_y + \sin\alpha_n k_z, \\ k_z' &= \cos\alpha_n k_z - \sin\alpha_n k_y. \end{aligned} \tag{7.7}$$

7.2.2 Calculation of the scattered fields

Step 1: Calculating the incoming wave

As mentioned before, the incoming wave is laterally limited in the y-direction, constant along the x-direction and propagating in the y-z-plane at oblique angles φ_0. Analytically, these

2-D wave bundles are a weighted superposition of plane waves that are propagating in various oblique directions (k_y, k_z) with amplitudes $w(k_y; \varphi_0)$ (cf. Eq. (2.54)). More precisely, the incoming wave packet is determined by an integral over a range of wavenumbers (or incidence angles φ) around the primary wavenumber k_{y_0} (or primary incidence angle φ_0) via

$$\Psi_{\mathrm{in}}(y,z) = \frac{1}{2\pi}\int w(k_y;k_{y_0})\mathrm{e}^{-\mathrm{i}k_z(z-z_0)}\mathrm{e}^{-\mathrm{i}k_y(y-y_0)}\mathrm{d}k_y \tag{7.8}$$

that represents a Fourier transform

$$\Psi_{\mathrm{in}}(y,z) = \mathscr{F}\{w(k_y;k_{y_0})\mathrm{e}^{-\mathrm{i}k_z(z-z_0)}\}[y-y_0] \tag{7.9}$$

with $k_y = k_0 n_1 \mathrm{sin}\varphi$ and $k_z = k_0 n_1 \mathrm{cos}\varphi = \sqrt{k_0^2 n_1^2 - k_y^2}$. The primary incidence angle of the overall wave bundle is φ_0, determined by the primary wavenumber $k_{y_0} = k_0 n_1 \mathrm{sin}\varphi_0$. The last two exponential terms depict the propagation in y-z-direction and (y_0, z_0) positions the focus of the beam. For our 2-D setting, Ψ indicates the principal electric or magnetic component E_x or H_x for TE or TM modes, respectively. The weight w is assumed to be a Gaussian function

$$w(k_y;k_{y_0}) = \mathrm{e}^{-\frac{(k_y-k_{y_0})^2}{w_k^2}} \tag{7.10}$$

and defines the shape of the incoming beam in lateral direction. Correspondingly, the Gaussian weight of half width is $w_k = 4\mathrm{cos}\varphi_0/W_c$, where W_c is the full lateral beam width perpendicular to the propagation direction [14].

In the next step, to calculate the angular spectrum, the incoming field from Eq. (7.8) must be rotated by the angle α_n to the local coordinate system $(y', z'; k_y', k_z')$. Then, the incoming field on the n-th element is

$$\Psi_{\mathrm{in},n}(y') = \frac{1}{2\pi}\int \mathrm{e}^{-\frac{(k_y'-k_{y_0}')^2}{w_k'^2}}\mathrm{e}^{\mathrm{i}k_z' z_0'}\mathrm{e}^{-\mathrm{i}k_y'(y'-x_0')}\mathrm{d}k_y' \tag{7.11}$$

or again via the Fourier transform

$$\Psi_{\mathrm{in},n}(y') = \mathscr{F}\{w(k_y';\varphi_0+\alpha)\mathrm{e}^{\mathrm{i}k_z' z'}\}[y'-y_0']. \tag{7.12}$$

Note that in the local coordinate system, the incoming wave reaches the surface at an incidence angle $\varphi_0 + \alpha$. This implicitly results in a rotation of the primary incidence wavenumber $k_{y_0}' = k_0 n_1 \mathrm{sin}(\varphi_0 + \alpha)$ and also of the Gaussian weight $w_k' = 4\mathrm{cos}(\varphi_0+\alpha)/W_c$. The focus (y_0', z_0') of the incident wave is adapted to the new coordinate system and since the origin is $(y_n, g(y_n))$, the field on the interface is given at $z' = 0$.

Step 2: Determination of the angular spectrum

The angular spectrum for the n-th rotated element is given by an inverse Fourier transform

$$A_n(k_y') = \int \Psi_{\mathrm{in},n}(y')\mathrm{rect}(\tfrac{y'-n\Delta y'}{\Delta y'})\mathrm{e}^{\mathrm{i}k_y' y'}\,\mathrm{d}y' \tag{7.13}$$

or

$$A_n(k_y') = \mathscr{F}^{-1}\{\Psi_{\mathrm{in},n}(y')\mathrm{rect}(\tfrac{y'-n\Delta y'}{\Delta y'})\}[k_y'], \tag{7.14}$$

with $\Delta y' = \Delta y / \cos\alpha_n$. The window function is used to guarantee that only the element under consideration has an influence and is selected to be of rectangular shape with

$$\mathrm{rect}(y) = \begin{cases} 1, & |y| \leq 1 \\ 0, & \text{otherwise.} \end{cases} \tag{7.15}$$

Of course, the window function can also be replaced by functions that achieve similar behavior, e.g., a Gaussian window function.

Step 3: Calculation of the scattered fields

The radiated fields (in forward or backward direction) generated from the n-th segment are calculated by propagating the fields from each element using their angular spectrum (Eq. (7.13)). Thus, the outgoing field from the n-th element, back-transformed in global coordinates (y, z), is

$$\Psi_{j,n}(y,z) = \frac{1}{2\pi} \int a_j(k_y') A_n(k_y') \mathrm{e}^{\pm \mathrm{i} k_z' \eta_n(y,z)} \mathrm{e}^{-\mathrm{i} k_y' \xi_n(y,z)} \mathrm{d}k_y', \qquad j \in \{\mathrm{in}, \mathrm{r}, \mathrm{t}\}, \tag{7.16}$$

or similarly by the Fourier transform

$$\Psi_{j,n}(y,z) = \mathscr{F}\{a_j(k_y') A_n(k_y') \mathrm{e}^{\pm \mathrm{i} k_z' \eta_n(y,z)}\}[\xi_n(y,z)], \qquad j \in \{\mathrm{in}, \mathrm{r}, \mathrm{t}\}, \tag{7.17}$$

where the negative sign in the exponential term refers to forward (transmitted) propagating waves and the positive sign to backward (reflected) propagating waves.

With $j = \mathrm{r}$ we indicate the reflected and with $j = \mathrm{t}$ the transmitted fields, respectively. This approach is also valid to determine the incoming field ($j = \mathrm{in}$) because Eq. (7.16) leads to an identical solution for the incoming field like Eq. (7.8). Depending on the considered field, the wavenumbers are

$$k_y = k_0 n_j \sin\varphi_j \quad \text{and} \quad k_z = k_0 n_j \cos\varphi_j, \tag{7.18}$$

i.e., for the incoming and reflected fields $n_\mathrm{r} = n_j = n_1$ and $\varphi_\mathrm{r} = \varphi_j = \varphi$, and for the transmitted field $n_\mathrm{t} = n_j = n_2$ and $\varphi_\mathrm{t} = \varphi_j = \beta$, where $\beta = \beta(\varphi)$ is the transmittance angle and determined by Snell's law [79]

$$n_1 \sin\varphi = n_2 \sin\beta. \tag{7.19}$$

Analogue to a simple plane wave interface, the wave amplitude functions $a_j(k_y)$ for this 2-D setting are defined by the Fresnel coefficients [79]. Since the shape of the incoming wave is given by $w(k_y)$ or $A_n(k_y')$ (cf. Eq. (7.16)), the incoming amplitude a_in is set to one. The coefficients for the reflected waves $a_\mathrm{r}(k_y) = r(\varphi(k_y))$ are

$$r_s = \frac{n_1 \cos\varphi - n_2 \cos\beta}{n_1 \cos\varphi + n_2 \cos\beta} \quad (\mathrm{TE}) \quad \text{and} \quad r_p = \frac{n_2 \cos\varphi - n_1 \cos\beta}{n_2 \cos\varphi + n_1 \cos\beta} \quad (\mathrm{TM}), \tag{7.20}$$

depending on the polarization of the incoming wave. For the transmitted field $a_\mathrm{t}(k_y) = t(\varphi(k_y)))$, the coefficients are

$$t_s = \frac{2 n_1 \cos\varphi}{n_1 \cos\varphi + n_2 \cos\beta} \quad (\mathrm{TE}) \quad \text{and} \quad t_p = \frac{2 n_1 \cos\varphi}{n_2 \cos\varphi + n_1 \cos\beta} \quad (\mathrm{TM}). \tag{7.21}$$

Our approach also allows k_z to become imaginary so that at high angles of incidence, leading to total reflection, evanescent waves are generated in the corresponding area.

Step 4: Superimposing to the overall solution

Finally, summing up the intermediate results for each of the $\mathcal{N}$ elements leads to the overall field solution (incoming, transmitted and reflected field)

$$\Psi_j(y,z) = \sum_{n=1}^{\mathcal{N}} \Psi_{j,n}(y,z) \qquad j \in \{\mathrm{in},\mathrm{r},\mathrm{t}\}. \tag{7.22}$$

7.2.3 Examples

Now, we show some specific configurations, where we apply the 2-D SASM with oblique elements (indicated as SASMo) and compare it to the approach from [46], where a general staircase approximation consisting of straight elements is used (indicated as SASMs). Additionally, full 2-D FEM COMSOL (indicated as C) solutions [22] are presented, serving as a reference solution. In COMSOL, we again make use of port boundary conditions to excite the structure with an incoming Gaussian beam and perfectly matched layers to simulate an infinite structure. The 2-D interface consists of a simple circular curve

$$g(y) = r - \sqrt{r^2 - y^2} \tag{7.23}$$

with curvature radius r. Such a configuration is able to focus the incoming beam and thus represents a simple lens. The material parameters are further given by $n_1 = 1$ and $n_2 = 2$ for a vacuum wavelength of $\lambda_0 = 1.55\,\mu$m. The incoming field is TE polarized with non-zero principal field component $\Psi = E_x$ that is propagating at oblique angles φ_0. We choose a Gaussian beam width of $W_c = 10\,\mu$m. The discretization is done by dividing the interface in $\mathcal{N} = 50$ elements (this applies also for the following sections) and all integrals are numerically calculated using numerical quadrature [23].

Figures 7.4–7.5 show the absolute field value of the electric field component $|E_x|$ for different curvature radii r and incidence angles φ_0. The following scenarios are shown from top to bottom: top views for the SASMo, SASMs and COMSOL (C) solution, field cross sections along the y-direction at the z-position of the focus and along a line through the focus in propagation direction. Contour lines are added for the first set of graphs at 2%, 5% and 10% of the absolute field to make the results more comparable. Generally, we observe that the curvature radius determines the position of the focal point in the z-direction, while the oblique incidence shifts the focal point along the x-axis.

One observes very good agreement with the COMSOL solution for both SASM approaches. However, the amplitude in the focal point using straight elements (SASMs) is slightly smaller to the reference FEM solution (C), especially for small curvature radii which can be best observed in the last two line graphs. Contrarily, the SASMo line plots match perfectly with the reference solution with just minor differences near the focal point.

Taking a closer look at geometrical optics [48], the focus of the beam can be predicted by the Lensmaker's equation for a single interface, which is

$$f = \frac{n_2 r}{n_2 - n_1}. \tag{7.24}$$

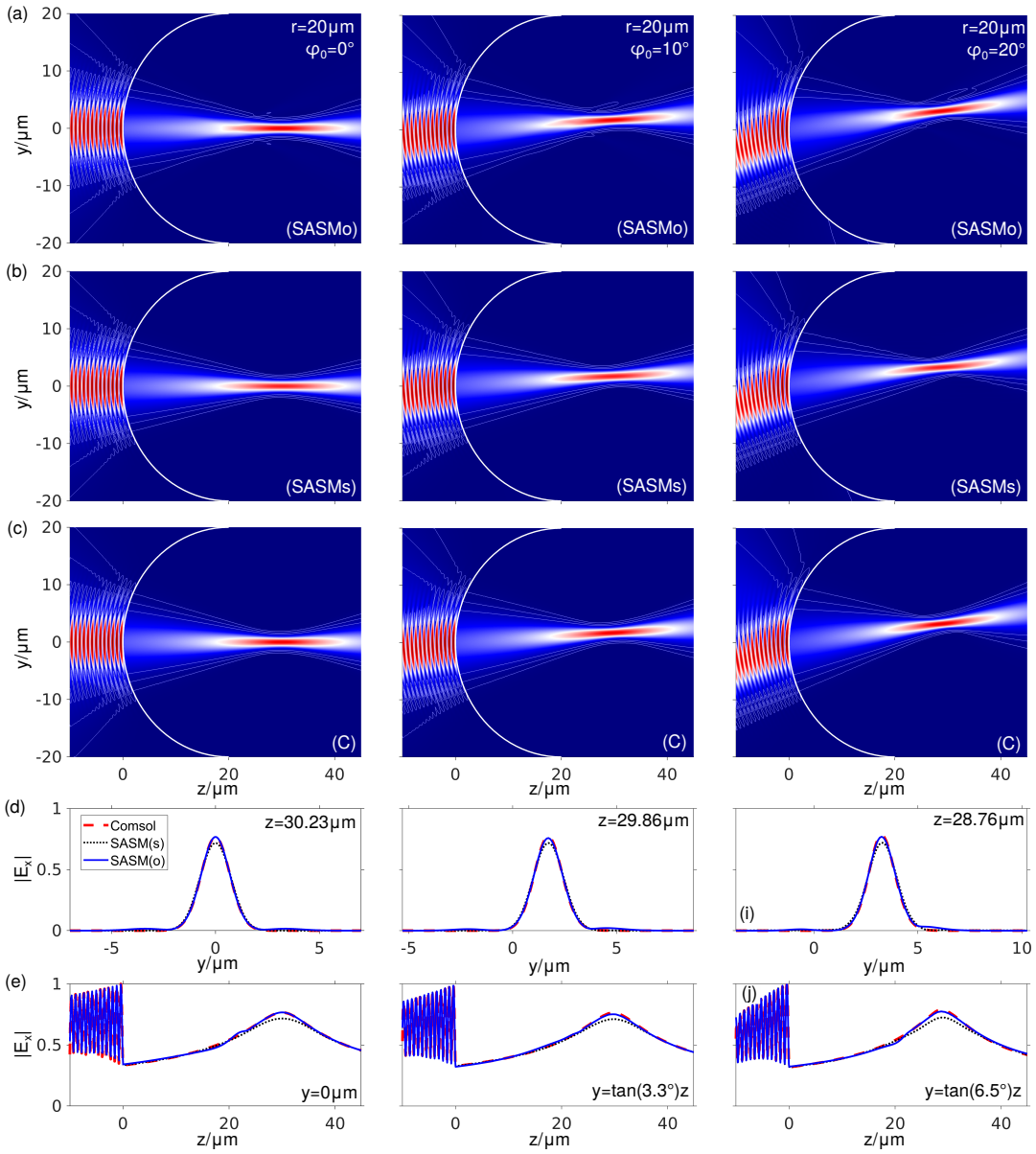

Figure 7.4: Field plots of the absolute electric field component $|E_x|$ for different incidence angles φ_0 and fixed curvature radius $r = 20\,\mu$m. Shown are the results using the SASMo (a), SASMs (b) and the corresponding COMSOL solution (c). Additionally, line plots for fixed z- and y-coordinate (d, e) along a line through the focus are shown. The contour lines mark the levels of the absolute field at 2%, 5% and 10% [75].

For the structures considered in Figures 7.4–7.5, focal spots at distances $f = 30\,\mu$m and $f = 60\,\mu$m for curvature radii $r = 20\,\mu$m or $r = 40\,\mu$m, respectively, are calculated. A comparison with the figures confirms the agreement with our results.

We can state that our oblique SASM approach shows good agreement with the reference solution and works slightly better than the SASMs, especially for small curvature radii. Further-

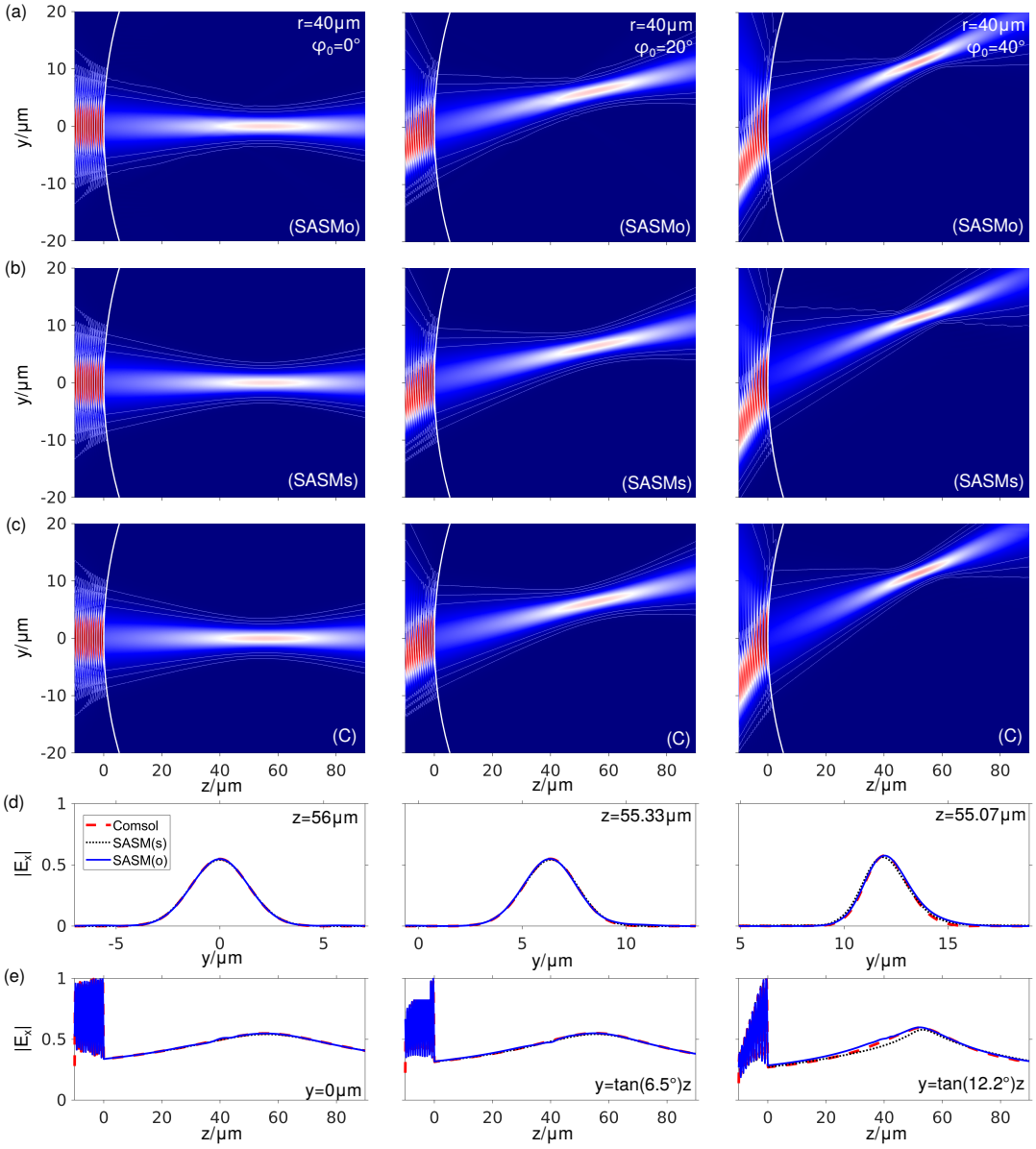

Figure 7.5: Field plots of the absolute electric field component $|E_x|$ for different incidence angles φ_0 and fixed curvature radius $r = 40\,\mu$m. Shown are the results using the SASMo (a), SASMs (b) and the corresponding COMSOL solution (c). Additionally, line plots for fixed z- and y-coordinate (d, e) along a line through the focus are shown. The contour lines mark the levels of the absolute field at 2%, 5% and 10% [75].

more, the approximation of the curved surface is also more accurate for even smaller values of discretization elements $\mathcal{N}$.

7.3 Two curved surfaces

Next, two of these curved interfaces are combined, as sketched in Figure 7.6. Here, the fields are propagating between the two surfaces resulting in a superposition of forward and backward propagating waves. Possible configurations are convex or concave lens systems that focus the incoming light at specific focal points.

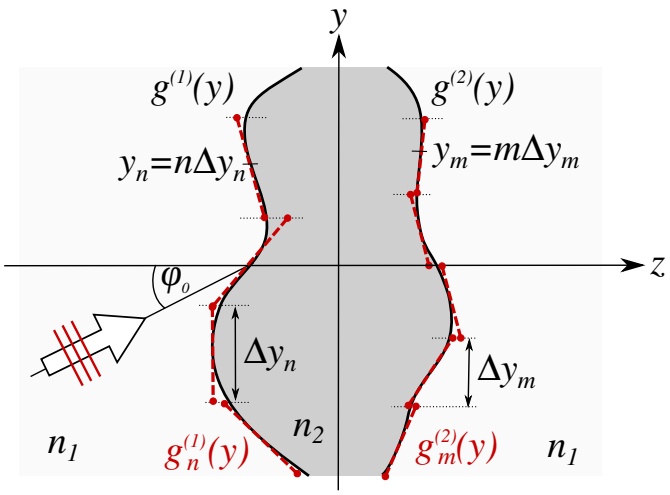

Figure 7.6: Two curved surfaces $g^{(1)}(y)$ and $g^{(2)}(y)$, separating outer regions with refractive index n_1 from an inner region with refractive index n_2. The incoming wave reaches the first surface at an incidence angle φ_0. The red dashed lines represent the approximation of the curved interfaces [75].

At first, we discuss the 2-D case again, meaning a structure that is constant along the x-direction with a field ansatz analogue to Eq. (7.4). Material parameters are n_2 in the middle layer surrounded by n_1 in the outer regions. Of course, three different materials are possible as well. The interface functions are $g^{(1)}(y)$ and $g^{(2)}(y)$. The incoming wave reaches the first surface at oblique angles of propagation φ_0.

To calculate the wave propagating in these configurations an adapted, cascaded approach of the stepwise ASM for a single interface, presented in Section 7.2, is applied. The method has to be extended for multiple reflections. After calculating the scattered fields from the first boundary, the transmitted field serves as the new incoming field on the second boundary. Then, the scattered fields from the second interface are calculated and the reflected field serves as the new incoming field for the first boundary again. This process needs to be repeated several times to achieve a suitable, convergent solution.

The discretization is carried out analogously to the process for a single interface in Section 7.2. Both interfaces are divided in $\mathcal{N}$ (first interface) or $\mathcal{M}$ (second interface) equidistant, tangential, piecewise flat surfaces $g_n^{(1)}(y)$ and $g_m^{(2)}(y)$ with center y_n or y_m and widths Δy_n or Δy_m with $n \in [1, \mathcal{N}]$ and $m \in [1, \mathcal{M}]$, respectively. The number of discretization elements does not have to be equal for both surfaces, but in this work we assume $\mathcal{N} = \mathcal{M}$. Again, for each element the coordinate system needs to be rotated by the inclination angle $\alpha_n^{(1)}$ or $\alpha_m^{(2)}$. Since we assume $\mathcal{N} = \mathcal{M}$, the angles are abbreviated as α_1 and α_2 in the following for a better overview. We

identify with (y', z') the rotated coordinate system for the first interface and with $(\hat{y}, \hat{z})$ the one for the second interface. Both are defined by Eq. (7.6), where the parameters for the respective interface are adjusted accordingly. The relation between the local coordinate systems is further determined by

$$\begin{aligned} y' =: \hat{\xi}_{n,m}(\hat{y}, \hat{z}) &= \cos(\alpha_2 - \alpha_1)\hat{y} + \cos\alpha_1(y_m - y_n) \\ &\quad - \sin(\alpha_2 - \alpha_1)\hat{z} + \sin\alpha_1(g^{(2)}(y_m) - g^{(1)}(y_n)), \\ z' =: \hat{\eta}_{n,m}(\hat{y}, \hat{z}) &= \cos(\alpha_2 - \alpha_1)\hat{z} + \cos\alpha_1(g^{(2)}(y_m) - g^{(1)}(y_n)) \\ &\quad + \sin(\alpha_2 - \alpha_1)\hat{y} - \sin\alpha_1(y_m - y_n), \end{aligned} \tag{7.25}$$

or

$$\begin{aligned} \hat{y} =: \xi'_{n,m}(y', z') &= \cos(\alpha_1 - \alpha_2)y' + \cos\alpha_2(y_n - y_m) \\ &\quad - \sin(\alpha_1 - \alpha_2)z' + \sin\alpha_2(g^{(1)}(y_n) - g^{(2)}(y_m)), \\ \hat{z} =: \eta'_{n,m}(y', z') &= \cos(\alpha_1 - \alpha_2)z' + \cos\alpha_2(g^{(1)}(y_n) - g^{(2)}(y_m)) \\ &\quad + \sin(\alpha_1 - \alpha_2)y' - \sin\alpha_2(y_n - y_m). \end{aligned} \tag{7.26}$$

The corresponding rotated wavenumbers are related as

$$\begin{aligned} k'_y &= \cos(\alpha_2 - \alpha_1)\hat{k}_y - \sin(\alpha_2 - \alpha_1)\hat{k}_z, \\ k'_z &= \cos(\alpha_2 - \alpha_1)\hat{k}_z + \sin(\alpha_2 - \alpha_1)\hat{k}_y \end{aligned} \tag{7.27}$$

or

$$\begin{aligned} \hat{k}_y &= \cos(\alpha_1 - \alpha_2)k'_y - \sin(\alpha_1 - \alpha_2)k'_z, \\ \hat{k}_z &= \cos(\alpha_1 - \alpha_2)k'_z + \sin(\alpha_1 - \alpha_2)k'_y. \end{aligned} \tag{7.28}$$

To calculate the propagating fields, we divide the derivation of the method for two interfaces in two parts by initially considering the first and second interface individually.

7.3.1 Scattered fields from the first interface

The angular spectrum on the first interface comprises two terms: the angular spectrum of the incoming wave bundle and a superposition of the angular spectra of all reflected fields from the second interface. Hence, the combined angular spectrum on the first interface is calculated via

$$A_n^{(1)}(k'_y) = A_{n,0}(k'_y) + \sum_{\nu=1}^{\infty} A_{n,\nu}(k'_y), \tag{7.29}$$

where $A_{n,0}(k'_y) = A_n(k'_y)$ identifies the angular spectrum of the incoming wave from Eq. (7.13) and the second summation is a Fourier transformation equivalent to Eq. (7.13)

$$A_{n,\nu}(k'_y) = \int \Psi_{\mathrm{in},n,\nu}(y')\mathrm{rect}\big(\tfrac{y' - n\Delta y'_n}{\Delta y'_n}\big)\mathrm{e}^{\mathrm{i}k'_y y'}\,\mathrm{d}y', \tag{7.30}$$

where the incoming field is the reflected field from the second interface

$$\Psi_{\mathrm{in},n,\nu}(y') = \frac{1}{2\pi}\sum_{m=1}^{\mathcal{M}} \int r(\hat{k}_y)A_{m,\nu}(\hat{k}_y)\mathrm{e}^{\mathrm{i}\hat{k}_z\eta'_{n,m}(y',0)}\mathrm{e}^{-\mathrm{i}\hat{k}_y\xi'_{n,m}(y',0)}\mathrm{d}\hat{k}_y. \tag{7.31}$$

Note that Eq. (7.31) depends on the angular spectrum from the second interface $A_{m,\nu}(\hat{k}_y)$. Thus, the whole process is iterative and needs to be calculated step by step.

Then, the scattered forward and backward fields from the first interface are a superposition of the individual solutions for each element

$$\Psi_j(y,z) = \frac{1}{2\pi}\sum_{n=1}^{\mathcal{N}} \int a_j(k_y') A_n^{(1)}(k_y') \mathrm{e}^{\pm \mathrm{i} k_z' \eta_n(y,z)} \mathrm{e}^{-\mathrm{i} k_y' \xi_n(y,z)} \mathrm{d}k_y', \tag{7.32}$$

where the negative sign refers to the transmitted ($j = \mathrm{t}$) and the positive sign to the reflected ($j = \mathrm{r}$) waves, respectively. The coordinate transformation from (y', z') to (ξ_n, η_n) is again given by Eq. (7.6) with the inclination angle α_1. Furthermore, the amplitudes are

$$a_j(k_y) = \begin{cases} t(k_y), & j = \mathrm{t} \text{ (transmitted wave)} \\ r(k_y), & j = \mathrm{r} \text{ (reflected wave)} \end{cases} \tag{7.33}$$

as introduced in Eqs. (7.20)–(7.21) depending on the considered polarization.

7.3.2 Scattered fields from the second interface

The angular spectrum for the second interface consists only of the angular spectra of the transmitted fields from the first surface. Thus,

$$A_m^{(2)}(\hat{k}_y) = \sum_{\nu=1}^{\infty} A_{m,\nu}(\hat{k}_y), \tag{7.34}$$

where the individual angular spectra for the n-th element is

$$A_{m,\nu}(\hat{k}_y) = \int \Psi_{\mathrm{in},m,\nu}(\hat{y}) \mathrm{rect}\big(\tfrac{\hat{y} - m\Delta\hat{y}_m}{\Delta\hat{y}_m}\big) \mathrm{e}^{\mathrm{i}\hat{k}_y \hat{y}} \mathrm{d}\hat{y} \tag{7.35}$$

and the incoming fields on the second interface are

$$\Psi_{\mathrm{in},m,\nu}(\hat{y}) = \frac{1}{2\pi}\sum_{n=1}^{\mathcal{N}} \int c_\nu(k_y') A_{n,\nu-1}(k_y') \mathrm{e}^{-\mathrm{i} k_z' \hat{\eta}_{n,m}(\hat{y},0)} \mathrm{e}^{-\mathrm{i} k_y' \hat{\xi}_{n,m}(\hat{y},0)} \mathrm{d}k_y' \tag{7.36}$$

with the amplitude

$$c_\nu(k_y) = \begin{cases} t(k_y), & \nu = 1 \\ r(k_y), & \text{otherwise} \end{cases} \tag{7.37}$$

from Eqs. (7.20)–(7.21) for the two polarizations. The radiated forward and backward fields from the second interface are then determined as

$$\Psi_j(y,z) = \frac{1}{2\pi}\sum_{m=1}^{\mathcal{M}} \int a_j(\hat{k}_y) A_m^{(2)}(\hat{k}_y) \mathrm{e}^{\pm \mathrm{i}\hat{k}_z \eta_m(y,z)} \mathrm{e}^{-\mathrm{i}\hat{k}_y \xi_m(y,z)} \mathrm{d}\hat{k}_y. \tag{7.38}$$

Again, $j \in \{\mathrm{r}, \mathrm{t}\}$ and the coordinate transformation (7.6) from (y', z') to (ξ_m, η_m) enters, but with the inclination angle for the second interface α_2.

7.3.3 Examples

Also for the structure consisting of two interfaces, we present some examples to validate our approach. Therefore, the results are again compared to full 2-D FEM solutions calculated with COMSOL. The two surfaces are circular functions of the form

$$g^{(i)}(y) = r_j \pm \sqrt{r_j^2 - y^2} + z_p \qquad j \in \{1, 2\}, \tag{7.39}$$

that can either describe a convex ($r_1 > 0$, $r_2 < 0$, $g^{(1)}$ with $-$, $g^{(2)}$ with $+$) or concave ($r_1 < 0$, $r_2 > 0$, $g^{(1)}$ with $+$, $g^{(2)}$ with $-$) lens. The refractive indices have to be chosen accordingly to focus the incoming beam. For a convex lens, we assume $n_1 = 1 < 3 = n_2$ and for the concave case $n_1 = 3 > 1 = n_2$. The displacement z_p moves the circle along the z-axis to position the interfaces. Furthermore, the Gaussian beam width is again $W_c = 10\,\mu$m and the operating wavelength is $\lambda_0 = 1.55\,\mu$m. The incoming field is TE polarized with principal field component $\Psi = E_x$, which is propagating at an incidence angles φ_0.

Eqs. (7.29)–(7.34) usually require an infinite number of calculations. But, to keep the simulation time low, we reduce this to a finite number. The change in the field amplitude decreases after each interface transition. Thus, we observe that convergence is reached, in general, after a few iterations. The number of iterations is chosen such that the maximum absolute level of the change in field amplitude on the second interface (cf. Eq. (7.36)) is below 0.5% of the initial input field. Typically, 6-10 iterations are required depending on the properties of the considered structure.

The results are shown in Figure 7.7 for convex (a)-(c) and concave (d) lenses with different curvature radii and normal incidence angle $\varphi_0 = 0°$. The left column shows the calculated SASMo results and the right column the corresponding 2-D COMSOL solutions, respectively. Furthermore, contour lines are indicated at different levels for a better comparison. The solutions are in very good agreement. Additionally, Figure 7.8 illustrates results for several convex lenses with oblique propagation angles $\varphi_0 > 0$ and different curvature radii r_1 and r_2. The corresponding COMSOL solution is also shown and good agreement is observed.

Again, the focus of the outgoing beam can be predicted by the Lensmaker's equation

$$\frac{1}{f} = \frac{n_2 - n_1}{n_1}\left(\frac{1}{r_1} - \frac{1}{r_2} + d\frac{(n_2 - n_1)}{r_1 r_2 n_1 n_2}\right), \tag{7.40}$$

for a lens [48] with thickness $d = |z_2 - z_1|$. This gives focal distances $f \in \{17.19, 21.44, 18.41, 32.14\}\,\mu$m for the structures considered in Figure 7.7 from (a)-(d).

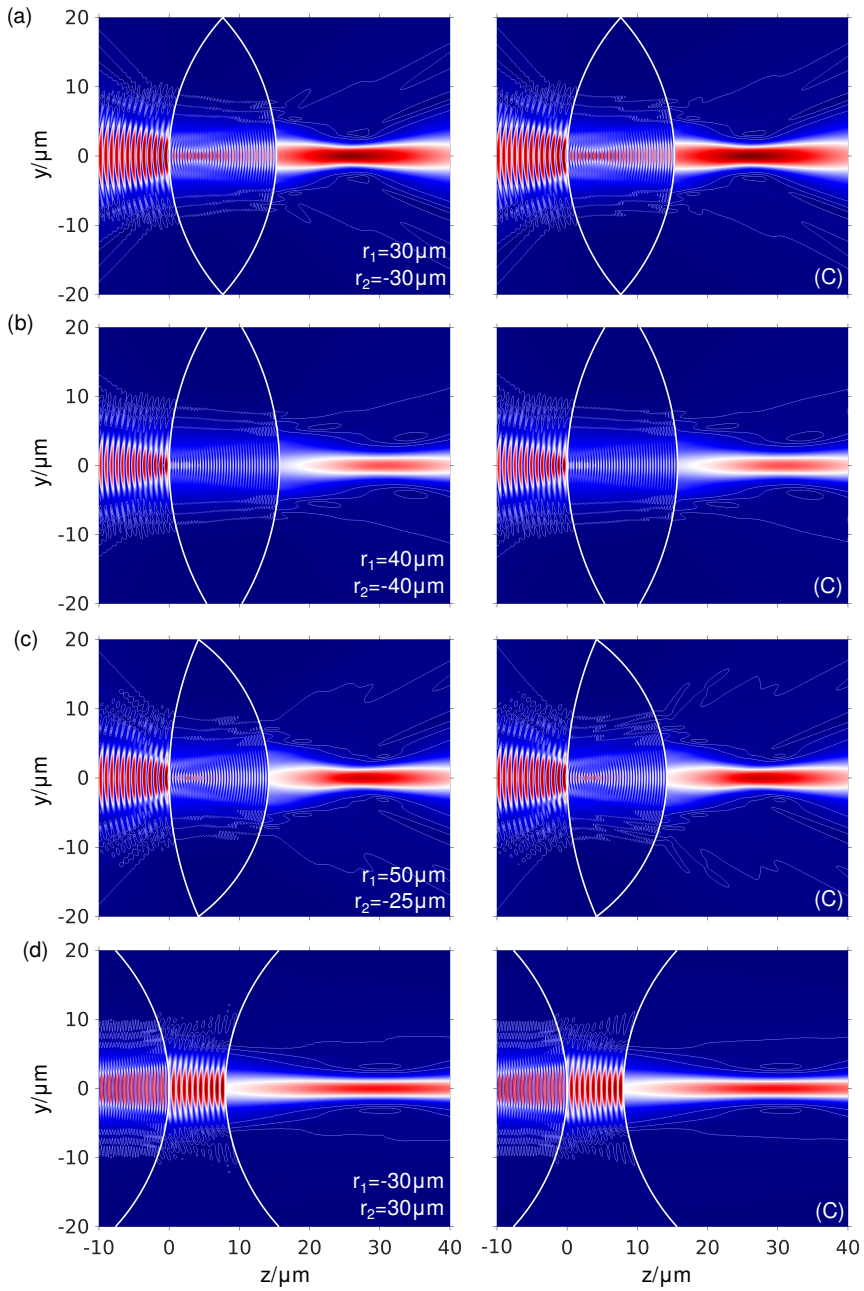

Figure 7.7: Field plots of the absolute electric field component $|E_x|$ for convex (a-c) and concave (d) lens configurations for different curvature radii r_1, r_2 and normal incidence angle $\varphi_0 = 0°$ using the SASMo (left column) and the corresponding COMSOL (C) solution (right column). The contour lines mark the levels of the absolute field at 2%, 5% and 10% [75].

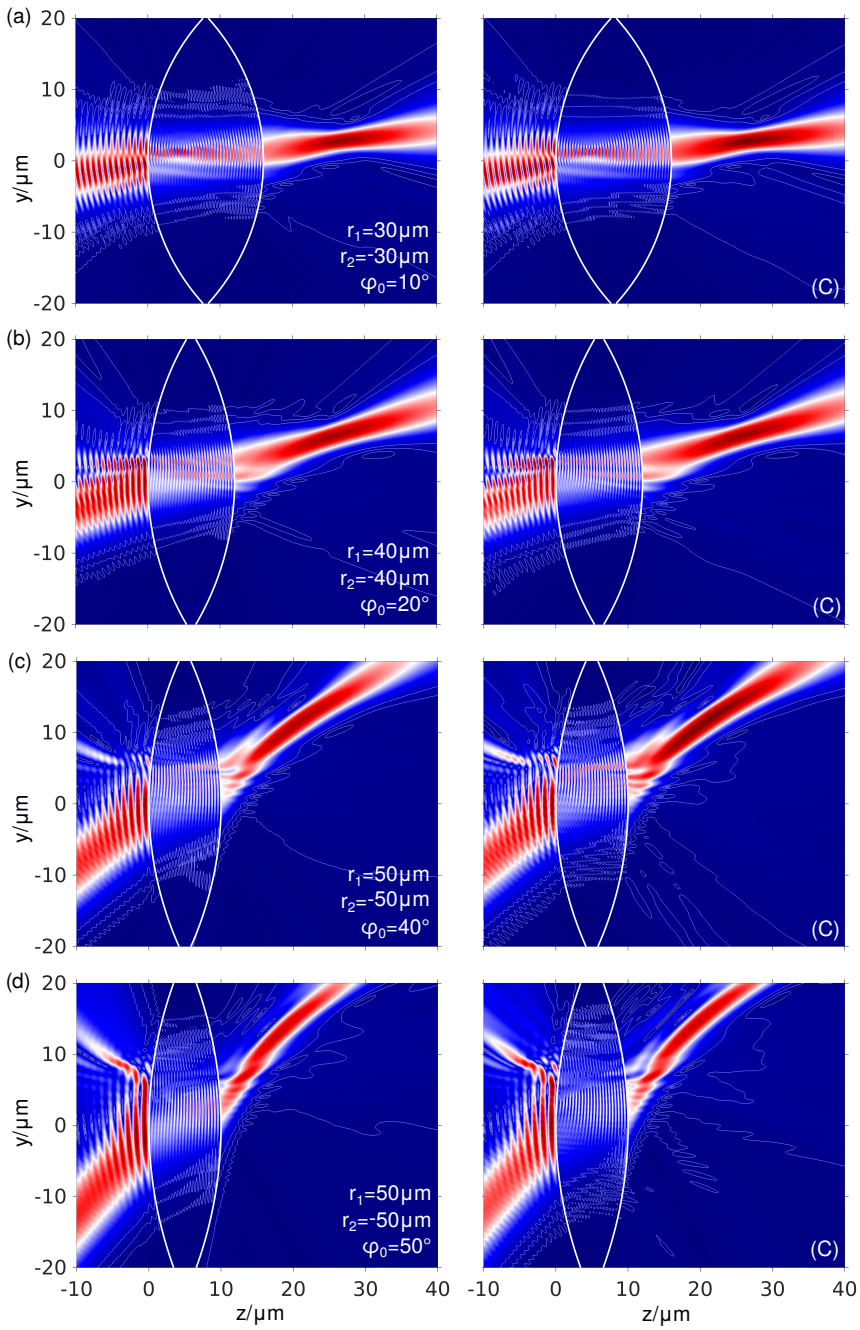

Figure 7.8: Field plots of the absolute electric field component $|E_x|$ for convex lens configurations with different curvature radii r_1, r_2 and incidence angles $\varphi_0 > 0°$. Shown are the results using the SASMo (left column) and the corresponding COMSOL (C) solution (right column). The contour lines mark the levels of the absolute field at 2%, 5% and 10% [75].

7.4 3-D slab waveguide lens

The more interesting case is the simulation of waves that propagate in dielectric slab waveguide lenses, as introduced in Figure 7.1. That means, we no longer assume that our structures are constant along the x-direction (cf. Figure 7.2 or Figure 7.6). Instead slab waveguides of specific thicknesses serve as the incoming and outgoing parts, as illustrated in Figure 7.9 (at first, just shown for a single interface). Therefore, the incoming wave is also no longer constant in that direction, but a semi-guided mode of the slab waveguide with a fully vectorial electromagnetic field dependence on all three spatial coordinates

$$\begin{pmatrix} \mathbf{E} \\ \mathbf{H} \end{pmatrix} (x, y, z) =: \mathbf{\Psi}(x, y, z). \tag{7.41}$$

The top view of the structure in Figure 7.9 (a) is identical to the 2-D case. Thus, again we consider an almost arbitrary interface given by the function $g(y)$. In contrast, the side view (b) comprises two dielectric slab waveguides with material parameters n_f, n_c and n_s in the core, cladding and substrate region, respectively. To ensure guidance, the refractive indices have to fulfill $n_f > n_c, n_s$. Furthermore, the waveguides have a thickness of d_1 and d_2. The incoming wave is a bundle of semi-guided waves of the left waveguide that is propagating at oblique primary angle φ_0 in the y-z-plane.

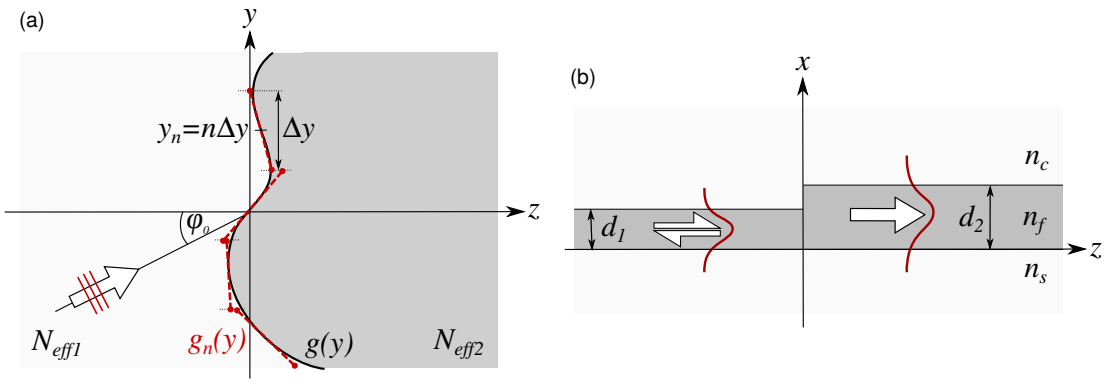

Figure 7.9: (a) Curved interface between two different slab regions. (b) Cross section of an interface between two slab waveguides of thicknesses d_1 and d_2 with refractive index n_f, n_c and n_s in the core and cladding regions [75].

To calculate the wave propagation in these 3-D structures, a combination of a modified version of the 2-D stepwise angular spectrum method (in the y-z-plane, cf. Section 7.2) with a set of 2.5-D solutions of the cross section (in the x-z-plane) is used. Similar to the 2-D case, the structure is discretized in a finite number of piecewise, flat elements $g_n(y)$ of width Δy, tangential to the boundary at position y_n. Generally, the SASM is then applied on each of these elements and superimposed to the overall solutions with some modifications.

In the 2-D case, the SASM was calculated as a superposition of plane waves that are constant along the x-axis and propagate in various directions (k_y, k_z). Now, these plane waves are replaced by fully vectorial 2.5-D solutions of the interface cross section in Figure 7.9 (b). The structure is assumed to be infinite in the y-direction. As before, the solution is required for a

range of incidence angles φ or wavenumbers k_y. Thus, the x-dependence of the 3-D fields in Eq. (7.41) is now determined by the 2-D COMSOL solution.

The SASM is further modified such that it operates with the effective refractive indices N_{eff_1} and N_{eff_2} of the corresponding slab waveguide modes instead of n_1 and n_2, as used before for the 2-D case. Now, the effective refractive indices model the propagation of the guided modes supported by the slabs. Note that potentially several modes are guided.

Applying these modifications to the steps from Section 7.2 results in the following: the incoming field $\Psi_{\mathrm{in},n}(y')$ (Eq. (7.11)) and the angular spectra $A_n(k_y')$ (Eq. (7.13)) can directly be adopted for the 3-D case, by just replacing n_1 with N_{eff_1} and n_2 with N_{eff_2}. Note that now TE and TM modes are potentially excited at the interfaces, leading to scattered fields for each polarization. Therefore, angular spectra for each guided mode have to be considered at the interface. Furthermore, the weight of the incoming field is no longer of Gaussian shape. We assume an incoming rib mode by placing an additional rib waveguide in front of the structure, as introduced in Section 2.4.

The scattered fields in the third step need to be modified, as the plane waves are now replaced by the 2-D COMSOL solutions for a range of incidence angles φ

$$\boldsymbol{\Psi}_n(x,y,z) = \frac{1}{2\pi}\int A_n(k_y')\underbrace{\{\boldsymbol{\Phi}_0(x;k_y')\mathrm{e}^{-\mathrm{i}k_z'\eta_n(x,z)} + \varrho(x,z)\}}_{\text{COMSOL solution}}\mathrm{e}^{-\mathrm{i}k_y'y'}\,\mathrm{d}k_y'. \tag{7.42}$$

Here, $\{\boldsymbol{\Phi}_0(x;k_y')\mathrm{e}^{-\mathrm{i}k_z'\eta_n} + \varrho\} =: \boldsymbol{\Phi}_{\mathrm{C}}(x,z;k_y')$ indicates the COMSOL solution for incidence wavenumber k_y', where $\boldsymbol{\Phi}_0$ is the vectorial oblique mode profile of the incoming wave and ϱ is a remainder. Since full vectorial 2.5-D COMSOL solutions are used, $\boldsymbol{\Psi}_n$ already includes the incoming, reflected and transmitted fields. Superposition leads to the overall 3-D field solution

$$\boldsymbol{\Psi}(x,y,z) = \sum_{n=1}^{\mathcal{N}} \boldsymbol{\Psi}_n(x,y,z). \tag{7.43}$$

Advantageous is that by considering full vectorial 2-D solutions of the cross section, as out-of-plane losses are fully taken into account. Additionally, compared to rigorous 3-D simulations, our approach requires less computational effort (time and memory space). We will remark on that later in this chapter.

7.4.1 Expansion of the 2-D COMSOL solution

Sometimes, the focal point is far away from the origin of the interface. This is especially observed for low refractive index contrasts and single interface structures. Therefore, depending on the waveguide and interface properties, the computational domain to calculate the 2.5-D COMSOL solutions needs to be quite large. Consequently, a large computational effort is required to generate the set of 2-D COMSOL solutions at different incidence angles.

This problem can be solved with the expansion of the fields. Since the slabs are constant in both directions $z \gtrless 0$, we can easily propagate the corresponding lossless 1-D slab modes in the respective direction analytically. To that end, the amplitudes of the 1-D mode profiles are extracted from the 2-D COMSOL solution for each guided mode in the incoming and outgoing slabs.

More precisely, the fields are extracted at two cross-section lines along the x-direction at positions $z = \pm z_t$ for the incoming/reflected and outgoing fields, assuming that the discontinuity is positioned at $z = 0$ (Figure 7.9 (b)).

The incoming and outgoing fields in the slabs of the 2-D COMSOL solution $\mathbf{\Phi}_\mathrm{C}$ can then be written as a superposition of all guided slab waveguide modes $\mathbf{\Psi}_p$ with amplitudes a_p, wavenumbers $k_{z,p}$ and a remaining scattered field $\mathbf{\Psi}_\mathrm{sc}$[2]

$$\mathbf{\Phi}_\mathrm{C}(x, z; k_y) = \sum_p a_p(k_y)\mathbf{\Psi}_p(x; k_y)\mathrm{e}^{\pm \mathrm{i}k_{z,p}z} + \mathbf{\Psi}_\mathrm{sc}(x, z; k_y), \tag{7.44}$$

where p counts the guided slab modes.

Again, we make use of the product from Eq. (2.44) to extract the amplitudes $a_p(k_y)$ by projecting the numerical field $\mathbf{\Phi}_C$ onto each of the slab modes $\mathbf{\Psi}_q$ at position z_t

$$(\mathbf{\Psi}_q, \mathbf{\Phi}_\mathrm{C})_x = \sum_p a_p(\mathbf{\Psi}_q, \mathbf{\Psi}_p)_x \mathrm{e}^{\pm \mathrm{i}k_{z,p}z_t} + (\mathbf{\Psi}_q, \mathbf{\Psi}_\mathrm{sc})_x. \tag{7.45}$$

Assuming mutual orthogonality of the guided slab modes $(\mathbf{\Psi}_q, \mathbf{\Psi}_p)_x = 0$, if $q \neq p$, orthogonality of the slab modes and the scattering field $(\mathbf{\Psi}_q, \mathbf{\Psi}_\mathrm{sc})_x = 0$, $\forall q$, and power normalization $(\mathbf{\Psi}_q, \mathbf{\Psi}_q)_x = 1$, the amplitudes are determined as

$$a_p = (\mathbf{\Psi}_p, \mathbf{\Phi}_\mathrm{C})_x \mathrm{e}^{\mp \mathrm{i}k_{z,p}z_t}. \tag{7.46}$$

The huge advantage of the extension is that the computational window in COMSOL can now be relatively small, independent from that used for the SASM, leading to substantial advantages in computation time and memory. Additionally, we choose the points z_t as small as possible, such that out-of-plane radiation losses occurring at the interface are almost fully decayed. In this way, almost no approximations apply when expanding the 2-D field solutions.

7.4.2 Single interface

In the following, 3-D results are shown for a single interface using the 3-D SASM. The incoming slab is assumed to have a thickness of $d_1 = 0.05\,\mu$m and the outgoing slab a thickness of $d_2 = 0.22\,\mu$m. We consider Si/SiO_2 waveguides with refractive indices $n_f = 3.45$ and $n_c = n_s = 1.45$ for vacuum wavelength $\lambda_0 = 1.55\,\mu$m. Both waveguides guide the fundamental TE and TM mode (cf. Table 2.1). The TE_0 mode of the adjoining rib waveguide, with rib width $W = 15\,\mu$m, height $d = 0.05\,\mu$m (identical to the incoming slab waveguide) and etch depth $d' = 0.02\,\mu$m, serves as the incoming field. The curvature is again defined as a circular function of the form

$$g(y) = r - \sqrt{r^2 - y^2} \tag{7.47}$$

with positive curvature radius r.

[2]This holds strictly only for the transverse components; see footnote 1 on page 24 for a detailed explanation.

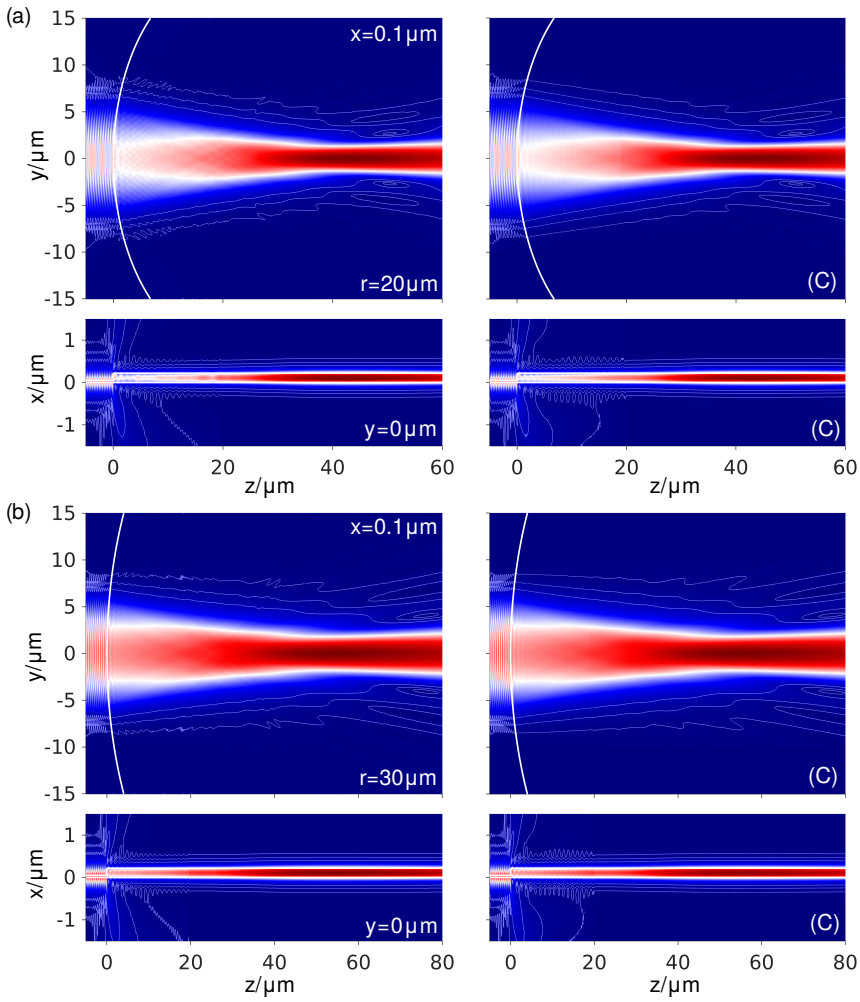

Figure 7.10: Top view (upper row) and side view (bottom row) of the absolute electric field $|E_y|$ for different curvature radii $r = 20\,\mu$m (a) and $r = 30\,\mu$m (b) and incidence angles $\varphi_0 = 0°$. The corresponding full vectorial 3-D COMSOL solution is shown on the right side (C). The contour lines mark the levels of the absolute field at 2%, 5% and 10% [75].

Figures 7.10–7.11 show a few examples for a single interface. Shown is the absolute value of the principal electric field component $|E_y|$ for different curvature radii and incidence angles. The upper row shows the top view of the field, while the bottom row illustrates the side view along the direction $y = \tan(\beta)z$, where β (see Eq. (7.19)) is the transmittance angle of the outgoing field. Note that despite the excitation by an adjacent rib waveguide, the rib itself is not shown in the plots, and only the fields in the slab regions are illustrated.

The 2.5-D COMSOL solutions of the cross section are calculated over a range of incidence angles from $\varphi = -85°$ to $\varphi = 85°$ with steps of $0.5°$ in the spatial area $z \in [-5, 20]\,\mu$m, where the discontinuity is positioned in $z = 0\ \mu$m, and the 2-D solution is further expanded with the method used in Section 7.4.1. Furthermore, for each element the solution needs to be rotated and shifted depending on the position of $g(y)$ and the inclination angles α_n.

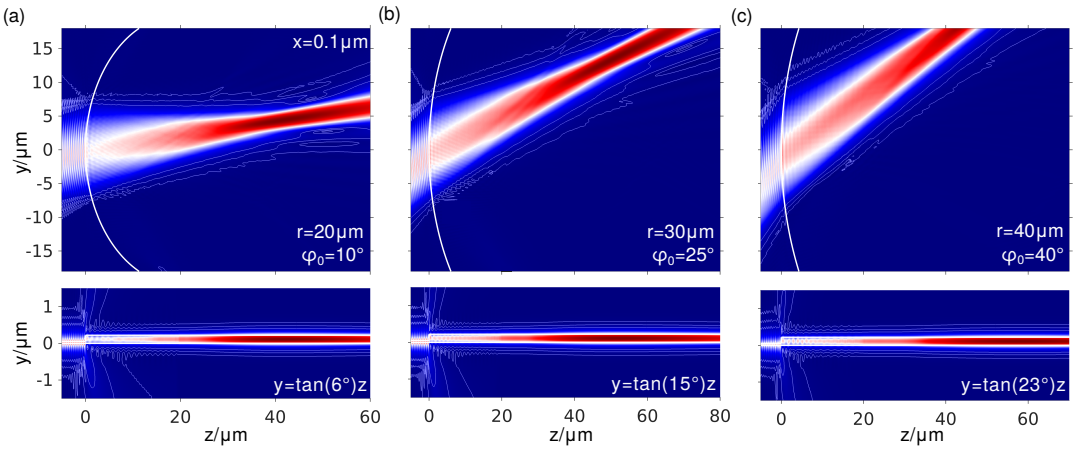

Figure 7.11: Top view (upper row) and side view (bottom row) of the absolute electric field $|E_y|$ for different curvature radii r and incidence angles $\varphi_0 > 0°$. The contour lines mark the levels of the absolute field at 2%, 5% and 10% [75].

For validation, Figure 7.10 compares our results to full rigorous 3-D FEM solutions calculated in COMSOL (shown on the right side of the figure). Here, we also use an etched rib waveguide, with the same parameters as mentioned before, to excite the structure. The incoming rib mode is calculated by using port boundary conditions and perfectly matched layers are added to simulate open boundaries. For the single interface, the focal point is quite far away from the origin of the boundary, therefore a large computational domain is required. For simplicity and analogue to the arguments introduced in Section 7.4.1, we simulate the full 3-D solution only in the range $z \in [-5, 20]\,\mu$m and extend it in both directions. Beyond this range, scattered non-guided fields are almost entirely absent, thus a good approximation is obtained. We observe very good agreement between our SASM results and the direct 3-D FEM solution.

The full 3-D FEM solutions are calculated in parallel on a SMP node with 32 cores and 1 TB RAM. This requires a calculation time of around 20 h and the full memory space is used to receive accurate 3-D solutions. Even then, the mesh did not fully converge, as there was not enough memory space available. In contrast, the SASM results are calculated on a computer with 16 cores and 32 GB RAM and the calculation took just about 10 minutes. Note that this does not include the constituting 2.5-D COMSOL solutions, as these were pre-calculated and can be used for arbitrary two interface configurations with the same layering. Furthermore, it should be noted that the 3-D COMSOL solution determines the full 3-D field, while our SASM evaluates the fields only on a cut plane as required for the presented field plots.

Comparably high losses already appear for a 3-D single curved interface as can best be observed in the side plots in Figures 7.10–7.11. To get an impression of these losses, it is advantageous to study the losses of the superimposed corresponding 2-D solutions. Therefore, Figure 7.12 shows the relative outgoing power for TE and TM modes (transmittance T and reflectance R) and the total outgoing power to guided modes P_{out} depending on the incidence angle φ for incoming TE_0 (a) or TM_0 (b) mode. We observe that losses can not be neglected especially for small incidence angles and TM excitation.

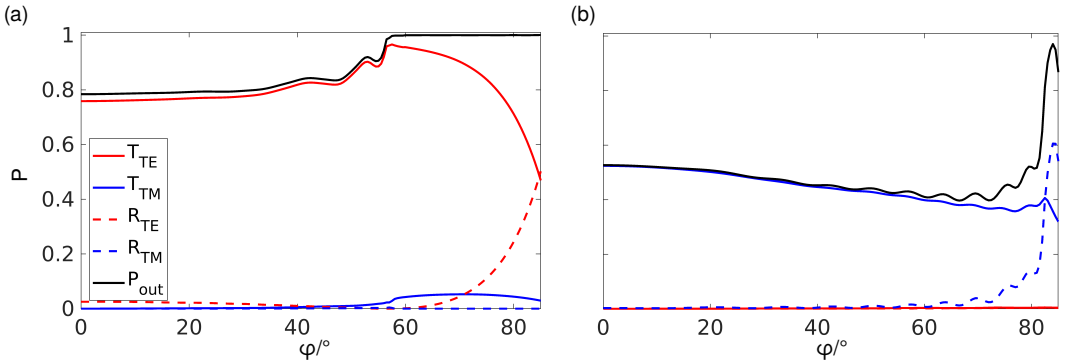

Figure 7.12: Reflection R and transmittance T for fundamental guided TE-/TM-modes depending on the incidence angle φ of the 2-D solutions for either TE (a) or TM (b) excitation [75].

However, from the theory in Section 2.3, we know that for incoming TE mode losses are fully suppressed beyond a specific incidence angle $\varphi_c = 57.23°$ and reflected TM waves are suppressed beyond $\varphi_m = 57.92°$. Transmitted TM waves do always exist.

7.4.3 Two interfaces

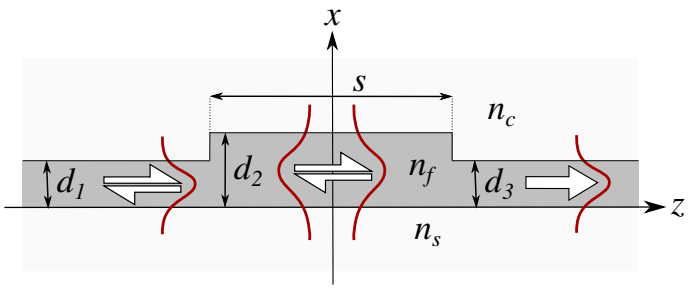

Figure 7.13: Cross section of a slab waveguide lens consisting of two interfaces at a distance s. Parameters are the thicknesses d_1, d_2 and d_3 and the refractive indices n_f in the core and n_c and n_s in the cladding regions.

For a configuration with two interfaces, the method needs to be modified according to Section 7.3. Now, potential TE and TM modes are propagating between the interfaces. Hence, the 2.5-D COMSOL solutions need to be calculated for both, TE and TM excitation. To simulate the two interfaces, we calculate the 2-D fields for each interface separately and then combine them to generate the full field.

Calculating the solution by directly including both interfaces requires a significantly larger number of 2-D fields. In addition to the angle of incidence φ, the distance s between the interfaces has to be varied depending on the position y. So we preferred calculating the interfaces separately. The disadvantage is that for small distances s between the two interfaces, radiating or evanescent waves resulting from one interface do not lead to further reflections or transmissions on the other interface. Only guided modes are assumed to propagate between the interfaces and generate the diffracted fields from each surface. We observe that for the configurations considered in this work, the approximation appears to be adequate.

A sketch of the side view is illustrated in Figure 7.13, the top view is identical to Figure 7.6. We assume a symmetric structure, i.e., incoming and outgoing slabs have identical height and the same refractive indices. The waveguide thickness in the middle is higher than the surrounding

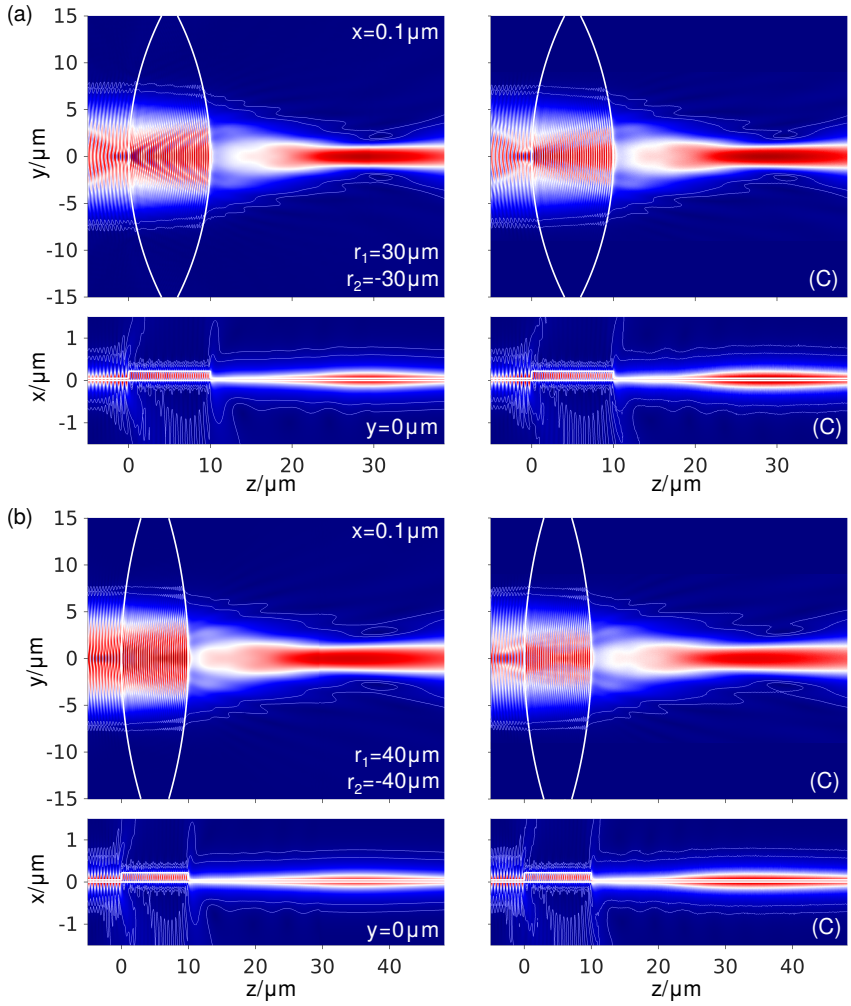

Figure 7.14: Top view (upper row) and side view (bottom row) of the absolute electric field $|E_y|$ for different curvature radii $r_1 = 30\,\mu$m, $r_2 = -30\,\mu$m (a) and $r_1 = 40\,\mu$m, $r_2 = -40\,\mu$m (b) and normal incidence $\varphi_0 = 0°$. The corresponding full vectorial 3-D COMSOL solution is shown on the right side (C). The contour lines mark the levels of the absolute field at 5% and 10% [75].

slabs but consists of the same refractive indices (of course, a configuration with etched middle part is also possible). The waveguide parameters are adopted from the single interface in Section 7.4.2, i.e., thicknesses $d_1 = d_3 = 0.05\,\mu$m, $d_2 = 0.22\,\mu$m and material parameters $n_f = 3.45$ and $n_c = n_s = 1.45$. The incoming wave is the fundamental TE mode of an adjoining rib waveguide of width $W = 15\,\mu$m, height $d = 0.05\,\mu$m and etch depth $d' = 0.02\,\mu$m (cf. Section 2.4). The constituting 2.5-D COMSOL solutions are again calculated in the area $z \in [-5, 20]\,\mu$m and extended with the method introduced in Section 7.4.1. To validate our results, the solutions are compared to full 3-D FEM solutions.

Figures 7.14–7.15 show the absolute electric field $|E_y|$ for different incidence angles and radii. Again the top (upper row) and side view (bottom row), along the direction of the outgoing

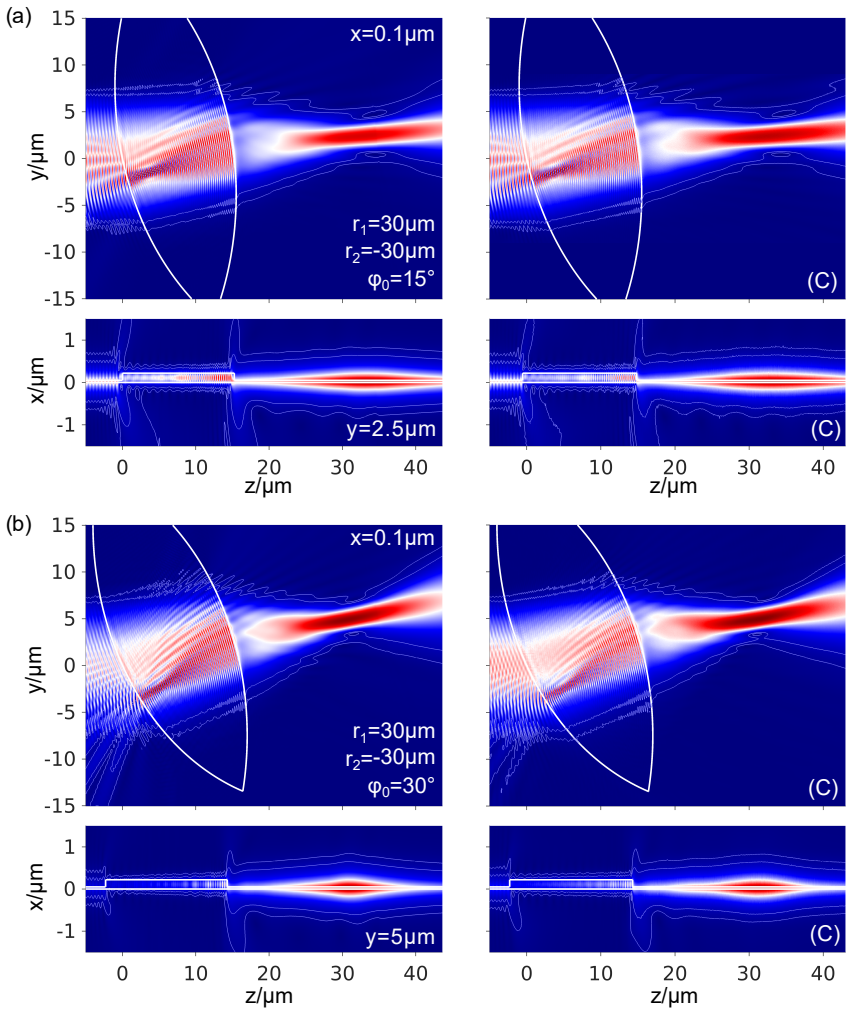

Figure 7.15: Top view (upper row) and side view (bottom row) of the absolute electric field $|E_y|$ for curvature radii $r_1 = 30\,\mu\text{m}, r_2 = -30\,\mu\text{m}$ and incidence angles $\varphi_0 = 15°$ (a), $\varphi_0 = 30°$ (b). The corresponding full vectorial 3-D COMSOL solution is shown on the right side (C). The contour lines mark the levels of the absolute field at 5% and 10% [75].

propagating beam, is shown. For clarity, the contour lines are only shown at the levels of 5% and 10% because the radiated fields produce a rather confusing field pattern. Note that for oblique incidence angles (Figure 7.15), it was easier to move the interfaces than to rotate the incident rib port in COMSOL. This shows the flexibility of the 3-D SASM.

The results fit well to the corresponding 3-D FEM solution despite the partially converged mesh of the COMSOL simulation and the piecewise linear approximations of the interfaces in the SASM. As can be clearly seen from the side views of the plots, losses can not be neglected for these high refractive index contrast waveguide lenses.

7.5 Optimization

The manipulation of light is one of the main challenges in integrated optics to achieve efficient on-chip integration in planar circuits [140]. Lenses are mostly used to project, focus and control the propagation of light from one point (the emitter) to another (the detector) within an optical system [131]. The optimal design of the lens must consider the beam width, side lobes, the efficiency and the imaging performance, which is restricted by the Rayleigh diffraction limit [48, 141–143]. Spherical aberrations and the lateral size of the focal spot can be customized by optimizing the curvature of the lens to meet special requirements for various applications [131, 144–146].

Rigorous numerical simulations of these waveguide lenses in full 3-D are rather expensive in terms of computational effort. Already the calculation of a single lens configuration, such as in Figures 7.14–7.15 (C), on a massively parallelized machine, takes about 20 h of computation time. This effort renders series of 3-D FEM simulations, as would be required for design optimization, practically impossible. Instead, we will apply the much faster and more memory economic SASM-technique. In the following, we show that standard optimization algorithms can be easily applied to 3-D waveguide lenses with two interfaces by using our SASM.

We make use of global optimizers, which are available in MATLAB's "Global Optimization Toolbox" [147]. Here, we choose the genetic (GA) and pattern search (PSA) algorithms because the integration of nonlinear constraints is directly possible and they provided the best results for our problem. After optimizing the structure with the global optimizer, a local optimizer is applied on the solution to yield a more accurate optimized result. We use a local "interior-point" solver [148–150], which is also directly implemented in MATLAB. While other solvers, not necessarily implemented in MATLAB, may fit better to the problem at hand and might be able to provide better and faster results, here, we just intend to show the applicability of our SASM approach for the purpose of design optimization.

7.5.1 Mathematical formulation

Optimization aims to find a maximum or minimum point $\mathbf{x}$ of an objective function f depending on certain constraints. This is mathematically expressed as

$$\min_{\mathbf{x}\in\mathbb{R}^n} f(\mathbf{x}) \qquad \text{subject to} \qquad \begin{array}{ll} c_j(\mathbf{x}) = 0, & j \in \mathcal{E} \\ c_j(\mathbf{x}) \geq 0, & j \in \mathcal{I}, \end{array} \tag{7.48}$$

where $\mathcal{E}$ and $\mathcal{I}$ are sets of indices for equality and inequality constraints, $\mathbf{x}$ is the vector of unknown variables, $f : \mathbb{R}^n \to \mathbb{R}$ with $n \geq 1$ is the objective or cost function and $c_j : \mathbb{R}^n \to \mathbb{R}$ are the constraint functions.

By defining a feasible set of points $\mathbf{x}$ that satisfy the constraints

$$\Omega = \{\mathbf{x} \mid c_j(\mathbf{x}) = 0, j \in \mathcal{E}, c_j(\mathbf{x}) \geq 0, j \in \mathcal{I}\}, \tag{7.49}$$

Eq. (7.48) can be written in a more compact form

$$\min_{\mathbf{x}\in\Omega} f(\mathbf{x}). \tag{7.50}$$

In some cases one is interested in the maximum of an objective function $f(\mathbf{x})$. For uniformity, this can be rewritten as an equivalent minimization problem

$$\min_{\mathbf{x}\in\Omega} \tilde{f}(\mathbf{x}), \tag{7.51}$$

with $\tilde{f}(\mathbf{x}) = -f(\mathbf{x})$.

A distinction is made between "constrained" and "unconstrained" optimization problems. An unconstrained optimization problem has no constraints, i.e., $\mathcal{E} = \mathcal{I} = \emptyset$, while the sets are not empty for constrained optimization problems. In this work, we will deal with constrained optimization problems, which are further divided in "linear" and "nonlinear" constraints. In the first case, the considered constraints and the objective function are linear and, in the second case, at least one of the constraint functions or the objective function has a nonlinear dependence on $\mathbf{x}$.

Many algorithms are created to seek local solutions for nonlinear optimization problem, meaning a point $\mathbf{x}$ at which the objective function is small compared to all other feasible points nearby. Finding the global solution, which is the point with the lowest objective function value of all feasible points, is mostly very difficult, especially for unconstrained optimization. In some cases, an improvement can be achieved by defining constraints that limit the region of feasible points.

7.5.2 Genetic algorithm

Generic algorithms are adaptive algorithms to find a global solution of an optimization problem. They are derivative-free, robust and applicable for many problems. The approach is based on the evolution process and natural selection ("survival of the fittest") [151–153].

Initially, a random population – generation – consisting of a certain amount of points – individuals – is created that covers the whole search space. The next generation is created by combining and adapting the fittest individuals of the old generation via selection, crossover and mutation. The new generation is then tested, whether they have an improved objective function value. This process is repeated until the population converged. In the following, the three operations are briefly described.

1. Selection:
   The best individuals – parents – of the current generation, i.e., those with the best objective function value, are directly copied/selected for the new generation. The better the objective function value, the higher the probability of contributing to the solution. These points are then selected for crossover and mutation to produce the individuals – children – for the new population.

2. Crossover:
   The selected parents from the previous step are mated to produce the children of the new generation. In this process, the crossing points correspond to the mated parents and are generated in different ways [152].

3. Mutation:
   Finally, some of the offspring are mutated by replacing their positions with random num-

bers from the search space, creating new "genetic" material. Mutation is done to maintain diversity within the population and to prevent premature defective convergence.

We can summarize the procedure of the algorithm with the following four steps:

1. Initialization of the population.
2. Evaluate objective function values.
3. Create a next generation via selection, crossover and mutation.
4. Go back to step 2 until convergence.

7.5.3 Pattern-search algorithm

Pattern-search is a derivative free optimization algorithm to find global solutions of a smooth objective function. Starting from the current point $x \in \Omega$, the method searches in a certain set of directions $\mathcal{D}$ for a point $x + \gamma p$, with $p \in \mathcal{D}$, with a lower objective function value $f(x + \gamma p) < f(x)$. In each direction, the objective function is evaluated at a specific step length γ. Thus, the points $x + \gamma p$ form a "stencil" around the current best point x. If an improvement is found, the corresponding point is identified as the new best point and the search process is repeated. If no point with lower function value is found, either the search lengths γ along the current search directions are increased or even new search directions are generated. However, the search directions or lengths are anyways updated (they shrink or grow depending on the system properties) after each step even if an improvement was achieved or not [138].

A sketch of the implementation is given by the following:

1. Initialization of a point x with step length γ and directions $p \in \mathcal{D}$.
2. Calculate the objective function values $f(x)$.
3. If the updated position exhibits a lower objective function value $f(x + \gamma p) < f(x)$ for some $p \in \mathcal{D}$, update $x \leftarrow x + \gamma p$ and increase γ.
   Otherwise, x is not shifted, but γ is decreased.
4. Go back to step 2 until convergence.

Pattern-search can further be used on a set of j points x_j with search directions $p_j \in \mathcal{D}_j$ and search length γ_j to search iteratively for optimized solutions [154–156].

7.5.4 Optimized 3-D slab waveguide lens

An appropriate objective function for optimization depends always on the application purpose. Here, we present one of many ways to optimize the planar slab waveguide lens. A conceivable goal is to maximize the transmittance or to minimize the spot size of the outgoing beam, e.g., for a better spatial resolution when it comes to image processing [30].

To combine both, we consider the maximum of the absolute field amplitude a_t of the transmitted field $\mathbf{\Psi}_\mathrm{t}$ (cf. Eq. (7.42)) at position (x_0, y, z_opt) normalized to the maximum amplitude a_in of the incoming wave $\mathbf{\Psi}_\mathrm{in}$ (cf. Eq. (7.11)) at position (x_0, y, z_0) as our figure of merit. Theoretically, the higher the output amplitude, the larger the transmission and the smaller the size of the focal point due to energy conservation. Due to the flexibility of the SASM, we assume a

primary incidence angle $\varphi_0 = 0°$, since the oblique incidence can always be realized by adjustments of the shapes $g_1(y)$ and $g_2(y)$, i.e., by rotating the lens boundaries accordingly. Thus, the maximum field amplitude of the incoming field $\mathbf{\Psi}_{\mathrm{in}}$ is given at position $(x_0, 0, z_0)$.

For simplicity, we interpolate the two interfaces using splines [23] to have as few unknowns as possible. Therefore, we define a specific number $\mathcal{P}$ of equally distributed basis points $\tilde{y}_j, j \in [1, \mathcal{P}]$, compactly written as the vector $\tilde{\mathbf{y}}$, along the y-direction of the computational domain and interpolate them using a cubic spline to receive $g_1(y)$ and $g_2(y)$. The variables for optimization are then given by $\tilde{z}_j^{(1)} = g_1(\tilde{y}_j)$ and $\tilde{z}_j^{(2)} = g_2(\tilde{y}_j)$, which we combine to $\tilde{\mathbf{z}} = (\tilde{\mathbf{z}}^{(1)}, \tilde{\mathbf{z}}^{(2)})^T$ with elements $\tilde{z}_j^{(k)}, k = 1, 2$. Here, we assume $\mathcal{P} = 9$ and a size of the computational domain in the y-direction limited to $y \in [-20, 20]\,\mu$m. As we consider the lens with two interfaces, optimization is carried out with 18 variables.

The transmitted field is sampled only along the y-direction at specific positions $z = z_{\mathrm{opt}}$, which is the position of the focal point in propagation direction that is to be optimized and $x_0 = 0.025\,\mu$m, which is a point in the core region of the outgoing slab. Hence, the field has to be evaluated explicitly only on a single line, which decreases the computation time of the SASM drastically.

Then, assuming $a_{\mathrm{in}} = |\mathbf{\Psi}_{\mathrm{in}}(x_0, 0, z_0)| = 1$ results in an objective function

$$\max_{\tilde{\mathbf{z}}} \Big(\max_{y} |\mathbf{\Psi}_{\mathrm{t}}(x_0, y, z_{\mathrm{opt}})| \Big). \tag{7.52}$$

We restrict our optimization only to a single component $\Psi = E_y$ in order to keep the required simulation time to a minimum, even if the amplitude of $|\mathbf{E}|$ would be more appropriate since it covers the full vectorial properties of the wave.

Further simplifications are implemented to make the SASM faster without changing the major field behavior: only the initial transition from the first to the second interface, thus setting $\nu = 1$ in Eq. (7.34), is considered, as the iterations between the two boundaries require most of the calculation time. Additionally, we reduce the number of elements to $\mathcal{N} = \mathcal{M} = 25$ (before, $\mathcal{N} = \mathcal{M} = 50$) for each interface. Applying these simplifications and evaluating the field only along the line $(x_0, y, z_{\mathrm{opt}})$, results in a computation time of 2 s per lens configuration (before around 10 minutes to calculate the 2-D cross sections in Section 7.4).

However, for the subsequent refinement steps, a local optimizer is applied. Unlike the global optimizer, the local one is applied to the full SASM without simplifications. Thus, the original settings from Section 7.4 are valid again, with $\mathcal{N} = \mathcal{M} = 50$ SASM elements and about 6-10 iterations. Then, the calculation time for a single lens configuration requires about 60 s.

We excite the structure with the quasi-TE_0 mode of a rib waveguide of width $W = 15\,\mu$m, height $d = 0.05\,\mu$m and etch depth $d' = 0.02\,\mu$m positioned at $z_0 = -10\,\mu$m in front of the structure. Refractive indices for the target wavelength $\lambda_0 = 1.55\,\mu$m and waveguide thicknesses for the lens configuration can be adopted from Section 7.4.3.

In addition to the just mentioned simplifications, some limitations on the boundaries are necessary to achieve reliable and physically correct optimization results. Thus, the following (nonlinear) constraints must be applied:

1. The interfaces are not allowed to cross each other and should be separated at least by a distance of the vacuum wavelength λ_0 to ensure that evanescent waves from one interface do not touch the other

$$g_1(y_n) < g_2(y_n) + \lambda_0, \quad n \in [1, \mathcal{N}]. \tag{7.53}$$

   The assumption that the condition only applies to the basis points $\tilde{y}_j, j \in [1, \mathcal{P}]$ is not sufficient, as the curves could still have intersections due to the spline interpolation.

2. We assume an upper and lower boundary for the interfaces given by the position of the incoming wave $l_b = z_0$ and the optimized point $u_b = z_{\mathrm{opt}}$

$$l_b < g_j(y_n) < u_b, \quad n \in [1, \mathcal{N}], \quad j \in \{1, 2\}. \tag{7.54}$$

3. To avoid multiple reflections, strong kinks in the interfaces are not allowed. Hence, we restrict the change in the angle of two adjoining elements by α_0

$$|\alpha_{j,n} - \alpha_{j,n+1}| < \alpha_0, \quad n \in [1, \mathcal{N} - 1], \quad j \in \{1, 2\}, \tag{7.55}$$

   where the individual angles are $\alpha_{j,n} = \tan^{-1}(\mathrm{d}g_j(y_n)))$.

7.5.4.1 Optimized focal point

In the first step, we only optimized the transmittance T. The result comprises a structure consisting of two parallel, (almost) straight boundaries rotated by an angle of approximately $59°$ with nearly full transmission. However, the outgoing beam is not focused and exhibits almost an identical width as the incoming beam. The shape becomes evident when re-considering Section 2.3 as losses are fully suppressed for incidence angles larger than φ_c. This applies for structures that are homogeneous in one outstanding direction, which is satisfied by the parallel straight boundaries. For the first interface, the angle needs to be larger than $\varphi_{c,1}(\mathrm{TE}) = 57.23°$ (for TE input), and for the second interface larger than $\varphi_{c,2}(\mathrm{TE}) = 30.91°$ (for TE input) or $\varphi_{c,2}(\mathrm{TM}) = 45.31°$ (for TM input) to suppress radiation losses. Apart from that, the parallel surfaces lead to a Fabry-Pérot effect to achieve high transmittance. Thus, such a structure is able to achieve full power transmission. Apparently, the optimizers are able to find the configurations (only slight curvatures in the boundaries due to the spline approximation lead to little reflections).

For the optimization of the outgoing amplitude, we start the two solvers with a population of 50 elements and an initial element matrix of points that represent rotated circular curvatures of arbitrary but suitable radii and incidence angles. GA converges after around 100, and PSA after around 250 iterations. Additionally, the local solver converged at around 90 iterations for both cases. The number of iterations depend strongly on the choice of the initial values. The optimizers stop when the predicted change in the objective function is less than a predefined function tolerance of 10^{-6}.

Note that our results do not necessarily represent a global optimum because the initial points strongly influence the behavior of the optimizer and its solution. We are aware that there could be better optimization tools and algorithms for this problem, e.g., a multi-objective optimizer can be used to optimize the amplitude and transmittance simultaneously. In the context of this

work, we only want to demonstrate the applicability of optimization algorithms to our SASM and highlight the versatility of the approach.

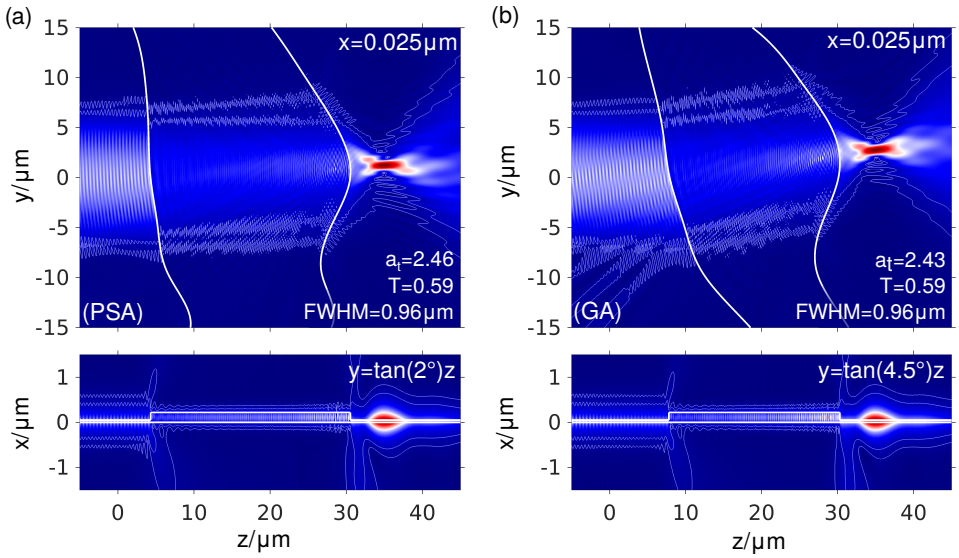

Figure 7.16: Top view (upper panel) an side view (lower panel) of the absolute electric field $|E_y|$ for the optimized lens structures using PSA (a) and GA (b). The respective transmitted amplitude a_t, the transmittance T and the full width at half maximum FWHM are indicated for both results.

Figure 7.16 shows the top (upper panel) and side (lower panel) view of the optimized lens when maximizing the amplitude a_t at a rather arbitrary position $z_\mathrm{opt} = 35\,\mu$m using pattern search (a) and genetic (b) algorithms. We fixed the adjustable parameters $l_b = -10\,\mu$m, $u_b = z_\mathrm{opt} = 35\,\mu$m (Eq. (7.54)) and $\alpha_0 = 45°$ (Eq. (7.55)). Shown is the E_y-component at fixed positions $x = 0.025\,\mu$m (top view) and along a path in the propagation direction of the outgoing beam (side view). The maximum outgoing amplitude a_t, the transmittance T and the beam size along the y-direction at full width half maximum (FWHM) are displayed for both results. In contrast to the optimization itself, where we only considered the outgoing E_y component, the displayed transmittance is calculated fully vectorial when post-processing the solution. Even though it is not shown in the field plots, the computational range in y-direction was chosen from $-20\,\mu$m to $20\,\mu$m, so that there is enough space to realize oblique outgoing beams.

To have a comparison, the lens configurations of the previous section (see Figures 7.14–7.15) exhibit outgoing amplitudes a_t that are in the range between 1.44 to 1.76 that belong to transmittance values from 55% to 58%. Note that when comparing the figures, the position in x-direction is now fixed to $x_0 = 0.025\,\mu$m (before $x_0 = 0.1\,\mu$m).

We observe that the transmittance did not increase compared to the circular lens configurations from Figures 7.14–7.15. However, we did not optimize the transmittance precisely. Instead, we optimized the amplitude of the outgoing wave in the focus plane, which has improved by a factor of around 1.4. We observe almost identical results for both optimizers. The interfaces differ mainly at the borders, but this has only a minor influence on the field behavior. Both solvers

give results that do not exhibit a large propagation angle relative to the rotation of the interfaces. Thus, losses are present and best visible in the side views of the plots. This can be explained, as we only considered the E_y component and did not optimize the transmittance directly. Probably, higher angles would widen the focal point resulting in a smaller amplitude. Thus, to achieve a result with lesser losses but still a focused outgoing beam with high amplitude, different optimizers or cost functions need to be used. The objective function could directly include the FWHM and the transmittance. Additionally, a multi-objective optimizer would be adequate for the purpose of simultaneously optimizing different objective functions.

Chapter 8

Modal matching method for 3-D simulations of waveguide tapers

The detection of single photons is one among the challenges faced in quantum optics [52]. One of the approaches in a framework of integrated optics is the integration of superconducting nanowire single-photon detectors (SNSPD) made of amorphous tungsten silicide on top of titanium in-diffused lithium niobate (Ti:LN) waveguides [53, 54, 157, 158]. The waveguides are fabricated by in-diffusing a titanium layer with a certain width and height on the surface of the lithium niobate (LN) crystals. SNSPDs are a standard tool for quantum photon detection [159, 160] due to their high efficiency [161] and low noise [162]. As long as no photon is absorbed, the detectors are superconducting below their critical temperature and no resistance is measured. After a photon is absorbed, the nanowires are heated up and the detector is no longer superconducting as the temperature reached the critical value. This leads to a short resistance and measurable voltage drop that can be detected with external connections to the nanowires [163].

However, a challenging task is the coupling efficiency, which is determined by the overlap between the guided mode of the Ti:LN waveguide and the position of the nanowires. The guided modes of the waveguide are mostly distributed in the LN substrate and therefore the overlap with the nanowires is small. A possible way to increase the detection rate is by applying an additional tapered silicon layer on top of the Ti:LN waveguide [53, 55]. Silicon has a higher refractive index than LN. Hence, the additional layer can be expected to pull up and to centralize the optical field closer to the nanowires.

In this chapter, we consider these Ti:LN waveguides with additional tapered silicon layer from a viewpoint of strictly classical guided-wave optics. Tapers are used to change the size or the shape of a mode to achieve a high coupling between waveguides of different cross sections [60–67]. In order to achieve a low-loss taper, one usually considers linear tapers [64] and makes them long enough so that the fundamental or first-order mode propagates through the waveguide without coupling to higher order or radiation modes [65]. However, non-linear tapers have also been introduced, which can be much shorter due to stretched regions of larger coupling strength [66, 67]. A variety of applications based on tapered waveguides have been presented, e.g., fiber-to-chip couplers [60, 164, 165], mode size converter [166], polarization-insensitive

couplers [67], polarization splitter and rotating devices [64, 167].

We are searching for taper geometries that lead to a high field overlap with the nanowires. For the simulation, we use a customized modal matching method [62, 63, 68, 87, 166, 168–171], which has its origin in the late 1960s [168, 172, 173] and started with the consideration of mode matching at a simple waveguide junction. Here, we introduce a stepwise modal matching technique to simulate the wave propagation in multiscale 3-D tapers by dividing the taper in a finite number of segments with constant cross sections.

Other simulation techniques are applicable as well, e.g., the beam propagation method [8]. Advantages of the mode matching method are that it can be easily used in combination with COMSOL Multiphysics to precisely discretize waveguides with cross sections of different scaling, and that optimization is much faster due to pre-calculation of the individual coupling coefficients for each transition step between the segments.

We start by introducing the birefringent LN material in Section 8.1. Then, to simulate the field behavior in the tapered part, we derive the theory of our finite element modal matching method (FEMMM) in Section 8.2. Examples for different taper geometries are shown in Section 8.3. Finally, we optimize the taper using a particle swarm algorithm implemented in MATLAB [174] and the results are presented in Section 8.4.

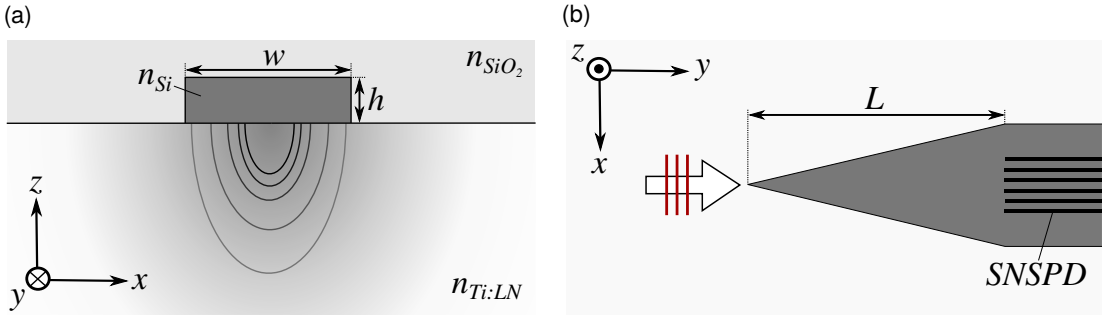

Figure 8.1: (a) Cross section of the Ti:LN waveguide with silicon layer of width w and height h on top covered by a SiO_2 layer. (b) Top view of the tapered silicon layer of length L. Additionally, the SNSPDs are illustrated beyond the tapered part.

A sketch of the structure under investigation is shown in Figure 8.1 with a cross section view (a) and a top view (b). The Ti:LN waveguide with refractive index profile $n_{\mathrm{Ti:LN}}$ is covered by a silicon layer of width $w = 3.0\,\mu$m, height $h = 60\,$nm and refractive index $n_{Si} = 3.48$. The silicon taper (here, for simplicity of linear shape) is of length L. The SNSPDs are sandwiched between the Ti:LN waveguide and the silicon top layer, starting after the taper section. The whole structure is covered with silicon dioxide which has a refractive index $n_{\mathrm{SiO_2}} = 1.36675$. We chose the values according to [53] for a vacuum wavelength $\lambda_0 = 1.55\,\mu$m. The structure is excited with the fundamental TE mode of the Ti:LN waveguide that is propagating in positive y-direction. In this chapter, we changed the coordinate system so that it fits to the crystalline Z-cut configuration of Ti:LN waveguides under study [175].

8.1 Refractive index profile

Lithium niobate is an anisotropic material with a trigonal crystal structure and characterized by a large electro-optic coefficient and large nonlinear second-order susceptibility [50]. Referring to the coordinate system for the present Z-cut Ti:LN waveguides, as introduced in Figure 8.1, the material is birefringent with the permittivity tensor

$$\varepsilon_r(x,z) = \begin{pmatrix} n_o^2 & 0 & 0 \\ 0 & n_o^2 & 0 \\ 0 & 0 & n_e^2 \end{pmatrix}, \tag{8.1}$$

where $n_o = 2.2112$ is the ordinary and $n_e = 2.1381$ is the extraordinary refractive index at the target wavelength $\lambda_0 = 1.55\,\mu$m.

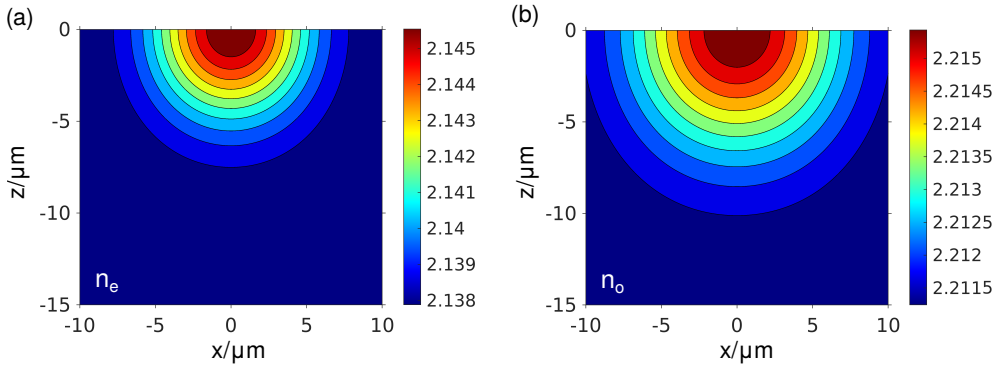

Figure 8.2: Extraordinary $n_e(x,z)$ (a) and ordinary $n_o(x,z)$ (b) refractive index profile of the Ti:LN waveguide.

After titanium in-diffusion, the refractive index profile becomes space-dependent and can be described by analytical functions [176]. Assuming that y is the propagation direction and x and z are the transverse coordinates, the refractive index profile is then given by

$$\varepsilon_r(x,y) = \begin{pmatrix} n_o^2(x,z) & 0 & 0 \\ 0 & n_o^2(x,z) & 0 \\ 0 & 0 & n_e^2(x,z) \end{pmatrix} \tag{8.2}$$

with the functions

$$\begin{aligned} n_e(x,z) &= n_e^{(0)} + d_e E c(x,z), \\ n_o(x,z) &= n_o^{(0)} + d_o (F c(x,z))^{\gamma}, \end{aligned} \tag{8.3}$$

the refractive indices for the bulk LN $n_e^{(0)} = 2.1381$ and $n_o^{(0)} = 2.2112$, the diffusion constants $D_x = 4.105$, $D_z = 4.85$, the profile constant $c = 1.0553 \times 10^{21}$ and the remaining constants $d_e = 0.8621$, $E = 1.2 \times 10^{-23}$, $d_o = 0.7083$, $F = 1.3 \times 10^{-25}$ and $\gamma = 0.55$ [176]. The concentration c is defined as

$$c(x,z) = c g(x) f(z), \tag{8.4}$$

where

$$g(x) = \frac{1}{2}\mathrm{erf}\left(\left(\frac{W}{2D_x}\right)\left(1+\frac{2x}{W}\right)\right) + \frac{1}{2}\mathrm{erf}\left(\left(\frac{W}{2D_x}\right)\left(1-\frac{2x}{W}\right)\right) \tag{8.5}$$

$$f(z) = \exp\left(-\frac{z^2}{D_z^2}\right) \tag{8.6}$$

with the titanium stripe width $W = 7\,\mu$m and the error function erf. The resulting refractive index profiles $n_e(x,z)$ and $n_o(x,z)$ are shown in Figure 8.2. The titanium in-diffusion results in a higher refractive index on the surface that is gradually decaying in the substrate. For more details on LN and the diffusion process, we refer the reader to [177].

8.2 Finite element modal matching method

In place of a prohibitively expensive rigorous full 3-D simulation of the taper problem, a fast and efficient modal matching method (MMM) can be used [63, 68, 77, 87, 166, 168–171]. The smooth taper is divided in $\mathcal{N}$ piecewise elements with constant cross sections using a staircase approximation, as illustrated in Figure 8.3 (a). The vectorial eigenmodes of each constant 2-D cross section then propagate along the waveguide segments. The theory behind this hybrid numerical/analytical mode matching method to simulate 3-D multiscale tapered waveguides is exemplary displayed for a single transition between two waveguide segments (see Figure 8.3 (b)). Analogously, this procedure can be applied to the entire structure to simulate the full 3-D taper.

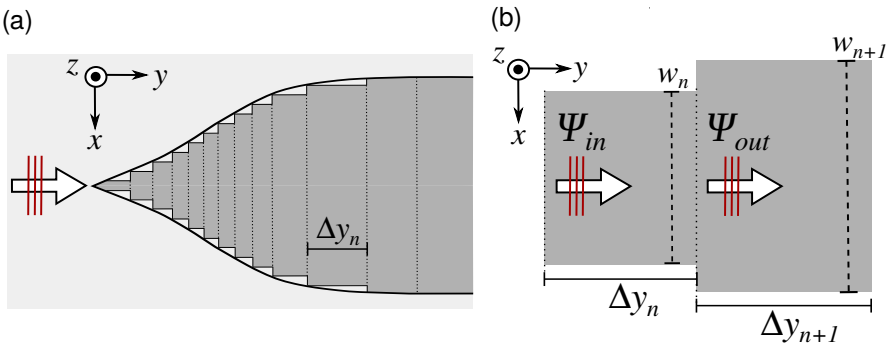

Figure 8.3: (a) Stepwise approximation of a full taper in $\mathcal{N}$ cascaded elements with constant cross sections and lengths $\Delta y_n, n \in [1, \mathcal{N}]$. (b) Transition between two waveguides of different widths w_n and w_{n+1} and lengths Δy_n and Δy_{n+1}, respectively.

A single transition consists of two waveguides with different cross sections, as shown in Figure 8.3 (b), i.e., for the configuration under study, two silicon layers of width w_n and w_{n+1} (but constant height h) are considered. Before deriving the method, we make two assumptions: only slightly varying neighboring cross sections are considered, i.e., $w_{n+1} = w_n + \Delta w$ with constant Δw, such that reflections at the transition between the two waveguides can be neglected. Thus, we assume only unidirectional propagation. Furthermore, the transfer of power to subsequent segments through non-guided modes is excluded.

The incoming waveguide of width w_n guides a set of modes with profiles $\mathbf{\Psi}_{\mathrm{in},p}(x,z)$ and propagation constant $k_{y,p}$. The overall incoming field is given by a superposition of all the incoming

modes with amplitudes a_p propagating in positive y-direction

$$\mathbf{\Psi}_{\mathrm{in}}(x,y,z) = \sum_p a_p \mathbf{\Psi}_{\mathrm{in},p}(x,z)\mathrm{e}^{-\mathrm{i}k_{y,p}y}. \tag{8.7}$$

The outgoing waveguide of width w_{n+1} supports a set of modes with mode profiles $\mathbf{\Psi}_{\mathrm{out},q}(x,z)$ and unknown amplitude a'_q. At the transition, after the incoming field propagates the distance Δy_n, the incoming and outgoing fields have to match[1]

$$\mathbf{\Psi}_{\mathrm{in}}(x,\Delta y_n,z) = \sum_p a_p \mathbf{\Psi}_{\mathrm{in},p}(x,z)\mathrm{e}^{-\mathrm{i}k_{y,p}\Delta y_n} = \sum_q a'_q \mathbf{\Psi}_{\mathrm{out},q}(x,z). \tag{8.8}$$

Projections on each of the outgoing modes, using the mode product $(\mathbf{\Psi}_{\mathrm{out},l},\cdot)_{x,z}$ from Eq. (2.43) for the l-th outgoing mode (with the roles of the coordinates adapted), and assuming normalized and orthogonal modes, i.e., $(\mathbf{\Psi}_{\mathrm{out},l},\mathbf{\Psi}_{\mathrm{out},q})_{x,z} = \delta_{lq}$ results in

$$\sum_p a_p(\mathbf{\Psi}_{\mathrm{out},l},\mathbf{\Psi}_{\mathrm{in},p})_{x,z}\mathrm{e}^{-\mathrm{i}k_{y,p}\Delta y_n} = \sum_q a'_q(\mathbf{\Psi}_{\mathrm{out},l},\mathbf{\Psi}_{\mathrm{out},q})_{x,z} = a'_l. \tag{8.9}$$

Thus,

$$a'_q = (\mathbf{\Psi}_{\mathrm{out},q},\mathbf{\Psi}_{\mathrm{in}})_{x,z}. \tag{8.10}$$

Assuming two incoming (with amplitudes a_1, a_2) and outgoing modes (with amplitudes a'_1, a'_2) results in

$$\begin{aligned} a'_1 &= a_1 c_{11}\mathrm{e}^{-\mathrm{i}k_{y,1}\Delta y_n} + a_2 c_{12}\mathrm{e}^{-\mathrm{i}k_{y,2}\Delta y_n} \\ a'_2 &= a_1 c_{21}\mathrm{e}^{-\mathrm{i}k_{y,1}\Delta y_n} + a_2 c_{22}\mathrm{e}^{-\mathrm{i}k_{y,2}\Delta y_n} \end{aligned} \tag{8.11}$$

with the coupling coefficients c_{qp} that represent the coupling efficiency from mode p to mode q

$$c_{qp} = (\mathbf{\Psi}_{\mathrm{out},q},\mathbf{\Psi}_{\mathrm{in},p})_{x,z}, \quad p,q \in \{1,2\}. \tag{8.12}$$

By applying this procedure to each element of the approximated taper leads to the field behavior of the complete 3-D tapered structure. The outgoing transmittance is directly given by the amplitude coefficients

$$T = \sum_q |a'_q|^2. \tag{8.13}$$

The length and shape of the taper can be controlled by the choice of varying segment lengths $\Delta y_n, n \in [1,\mathcal{N}]$ for each individual element, while the width is constantly widening by Δw with each segment, as shown in Figure 8.3 (a).

The vectorial 2-D mode profiles $\mathbf{\Psi}$ are calculated using the finite element software COMSOL Multiphysics [22] to discretize the different scales of the small Si-layer ($3\,\mu\mathrm{m} \times 0.06\,\mu\mathrm{m}$) and the large LN substrate ($20\,\mu\mathrm{m} \times 15\,\mu\mathrm{m}$) precisely. Thus, we call this ansatz the finite element modal matching method (FEMMM) [77]. By pre-calculating the power overlap products (8.12) once for each combination of cross-sections, different taper geometries can be simulated within milliseconds. Thus, this enables highly efficient optimization procedures.

[1] This holds strictly only for the transverse components; see footnote 1 on page 24 for a detailed explanation.

8.3 Tapered silicon layer on Ti:LN waveguides

At first, we have a look at the guided mode profiles of the Ti:LN waveguide itself (without additional silicon layer). The structure guides fundamental TE and TM modes with slightly different effective refractive indices $N_{\mathrm{TE}_0} = 2.2127$ and $N_{\mathrm{TM}_0} = 2.1398$. Power normalized field plots of the absolute electric field $|\mathbf{E}|$ are illustrated in Figure 8.4. The modes have their maximum field amplitude some micrometers below the waveguide surface, therefore the overlap with the nanowires is really small. Thus, the absorption is low and only a few photons are detected.

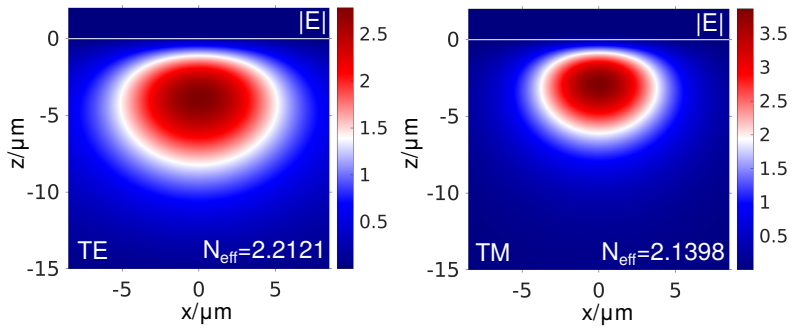

Figure 8.4: Absolute electric field value $|\mathbf{E}|$ (in V/μm) of the TE and TM mode profiles of the Ti:LN waveguide. The fields are power normalized to unit power.

Therefore, a silicon ridge waveguide of width $w = 3.0\,\mu$m with a higher refractive index than the LN waveguide, is placed on top of the structure to pull the mode up. The composite configuration guides a TM mode and two TE modes. We assume excitation of the structure with the fundamental TE mode of the Ti:LN waveguide. Thus, excitation of TM modes can be neglected due to the different polarization character and we only concentrate on the guided TE modes of the composited structure in the following. The two relevant TE mode profiles are illustrated in Figure 8.5 (a, b). Note that we are not looking at the tapered structure yet, but at the silicon layer of full width $w = 3.0\,\mu$m. Again, the normalized absolute field value $|\mathbf{E}|$ is shown. Figure 8.5 (a) shows the silicon mode that is mainly concentrated in the silicon layer and is indicated as Si-mode. Additionally, Figure 8.5 (b) shows the guided "supermode", indicated as Si:LN-mode, with field amplitudes in both, the silicon and LN layers. The Si-mode has a higher effective refractive index than the Si:LN-mode. Thus, it represents, in a sense, the fundamental mode of the waveguide composition.

As for the specific shape of the taper, as a first trial, one could assume a constant silicon width $w = 3.0\,\mu$m over the full length L. Then, the incoming guided TE_0 mode of the Ti:LN waveguide reaches the composite structure of full width. Due to this abrupt transition, only little power is transmitted to the Si-mode, which is about 20% (75% is transmitted to the Si:LN-mode and about 5% is lost to radiation). Thus, it is potentially advantageous to taper the silicon layer to achieve a smooth transition between Ti:LN waveguide and the composed configuration with additional silicon layer. Thereby, the mode power is slowly pulled up to the fundamental Si-mode so that the field intensity is mainly concentrated in the silicon layer and the overlap with the nanowires is larger. Hence, one expects a better efficiency of the envisioned detectors.

The power transmitted to each mode depends strongly on the length and shape of the taper. To get an overview of the guided modes in the taper depending on the width w, Figure 8.5 (c)

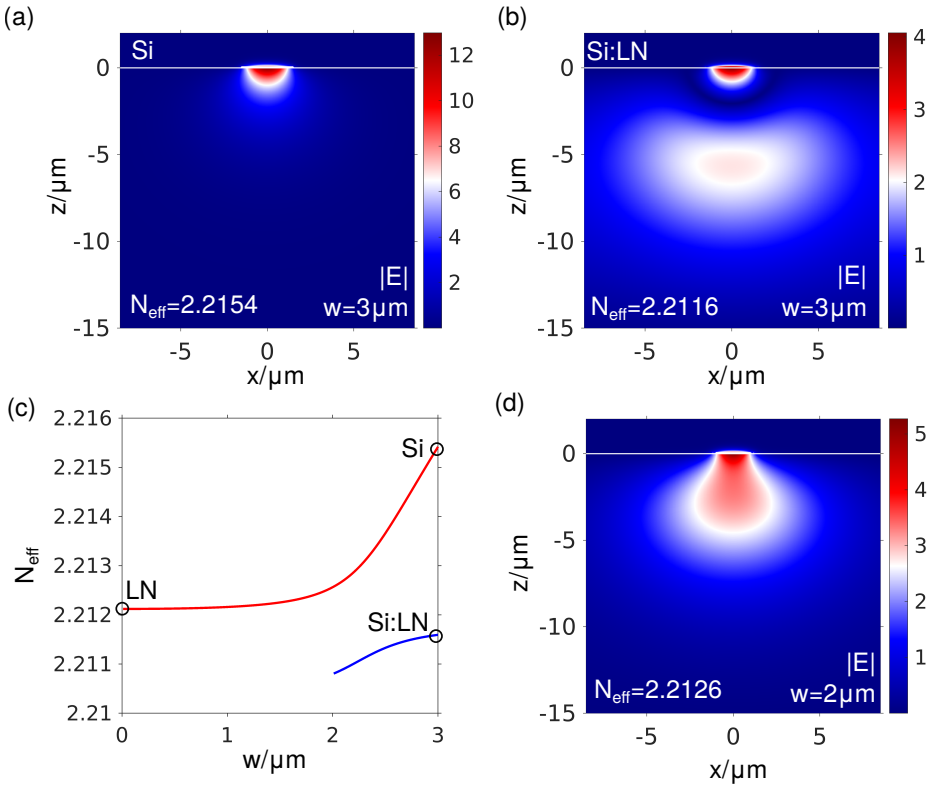

Figure 8.5: Relevant mode profiles $|\mathbf{E}|$ (in V/ μm) of the Si-mode (a) and Si:LN-mode (b) at full silicon width $w = 3.0\,\mu$m. (c) Effective refractive indices N_{eff} of the in-diffused waveguide with silicon layer on top versus the waveguide width w. (d) Mode profile $|\mathbf{E}|$ (in V/ μm) at an intermediate width $w = 2.0\,\mu$m.

shows the effective refractive indices of the two modes. It can be noted that the Si:LN-mode (blue curve) exists only beyond a certain width $w \approx 2.0\,\mu$m. For smaller widths, only one (relevant) mode is guided that belongs to the red curve. For $w = 0\,\mu$m the mode is equal to the incoming TE_0 mode of the Ti:LN waveguide in Figure 8.4. Looking at the field distribution for increasing width w, this mode becomes more and more localized in the silicon layer up to a mode that is fully guided in the silicon core – the Si-mode from Figure 8.5 (a). Thus, the mode that belongs to the red curve exhibits a transition from the TE_0 mode of the pure Ti:LN waveguide to the Si-mode of the composed structure.

For our studies, we search for a high transmission to the Si-mode to guarantee a large overlap with the position of the nanowires. But, the transition from the incoming Ti:LN mode to the Si-mode is disturbed by the presence of the Si:LN-mode, as seen in Figure 8.5 (c). To overcome this, the first idea is to choose a different final width of the silicon taper so that a second mode does not exist. So we end the taper at a width of $w = 2.0\,\mu$m. Then, the power needs to fully pass to that mode for sufficiently large taper lengths. But at a width of $w \approx 2.0\,\mu$m, the field is still strong in the region of the LN waveguide, as illustrated in Figure 8.5 (d), and is not yet fully localized in the silicon region. Thus, the width needs to be increased further, taking into account that coupling to the Si:LN-mode is possible.

We search for taper geometries and lengths that lead to full transmission to the Si-mode even in the presence of the Si:LN-mode. We denote the amplitude coefficients for the Si-mode as a_1 and that of the Si:LN-mode with a_2 in the following. Therefore, we make use of the unidirectional finite element modal matching method (cf. Section 8.2), dividing the taper in $\mathcal{N}$ elements with constant cross sections using a staircase approximation. The modes for each of the $\mathcal{N}$ cross sections are calculated using the FEM mode analysis in COMSOL Multiphysics [22].

8.3.1 Linear taper

We start with the analysis of a simple linear taper, as sketched in Figure 8.1 (b), meaning the distance in propagation direction Δy_n is equal for each of the $n \in [1, \mathcal{N}]$ elements. To check the convergence of our approach and the amount of required elements, we divide the taper in $\mathcal{N} \in \{10, 30, 60, 100, 150, 300\}$ elements, i.e., the width is increased by $\Delta w \in \{0.3, 0.1, 0.05, 0.03, 0.02, 0.01\}\,\mu$m. For sufficiently large taper lengths, the power should almost fully couple to the Si-mode and nearly nothing to the Si:LN-mode.

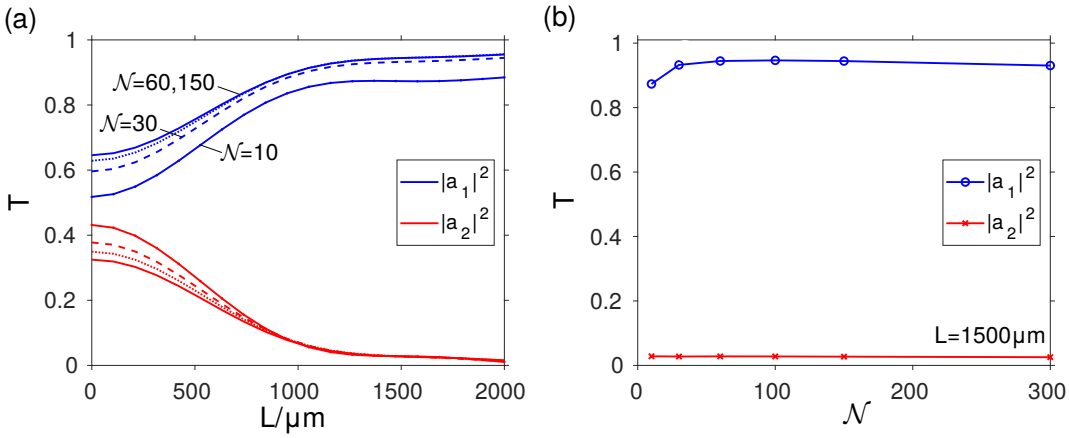

Figure 8.6: Transmittance values $|a_1|^2$ (Si-mode) and $|a_2|^2$ (Si:LN-mode) for a linear taper as a function of (a) the taper length L and for different number of elements $\mathcal{N}$ or (b) depending on the number of elements $\mathcal{N}$ for fixed length $L = 1500\,\mu$m.

Figure 8.6 shows the power transmitted to both modes for linear tapers of different lengths L and different number of elements $\mathcal{N}$. The outgoing power is pictured for different taper lengths L and different number of elements $\mathcal{N}$ in(a). As expected, for increasing taper lengths, the power is almost fully coupled to the Si-mode. However, a certain number of elements is required, otherwise the smooth taper is not precisely approximated and additional losses are predicted as numerical effects. We can state that taper lengths larger than $L = 1500\,\mu$m are necessary to achieve almost full power transmission to the Si-mode. Additionally, in Figure 8.6 (b) results for varying number of elements and fixed taper length $L = 1500\,\mu$m are presented. The power coupled to the Si-mode converges for increasing number of elements. Already for a quite low number of elements $\mathcal{N} = 60$, the results show sufficient accuracy. Note that for $\mathcal{N} = 300$, the power again decreases slightly because the higher the number of elements, the higher the involved inaccuracies. Therefore, we choose $\mathcal{N} = 150$, i.e., $\Delta w = 0.02\,\mu$m, for the following simulations.

8.3.2 Coupling efficient taper

To decrease the length of the taper, we now investigate more complex structures [67]. To that end, we consider the coupling efficiency of the two modes, which depends strongly on the waveguide width w_n of the approximated elements. Generally, strong coupling can be expected when the effective refractive indices are relatively close to each other. Then, the modes are almost degenerate and are able to interact with each other. Looking again at Figure 8.5 (a) shows that the effective indices are the closest in the area around $w = 2.3\,\mu$m.

Hence, we should create a structure that is long in the area of strong coupling and short in the area of low coupling. A sketch of this concept is shown in Figure 8.7. The taper is divided in three parts: the first part (tip) of length L_1 is quickly widening up to the width w_1, the longer middle part of length L' is slowly increasing up to a width of w_2, and the last part (tail) increases up to the full width $w = 3.0\,\mu$m over a length L_2. The complete taper has a full length of $L = L_1 + L' + L_2$. As the coupling is the strongest in the area around $w = 2.3\,\mu$m, we fix $w_1 = 2.2\,\mu$m and $w_2 = 2.5\,\mu$m. Furthermore, we assume small but arbitrary lengths of $L_1 = L_2 = 10\,\mu$m for the tip and the tail and vary only the length of the middle layer L'.

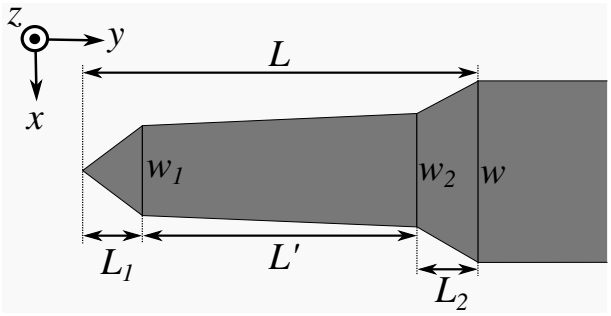

Figure 8.7: Adjusted taper structure with rapidly increasing tip (of length L_1) and tail (of length L_2). The slowly varying middle part is of length L' and starts from a width w_1 to a width w_2. The waveguide exhibits a total length $L = L_1 + L' + L_2$ with a final width of $w = 3.0\,\mu$m.

For such a tip-and-tail taper, the power $|a_1|^2$ transmitted to the Si-mode is shown in Figure 8.8 as a function of the overall length, i.e., for varying length L'. We see that 95.5% power transmission to the Si-mode is already achieved for a taper length of $L = 322\,\mu$m, which is much smaller compared to the linear taper (around $1000\,\mu$m is necessary). Furthermore, we observe an oscillating behavior for increasing length L, which is due to the interference of the two guided modes in the middle part.

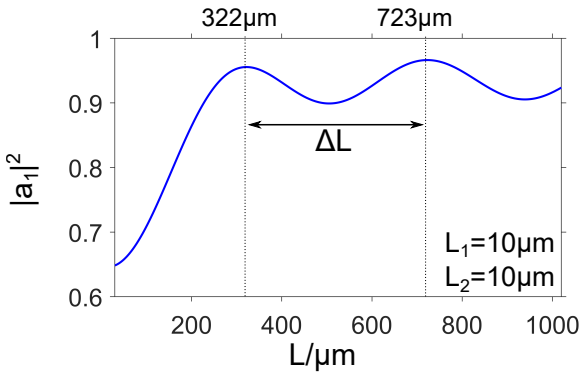

Figure 8.8: Transmission to the Si-mode $|a_1|^2$ versus the total taper length $L = L_1 + L' + L_2$ for varying middle part L' and fixed lengths $L_1 = L_2 = 10\,\mu$m.

The distance between two peaks is approximately given by

$$\Delta L \approx \frac{\lambda_0}{2|N_{\text{eff},1} - N_{\text{eff},2}|}. \tag{8.14}$$

For our case, assuming effective indices $N_{\text{eff},1} = 2.21309$ (Si-mode) and $N_{\text{eff},2} = 2.21112$ (Si:LN-mode) that belong to a width of $w = 2.3\,\mu$m, results in $\Delta L \approx 393\,\mu$m. Note that the width is not constant over the full length of the middle layer. Therefore, this value does not fit precisely, but as an estimation this result fits sufficiently well. Thus, with such a split taper structure, much higher transmissions can be achieved for smaller total taper lengths compared to the linear taper.

8.4 Optimization

In the last step, we want to increase the transmittance even further and also confirm the three-part taper shape. To that end, the structure is now optimized using particle swarm optimization (PSO) implemented in MATLAB [174]. This solver was chosen as it was the most efficient and fastest optimizer available in MATLAB's "Global Optimization Toolbox" [147] for the taper optimization. After applying PSO to our problem, we additionally ran a local "interior-point" solver [148], directly implemented in MATLAB, to obtain an even more accurate solution, starting from the relatively rough solution found by the PSO.

Again, the goal is to optimize an objective function (cf. Section 7.5.1). More precisely, we are searching for high transmittance values to the Si-mode for fixed taper length $L = L_f$. Therefore, we define our cost function or objective function, as

$$\min_{\mathbf{z}} f(\mathbf{z}) = \min_{\mathbf{z}} \left(\alpha|L_f - L(\mathbf{z})| - \beta|a_1(\mathbf{z})|^2\right), \tag{8.15}$$

where $\mathbf{z} = (\Delta z_1, ..., \Delta z_{\mathcal{N}})^T$ comprises all $\mathcal{N}$ element lengths $\Delta z_n, n \in [1, \mathcal{N}]$ of the individual cross sections and $a_1(\mathbf{z})$ identifies the transmission coefficient to the Si-mode. Thus, $|a_1(\mathbf{z})|^2$ represents the transmittance, and

$$L(\Delta\mathbf{z}) = \sum_{n=1}^{\mathcal{N}} \Delta z_n \tag{8.16}$$

is the length of the optimized taper. With α and β, we insert weighing constants, which we fix to $\alpha = 1/L_f$ and $\beta = 1$ to emphasize the transmittance. The optimal value of this function is given by $f(\mathbf{z}_{\text{opt}}) = -1$ with $L = L_f$ and $|a_1|^2 = 1$.

We start by explaining the basic concept of PSO in Section 8.4.1 before showing the optimized results in Section 8.4.2.

8.4.1 Particle swarm optimization

The particle swarm optimization (PSO) algorithm was introduced by Eberhart and Kennedy in 1995 [178]. It is an iterative population based search algorithm inspired by the social behavior of insects for the optimization of nonlinear functions. The concept is quite easy and briefly explained in the following [179–181].

The method is initialized with a population – a swarm – of arbitrary size, where each j-th entity – a particle – exhibits a random position $\mathbf{z}_j \in \Omega$, in the search space Ω, with velocity $\mathbf{v}_j$. The position corresponds to a certain objective function value $f(\mathbf{z}_j)$ and the velocity determines the movement of the particle. During iteration, each particle keeps track of its coordinates associated with the current best position.

A single particle is useless, but a swarm of particles that know and interact with each other is powerful. The so far best known position of the particle is given by $p_{j,\mathrm{best}}$ and the best position of the neighboring particles by $p_{g,\mathrm{best}}$. In each step, the velocity is updated depending on the best known position $p_{j,\mathrm{best}}$ and current velocity v_j of the particle itself, and the best position $p_{g,\mathrm{best}}$ of the neighboring particles via

$$\begin{aligned} \mathbf{v}_j &\leftarrow w\mathbf{v}_j + c_1\gamma_1(p_{j,\mathrm{best}} - \mathbf{z}_j) + c_2\gamma_2(p_{g,\mathrm{best}} - \mathbf{z}_j) \\ \mathbf{z}_j &\leftarrow \mathbf{z}_j + \mathbf{v}_j \end{aligned} \tag{8.17}$$

with positive constants c_1, c_2 (confidence in its best performance and the best performance of the swarm), $\gamma_1, \gamma_2 \in (0, 1)$ two random variables and w is the initial weight (confidence in its own movement) [179–181]. Thus, the new velocity then determines the movement of the particle and its new position, corresponding to the new objective function value. After each iteration, it is checked whether the new function value $p_j = f(\mathbf{z}_j)$ at position $\mathbf{z}_j$ has improved compared to the best positions $p_{j,\mathrm{best}}$ and $p_{g,\mathrm{best}}$. If the position of the particle has improved, the best position is updated. The method is repeated several times until either a certain number of iterations or a minimum error is reached. The following gives an overview of the implementation:

1. Initialization of the swarm with random positions $\mathbf{z}_j$ and velocity $\mathbf{v}_j$ in the multidimensional search space.
2. Evaluation of the particle's objective function value $p_j = f(\mathbf{z}_j)$ and comparison to its personal best $p_{j,\mathrm{best}}$. If the current value is better, update $p_{j,\mathrm{best}} = p_j$.
3. Identification of the personal best in each particle's neighborhood and assign it to $p_{g,\mathrm{best}}$.
4. Change the velocity and position of the particle accordingly to Eq. (8.17).
5. Go back to step 2 until convergence.

8.4.2 Results

When using MATLAB's implementation of the particle swarm algorithm for optimization, we can define lower $l_b = 0.05\,\mu$m (the value is chosen slightly higher than zero to reflect on the resolution of the fabrication process) and upper $u_b = L_f$ bounds for each of the $\mathcal{N}$ element lengths. Furthermore, we assume a population size of 100 elements and randomize the start points of the PSO by choosing an initial swarm matrix

$$\mathsf{Z}_0 = l_b + \mathsf{A}(u_b - l_b), \tag{8.18}$$

where A is a matrix with randomly created elements $a_{ij} \in (0, 1)$. Additionally, we add the modified, coupling efficient taper structure from Section 8.3.2 as an initial point as it gave already good results.

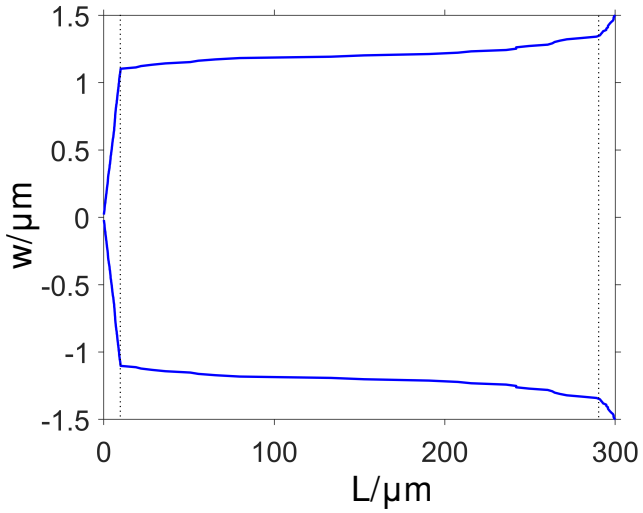

Figure 8.9: Optimized shape of the taper using PSO for a desired taper length $L_f = 300\,\mu$m.

L_f	$200\,\mu$m	$300\,\mu$m	$400\,\mu$m
PSO	0.9486	0.9704	0.9709
linear taper	0.6669	0.6909	0.7213

Table 8.1: Comparison of the linear taper and optimized taper using PSO for different taper lengths $L = L_f$. Displayed is the transmittance value $|a_1|^2$ to the Si-mode.

The optimized taper structure for a fixed length of $L_f = 300\,\mu$m is shown in Figure 8.9. The solver converged after around 150 iterations with a computation time of about 5 s (a single function call requires approximately 5 ms). As expected, a separation in three parts is necessary, where the middle part is the longest with widths around $2.3\,\mu$m. The corresponding transmittance value $|a_1|^2$ is determined to be 97%. Additionally, further optimized transmittance results are displayed in Table 8.1 for different taper lengths L_f. Here, the values are further compared to the corresponding transmission value of a linear taper of identical length $L = L_f$. The optimized structures achieve significantly higher transmission values for identical taper lengths. Even if not shown, the shapes of the optimized taper for lengths $L_f = 200\,\mu$m or $L_f = 400\,\mu$m are almost identical to Figure 8.9, scaled to the respective lengths. The results confirm our suggestions that the coupling is the strongest in the area around $w = 2.3\,\mu$m and the taper needs to be divided into three parts to yield high transmission values to the Si-mode for comparably small taper lengths. Furthermore, we can state that the FEMMM offers a very fast and efficient method to optimize the shape functions of multiscale 3-D tapers within seconds (note that this does not include the pre-calculation of the mode profiles and overlap products, which need some hours of calculation time depending on the number of approximation elements $\mathcal{N}$).

Chapter 9

Nonlinear interaction in LNOI waveguides[1]

Lithium niobate on insulators (LNOI) combine the large second-order nonlinear susceptibility of lithium niobate (LN) and the advantages of silicon photonics on the same platform, and are used for a wide range of nonlinear interactions relevant for integrated quantum photonic circuits [70, 183]. We are particularly interested in the process of parametric down-conversion (PDC) for the generation of entangled photon pairs [56,57,69]. Especially for quantum telecommunication, sources of entangled photons that exhibit different properties are required as they reduce mode chromatic dispersion, propagate long distances [184] and improve the quantum light-matter interaction [182, 185].

The PDC process is an important effect in quantum optics because of its excellent properties and wide applicational use, e.g., in photon engineering [186], quantum cryptography [187], photon interference [188] or, as already mentioned, the entanglement between signal and idler photons [189, 190].

In PDC, a pump pulse at high frequency interacts with a nonlinear optical crystal and generates signal and idler photons of lower frequency. For this to happen, the fields must meet a certain phase-matching condition and have a large field overlap [191]. Generally, signal and idler photons have orthogonal polarizations and different group velocities (they are not degenerate). Thus, they neither propagate together nor do they fulfill the phase-matching. While in bulk systems this delay can be easily compensated, it requires more complex structures in integrated photonics to generate degenerate signal and idler photons [73, 74]. However, we do not want to go into the details of quantum optics, but show how the process can be realized using optical waveguides supporting (quasi) degenerate modes. For more details on nonlinear optics, we refer the reader to [50, 191, 192].

In this chapter, we present the nonlinear interaction of modes in LNOI rib waveguides with anisotropic LN core layer on a silicon dioxide substrate. We investigate these waveguides in Z-cut and X-cut configurations and demonstrate how the geometry of the rib needs to be adjusted

[1] Sections 9.1–9.2 are based on the publication [182] of the candidate.

to achieve degenerate signal and idler modes that propagate together, i.e., fulfill the phase-matching condition for nonlinear interaction.

In Section 9.1, we briefly review certain aspects of the theory of nonlinear optics, focusing especially on the process of parametric down-conversion [50]. Then, we present different scenarios for the nonlinear interaction in rib waveguide structures in Sections 9.2–9.4. We show that quasi-phase-matched as well as phase-matched structures exhibit a strong interaction of the involved fields. The last Section 9.4 contains a proposal on a concept, where the oblique excitation scheme, as discussed in Chapters 4–6, can be exploited to realize phase-matching for enhanced nonlinear interaction of guided waves.

9.1 Classical nonlinear optics

So far, the response of an optical medium to an external electric field was described by the linear equation [50]

$$\tilde{\mathbf{P}} = \varepsilon_0 \chi^{(1)} \tilde{\mathbf{E}}, \tag{9.1}$$

where $\tilde{\mathbf{P}}$ is the dielectric polarization and $\chi^{(1)}$ is the linear susceptibility of the material. The constitutive equation for the electric field and electric displacement is then simply given by

$$\tilde{\mathbf{D}} = \varepsilon_0 \tilde{\mathbf{E}} + \tilde{\mathbf{P}} = \varepsilon_0 \varepsilon_r \tilde{\mathbf{E}} \tag{9.2}$$

with $\varepsilon_r = 1 + \chi^{(1)}$ the relative permittivity.

When substantially strong electric fields are present, the linear approximation is no longer sufficient and higher order contributions become important as well. The polarization needs to be expressed through a series expansion $\tilde{\mathbf{P}} = \tilde{\mathbf{P}}^{(1)} + \tilde{\mathbf{P}}^{(\mathrm{NL})}$ with a linear part $\tilde{\mathbf{P}}^{(1)} = \varepsilon_0 \chi^{(1)} \tilde{\mathbf{E}}$ and an additional non-linear part $\tilde{\mathbf{P}}^{(\mathrm{NL})}$ [50]. Accordingly, the electric material equation can be written as

$$\tilde{\mathbf{D}} = \varepsilon_0 \tilde{\mathbf{E}} + \tilde{\mathbf{P}} = \varepsilon_0 \tilde{\mathbf{E}} + \varepsilon_0 \sum_j \chi^{(j)} \tilde{\mathbf{E}}^j = \varepsilon_0 \varepsilon_r \tilde{\mathbf{E}} + \tilde{\mathbf{P}}^{(\mathrm{NL})} \tag{9.3}$$

with the nonlinear polarization term

$$\tilde{\mathbf{P}}^{(\mathrm{NL})} = \varepsilon_0 \sum_{j \geq 2} \chi^{(j)} \tilde{\mathbf{E}}^j = \tilde{\mathbf{P}}^{(2)} + \tilde{\mathbf{P}}^{(3)} + ..., \tag{9.4}$$

the j-th order nonlinear susceptibilities $\chi^{(j)}$ and polarizations $\tilde{\mathbf{P}}^{(j)}$.

We again consider fields $(\tilde{\mathbf{E}}, \tilde{\mathbf{H}})^T$ in the frequency domain with angular frequency ω that solve the nonlinear Maxwell equations in the frequency domain [50]

$$\nabla \times \tilde{\mathbf{E}} = -\mathrm{i}\omega\mu_0 \tilde{\mathbf{H}} \qquad \text{and} \qquad \nabla \times \tilde{\mathbf{H}} = \mathrm{i}\omega\varepsilon_0\varepsilon_r \tilde{\mathbf{E}} + \mathrm{i}\omega \tilde{\mathbf{P}}^{(\mathrm{NL})}. \tag{9.5}$$

They can be transformed to a nonlinear wave equation for the electric field in regions with constant refractive index [50]

$$\Delta \tilde{\mathbf{E}} + k_0^2 \varepsilon_r \tilde{\mathbf{E}} = -\frac{\omega^2}{\varepsilon_0 c_0^2} \tilde{\mathbf{P}}^{\mathrm{NL}}. \tag{9.6}$$

We are particularly interested in second-order nonlinear optical interactions in media, where the second-order nonlinear susceptibility $\chi^{(2)}$ is non-zero. The presence of this term allows the creation of electric fields at different frequencies. Considering two fields $\tilde{\mathbf{E}}_1 \mathrm{e}^{\mathrm{i}\omega_1 t}$ and $\tilde{\mathbf{E}}_2 \mathrm{e}^{\mathrm{i}\omega_2 t}$ at different frequencies ω_1 and ω_2, respectively, results in various frequency components of the second-order nonlinear polarization

$$\begin{aligned}
\tilde{\mathbf{P}}^{(2)}(2\omega_1) &= \varepsilon_0 \chi^{(2)} \tilde{\mathbf{E}}_1^2, && \text{(SHG)} \\
\tilde{\mathbf{P}}^{(2)}(2\omega_2) &= \varepsilon_0 \chi^{(2)} \tilde{\mathbf{E}}_2^2, && \text{(SHG)} \\
\tilde{\mathbf{P}}^{(2)}(\omega_1 + \omega_2) &= 2\varepsilon_0 \chi^{(2)} \tilde{\mathbf{E}}_1 \tilde{\mathbf{E}}_2, && \text{(SFG)} \\
\tilde{\mathbf{P}}^{(2)}(\omega_1 - \omega_2) &= 2\varepsilon_0 \chi^{(2)} \tilde{\mathbf{E}}_1 \tilde{\mathbf{E}}_2^*, && \text{(DFG)} \\
\tilde{\mathbf{P}}^{(2)}(0) &= 2\varepsilon_0 \chi^{(2)} (\tilde{\mathbf{E}}_1 \tilde{\mathbf{E}}_1^* + \tilde{\mathbf{E}}_2 \tilde{\mathbf{E}}_2^*). && \text{(OR)}
\end{aligned} \tag{9.7}$$

Here, we omitted the space dependence (x, y, z) for clarity. Three different processes can generate fields at a new frequency ω_3: second-harmonic generation (SHG) at $\omega_3 = 2\omega$ (where $\omega = \omega_1$ or $\omega = \omega_2$), difference-frequency generation (DFG) at $\omega_3 = \omega_1 - \omega_2$ and sum-frequency generation (SFG) at $\omega_3 = \omega_1 + \omega_2$. The last one is optical rectification (OR).

Typically, only one process is present at a time since a specific phase-matching condition (see Section 9.1.2) needs to be satisfied. But, this is usually just fulfilled for one of the frequencies ω_3. In an analogous manner, the third order nonlinear polarization term leads to processes at 3ω, called third harmonic generation [191].

9.1.1 Nonlinear coupling in waveguides

For a specific waveguide structure with constant cross section (in the x-y-plane) along the propagation direction z, we can write the electric and magnetic field as a complete set of forward and backward propagating waves with propagation constants $k_{z,q}$ and amplitudes $a_q(z)$, varying with the propagation distance z at frequency ω,

$$\begin{pmatrix} \tilde{\mathbf{E}} \\ \tilde{\mathbf{H}} \end{pmatrix} (x, y, z) = \sum_q \frac{a_q(z)}{\sqrt{N_q}} \begin{pmatrix} \mathbf{E}_q \\ \mathbf{H}_q \end{pmatrix} (x, y) \mathrm{e}^{\mp \mathrm{i} k_{z,q} z}. \tag{9.8}$$

The couple $(\mathbf{E}_q, \mathbf{H}_q)^T$ identifies the mode profiles in the transverse plane propagating in $\pm z$-direction. We introduce a power normalization coefficient

$$N_q = \frac{1}{4} \int_A (\mathbf{E}_q^* \times \mathbf{H}_q + \mathbf{E}_q \times \mathbf{H}_q^*) \cdot \mathbf{e}_z \mathrm{d}A. \tag{9.9}$$

Here, we use the value N_q instead of P_q, as introduced in Eq. (2.42), to avoid confusion with the polarization $\hat{\mathbf{P}}$.

This mode expansion ansatz is the fundamental formalism of the coupled mode theory [192, 193]. The evaluation of amplitudes $a_q(z)$ is then governed by the coupled amplitude equations. They are derived by considering the Lorentz reciprocity theorem (cf. Eq. (2.40))

$$\partial_z \int_A \mathbf{F} \cdot \mathbf{e}_z \mathrm{d}A = \int_A \nabla \cdot \mathbf{F} \mathrm{d}A \tag{9.10}$$

with $\mathbf{F} = \tilde{\mathbf{E}}_q^* \times \tilde{\mathbf{H}} + \tilde{\mathbf{E}} \times \tilde{\mathbf{H}}_q^*$. By inserting our ansatz from Eq. (9.8) and the nonlinear Maxwell equations (9.5) in the reciprocity theorem and applying the mode orthogonality relation from Eq. (2.43), the amplitudes change according to

$$\partial_z a_q(z) = -\frac{\mathrm{i}\omega}{4\sqrt{N_q}} \mathrm{e}^{\pm \mathrm{i} k_{z,q} z} \int \mathbf{E}_q^*(x,y) \cdot \tilde{\mathbf{P}}^{(\mathrm{NL})}(x,y,z) \mathrm{d}A. \tag{9.11}$$

9.1.2 Parametric down-conversion

In addition to the processes mentioned above, there are also processes that function in a complete reverse manner. We are especially interested in the process of parametric down-conversion (PDC), i.e., a field $\mathbf{E}_3$ at frequency ω_3 can split into two new fields $\mathbf{E}_1$ and $\mathbf{E}_2$ at lower frequencies ω_1 and ω_2, respectively, with $\omega_3 = \omega_1 + \omega_2$ [191].

Without going too much into details, the coupled amplitude equations (9.11) for the PDC process are derived in the following. Here, three modes at different frequencies are interacting: ω_3 belongs to the pump mode and ω_1 and ω_2 to the signal and idler modes. Considering only these three relevant forward propagating modes, we can set $q \in \{1,2,3\}$ in Eq. (9.11). Hence, for each mode the amplitude is described by the differential equation (9.11) with the corresponding frequency. The nonlinear polarization density components are [50]

$$\begin{aligned}
\tilde{\mathbf{P}}_1^{(\mathrm{NL})}(\omega_1 = \omega_3 - \omega_2) &= \frac{2a_2^* a_3 \varepsilon_0}{\sqrt{N_2 N_3}} \chi^{(2)} \mathbf{E}_2^* \mathbf{E}_3 \mathrm{e}^{-\mathrm{i}(k_{z,3} - k_{z,2})z}, \\
\tilde{\mathbf{P}}_2^{(\mathrm{NL})}(\omega_2 = \omega_3 - \omega_1) &= \frac{2a_1^* a_3 \varepsilon_0}{\sqrt{N_1 N_3}} \chi^{(2)} \mathbf{E}_1^* \mathbf{E}_3 \mathrm{e}^{-\mathrm{i}(k_{z,3} - k_{z,1})z}, \\
\tilde{\mathbf{P}}_3^{(\mathrm{NL})}(\omega_3 = \omega_1 + \omega 2) &= \frac{2a_1 a_2 \varepsilon_0}{\sqrt{N_1 N_2}} \chi^{(2)} \mathbf{E}_1 \mathbf{E}_2 \mathrm{e}^{-\mathrm{i}(k_{z,1} + k_{z,2})z},
\end{aligned} \tag{9.12}$$

which results in

$$\begin{aligned}
\partial_z a_1(z) &= -\frac{\mathrm{i}\omega_1 \varepsilon_0}{2\sqrt{N_1 N_2 N_3}} a_2^* a_3 \mathrm{e}^{-\mathrm{i}\Delta k z} \int \sum_{j,m,l=x,y,z} \chi_{jml}^{(2)} E_{j,1}^* E_{m,2}^* E_{l,3} \mathrm{d}A, \\
\partial_z a_2(z) &= -\frac{\mathrm{i}\omega_2 \varepsilon_0}{2\sqrt{N_2 N_1 N_3}} a_1^* a_3 \mathrm{e}^{-\mathrm{i}\Delta k z} \int \sum_{j,m,l=x,y,z} \chi_{jml}^{(2)} E_{j,2}^* E_{m,1}^* E_{l,3} \mathrm{d}A, \\
\partial_z a_3(z) &= -\frac{\mathrm{i}\omega_3 \varepsilon_0}{2\sqrt{N_3 N_1 N_2}} a_1 a_2 \mathrm{e}^{\mathrm{i}\Delta k z} \int \sum_{j,m,l=x,y,z} \chi_{jml}^{(2)} E_{j,3}^* E_{m,1} E_{l,2} \mathrm{d}A
\end{aligned} \tag{9.13}$$

with $\Delta k = k_{z,3} - k_{z,1} - k_{z,2}$ as the phase mismatch. Note, that the frequency dependence of $\chi^{(2)}$ is directly neglected by applying Kleinman's symmetry condition (see Section 9.1.3) for the processes considered in this work [50].

For convenience, we define the complex values κ_1, κ_2 and κ_3 via

$$\begin{aligned}
\kappa_1 &= \frac{\omega_1 \varepsilon_0}{2\sqrt{N_1 N_2 N_3}} \int \sum_{j,m,l=x,y,z} \chi_{jml}^{(2)} E_{j,1}^* E_{m,2}^* E_{l,3} \mathrm{d}A, \\
\kappa_2 &= \frac{\omega_2 \varepsilon_0}{2\sqrt{N_2 N_1 N_3}} \int \sum_{j,m,l=x,y,z} \chi_{jml}^{(2)} E_{j,2}^* E_{m,1}^* E_{l,3} \mathrm{d}A, \\
\kappa_3 &= \frac{\omega_3 \varepsilon_0}{2\sqrt{N_3 N_2 N_1}} \int \sum_{j,m,l=x,y,z} \chi_{jml}^{(2)} E_{j,3}^* E_{m,1} E_{l,2} \mathrm{d}A.
\end{aligned} \tag{9.14}$$

The coupled amplitude equations are then simplified as

$$\begin{aligned}\partial_z a_1(z) &= -\mathrm{i}\kappa_1 a_2^* a_3 \mathrm{e}^{-\mathrm{i}\Delta k z},\\ \partial_z a_2(z) &= -\mathrm{i}\kappa_2 a_1^* a_3 \mathrm{e}^{-\mathrm{i}\Delta k z},\\ \partial_z a_3(z) &= -\mathrm{i}\kappa_3 a_1 a_2 \mathrm{e}^{\mathrm{i}\Delta k z}.\end{aligned} \tag{9.15}$$

For the waveguide structure considered in this work, we can assume a no pump depletion approximation, i.e., a_3 is constant. Hence, with $\kappa_1' = \kappa_1 a_3$ and $\kappa_2' = \kappa_2 a_3$, we can define the differential equations as

$$\begin{aligned}\partial_z a_1(z) &= -\mathrm{i}\kappa_1' a_2^* \mathrm{e}^{-\mathrm{i}\Delta k z},\\ \partial_z a_2(z) &= -\mathrm{i}\kappa_2' a_1^* \mathrm{e}^{-\mathrm{i}\Delta k z}.\end{aligned} \tag{9.16}$$

Generally, when considering a non phase-matched structure $\Delta k \neq 0$, the solution to these differential equations oscillates with the propagation distance z and the magnitude is mainly determined by the values of κ_1 and κ_2. To overcome this oscillating behavior, a quasi-phase-matched periodically poled structure can be constructed with poling period $\Lambda = \frac{2\pi}{\Delta k}$ [50].

9.1.3 Properties of the nonlinear susceptibility

Now, we briefly give some formal properties of the $\chi^{(2)}$-tensor. The second-order nonlinear susceptibility can be drastically simplified when applying some symmetry conditions because not all elements are independent from each other [50]. Generally, $\chi^{(2)}$ is a 3-rank tensor, but when applying Kleinman's symmetry conditions (considering lossless media)

$$\chi^{(2)}_{jml} = \chi^{(2)}_{ljm} = \chi^{(2)}_{mlj} = \chi^{(2)}_{lmj} = \chi^{(2)}_{mjl} = \chi^{(2)}_{jlm}, \tag{9.17}$$

which predicts full permutation symmetry of the tensor. This implies independence of the frequency and a contracted notation $d_{jn} = \frac{1}{2}\chi^{(2)}_{jml}$ can be defined. The indices are related to the rules in the following table.

ml	11	22	33	23,32	31,13	12,21
n	1	2	3	4	5	6

Then, the d-coefficient is given by the matrix

$$d = \begin{pmatrix} d_{11} & d_{12} & d_{13} & d_{14} & d_{15} & d_{16} \\ d_{16} & d_{22} & d_{23} & d_{24} & d_{14} & d_{12} \\ d_{15} & d_{24} & d_{33} & d_{23} & d_{13} & d_{14} \end{pmatrix} \tag{9.18}$$

with elements d_{jn}. In this chapter, we focus on LN materials that exhibit a specific trigonal crystal structure. This further restricts the form of the d-matrix to [50]

$$d = \begin{pmatrix} 0 & 0 & 0 & 0 & d_{31} & -d_{22} \\ -d_{22} & d_{22} & 0 & d_{31} & 0 & 0 \\ d_{31} & d_{31} & d_{33} & 0 & 0 & 0 \end{pmatrix} \tag{9.19}$$

with the values $d_{33} \approx 25$ pm/V, $d_{31} \approx 4.6$ pm/V and $d_{22} \approx 2.2$ pm/V adopted from [194, 195]. Then, the nonlinear second-order polarization density from Eq. (9.12) can be written as

$$\begin{aligned}
\tilde{\mathbf{P}}_1^{(\mathrm{NL})} &= \frac{4\varepsilon_0 a_2^* a_3}{\sqrt{N_2 N_3}} d[\mathbf{E}_2^*, \mathbf{E}_3] \mathrm{e}^{-\mathrm{i}(k_{z,3}-k_{z,2})z}, \\
\tilde{\mathbf{P}}_2^{(\mathrm{NL})} &= \frac{4\varepsilon_0 a_1^* a_3}{\sqrt{N_1 N_3}} d[\mathbf{E}_1^*, \mathbf{E}_3] \mathrm{e}^{-\mathrm{i}(k_{z,3}-k_{z,1})z}, \\
\tilde{\mathbf{P}}_3^{(\mathrm{NL})} &= \frac{4\varepsilon_0 a_1 a_2}{\sqrt{N_1 N_2}} d[\mathbf{E}_1, \mathbf{E}_2] \mathrm{e}^{-\mathrm{i}(k_{z,1}+k_{z,2})z},
\end{aligned} \tag{9.20}$$

with

$$[\mathbf{E}_i, \mathbf{E}_j] = \begin{pmatrix} E_{i,x}E_{j,x} \\ E_{i,y}E_{j,y} \\ E_{i,z}E_{j,z} \\ E_{i,y}E_{j,z} + E_{i,z}E_{j,y} \\ E_{i,x}E_{j,z} + E_{i,z}E_{j,x} \\ E_{i,x}E_{j,y} + E_{i,y}E_{j,x} \end{pmatrix}, \quad i,j \in \{1,2,3\}, \tag{9.21}$$

which simplifies (9.14) to

$$\begin{aligned}
\kappa_1 &= \frac{\omega_1 \varepsilon_0}{\sqrt{N_1 N_2 N_3}} \int \sum_{j=x,y,z} E_{j,1}^* \sum_{n=1}^{6} d_{jn} [\mathbf{E}_2^*, \mathbf{E}_3]_n dA, \\
\kappa_2 &= \frac{\omega_2 \varepsilon_0}{\sqrt{N_2 N_1 N_3}} \int \sum_{j=x,y,z} E_{j,2}^* \sum_{n=1}^{6} d_{jn} [\mathbf{E}_1^*, \mathbf{E}_3]_n dA, \\
\kappa_3 &= \frac{\omega_3 \varepsilon_0}{\sqrt{N_3 N_1 N_2}} \int \sum_{j=x,y,z} E_{j,3}^* \sum_{n=1}^{6} d_{jn} [\mathbf{E}_1, \mathbf{E}_2]_n dA.
\end{aligned} \tag{9.22}$$

9.2 Quasi-phase-matched structures

A general 2-D sketch of the LNOI rib waveguide is shown in Figure 9.1 with either X-cut (y is propagation direction) or Z-cut (x is propagation direction) coordinate system. The structure is assumed to have a constant cross section along the propagation direction and the optical axis of the crystal is always along the z-direction. The width of the waveguide is given by w, the height by τ and the etch depth by h. Additionally, the angle θ is introduced to include manufacturing tolerances and is fixed to $45°$ initially. We are searching for degenerate signal and idler modes ($\omega_1 = \omega_2$) at wavelength $\lambda_{s,i} = 1.55\,\mu$m and pump modes ($\omega_3 = \omega_1 + \omega_2$) at $\lambda_p = 0.775\,\mu$m.

The corresponding refractive index values are displayed in Table 9.1 for both relevant wavelengths. Respective wavelength scans are shown in Figure 9.2. The refractive index values for silicon dioxide are adopted from [196]. For lithium niobate, measurements using spectroscopic ellipsometry are fitted using a Tauc-Lorentz oscillator model [197], as introduced in [182].

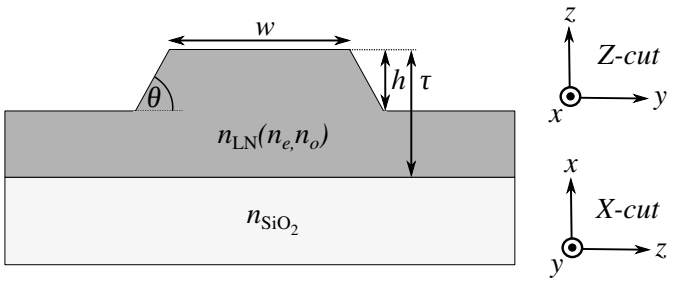

Figure 9.1: 2-D sketch of the LNOI rib waveguide of width w, height τ, etch depth h and angle θ. Different coordinate systems are applied for either X- or Z-cut structures [182].

	SiO_2	LN	
	n_{SiO_2}	n_e	n_o
$\lambda_p = 0.775\,\mu$m	1.4589	2.1565	2.2242
$\lambda_{s,i} = 1.55\,\mu$m	1.4483	2.122	2.1837

Table 9.1: Refractive index values for signal/idler wavelength $\lambda_{s,i} = 1.55\,\mu$m and pump wavelength $\lambda_p = 0.775\,\mu$m for the structure in Figure 9.1 [182].

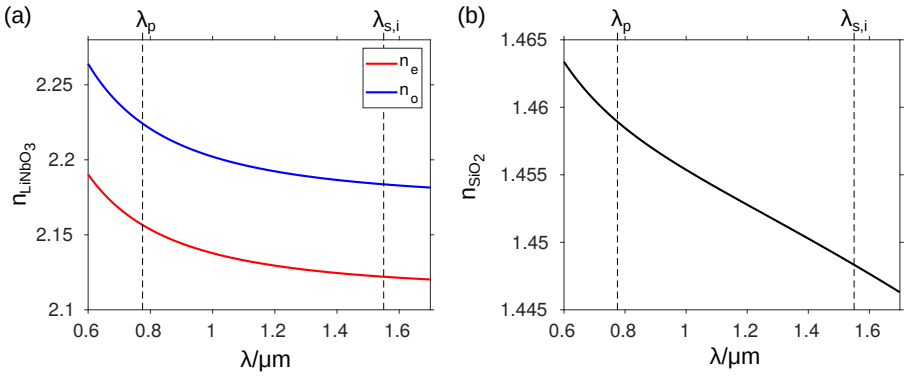

Figure 9.2: Wavelength dependence of the refractive index for (a) lithium niobate (ordinary n_o (blue line) and extraordinary n_e (red line) refractive index) and (b) silicon. Corresponding signal, idler $\lambda_{s,i}$ and pump λ_p wavelengths from Table 9.1 are marked by the vertical dashed lines [182].

The nonlinear interaction of the optical fields is described by the coupled amplitude equations (Eq. (9.15); depending on the orientation of the crystal, the propagation direction has to be adapted properly, cf. Figure 9.1) and more specifically by the magnitude of the κ-coefficients (see Eq. (9.22)) and the phase-matching Δk or the poling period Λ [50]. When considering the κ-coefficients, the relevant area for integration is limited to the LN layer, which only has a non-zero second-order susceptibility. Furthermore, we can identify the equality

$$\kappa_1 = \kappa_2 = \frac{1}{2}\kappa_3^* =: \kappa \tag{9.23}$$

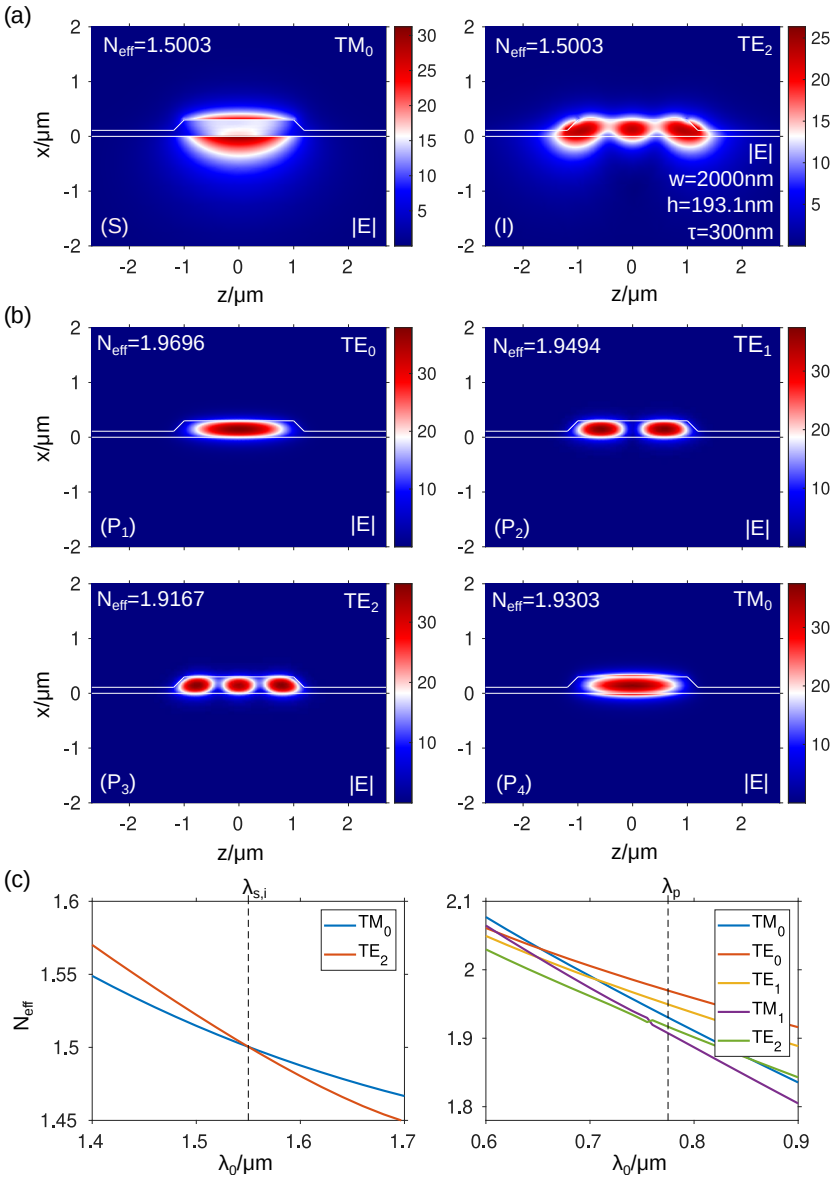

Figure 9.3: X-cut structure with geometry parameters $w = 2000\,\text{nm}$, $h = 193.1\,\text{nm}$ and $\tau = 300\,\text{nm}$. Field plots of the absolute electric field $|\mathbf{E}|$ (in $\text{V}/\,\mu\text{m}$) for (a) signal (S) and idler (I) modes and (b) possible pump modes (P_1)-(P_4). (c) The effective refractive index N_{eff} versus the wavelength λ_0 for signal and idler modes (left plot) and possible pump modes (right plot). All modes are power normalized, i.e., $\int S_y \mathrm{d}A = 1\,\text{W}$ [182].

because of the symmetry of the $\chi^{(2)}$-tensor [50]. Therefore, we will only indicate the value for κ in the following. When considering degenerate signal and idler modes, the phase-matching $\Delta k = 0$ is never fulfilled for the structures considered in this section. Hence, a quasi-phase-matching, determined by the poling period Λ, is needed to suppress an oscillating behavior of the amplitudes.

To calculate the guided modes (degenerate signal/idler and pump modes), we made use of the

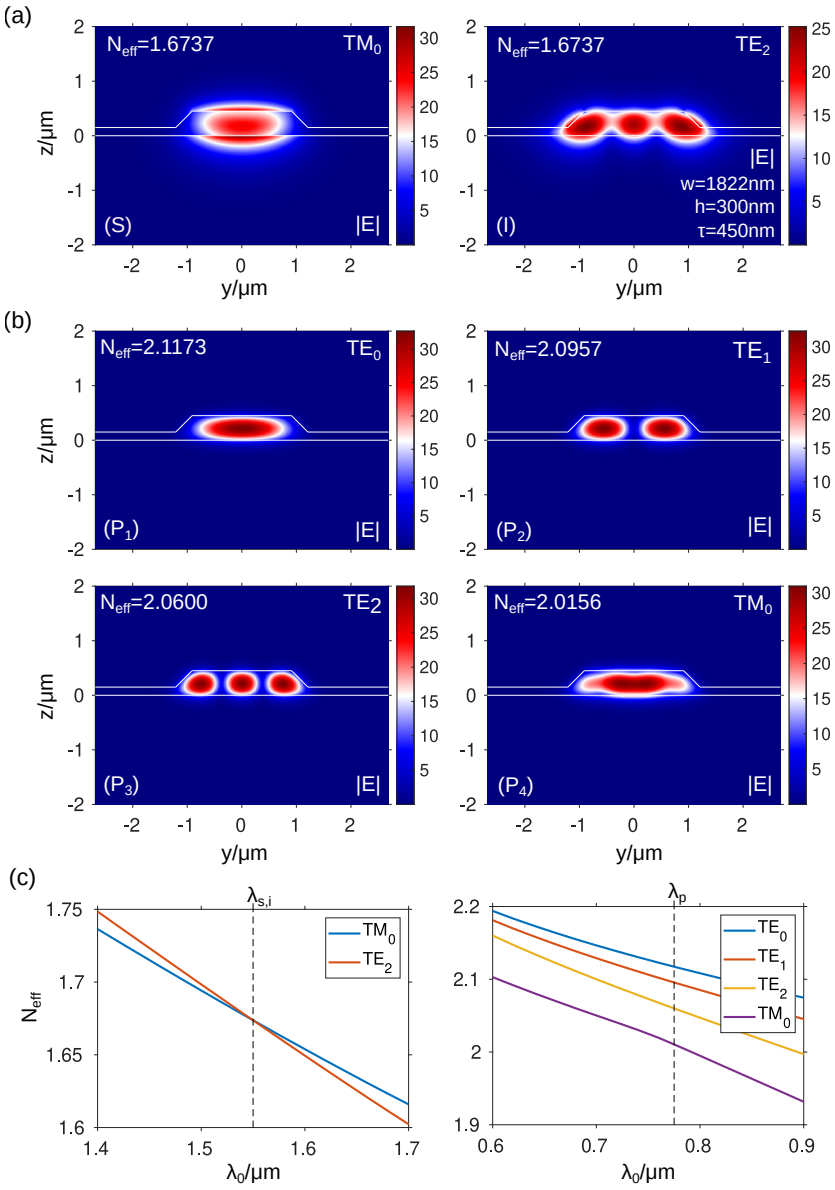

Figure 9.4: Z-cut structure with geometry parameters $w = 2000\,\text{nm}$, $h = 300\,\text{nm}$ and $\tau = 450\,\text{nm}$. Field plots of the absolute electric field $|\mathbf{E}|$ (in $\text{V}/\,\mu\text{m}$) for (a) signal (S) and idler (I) modes and (b) possible pump modes (P_1)-(P_4). (c) The effective refractive index N_{eff} versus the wavelength λ_0 for signal and idler modes (left plot) and possible pump modes (right plot). All modes are power normalized, i.e., $\int S_x \mathrm{d}A = 1\,\text{W}$ [182].

finite element mode analysis solver in COMSOL Multiphysics [22]. For simplicity, searching for suitable modes is carried out in reverse to the PDC process itself: we first look for degenerate signal and idler modes at $\lambda_{s,i} = 1.55\,\mu\text{m}$ by varying the geometry parameters w, h and τ of the waveguide. The resulting geometry then determines the corresponding variety of possible pump modes at $\lambda_p = 0.775\,\mu\text{m}$.

The calculated $|\kappa|$-coefficients for different pump modes (TE_0-TE_2 and TM_0) are displayed in Table 9.2 for X-cut and Z-Cut, respectively. In both systems, the appropriate degenerate signal and idler modes are the TM_0 and TE_2 mode. Field plots of the absolute electric field $|\mathbf{E}|$ are shown in Figure 9.3 (a, b) for the Z-cut structure and in Figure 9.4 (a, b) for the X-cut structure with corresponding wavelength scans of the effective refractive index in (c). We see that the signal and idler modes are degenerate at the desired wavelength $\lambda_{s,i} = 1.55\,\mu$m. Additionally, the poling period Λ is shown in the table. The greatest value of $|\kappa|$ is achieved by the Z-cut structure for the TE_2 pump mode with an absolute value of $220.40\,\mathrm{W}^{-1/2}\,\mathrm{m}^{-1}$. To get an impression of the magnitude of this result, standard bulk LN waveguides exhibit coupling coefficients that are approximately three times smaller ($|\kappa| \approx 70\,\mathrm{W}^{-1/2}\,\mathrm{m}^{-1}$) than our best value [192]. This can be explained by the fact that the mode matching is higher when localized fields in the rib waveguide are considered and losses are not taken into account. Thus, our quasi-phase-matched structure can be used as a flexible source of entangled photons that propagate together, but have different polarizations, spatial mode profiles and frequency distributions [182].

	X-cut				Z-cut			
pump	TE_0	TE_1	TE_2	TM_0	TE_0	TE_1	TE_2	TM_0
$\lvert\kappa\rvert[\mathrm{W}^{-1/2}\,\mathrm{m}^{-1}]$	11.54	34.87	7.44	40.15	65.91	9.50	220.40	1.86
$\Lambda[\,\mu\mathrm{m}]$	1.65	1.73	1.86	1.80	1.75	1.84	2.01	2.27

Table 9.2: Calculated coefficients $|\kappa|$ and periods Λ for the X-cut and Z-cut structure for different pump modes. Signal and idler modes are assumed to be the TM_0 and TE_2 mode, respectively. Corresponding field plots are shown in Figure 9.3 (a, b) and Figure 9.4 (a, b).

9.3 Phase-matched structures

The structures considered in Section 9.2 do not fulfill the phase-matching condition

$$\Delta k = k_p - k_s - k_i \qquad \text{or} \qquad N_p - \frac{1}{2}(N_s - N_i) = 0, \tag{9.24}$$

because the effective indices of the considered pump modes N_p are always higher than the mean value of the mode index of the signal N_s and idler N_i mode. To fulfill the phase-matching, it may be advantageous to consider even higher order pump modes (with lower mode index) and low order/fundamental signal and idler modes (with higher mode indices). Therefore, we calculated the effective mode indices of a variety of guided signal and idler and corresponding pump modes by again varying the geometry parameters w, h and τ. Furthermore, we chose different edge angles $\theta \in \{45, 90\}^\circ$.

We could find intersection points that satisfy the phase-matching condition for the X-cut and Z-cut structure. Here, it turned out that the fundamental $TE_{0,0}$ and $TM_{0,0}$ modes (we now use two indices to characterize the modes, as we also consider modes with horizontal modal lines) are the best choice as signal and idler modes since they have the largest effective refractive indices. Hence, the mean value is also high. The choice of the pump mode varies ($TM_{1,1}$, $TE_{1,1}$ or $TE_{2,0}$) depending on the considered structure (X-cut or Z-cut and $\theta = 45^\circ$ or $\theta = 90^\circ$). The field profiles of the derived modes are shown in Figure 9.5 (X-cut for (a) $\theta = 45^\circ$ and (b) $\theta = 90^\circ$) and in Figure 9.6 (Z-cut for (a) $\theta = 45^\circ$ and (b) $\theta = 90^\circ$). The corresponding values for the

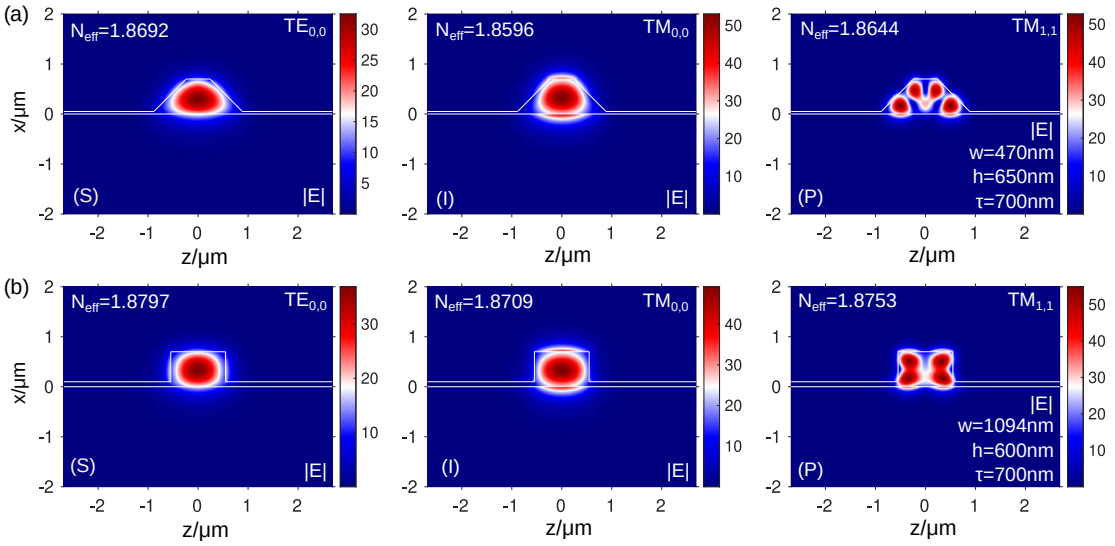

Figure 9.5: Mode profiles of the absolute electric field $|\mathbf{E}|$ (in $\mathrm{V}/\,\mu\mathrm{m}$) for signal (S), idler (I) and pump (P) mode for the phase-matched X-cut structure. (a) $\theta = 45°$, (b) $\theta = 90°$. All modes are power normalized, i.e., $\int S_y \mathrm{d}A = 1\,\mathrm{W}$.

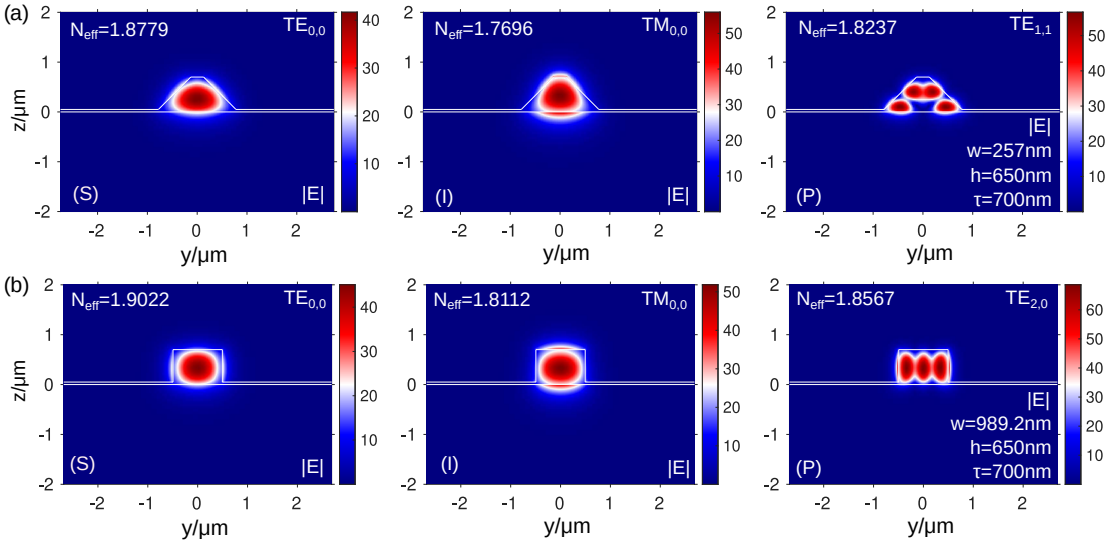

Figure 9.6: Mode profiles of the absolute electric field $|\mathbf{E}|$ (in $\mathrm{V}/\,\mu\mathrm{m}$) for signal (S), idler (I) and pump (P) mode for the phase-matched Z-cut structure. (a) $\theta = 45°$, (b) $\theta = 90°$. All modes are power normalized, i.e., $\int S_x \mathrm{d}A = 1\,\mathrm{W}$.

κ-coefficient are displayed in Table 9.3. The highest value is achieved for the Z-cut structure with the $\mathrm{TE}_{2,0}$ pump mode, angle $\theta = 90°$ and a magnitude of $|\kappa| = 58.51\,\mathrm{W}^{-1/2}\,\mathrm{m}^{-1}$, which is comparable to bulk LN [192]. The phase-matching is now directly fulfilled. Thus, a periodic poling is not required anymore, but signal and idler photons do not propagate together because of different effective refractive indices.

	X-cut		Z-cut	
	45°	90°	45°	90°
pump	$TM_{1,1}$	$TM_{1,1}$	$TE_{1,1}$	$TE_{2,0}$
$\lvert\kappa\rvert[W^{-1/2}\,m^{-1}]$	1.58	2.80	21.99	58.51

Table 9.3: Calculated coefficients $|\kappa|$ for the X-cut and Z-cut structure ($\theta = 45°$ and $\theta = 90°$) for suitable phase-matched pump modes. Signal and idler modes are assumed to be the $TM_{0,0}$ and $TE_{0,0}$ mode, respectively. Corresponding field plots are shown in Figure 9.5 and Figure 9.6.

9.4 Oblique excitation pumpscheme

Another possibility to fulfill the phase-matching is by considering a different type of excitation. Before, the pump mode was fully guided by the rib waveguide. Now, we want to come back to our approach of semi-guided waves in slab waveguide structures, as introduced in Section 2.3. Instead of defining the pump mode as a guided mode of the rib waveguide, it is possible to excite the structure from the left with an incoming semi-guided wave at oblique angles of incidence. The oblique wave is then propagating and interfering between the rib edges and, at specific incidence angles, excites a mode in the rib waveguide – a leaky pump mode. Additionally, trenches are etched next to the rib to act as reflectors and amplify the field amplitude in the central part further. Signal and idler remain guided modes of the rib waveguide.

A schematic sketch is shown in Figure 9.7 of the cross section (a) and the top view (b). Identical to Figure 9.1, the geometry parameters are again given by w, τ, h and $\theta = 90°$. The trenches are etched at a distance γ next to the rib and have a rather arbitrary width of $s = 50\,\text{nm}$ (the value can also be adapted to wider trenches). The incoming wave is the fundamental TE mode guided at oblique angles of propagation φ. Additionally, corresponding field pattern and propagation directions for signal, idler and pump modes are illustrated in the sketch.

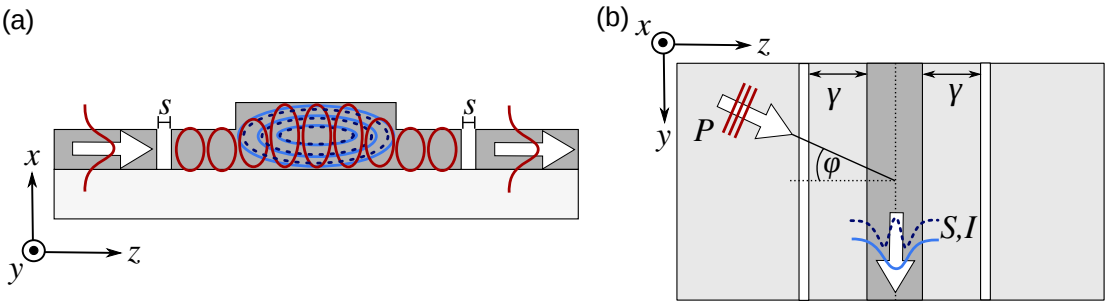

Figure 9.7: Oblique excitation of the LNOI rib waveguide structure for the X-cut configuration. (a) Cross section view; parameters are identical to Figure 9.1 with additional trenches of width s and distance γ next to the rib waveguide. (b) Top view; oblique excitation at angle φ. Signal (S), idler (I) and pump (P) mode profiles are illustrated.

Before simulating the structure, some theoretical considerations are necessary. The pump mode is propagating in the y-z-plane (X-cut) at oblique angles of incidence φ with – in general – non-zero wavenumbers k_y and k_z, depending on φ. To take into account the anisotropy of the LN slab of thickness $\tau - h$, for the present approximate reasoning, we distinguish two cases: if the incoming wave is fully propagating in y-direction, the relevant refractive index seen by

the TE wave (with electric field component E_z) is given by the ordinary value n_e. Otherwise, if the wave is propagating only in z-direction (with non-zero electric field component E_y), the structure sees the extraordinary refractive index n_o. Therefore, we identify with N_o and N_e the effective refractive indices for the two slab waveguide configurations with either n_o or n_e core index. Thus, by considering oblique excitation, both values have influence on the wavenumbers given by $k_y = k_0 N_{\text{eff}} \sin\varphi$ and $k_z = k_0 N_{\text{eff}} \cos\varphi$. Here, $k_0 = \frac{2\pi}{\lambda_p}$ corresponds to the pump wavelength and the oblique effective refractive index N_{eff} is approximated as

$$N_{\text{eff}} \approx \sqrt{N_e^2 \sin^2\varphi + N_o^2 \cos^2\varphi}. \tag{9.25}$$

For efficient resonant excitation of the leaky pump wave, the wavenumber of the incoming slab mode in y-direction k_y has to match the real part of the wavenumber $k_p = k_0 N_p$ of the corresponding pump mode. Thus,

$$k_0 \text{Re}\{N_p\} = k_0 N_{\text{eff}} \sin\varphi. \tag{9.26}$$

Now also considering the phase-matching $\Delta k = k_p - k_s - k_i = 0$ with $\lambda_s = \lambda_i = 2\lambda_p$ yields the equation

$$2\sin\varphi \sqrt{N_e^2 \sin^2\varphi + N_o^2 \cos^2\varphi} - N_s - N_i = 0, \tag{9.27}$$

which determines the incidence angle φ for given values of N_s and N_i. Note that the former considerations concern only the real parts of k_p.

As an advantage of this excitation scheme, the angle of incidence can be adjusted to fulfill the phase-matching condition for quite arbitrary geometry. Rather randomly, we fix the width $w = 2000\,\text{nm}$, the height $\tau = 700\,\text{nm}$ and the etch depth $h = 450\,\text{nm}$ so that the $\text{TM}_{0,0}$ mode and the $\text{TE}_{2,0}$ mode, serving as the signal and idler modes, are guided in the structure. The precise fundamental ordinary N_o and extraordinary N_e effective refractive index values of the adjoining slab waveguide modes of thickness $\tau - h = 0.25\,\mu\text{m}$ are displayed in Table 2.1. We excite the structure with the fundamental TE slab mode.

The trench distance γ was also chosen quite randomly, at first. The mode indices of the signal and idler fields determine the incidence angle φ (c.f. Eq. (9.27)) at which the structure is excited and that determines the real part of the corresponding pump mode (see Eq. (9.26)). For fixed incidence angle, the distance γ of the trenches is then arranged such that full transmission is achieved. This leads to strong field intensities in the central rib region.

The resulting modes for the configuration that fulfill the phase-matching condition are shown in Figure 9.8. The corresponding incidence angle is $\varphi = 70.24°$ and the trench distance was determined as $\gamma = 641.4\,\text{nm}$, which leads to a transmittance of $T > 0.99$. As mentioned before, the corresponding pump mode is a leaky mode with complex wavenumber or effective refractive index.

We are aware that this section considers a completely different excitation scheme. Thus, the κ-coefficients are not directly comparable to those calculated in Sections 9.2–9.3. Furthermore, normalization of the leaky pump mode is difficult, as the field profile is not limited to a finite domain. To that end, we normalize the leaky pump mode to the size of the computational

domain, which, of course, is variable and thus the normalization coefficient N_3 is not uniquely defined. However, the amplitude of the leaky mode is only varying slightly when changing the computational domain (increasing the computational domain in z-direction by $1\ \mu$m decreases the field amplitude of the "normalized" mode in the range of 0.005). This is due to the presence of the trenches that localize the main field amplitude in the region of the rib waveguide. Thus, we can compare the coupling coefficients up to a certain degree.

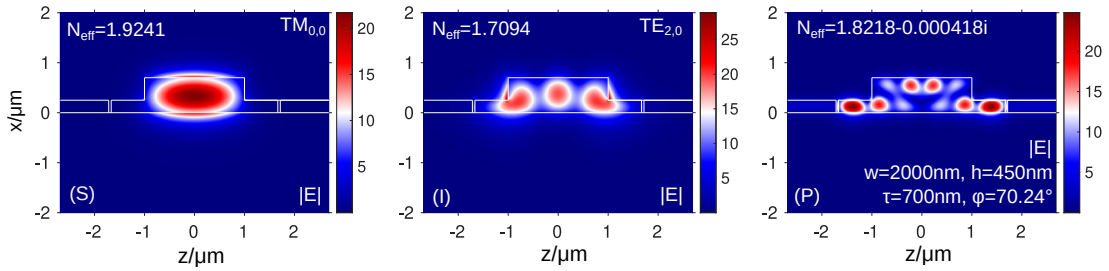

Figure 9.8: Field plots of the absolute electric field value $|\mathbf{E}|$ (in $\mathrm{V}/\ \mu\mathrm{m}$) for signal (S), idler (I) and leaky pump (P) modes for the X-cut configuration with oblique excitation. All modes are power normalized, i.e., $\int S_y \mathrm{d}A = 1\,\mathrm{W}$.

Considering the "normalized" leaky pump mode leads to a magnitude of $|\kappa| = 9.29\,\mathrm{W}^{-1/2}\,\mathrm{m}^{-1}$. Alternatively, since we actually excite the structure with a port from the left that has an input power of $1\,\mathrm{W/m}$, the value of the pump amplitude is fixed to $a_3 \approx 1.76 \times 10^4\,\mathrm{W}^{1/2}$. Thus, we can identify $|\kappa'| = |\kappa a_3| \approx 1.64 \times 10^5\,\mathrm{m}^{-1}$ (cf. Eq. (9.16)). The value for $|\kappa|$ is (up to some degree) comparable to the previous results in Sections 9.2–9.3 and thus does not lead to stronger interaction of the fields.

It should be noted that we chose a rather arbitrary structure for our calculations and only considered the X-cut configuration, so there may be structures with even better performance. Furthermore, the transmission values are very sensitive to changes in the distance of the trenches. For the fabrication of such a structure, further investigations are necessary. For the purpose of this work, the aim was to determine whether an interaction is possible or not, i.e., values other than zero occur. Hence, we can state that oblique excitation of the LNOI rib waveguide can lead to nonlinear interaction of the fields.

Chapter 10

Conclusion and outlook

In this work, we discuss different semi-analytical and numerical methods to describe the wave propagation in integrated optical waveguides. Initially, we briefly recapitulate some basic concepts of optical waveguide theory, starting with Maxwell's equations, dielectric slab waveguides and optical fibers. We are interested in the excitation of 2.5-D slab waveguide configurations with semi-guided waves at oblique angles of propagation. Modal properties are derived and critical angles are identified beyond which power transfer to specific outgoing modes is suppressed. Thus, the structures operate without losses. Furthermore, we discuss the excitation of laterally limited 3-D wave bundles in these 2-D structures by assuming wide and shallow etched rib waveguides placed in front of the configurations. The subsequent topics of this thesis make use of this theory and can be divided in three parts:

Oblique excitation of 2-D slab waveguide configurations:

Our investigations concern dielectric bent slab waveguides that support a continuum of full vectorial spiral modes. A semi-analytical ansatz is derived, leading to an eigenvalue equation that needs to be solved for complex wavenumbers. Our approach covers the whole range from bend modes at normal incidence with pronounced radiation losses, over the lesser damped spiral modes, to the lossless OAM modes at angles larger than the critical angle. Results for low and high refractive index contrasts are presented, including the calculated complex wavenumbers and the corresponding mode profiles. For the high refractive index contrast, the mode confinement increases so that the effect of the curvature becomes visible only at smaller bends. For increasing curvature radius and incidence angle, we observe a reduction in losses and even almost lossless spiral modes at angles smaller than the critical angle.

Connecting straight slab waveguides with bent segments results in the considered corner and step configurations. We are searching for structures that satisfy the resonance condition at full transmission for different angles of incidence, radii of curvature and vertical step heights. For large radii the incoming wave is almost completely transmitted for arbitrary angles and heights, while substantial reflections are observed for small radii. Here, full transmission is only achieved for certain heights and angles, as a Fabry-Pérot-like resonance effect appears when scanning over the step height.

To consider more realistic 3-D settings, the step structure is further investigated for incoming

laterally limited bundles of semi-guided waves. Rib waveguides are placed in front and at the output to calculate the 3-D transmittances, which depend strongly on the beam width. To achieve results comparable to the 2-D case, a relatively wide range of wavenumbers have to fulfill the resonance condition. This is mainly only valid for larger curvature radii, where the resonance effect has little influence. For small curvature radii, slightly larger rib widths are required. Thus, 3-D bend structures with comparatively small lateral widths can achieve high transmittances.

Furthermore, a four-port lossless microresonator with either one or two standing-wave type optical rectangular micro-strip cavities is demonstrated as a power divider or add-drop filter. We observe resonance behavior for specific incidence angles, fixed gap distances and rather arbitrary cavity dimensions. For a single cavity at resonance, the power is equally dropped to each of the four output ports, as the incoming mode evanescently excites the cavity mode which in turn radiates back evenly in the upper and lower slabs. Assuming two identical cavities of specific separation, the structure is able to transport the complete input power to the forward drop with full transmission. The strength of the interaction between slab and cavity depends strongly on the gap distance. Furthermore, we briefly introduce resonators with a circular cavity. At resonance, degenerate high angular order OAM modes are evanescently excited by the incoming oblique semi-guided wave of the adjoining slab waveguide.

Slab waveguide lens:

A stepwise angular spectrum method is presented to calculate the wave propagation in 3-D planar, dielectric slab waveguide lenses. The method approximates the curved surface by a finite number of flat, plane elements, tangential to the interface. For each element, its angular spectrum determines the field behavior of the reflected and transmitted waves. Superposition of the partial contributions leads to the overall solution. We study the configurations in both, 2-D and 3-D. In 2-D, the configuration consists of different materials separated by a curved interface, while in 3-D, slab waveguides with different heights connected by curved surfaces are considered. For the latter, the method is used in combination with vectorial 2.5-D COMSOL solutions of the cross section for achieving full vectorial 3-D solutions. For validation, the presented examples are compared to rigorous 3-D FEM solutions and a substantial lower computational effort is observed.

Due to the versatility and efficiency of our SASM approach, optimization algorithms are easily applied to our method. The advantage is that the field in the sectional area can be evaluated without having to calculate the entire 3-D field, which is useful for an efficient and fast optimization. We apply a genetic and pattern search algorithm implemented in MATLAB. The results are shown for an optimized maximum outgoing field amplitude to reduce the focal beam width. Here, we just demonstrate the use of optimization tools on our method. This can be further extended when applying alternative optimization tools, e.g., a multi objective optimizer or by adjusting the cost function to yield even better results depending on the type of application.

Additionally, one could study 3-D slab waveguide lenses with “thick” incoming and outgoing waveguides and an etched, thin middle part. In order to focus, the lens must be of concave shape. Applying the SASM is straightforward and similar to the convex lens configurations considered in this work. Both configurations can be easily compared, e.g., concerning critical angles, losses or polarization coupling.

Integrated waveguides used for quantum optics:

A unidirectional finite element modal matching method is presented to calculate the wave propagation in 3-D multiscale tapered waveguides. The method is based on a staircase approximation of the taper, where eigenmodes of the 2-D cross sections calculated with COMSOL are propagated along the segments. We consider titanium in-diffused lithium niobate waveguides that guide fundamental modes with a field maximum some micrometers below the waveguide surface. For photon absorption, superconducting nanowires are placed on top of the surface. To pull up the mode profile closer to the nanowires and increase the detection rate, an additional silicon layer of tapered shape is added. Examples for different taper geometries using the modal matching method are shown. We are interested in high transmittances to the silicon mode to increase the detection rate. Considering the coupling efficiency of the structure along the taper width allows to predict an optimized taper shape that consists of three parts with a large, strong coupling efficient middle section. To validate our suggestions, we apply a particle swarm optimization algorithm implemented in MATLAB. The results fit to the predicted coupling efficient shape.

Finally, the nonlinear interaction of waves in LNOI rib waveguides is studied, with emphasis on the parametric down-conversion process. By suitably varying the rib geometry, degenerate modes can be identified that directly satisfy the phase-matching condition (but require a higher order pump mode). Alternatively, guided modes of lower order are quasi phase-matched by periodic poling of the waveguide. In both cases, strong nonlinear interaction is identified, where the pump, signal and idler modes are guided by the rib waveguide. Furthermore, an alternative scheme has been proposed, where the structure is excited via an oblique semi-guided pump mode that is guided by the adjoining slab of the rib waveguide. By adjusting the angle of incidence accordingly, the phase matching can be directly fulfilled. For fabrication purposes, further investigations are necessary, but we could confirm that, in principle, the oblique pump scheme leads to nonlinear interaction of the involved fields. However, the examples in this work are not yet optimized and there may exist structures that show even stronger interaction.

Literature

[1] R. G. Hunsperger. *Integrated optics*, volume 4. Springer, 1995.

[2] A. H. Atabaki, S. Moazeni, F. Pavanello, H. Gevorgyan, J. Notaros, L. Alloatti, M. T. Wade, C. Sun, S. A. Kruger, H. Meng, et al. Integrating photonics with silicon nanoelectronics for the next generation of systems on a chip. *Nature*, 556(7701):349–354, 2018.

[3] R. Soref. The past, present, and future of silicon photonics. *IEEE Journal of Selected Topics in Quantum Electronics*, 12(6):1678–1687, 2006.

[4] W. Bogaerts, R. Baets, P. Dumon, V. Wiaux, S. Beckx, D. Taillaert, B. Luyssaert, J. Van Campenhout, P. Bienstman, and D. Van Thourhout. Nanophotonic waveguides in silicon-on-insulator fabricated with CMOS technology. *Journal of Lightwave Technology*, 23(1):401–412, 2005.

[5] S. Wu, X. Mu, L. Cheng, S. Mao, and H. Y. Fu. State-of-the-art and perspectives on silicon waveguide crossings: A review. *Micromachines*, 11(3):326, 2020.

[6] X. Chen, C. Li, and H. K. Tsang. Device engineering for silicon photonics. *NPG Asia Materials*, 3(1):34–40, 2011.

[7] S. K. Selvaraja and P. Sethi. Review on optical waveguides. *Emerging Waveguide Technology*, 95, 2018.

[8] K. Okamoto. *Fundamentals of Optical Waveguides*. Academic Press, SanDiego, 2000.

[9] C. Vassallo. *Optical Waveguide Concepts*. Elsevier, Amsterdam, 1991.

[10] M. Hammer, L. Ebers, and J. Förstner. Oblique evanescent excitation of a dielectric strip: A model resonator with an open optical cavity of unlimited Q. *Optics Express*, 27(7):9313–9320, 2019.

[11] M. Hammer, L. Ebers, A. Hildebrandt, A. Alhaddad, and J. Förstner. Oblique semi-guided waves: 2-D integrated photonics with negative effective permittivity. *2018 IEEE 17th International Conference on Mathematical Methods in Electromagnetic Theory (MMET)*, pages 5–9, 2018.

[12] M. Hammer, L. Ebers, and J. Förstner. Oblique quasi-lossless excitation of a thin silicon slab waveguide: a guided-wave variant of an anti-reflection coating. *Journal of the Optical Society of America B*, 36(9):2395–2401, 2019.

[13] L. Ebers, M. Hammer, and J. Förstner. Oblique incidence of semi-guided planar waves on slab waveguide steps: effects of rounded edges. *Optics Express*, 26(14):18621–18632, 2018.

[14] M. Hammer, A. Hildebrandt, and J. Förstner. Full resonant transmission of semi-guided planar waves through slab waveguide steps at oblique incidence. *Journal of Lightwave Technology*, 34(3):997–1005, 2016.

[15] M. Hammer. Oblique incidence of semi-guided waves on rectangular slab waveguide discontinuities: A vectorial QUEP solver. *Optics Communications*, 338:447–456, 2015.

[16] M. Hammer, A. Hildebrandt, and J. Förstner. How planar optical waves can be made to climb dielectric steps. *Optics Letters*, 40(16):3711–3714, 2015.

[17] F. Çivitci, M. Hammer, and H. J. W. M. Hoekstra. Semi-guided plane wave reflection by thin-film transitions for angled incidence. *Optical and Quantum Electronics*, 46(3):477–490, 2014.

[18] L. Ebers, M. Hammer, and J. Förstner. Spiral modes supported by circular dielectric tubes and tube segments. *Optical and Quantum Electronics*, 49(4):176, 2017.

[19] M. Hammer, L. Ebers, and J. Förstner. Resonant evanescent excitation of guided waves with high-order optical angular momentum. *Journal of the Optical Society of America B*, 38(5):1717–1728, 2021.

[20] M. Hammer, L. Ebers, and J. Förstner. Configurable lossless broadband beam splitters for semi-guided waves in integrated silicon photonics. *OSA Continuum*, 2021. accepted.

[21] M. Hammer, L. Ebers, and J. Förstner. Hybrid coupled mode modelling of the evanescent excitation of a dielectric tube by semi-guided waves at oblique angles. *Optical and Quantum Electronics*, 52(472), 2020.

[22] COMSOL Multiphysics GmbH, Göttingen, Germany. https://www.comsol.de.

[23] M. Hanke-Bourgeois. *Grundlagen der Numerischen Mathematik und des Wissenschaftlichen Rechnens*. Vieweg+Teubner Verlag, 2008.

[24] W. Arendt and K. Urban. *Partielle Differenzialgleichungen*. Springer Berlin Heidelberg, 2018.

[25] P. Prakash Koonath and B. Jalali. Multilayer 3-D photonics in silicon. *Optics Express*, 15(20):12686–12691, 2007.

[26] P. Koonath, T. Indukuri, and B. Jalali. Monolithic 3-D silicon photonics. *Journal of Lightwave Technology*, 24(4):1796–1804, 2006.

[27] N. Sherwood-Droz and M. Lipson. Scalable 3D dense integration of photonics on bulk silicon. *Optics Express*, 19(18):17758–17765, 2011.

[28] L. Ebers, M. Hammer, M. B. Berkemeier, A. Menzel, and J. Förstner. Coupled microstrip-cavities under oblique incidence of semi-guided waves: a lossless integrated optical add-drop filter. *OSA Continuum*, 2(11):3288–3298, 2019.

[29] I. Chremmos, N. Uzunoglu, and O. Schwelb, editors. *Photonic Microresonator Research and Applications*. Springer Series in Optical Sciences, Vol. 156. Springer, London, 2010.

[30] K. Iizuka. *Engineering Optics*, volume 35. Springer, 2008.

[31] S. Kou, C. Sheppard, and J. Lin. Calculation of the volumetric diffracted field with a three-dimensional convolution: the three-dimensional angular spectrum method. *Optics Letters*, 38:5296–8, 2013.

[32] T. Shimobaba, N. Masuda, and T. Ito. Arbitrary shape surface Fresnel diffraction. *Optics Express*, 20(8):9335–9340, 2012.

[33] S. Odate, C. Koike, H. Toba, T. Koike, A. Sugaya, K. Sugisaki, K. Otaki, and K. Uchikawa. Angular spectrum calculations for arbitrary focal length with a scaled convolution. *Optics Express*, 19(15):14268–14276, 2011.

[34] Y. Wang, S. Yan, A. T. Friberg, D. Kuebel, and T. D. Visser. Electromagnetic diffraction theory of refractive axicon lenses. *Journal of the Optical Society of America A*, 34(7):1201–1211, 2017.

[35] P. Wu and T. Stepinski. Extension of the angular spectrum approach to curved radiators. *The Journal of the Acoustical Society of America*, 105(5):2618–2627, 1999.

[36] K. Yamamoto, Y. Ichihashi, T. Senoh, R. Oi, and T. Kurita. Calculating the Fresnel diffraction of light from a shifted and tilted plane. *Optics Express*, 20(12):12949–12958, 2012.

[37] K. Matsushima. Shifted angular spectrum method for off-axis numerical propagation. *Optics Express*, 18(17):18453–18463, 2010.

[38] S. De Nicola, A. Finizio, G. Pierattini, P. Ferraro, and D. Alfieri. Angular spectrum method with correction of anamorphism for numerical reconstruction of digital holograms on tilted planes. *Optics Express*, 13:9935–40, 2005.

[39] J. Stock, N. G. Worku, and H. Gross. Coherent field propagation between tilted planes. *Journal of the Optical Society of America A*, 34(10):1849–1855, 2017.

[40] K. Matsushima, H. Schimmel, and F. Wyrowski. Fast calculation method for optical diffraction on tilted planes by use of the angular spectrum of plane waves. *Journal of the Optical Society of America A*, 20(9):1755–1762, 2003.

[41] L. Onural. Exact solution for scalar diffraction between tilted and translated planes using impulse functions over a surface. *Journal of the Optical Society of America A*, 28(3):290–295, 2011.

[42] S. H. Wiersma, P. Török, T. D. Visser, and P. Varga. Comparison of different theories for focusing through a plane interface. *Journal of the Optical Society of America A*, 14(7):1482–1490, 1997.

[43] S. Guha and G. D. Gillen. Vector diffraction theory of refraction of light by a spherical surface. *Journal of the Optical Society of America B*, 24(1):1–8, 2007.

[44] E. Şahin and L. Onural. Scalar diffraction field calculation from curved surfaces via Gaussian beam decomposition. *Journal of the Optical Society of America A*, 29(7):1459–1469, 2012.

[45] G. B. Esmer, L. Onural, and H. M. Ozaktas. Exact diffraction calculation from fields specified over arbitrary curved surfaces. *Optics Communications*, 284(24):5537 – 5548, 2011.

[46] C.-Y. Hwang, S. Oh, I.-K. Jeong, and H. Kim. Stepwise angular spectrum method for curved surface diffraction. *Optics Express*, 22(10):12659–12667, 2014.

[47] J.W. Goodman. *Introduction to Fourier Optics*. MaGraw-Hill, 2nd edition, 1996.

[48] M. Born and E. Wolf. *Principles of Optics, 7th. ed.* Cambridge University Press, Cambridge, UK, 1999.

[49] G. Kirchhoff. Zur Theorie der Lichtstrahlen. *Annalen der Physik*, 254(4):663–695, 1883.

[50] R. W. Boyd. *Nonlinear Optics, Third Edition*. Academic Press, Inc., USA, 3rd edition, 2008.

[51] W. Sohler, H. Hu, R. Ricken, V. Quiring, C. Vannahme, H. Herrmann, D. Büchter, S. Reza, W. Grundkötter, S. Orlov, H. Suche, R. Nouroozi, and Y. Min. Integrated optical devices in lithium niobate. *Optics & Photonics News*, 19(1):24–31, 2008.

[52] J. Wang, F. Sciarrino, A. Laing, and M. G. Thompson. Integrated photonic quantum technologies. *Nature Photonics*, 14(5):273–284, 2019.

[53] J. P. Höpker, V. B. Verma, M. Protte, R. Ricken, V. Quiring, C. Eigner, L. Ebers, M. Hammer, J. Förstner, C. Silberhorn, R. P. Mirin, S. Woo Nam, and T. J. Bartley. Integrated superconducting nanowire single-photon detectors on titanium in-diffused lithium niobate waveguides. *Journal of Physics: Photonics*, 3(3):034022, 2021.

[54] J. P. Höpker, M. Bartnick, E. Meyer-Scott, F. Thiele, S. Krapick, N. Montaut, M. Santandrea, H. Herrmann, S. Lengeling, R. Ricken, V. Quiring, T. Meier, A. Lita, V. Verma, T. Gerrits, S. Woo Nam, C. Silberhorn, and T. J. Bartley. Towards integrated superconducting detectors on lithium niobate waveguides. *arXiv:1708.06232 [physics.ins-det]*, 2017.

[55] M. Protte, L. Ebers, M. Hammer, J. P. Höpker, M. Albert, V. Quiring, C. Meier, J. Förstner, C. Silberhorn, and T. J. Bartley. Towards semiconductor-superconductor-crystal hybrid integration for quantum photonics. In *OSA Quantum 2.0 Conference*, page QTh7A.8. Optical Society of America, 2020.

[56] G.-T. Xue, Y.-F. Niu, X. Liu, J.-C. Duan, W. Chen, Y. Pan, K. Jia, X. Wang, H.-Y. Liu, Y. Zhang, et al. Ultrabright multiplexed energy-time-entangled photon generation from lithium niobate on insulator chip. *Physical Review Applied*, 15(6):064059, 2021.

[57] J.-C. Duan, J.-N. Zhang, Y.-J. Zhu, C.-W. Sun, Y.-C. Liu, P. Xu, Z. Xie, Y.-X. Gong, and S.-N. Zhu. Generation of narrowband counterpropagating polarization-entangled photon pairs based on thin-film lithium niobate on insulator. *JOSA B*, 37(7):2139–2145, 2020.

[58] P. R. Sharapova, K. H. Luo, H. Herrmann, M. Reichelt, T. Meier, and C. Silberhorn. Toolbox for the design of $LiNbO_3$-based passive and active integrated quantum circuits. *New Journal of Physics*, 19(12):123009, 2017.

[59] N. Montaut, L. Sansoni, E. Meyer-Scott, R. Ricken, V. Quiring, H. Herrmann, and C. Silberhorn. High-efficiency plug-and-play source of heralded single photons. *Physical Review Applied*, 8(2), 2017.

[60] O. Mitomi, K. Kasaya, and H. Miyazawa. Design of a single-mode tapered waveguide for low-loss chip-to-fiber coupling. *IEEE Journal of Quantum Electronics*, 30(8):1787–1793, 1994.

[61] M. Reed, P. Sewell, T. M. Benson, and P. C. Kendall. Efficient propagation algorithm for 3D optical waveguides. *IEE Proceedings-Optoelectronics*, 145(1):53–58, 1998.

[62] P. Suchoski and R. V. Ramaswamy. Design of single-mode step-tapered waveguide sections. *IEEE Journal of Quantum Electronics*, 23(2):205–211, 1987.

[63] J. Mu and W.-P. Huang. Complex coupled-mode theory for tapered optical waveguides. *Optics Letters*, 36(6):1026–1028, 2011.

[64] D. Dai, Y. Tang, and J. E. Bowers. Mode conversion in tapered submicron silicon ridge optical waveguides. *Optics Express*, 20(12):13425–13439, 2012.

[65] Y. Fu, T. Ye, W. Tang, and T. Chu. Efficient adiabatic silicon-on-insulator waveguide taper. *Photonics Research*, 2(3):A41–A44, 2014.

[66] B. Luyssaert, P. Bienstman, P. Vandersteegen, P. Dumon, and R. Baets. Efficient nonadiabatic planar waveguide tapers. *Journal of Lightwave Technology*, 23(8):2462, 2005.

[67] H. Zhou, J. Sun, J. Gao, J. Jiang, and Y. Zhou. Design of compact and efficient polarization-insensitive taper coupler for SiGe photonic integration. *Optics Express*, 24(21):23784–23797, 2016.

[68] A. D. Olver, Institution of Electrical Engineers, P. J. B. Clarricoats, L. Shafai, and A. A. Kishk. *Microwave Horns and Feeds*. IEE electromagnetic waves series. IEE, 1994.

[69] N. Gisin, G. Ribordy, W. Tittel, and H. Zbinden. Quantum cryptography. *Reviews of Modern Physics*, 74(1):145, 2002.

[70] J. Wang, F. Sciarrino, A. Laing, and M. G. Thompson. Integrated photonic quantum technologies. *Nature Photonics*, 14(5):273–284, 2020.

[71] Y. Qi and Y. Li. Integrated lithium niobate photonics. *Nanophotonics*, 9(6):1287–1320, 2020.

[72] A. Boes, B. Corcoran, L. Chang, J. Bowers, and A. Mitchell. Status and potential of lithium niobate on insulator (LNOI) for photonic integrated circuits. *Laser & Photonics Reviews*, 12(4):1700256, 2018.

[73] A. Pan, C. Hu, C. Zeng, and J. Xia. Fundamental mode hybridization in a thin film lithium niobate ridge waveguide. *Optics Express*, 27(24):35659–35669, 2019.

[74] R. Luo, Y. He, H. Liang, M. Li, and Q. Lin. Highly tunable efficient second-harmonic generation in a lithium niobate nanophotonic waveguide. *Optica*, 5(8):1006–1011, 2018.

[75] L. Ebers, M. Hammer, and J. Förstner. Light diffraction in slab waveguide lenses simulated with the stepwise angular spectrum method. *Optics Express*, 28(24):36361–36379, 2020.

[76] L. Ebers, M. B. Berkemeier, A. Menzel, M. Hammer, and J. Förstner. Integrated optical add-drop filter based on oblique excitation of rectangular microstrip-cavities. 8th doctoral conference on optics, DoKDoK 2019, Eisenach, Germany, Proceedings, 2019.

[77] L. Ebers, M. Hammer, J.P. Höpker, T. Bartley, and J. Förstner. Unidirectional vectorial eigenmode propagation for multiscale tapered waveguides in 3D. XXVII International Workshop on Optical Wave & Waveguide Theory and Numerical Modelling, OWTNM2019, Málaga, Spain, Proceedings 19, 2019.

[78] A. W. Snyder and J. D. Love. *Optical Waveguide Theory*. Chapman and Hall, London, New York, 1983.

[79] J. D. Jackson. *Classical Electrodynamics, 3rd. ed.* Wiley, New York, 1998.

[80] M. Hammer. OMS — 1-D mode solver for dielectric multilayer slab waveguides. http://www.computational-photonics.eu/oms.html.

[81] N. Bozinovic, Y. Yue, Y. Ren, M. Tur, P. Kristensen, H. Huang, A. E. Willner, and S. Ramachandran. Terabit-scale orbital angular momentum mode division multiplexing in fibers. *Science*, 340(6140):1545–1548, 2013.

[82] L. Wang, P. Vaity, S. Chatigny, Y. Messaddeq, L. A. Rusch, and S. LaRochelle. Orbital-angular-momentum polarization mode dispersion in optical fibers. *Journal of Lightwave Technology*, 34(8):1661–1671, 2016.

[83] S. D. Johnson, Z. Ma, M. J. Padgett, and S. Ramachandran. Measurement of the spin-orbit coupling interaction in ring-core optical fibers. *OSA Continuum*, 2(10):2975–2982, 2019.

[84] C. Manolatou, M. J. Khan, S. Fan, P. R. Villeneuve, H. A. Haus, and J. D. Joannopoulos. Coupling of modes analysis of resonant channel add-drop filters. *IEEE Journal of Quantum Electronics*, 35(9):1322–1331, 1999.

[85] M. Abramowitz and I. A. Stegun. *Handbook of Mathematical Functions*. National Bureau of Standards, Washington, D.C., 1964.

[86] A. Kapoor and G. S. Singh. Mode classification in cylindrical dielectric waveguides. *Journal of Lightwave Technology*, 18(6):849–852, 2000.

[87] D. Marcuse. *Theory of Dielectrical Optical Waveguides, 2nd edition*. Academic Press, London, 1991.

[88] E. A. Bezus, L. L. Doskolovich, D. A. Bykov, and V. A. Soifer. Spatial integration and differentiation of optical beams in a slab waveguide by a dielectric ridge supporting high-Q resonances. *Optics Express*, 26(19):25156–25165, 2018.

[89] G. Sewell. *The numerical solution of ordinary and partial differential equations*, volume 75. John Wiley & Sons, 2005.

[90] RF Module User's Guide, version 5.4, COMSOL, Inc, www.comsol.com.

[91] COMSOL Multiphysics Reference Manual, version 5.5, COMSOL, Inc, www.comsol.com.

[92] S. G. Johnson. Notes on perfectly matched layers (PMLs). *arXiv:2108.05348 [cs.CE]*, 2021.

[93] L. Ebers. Oblique semi-guided waves: Modeling quasi-2-D waveguide optics with COMSOL. *Master Thesis, Paderborn University*, 2017.

[94] L. Ebers. Schiefwinklige Lichtausbreitung in gekrümmten dielektrischen Schichtwellenleitern. *Bachelor Thesis, Paderborn University*, 2015.

[95] M. K. Chin, D. Y. Chu, and S.-T. Ho. Estimation of the spontaneous emission factor for microdisk lasers via the approximation of whispering gallery modes. *Journal of Applied Physics*, 75(7):3302–3307, 1994.

[96] J. A. Lock. Morphology-dependent resonances of an infinitely long circular cylinder illuminated by a diagonally incident plane wave or a focused Gaussian beam. *Journal of the Optical Society of America A*, 14(3):653–661, 1997.

[97] H. G. L. Schwefel, A. D. Stone, and H. E. Tureci. Polarization properties and dispersion relations for spiral resonances of a dielectric rod. *Journal of the Optical Society of America B*, 22(11):2295–2307, 2005.

[98] A. W. Poon, R. K. Chang, and J. A. Lock. Spiral morphology-dependent resonances in an optical fiber: effects of fiber tilt and focused Gaussian beam illumination. *Optics Letters*, 23(14):1105–1107, 1998.

[99] K. R. Hiremath, M. Hammer, R. Stoffer, L. Prkna, and J. Čtyroký. Analytical approach to dielectric optical bent slab waveguides. *Optical and Quantum Electronics*, 37(1-3):37–61, 2005.

[100] *Maple 2016* technical computing software. https://www.maplesoft.com/products/maple/.

[101] W. H. Press, S. A. Teukolsky, W. T. Vetterling, and B. P. Flannery. *Numerical Recipes in C, 2nd ed.* Cambridge University Press, 1992.

[102] R. A. Soref, E. Cortesi, F. Namavar, and L. Friedman. Vertically integrated silicon-on-insulator waveguides. *IEEE Photonics Technology Letters*, 3(1):22–24, 1991.

[103] R. Sun, M. Beals, A. Pomerene, J. Cheng, C.-Y. Hong, L. Kimerling, and J. Michel. Impedance matching vertical optical waveguide couplers for dense high index contrast circuits. *Optics Express*, 16(16):11682–11690, 2008.

[104] J. F. Bauters, M. L. Davenport, M. J. R. Heck, J. K. Doylend, A. Chen, A. W. Fang, and J. E. Bowers. Silicon on ultra-low-loss waveguide photonic integration platform. *Optics Express*, 21(1):544–555, 2013.

[105] P. Dong and A. G. Kirk. Compact grating coupler between vertically stacked silicon-on-insulator waveguides. volume 5357, pages 135–142, 2004.

[106] J. T. Bessette and D. Ahn. Vertically stacked microring waveguides for coupling between multiple photonic planes. *Optics Express*, 21(11):13580–13591, 2013.

[107] A. Hildebrandt, A. Alhaddad, M. Hammer, and J. Förstner. Oblique incidence of semi-guided waves on step-like folds in planar dielectric slabs: Lossless vertical interconnects in 3-D integrated photonic circuits. *Proceedings of SPIE*, 9750:9750 – 9750 – 7, 2016.

[108] B. E. Little, S. T. Chu, H. A. Haus, J. Foresi, and J.-P. Laine. Microring resonator channel dropping filters. *Journal of Lightwave Technology*, 15(6):998–1005, 1997.

[109] W. Bogaerts, P. De Heyn, T. Van Vaerenbergh, K. De Vos, S. Kumar Selvaraja, T. Claes, P. Dumon, P. Bienstman, D. Van Thourhout, and R. Baets. Silicon microring resonators. *Laser & Photonics Reviews*, 6(1):47–73, 2012.

[110] E. A. J. Marcatili. Slab-coupled waveguides. *The Bell System Technical Journal*, 53(4):645–674, 1974.

[111] D. R. Rowland and J. D. Love. Evanescent wave coupling of whispering gallery modes of a dielectric cylinder. *IEE Proceedings, Pt. J*, 140(3):177–188, 1993.

[112] M. K. Chin and S. T. Ho. Design and modeling of waveguide-coupled single-mode microring resonators. *Journal of Lightwave Technology*, 16(8):1433–1446, 1998.

[113] S. V. Boriskina and A. I. Nosich. Radiation and absorption losses of the whispering-gallery-mode dielectric resonators excited by a dielectric waveguide. *IEEE Transactions on Microwave Theory and Techniques*, 47(2):224–231, 1999.

[114] M. Hammer. Resonant coupling of dielectric optical waveguides via rectangular microcavities: The coupled guided mode perspective. *Optics Communications*, 214(1–6):155–170, 2002.

[115] M. Lohmeyer. Mode expansion modeling of rectangular integrated optical microresonators. *Optical and Quantum Electronics*, 34(5):541–557, 2002.

[116] E. A. Bezus, D. A. Bykov, and L. L. Doskolovich. Bound states in the continuum and high-Q resonances supported by a dielectric ridge on a slab waveguide. *Photonics Research*, 6(11):1084–1093, 2018.

[117] S. Fan, P. R. Villeneuve, J. D. Joannopoulos, and H. A. Haus. Channel drop tunneling through localized states. *Physical Review Letters*, 80(5):960–963, 1998.

[118] S. Fan, P. R. Villeneuve, J. D. Joannopoulos, M. J. Khan, C. Manolatou, and H. A. Haus. Theoretical analysis of channel drop tunneling processes. *Physical Review B*, 59(24):15882–15892, 1999.

[119] H. A. Haus and Y. Lai. Theory of cascaded quarter wave shifted distributed feedback resonators. *IEEE Journal of Quantum Electronics*, 28(1):205–213, 1992.

[120] M. A. Popović, C. Manolatou, and M. R. Watts. Coupling-induced resonance frequency shifts in coupled dielectric multi-cavity filters. *Optics Express*, 14(3):1208–1222, 2006.

[121] S. Fan, P. R. Villeneuve, J. D. Joannopoulos, and H. A. Haus. Channel drop filters in photonic crystals. *Optics Express*, 3(1):4–11, 1998.

[122] K. R. Hiremath and M. Hammer. Circular integrated optical microresonators: Analytical methods and computational aspects. In I. Chremmos, N. Uzunoglu, and O. Schwelb, editors, *Photonic Microresonator Research and Applications*, Springer Series in Optical Sciences, Vol. 156, pages 29–59. Springer, London, 2010.

[123] S. S. R. Oemrawsingh, J. A. W. van Houwelingen, E. R. Eliel, J. P. Woerdman, E. J. K. Verstegen, J. G. Kloosterboer, et al. Production and characterization of spiral phase plates for optical wavelengths. *Applied Optics*, 43(3):688–694, 2004.

[124] M. W. Beijersbergen, L. Allen, H. E. L. O. van der Veen, and J. P. Woerdman. Astigmatic laser mode converters and transfer of orbital angular momentum. *Optics Communications*, 96(1):123–132, 1993.

[125] L. Zhu and J. Wang. Arbitrary manipulation of spatial amplitude and phase using phase-only spatial light modulators. *Scientific Reports*, 4(1):1–7, 2014.

[126] Z. Lin, A. Wang, L. Xu, X. Zhang, B. Sun, C. Gu, and H. Ming. Generation of optical vortices using a helical fiber Bragg grating. *Journal of Lightwave Technology*, 32(11):2152–2156, 2014.

[127] L. Fang and J. Wang. Mode conversion and orbital angular momentum transfer among multiple modes by helical gratings. *IEEE Journal of Quantum Electronics*, 52(8):1–6, 2016.

[128] Y. Yan, J. Wang, L. Zhang, J.-Y. Yang, I. M. Fazal, N. Ahmed, B. Shamee, A. E. Willner, K. Birnbaum, and S. Dolinar. Fiber coupler for generating orbital angular momentum modes. *Optics Letters*, 36(21):4269–4271, 2011.

[129] J. Fan, J. Zhao, L. Shi, N. Xiao, and M. Hu. Two-channel, dual-beam-mode, wavelength-tunable femtosecond optical parametric oscillator. *Advanced Photonics*, 2(4):045001, 2020.

[130] M. Hammer. Guided wave interaction in photonic integrated circuits — a hybrid analytical / numerical approach to coupled mode theory. In A. Agrawal, T. Benson, R. DeLaRue, and G. Wurtz, editors, *Recent Trends in Computational Photonics*, volume 204 of *Springer Series in Optical Sciences*, chapter 3, pages 77–105. Springer, Cham, 2017.

[131] K. Huang, F. Qin, H. Liu, H. Ye, C.-W. Qiu, M. Hong, B. Luk'yanchuk, and J. Teng. Planar diffractive lenses: fundamentals, functionalities, and applications. *Advanced Materials*, 30(26):1704556, 2018.

[132] G. Hatakoshi, H. Inoue, K. Naito, S. Umegaki, and S. Tanaka. Optical waveguide lenses. *Optica Acta: International Journal of Optics*, 26(8):961–968, 1979.

[133] P. K. Tien, S. Riva-Sanseverino, R. J. Martin, and G. Smolinsky. Two-layered construction of integrated optical circuits and formation of thin-film prisms, lenses, and reflectors. *Applied Physics Letters*, 24(11):547–549, 1974.

[134] W. Chang and P. Ashley. Fresnel lenses in optical waveguides. *IEEE Journal of Quantum Electronics*, 16(7):744–754, 1980.

[135] D. W. Hewak and J. W. Y. Lit. Solution deposited optical waveguide lens. *Applied Optics*, 28(19):4190–4198, 1989.

[136] K. E. Spaulding and G. M. Morris. Achromatic waveguide lenses. *Applied Optics*, 30(18):2558–2569, 1991.

[137] K. E. Spaulding, G. M. Morris, and J. C. Brazas. Achromatic mode-index/diffractive waveguide lens. *Journal of Lightwave Technology*, 10(12):1855–1859, 1992.

[138] J. Nocedal and S. Wright. *Numerical Optimization*. Springer New York, 2006.

[139] M. K. Kim. Digital holographic microscopy. In *Digital Holographic Microscopy*, pages 149–190. Springer, 2011.

[140] J. Marques-Hueso, L. Sanchis, B. Cluzel, F. A. de Fornel, and J. P. Martínez-Pastor. Properties of integrated photonic lenses: bandwidth, chromatic aberration, and polarization dependence. *Optical Engineering*, 52(9):091710, 2013.

[141] L. Rayleigh. XII. On the manufacture and theory of diffraction-gratings. *The London, Edinburgh, and Dublin Philosophical Magazine and Journal of Science*, 47(310):81–93, 1874.

[142] G. B. Airy. On the diffraction of an object-glass with circular aperture. *Transactions of the Cambridge Philosophical Society*, 5:283, 1835.

[143] E. Abbe. Contributions to the theory of the microscope and the nature of microscopic vision. *SPIE Milestone Series*, 178:12–17, 2004.

[144] H. Ren and S.-T. Wu. *Introduction to adaptive lenses*, volume 75. John Wiley & Sons, 2012.

[145] R. G. González-Acuña and H. Chaparro Romo. General formula for bi-aspheric singlet lens design free of spherical aberration. *Applied Optics*, 57:9341, 2018.

[146] Y. Liu and X. Zhang. Recent advances in transformation optics. *Nanoscale*, 4(17):5277–5292, 2012.

[147] MATLAB Optimization Toolbox. *version 9.9.0 (R2020ba)*. The MathWorks Inc., Natick, Massachusetts, 2021.

[148] R. H. Byrd, J. C. Gilbert, and J. Nocedal. A trust region method based on interior point techniques for nonlinear programming. *Mathematical programming*, 89(1):149–185, 2000.

[149] R. H. Byrd, M. E. Hribar, and J. Nocedal. An interior point algorithm for large-scale nonlinear programming. *SIAM Journal on Optimization*, 9(4):877–900, 1999.

[150] R. A. Waltz, J. L. Morales, J. Nocedal, and D. Orban. An interior algorithm for nonlinear optimization that combines line search and trust region steps. *Mathematical programming*, 107(3):391–408, 2006.

[151] Y. J. Cao and Q. H. Wu. Teaching genetic algorithm using matlab. *International Journal of Electrical Engineering Education*, 36(2):139–153, 1999.

[152] O. Kramer. Genetic algorithms. In *Genetic Algorithm Essentials*, pages 11–19. Springer, 2017.

[153] D. E. Goldberg. Genetic algorithms in search, optimization, and machine learning. addison. *Reading*, 1989.

[154] A. L. Custódio, J. F. A. Madeira, A. I. F. Vaz, and L. N. Vicente. Direct multisearch for multiobjective optimization. *SIAM Journal on Optimization*, 21(3):1109–1140, 2011.

[155] P. Bratley and B. L. Fox. Algorithm 659: Implementing Sobol's quasirandom sequence generator. *ACM Transactions on Mathematical Software (TOMS)*, 14(1):88–100, 1988.

[156] M. Fleischer. The measure of pareto optima applications to multi-objective metaheuristics. In *International Conference on Evolutionary Multi-Criterion Optimization*, pages 519–533. Springer, 2003.

[157] M.G. Tanner, L. S. E. Alvarez, W. Jiang, R.J. Warburton, Z.H. Barber, and R.H. Hadfield. A superconducting nanowire single photon detector on lithium niobate. *Nanotechnology*, 23(50):505201, 2012.

[158] E. Smirnov, A. Golikov, P. Zolotov, V. Kovalyuk, M. Lobino, B. Voronov, A. Korneev, and G. Goltsman. Superconducting nanowire single-photon detector on lithium niobate. *Journal of Physics: Conference Series*, 1124:051025, 2018.

[159] A. Vetter, S. Ferrari, P. Rath, R. Alaee, O. Kahl, V. Kovalyuk, S. Diewald, G. N. Goltsman, S. Korneev, C. Rockstuhl, et al. Cavity-enhanced and ultrafast superconducting single-photon detectors. *Nano Letters*, 16(11):7085–7092, 2016.

[160] F. Marsili, V. B. Verma, J. A. Stern, S. Harrington, A. E. Lita, T. Gerrits, I. Vayshenker, B. Baek, M. D. Shaw, R. P. Mirin, and et al. Detecting single infrared photons with 93% system efficiency. *Nature Photonics*, 7(3):210–214, 2013.

[161] D. V. Reddy, R. R. Nerem, S. Woo Nam, R. P. Mirin, and V. B. Verma. Superconducting nanowire single-photon detectors with 98% system detection efficiency at 1550 nm. *Optica*, 7(12):1649–1653, 2020.

[162] Y. Hochberg, I. Charaev, S.-W. Nam, V. Verma, M. Colangelo, and K. K. Berggren. Detecting sub-GeV dark matter with superconducting nanowires. *Physics Review Letters*, 123:151802, 2019.

[163] C. M. Natarajan, M. G. Tanner, and R. H. Hadfield. Superconducting nanowire single-photon detectors: physics and applications. *Superconductor Science and Technology*, 25(6):063001, 2012.

[164] V. R. Almeida, R. R. Panepucci, and M. Lipson. Nanotaper for compact mode conversion. *Optics Letters*, 28(15):1302–1304, 2003.

[165] M. Lipson. Guiding, modulating, and emitting light on silicon-challenges and opportunities. *Journal of Lightwave Technology*, 23(12):4222–4238, 2005.

[166] J. Zou, Y. Yu, M. Ye, L. Liu, S. Deng, X. Xu, and X. Zhang. Short and efficient mode-size converter designed by segmented-stepwise method. *Optics Letters*, 39(21):6273–6276, 2014.

[167] G. L. James. Analysis and design of TE_{11}-to-HE_{11} corrugated cylindrical waveguide mode converters. *IEEE Transactions on Microwave Theory and Techniques*, 29(10):1059–1066, 1981.

[168] A. Milton and W. Burns. Mode coupling in optical waveguide horns. *IEEE Journal of Quantum Electronics*, 13(10):828–835, 1977.

[169] D. Marcuse. Radiation losses of tapered dielectric slab waveguides. *The Bell System Technical Journal*, 49(2):273–290, 1970.

[170] P. G. Suchoski and V. Ramaswamy. Exact numerical technique for the analysis of step discontinuities and tapers in optical dielectric waveguides. *Journal of the Optical Society of America A*, 3(2):194–203, 1986.

[171] A. R. Nelson. Coupling optical waveguides by tapers. *Applied Optics*, 14(12):3012–3015, 1975.

[172] A. Wexler. Solution of waveguide discontinuities by modal analysis. *IEEE Transactions on Microwave Theory and Techniques*, 15(9):508–517, 1967.

[173] P. H. Masterman and P. J. B. Clarricoats. Computer field-matching solution of waveguide transverse discontinuities. In *Proceedings of the Institution of Electrical Engineers*, volume 118, pages 51–63. IET, 1971.

[174] MATLAB. *version 9.9.0 (R2020b)*. The MathWorks Inc., Natick, Massachusetts, 2021.

[175] S. Sanna and W. G. Schmidt. Lithium niobate x-cut, y-cut, and z-cut surfaces from ab initio theory. *Physical Review B*, 81(21):214116, 2010.

[176] E. Strake, G.P. Bava, and I. Montrosset. Guided modes of Ti:$LiNbO_3$ channel waveguides: a novel quasi-analytical technique in comparison with the scalar finite-element method. *Journal of Lightwave Technology*, 6(6):1126–1135, 1988.

[177] R. S. Weis and T. K. Gaylord. Lithium niobate: Summary of physical properties and crystal structure. *Applied Physics A: Materials Science & Processing*, 37(4):191–203, 1985.

[178] J. Kennedy and R. C. Eberhart. A discrete binary version of the particle swarm algorithm. In *1997 IEEE International conference on systems, man, and cybernetics. Computational Cybernetics and Simulation*, volume 5, pages 4104–4108. IEEE, 1997.

[179] A. P. Engelbrecht. *Fundamentals of computational swarm intelligence*. John Wiley & Sons, Inc., 2006.

[180] J. Sadri and C. Y. Suen. A genetic binary particle swarm optimization model. In *2006 IEEE International Conference on Evolutionary Computation*, pages 656–663. IEEE, 2006.

[181] R. Poli, J. Kennedy, and T. Blackwell. Particle swarm optimization. *Swarm Intelligence*, 1(1):33–57, 2007.

[182] L. Ebers, A. Ferreri, M. Hammer, M. Albert, C. Meier, J. Förstner, and P. R. Sharapova. Flexible source of correlated photons based on LNOI rib waveguides. *arXiv:2110.10562 [quant-ph]*, 2021.

[183] S. Saravi, T. Pertsch, and F. Setzpfandt. Lithium niobate on insulator: An emerging platform for integrated quantum photonics. *Advanced Optical Materials*, page 2100789, 2021.

[184] F. Monteiro, A. Martin, B. Sanguinetti, H. Zbinden, and R. T. Thew. Narrowband photon pair source for quantum networks. *Optics Express*, 22(4):4371–4378, 2014.

[185] V. Prakash, L. C. Bianchet, M. T. Cuairan, P. Gomez, N. Bruno, and M. W. Mitchell. Narrowband photon pairs with independent frequency tuning for quantum light-matter interactions. *Optics Express*, 27(26):38463–38478, 2019.

[186] S. Carrasco, A. V. Sergienko, B. E. A. Saleh, M. C. Teich, J. P. Torres, and L. Torner. Spectral engineering of entangled two-photon states. *Physical Review A*, 73(6):063802, 2006.

[187] Y. Luo and K. T. Chan. Quantum cryptography with entangled multiphotons of the same polarization. *Physical Review A*, 70(4):042302, 2004.

[188] R. Ghosh, C. K. Hong, Z. Y. Ou, and L. Mandel. Interference of two photons in parametric down conversion. *Physical Review A*, 34(5):3962, 1986.

[189] Y. H. Shih, A. V. Sergienko, M. H. Rubin, T. E. Kiess, and C. O. Alley. Two-photon entanglement in type-II parametric down-conversion. *Physical Review A*, 50(1):23, 1994.

[190] M. H. Rubin, D. N. Klyshko, Y. H. Shih, and A. V. Sergienko. Theory of two-photon entanglement in type-II optical parametric down-conversion. *Physical Review A*, 50(6):5122, 1994.

[191] C. Couteau. Spontaneous parametric down-conversion. *Contemporary Physics*, 59(3):291–304, 2018.

[192] T. Suhara and M. Fujimura. *Waveguide Nonlinear-Optic Devices*. Springer-Verlag Berlin Heidelberg, 2003.

[193] M. Kolesik and J. V. Moloney. Nonlinear optical pulse propagation simulation: From Maxwell's to unidirectional equations. *Physical Review E*, 70(3):036604, 2004.

[194] C. Wang, C. Langrock, A. Marandi, C. Jankowski, M. Zhang, B. Desiatov, M. M. Fejer, and M. Lončar. Ultrahigh-efficiency wavelength conversion in nanophotonic periodically poled lithium niobate waveguides. *Optica*, 5(11):1438–1441, 2018.

[195] I. Shoji, T. Kondo, A. Kitamoto, M. Shirane, and R. Ito. Absolute scale of second-order nonlinear-optical coefficients. *JOSA B*, 14(9):2268–2294, 1997.

[196] C. M. Herzinger, B. Johs, W. A. McGahan, J. A. Woollam, and W. Paulson. Ellipsometric determination of optical constants for silicon and thermally grown silicon dioxide via a

multi-sample, multi-wavelength, multi-angle investigation. *Journal of Applied Physics*, 83(6):3323–3336, 1998.

[197] G. E. Jellison Jr. and F. A. Modine. Parameterization of the optical functions of amorphous materials in the interband region. *Applied Physics Letters*, 69(3):371–373, 1996.

List of Figures

List of Tables

Notations

Acronym	Meaning
ASM	Angular spectrum method
BEM	Boundary element method
BC	Boundary condition
CMOS	Complementary metal-oxide semiconductor
DFG	Difference-Frequency Generation
FDTD	Finite difference time domain method
FEM	Finite element method
FEMMM	Finite element modal matching method
GA	Genetic algorithm
FIT	Finite integration method
LN	Lithium niobate
LNOI	Lithium niobate on insulator
MMM	Modal matching method
OAM	Orbital angular momentum
OR	Optical rectification
PDC	Parametric down-conversion
PDE	Partial differential equation
PEC	Perfect electric conductor
PML	Perfectly matched layer
PSA	Pattern search algorithm
PSO	Particle swarm optimization
SASM	Stepwise angular spectrum method
SFG	Sum-frequency generation
SHG	Second-harmonic generation
SNSPD	Superconducting nanowire single photon detector
TEM	Transverse electromagnetic
TE	Transverse electric
Ti:LN	Titanium in-diffused lithium niobate
TM	Transverse magnetic

Symbols

Symbol	Meaning
$\mathbf{E}$	Electric field
$\mathbf{H}$	Magnetic field
$\mathbf{D}$	Electric displacement
$\mathbf{B}$	Magnetic flux density
$\mathbf{P}$	Polarization density
$\mathbf{J}$	Current density
t	Time
(x, y, z)	Cartesian coordinates
ω	Angular frequency
k_0	Vacuum wavenumber
c_0	Speed of light
λ_0	Vacuum wavelength
ϵ_0	Vacuum permittivity
μ_0	Vacuum permeability
$\mathbf{P}$	Polarization
$\mathbf{M}$	Magnetization
χ	Susceptibility
ϵ_r	Relative permittivity
μ_r	Relative permeability
k_x, k_y, k_z, k_θ	Wavenumbers in x-, y-, z-, θ-direction
$\mathbf{S}$	Poynting vector
n_c, n_s, n_f	Refractive indices (cladding, substrate, core)
N_{eff}	Effective refractive index
r	Curvature radius
(ρ, θ, y)	Cylindrical coordinates
ν	Angular order
P	Time-averaged power
φ	Incidence angle
$\varphi_s, \varphi_c, \varphi_m$	Critical incidence angles
φ_0	Primary incidence angle
k_{y_0}	Primary wavenumber
R	Reflectance
T	Transmittance